Author:
Reis, Teresa M D

Title:
Uncertainty Quantification and Management on Aircraft Weight Estimation

Uncertainty Quantification and Management on Aircraft Weight Estimation

By

TERESA MARGARIDA DANTAS DOS REIS

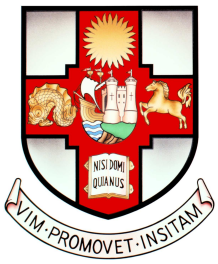

Department of Aerospace Engineering
UNIVERSITY OF BRISTOL

A dissertation submitted to the University of Bristol in accordance with the requirements of the degree of DOCTOR OF PHILOSOPHY in the Faculty of Engineering.

NOVEMBER 2020

Word count: 61884

"Einstein never accepted quantum mechanics because of this element of chance and uncertainty. He said: God does not play dice. It seems that Einstein was doubly wrong. The quantum effects of black holes suggests that not only does God play dice, He sometimes throws them where they cannot be seen."

STEPHEN HAWKING

Abstract

Weight is a key element in aircraft design, having a major influence on its performance and being a common factor to all disciplines involved in the decision making process: aerodynamics, structural sizing, materials, loads, geometry, cost, manufacturing, etc. To ensure an optimal trade-off is achieved, alongside a smooth convergence to the desired final aircraft weight, it is essential to be able to model the aircraft weight estimation process throughout the design, including assessment of uncertainty, sensitivity and risk.

Weight estimation processes and uncertainty analysis are well established bodies of literature; and uncertainty in the aircraft design process has been a topic much explored in recent years, both in academia and in industry. Applications of uncertainty quantification in aeroelasticity, including uncertainty in aircraft design features and structural sizing, aircraft life-cycle cost, aircraft's environmental impacts, aeroelastic stability and aerodynamic characteristics, have been studied independently and for the purposes of robust and reliability-based design optimisations. On the other hand, by analysing the industrial processes and methodologies, the need to integrate empirical evidence, from physics-based models and statistical evidence, when assessing weight uncertainty at project milestones is identified. The unification of UQ and weight estimation in aircraft design into a framework that can deliver exhaustive, meaningful and innovative technical information, not only for the purposes of optimisation but also for risk and project management assessments, was lacking; The present work is set out to close this gap.

Historical aircraft data is explored in order to trace patterns and trends on weight data, for the objective of concluding on its drivers, causes and sensitivities and ultimately help predict its fluctuations. The aircraft data proves scarce to constitute statistical evidence and the lack of standardisation in reporting is appointed. For these reasons, a framework has been developed that emulates the weight convergence corridor for an aircraft wing. It combines a traditional wing-box sizing method for primary weight with alternative methods for secondary weight. The alternative methods mimic the different phases of design in the aircraft development cycle. Maturity of design translates to the status of the information available, which translates to accuracy in the weight estimation method in use. This process incorporates uncertainty in the form of modelling the desired input parameters as Probability Density Functions (PDFs). The uncertain input space may include wing and engine planform geometry, wing-box material properties, load cases, general aircraft weights and fuselage dimensions. Design features and aircraft components are correlated and therefore an underlying dependency grid prevails. Combining the PDFs on the grid propagates the uncertainty towards an ultimate distribution of the total wing weight. The methodology is demonstrated on a representative commercial jet airliner wing.

This work investigates the use of the framework developed for wing weight estimation by quantifying design sensitivities impact on wing weight. This includes the effect of uncertainties on: the aerodynamic loads, stress and sizing parameters; the material properties, specifically the stress allowable, of the wing-box; the stress formulae and activation of stress constraints; an external mass such as the engine properties; and the secondary structure weight. The results are combined into a weight convergence corridor, where the final wing weight can be compared against a target weight with a reliability requirement. As design features become fixed and information matures, uncertainty in the weight convergence corridor decreases, and that translates to a narrowing uncertainty band in the corridor.

Uncertainty is inherently present in our world, and engineering is no exception. It is crucial that UQ becomes an integral part of all engineered systems; only then can they become more reliable.

Acknowledgements

I would first like to thank my advisor Prof. Jonathan E. Cooper for his experienced guidance and support throughout my time at the University of Bristol in development of this research, concluded in the writing of the present thesis. I would also like to acknowledge my industrial advisor Judith Cheeseman, for her practical insight and constant encouragement. Lastly, I would like to thank Sarah Hassall for the incredible work she has done at managing this project and everyone involved.

The research leading to these results was funded by the Innovate UK Agile Wing Integration Project (TSB-113041) which was led by Airbus. I gratefully acknowledge Innovate UK for funding this project, and Airbus for providing the XRF1 test-case as a mechanism for demonstration of the approaches presented in this work, and allowing access to its processes and methodologies. Particularly, I would like to thank the Mass Properties team for their input and on-site mentoring.

This research has been filled with valuable collaborations, of which I would like to highlight a few. Jorge Bes-Torres, at Airbus, has contributed to the uncertainty modelling for weight estimation process definition. Through Airbus, I have been involved in stimulating discussions on all things uncertainty, structured expert judgement and risk assessment, involving Roger Cooke, Sanjiv Sharma and Jimmy Tai, from the Georgia Institute of Technology. Dario Calderon has provided the structural sizing routine that is integrated in the uncertainty quantification framework presented in this work. Simon Neild has helped focus and direct the innovation of this research, and provided valuable advice with regard to the structure of this thesis. I would like to acknowledge all of these collaborators, I am very grateful for the opportunity to work together.

Since the very first day I landed in Bristol, I have felt welcomed and at-home, in large part thanks to the amazing people I met along the way and that helped make these four years so special. A warm thank you to Evan and Alex Georgiades at Airbus for our thought-provoking life discussions over coffee or lunch. My colleagues in QB2.80 - Abdel, Andy, Chris, Dan (and Will) - for daily distraction through chats and trivia, the occasional after work pints, and the entertainment at workshops and conferences. My friend Tiago, who introduced me to a lovely bunch of fellow Portuguese in Bristol, helped me not forget how to speak my own language, and is always a phone call away for anything at all. My flatmates, friends, my Bristolean family, not of blood but of heart - Casey, Alessia, Dani, Gaetano, Michi, Cyril and Kostas. With a special thank you to Elpida, for always being ready to brave the world with me (or the woods, with bikes on our backs); whose tenacity and thirst for life are an inspiration to me. Somewhere along the corridors of Queen's Building, I also stumbled upon a fellow nerdy soul called Alex, whom I thank for partnering with me along this journey, in every way, and being an unwavering support.

I would like to acknowledge my friends from before and always, that made travelling home or meeting abroad feel so special, easing the pain of missing out, and for whom I am so grateful. I would like to thank my "mãe e pai", my siblings - Vasco, Zeca, Laura and Álvaro, and the rest of my family for being my rock, for believing in me more than I ever will (yes, this still stands from the MSc's thesis) and for being my biggest fans.

Author's declaration

I declare that the work in this dissertation was carried out in accordance with the requirements of the University's Regulations and Code of Practice for Research Degree Programmes and that it has not been submitted for any other academic award. Except where indicated by specific reference in the text, the work is the candidate's own work. Work done in collaboration with, or with the assistance of, others, is indicated as such. Any views expressed in the dissertation are those of the author.

SIGNED: ..... DATE: .....

Table of Contents

List of Tables

List of Figures

Figure **Page**

NOMENCLATURE

Abbreviations

A/C	aircraft
AAT	All-At-Once
ANN	Artificial Neural Networks
BBN	Bayesian Belief Nets
BCS	Best Case Scenario
CAD	Computer-Aided Design
CDF	Cumulative Distribution Function
CFD	Computational Fluid Dynamics
CI	Confidence Interval
DST	Dempster-Shafer Theory
DT	Digital Transformation
EDA	Exploratory Data Analysis
EE	Expert Elicitation
FEM	Finite Element Model
GEV	Generalised Extreme Value
GP	Gaussian Process
HFM	High Fidelity Model
IoI	Interval of Interest
KPI	Key Performance Indicator

LCC	Life-Cycle Cost
LFM	Low Fidelity Model
LHS	Latin Hypercube Sampling
MCS	Monte Carlo Simulation
MDO	Multidisciplinary Design Optimisation
MFM	Multi Fidelity Model
ML	Maturity Level
MTOW	Maximum Take-Off Weight
MWE	Manufacturing Weight Empty
MZFW	Maximum Zero Fuel Weight
NIPC	Non-Intrusive Polynomial Chaos
OAT	One-At-a-Time
OWE	Operational Weight Empty
PC	Polynomial Chaos
PCC	Pearson's Correlation Coefficient
PCE	Polynomial Chaos Expansion
PDF	Probability Density Function
PMS	Probabilistic Margin Setting
QoI	Quantity of Interest
RBDO	Reliability-based Design Optimisation
RDO	Robust Design Optimisation
SA	Sensitivity Analysis
SEJ	Structured Expert Judgement
SI	Sensitivity Indices
SRC	Standardised Regression Coefficients

SRCC	Spearman's Rank Correlation Coefficient
SRCI	Standard Regression Coefficients (sensitivity) Indices
SRRC	Standardised Rank Regression Coefficients
TOW	Take-Off Weight
UQ	Uncertainty Quantification
UQ&M	Uncertainty Quantification and Management
VLM	Vortex Lattice Method
VoI	Variable of Interest
WCS	Worst Case Scenario
WeiCoS	WEIght COnvergence Simulation framework
WEM	Weight Estimation Method
WP	Work-Package
WUA	Weight's Uncertainty Assessment tool
ZFW	Zero Fuel Weight

Greek characters

β	reliability level
ϵ	absolute errors
η	relative error
μ	location of the central tendency of a PDF - mean
σ	standard deviation
σ^2	variability of the central tendency of a PDF - variance
$\widetilde{\mu_3}$	skewness

Latin characters

$\mathbb{X}_{\text{posterior}}$	Input parameter subspace obtained from backpropagation
$\mathbb{X}_{\text{prior}}$	Input parameter space

σ_{allow}	wing-box stress allowable - tensile strength
σ_{skn}	skins' bending stress
$\sigma^{v}_{\text{skn}}/\sigma_{\text{allow}}$	Von Mises stress for skins
σ_{spr}	spars' bending stress
$\sigma^{v}_{\text{spr}}/\sigma_{\text{allow}}$	Von Mises stress for spars
σ_{stg}	stringers' bending stress
$\sigma_{\text{stg}}/\sigma_{\text{cc}}$	stringer local buckling stress
$\sigma_{\text{stg}}/\sigma_{\text{col}}$	column buckling stress of the skin-stringer panel
σ_P	Principal stress
τ_{skn}	skins' shear stress
τ_{spr}	spars' shear stress
a_{spr}	aft spar location
A_{stg}	stringers' surface Area
c_{box}	wing-box chord
f	fuel fraction
f_{spr}	front spar location
f_c	complexity factor
f_d	documentation factor
f_r	robustness factor
F_x	axial shear
F_y	horizontal shear
F_z	vertical shear
h	altitude
h_{spr}	wing-box height
k	kurtosis

$k_{d_{\text{mle}}}$	factor for depth of movable leading edge structure
$k_{l_{\text{mle}}}$	factor for length of movable leading edge structure
L/D	Lift-to-Drag ratio
l_{box}	wing-box length
M	Mach number
M_x	torque
M_y	out-of-plane bending moment
M_z	in-plane bending moment
n	load factor
P_f	Probability of failure
q_{D}	dynamic pressure
q_α	α quantile
R	range
R^2	coefficient of determination
S_w	wing's surface area
SFC	Specific Fuel Consumption
T	thrust
t_{skn}	skins' thickness
t_{spr}	spars' thickness
u	uncertainty
V	flight speed
W	nominal weight
W_{le}	leading edge weight
W_{PW}	primary weight
W_{skn}	skins weight

W_{spr}	spars weight
W_{stg}	stringers weight
W_{SW}	secondary weight
W_{Wing}	wing weight
CI	Correlation Indices
CL	Confidence Level
F	Farrar's efficiency factor
FLE	Fixed Leading Edge
FTE	Fixed Trailing Edge
MLE	Movable Leading Edge
MTE	Movable Trailing Edge
RP	Rib Pitch
SF	Safety Factor
SP	Stringer Pitch

CHAPTER 1

INTRODUCTION AND BACKGROUND

Weight is a key performance indicator for the development of a new or a derivative aircraft programme [2]. Raymer describes the weight engineer as the "referee" of the design cycle, that communicates to all the design disciplines, as illustrated in Fig.1.1: the aircraft's mission requirements and performance, its structural sizing, aerodynamics, loads and loadability studies, its geometry, materials, systems, manufacturing and cost. Weight is a common primary figure of merit, crucial for comparing and contrasting various design decisions and any step in the development process is taken with the impact on weight in mind [3].

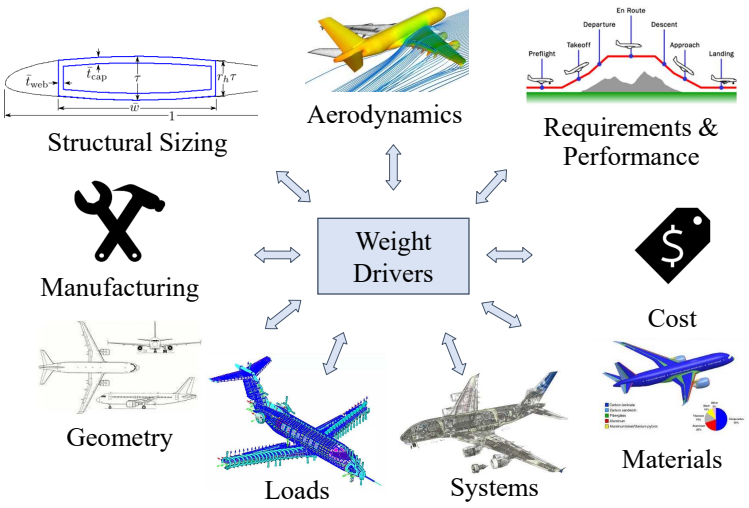

FIGURE 1.1. Weight driver disciplines.

When considering the complexity of today's large civil aircraft, how interdependent are the numerous disciplines involved and how much of the aircraft final design is unknown in the early

phases of design, the weight estimation task might seem close to impossible, yet it plays a critical role in ensuring a successful product for both manufacturer and customer [4].

Nevertheless, aircraft operate in an uncertain world and despite continuous progress and ground breaking research on the weight estimation processes, it is inevitable that the design is not devoid of uncertainty. Uncertainty is a broadly used term, as it extends to uncertainty in the final design solution, uncertainty in the models used, whether these are more or less complex, scaling, statistical or physics based, and uncertainty in the input parameters variability.

* * *

Weight and mass are going to be used interchangeably in this document.

1.1 Aircraft weight engineering

Weight engineering or mass properties is a discipline present in most transport and logistics industries. In aeronautics, weight engineering was pioneered in the 1930's, when size, weight and most importantly relatively low useful load to gross weight ratios pointed to the need for a separate engineering department to predict and control the weight and centre of gravity of new designs. More recently, advances in jet propulsion, composite materials and transonic flight add to the complexity and responsibility of weight engineering [5].

1.1.1 Weight definitions

In aircraft weight engineering, there are four main reference weight definitions distinguished: MWE, OWE, ZFW and TOW; shown in Fig.1.2.

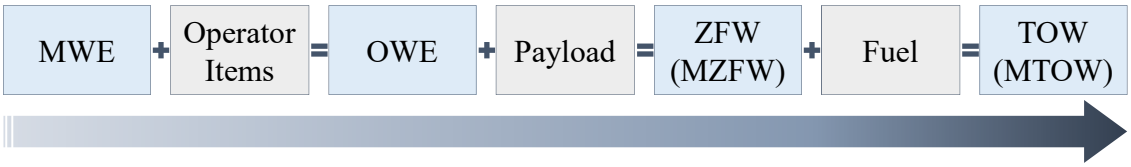

FIGURE 1.2. Reference aircraft weight definitions.

The **Manufacturing Weight Empty** MWE consists of the airframe weight, propulsion system, systems, including fluids contained in closed systems, furnishings, including fittings and carpet, and other equipment that is an integral part of a particular aircraft configuration. The **Operational Weight Empty** OWE refers to the MWE with the addition of operational items including crew and their luggage, unusable fuel, open systems fluids, aircraft documents, passenger seats, galleys, catering pallets and baggage containers and emergency equipment. The OWE is the weight of an aircraft ready to operate. The **Zero Fuel Weight** ZFW introduces payload (passengers and any cargo or freight) to an OWE aircraft, but with zero fuel. MZFW corresponds to carrying the maximum possible payload. Finally, the **Take-Off Weight** TOW is

the weight of the aircraft ready to take-off, including the fuel required for the given mission. The combination of payload and fuel can be such that MTOW is reached, i.e. the maximum weight at which the aircraft is allowed to take-off. This can be for maximum payload or less (MZFW or not) and necessary fuel to achieve MTOW, assuming it has not reached capacity level.

1.1.2 Weight Estimation Methods (WEMs)

Weight Estimation is the ability to determine any aircraft part, system or component mass and identifying their main drivers and sensitivities, by analysing all the requirements and disciplines involved in the design. It is a complex task, hindered by the numerous design alternatives, hundreds of thousands aircraft parts, many of which interdependent, and various performance, air-worthiness, operational and technical requirements. It is also, however, an essential part of the design process and any design decision is assessed with the weight impact in mind.

There are many different WEMs that vary in complexity, computational expense and accuracy. They are continuously being revised, enhanced and refined with new research and technology. One of the current biggest challenges in the field is taking the existing methods used for conventional aircraft designs and making them applicable for unconventional designs [6–9].

WEMs can be broadly classified into three categories: scaling, statistical and physics-based [10]. The method chosen to estimate the weight of any component is dependent on the amount and maturity of the information available for the calculation, how far into the design process the product development is and how much computational and time efforts are to be expended. Given recent advances in technologies and super-computing, the latter has become less relevant.

The aircraft's design process is an iterative process and the WEMs are consistent with that. They evolve with the process and the estimations should always reflect the best and most realistic weight, given the set of inputs available, at any given point in the design process.

1.1.2.1 Scaling

The simplest way to estimating something is by scaling it from something else that is known. For example: a ratio of areas can be applied to calculate the weight of a fuselage door, assuming the loading the door will bear is typical of the door used for reference; a load increase factor used to determine a primary structure component; a density increase factor or material strength for a change in material; the initial MTOW can be estimated by comparison to a similar aircraft, both in dimension and mission.

Selecting the right reference, scaling parameters and the weight's sensitivity to the scaling ratio are key elements for a good weight estimate. It is crucial to understand the specific component weight's proportion that will change due to a variation in a particular weight driving parameter, which can be ambiguous. The accuracy of the scaling factor and scaling parameter is dependent on detailed knowledge of the driving design considerations' impacts on the aircraft

weight. Changes on the driving load cases, failure modes and manufacturing concepts need meticulous studies so that a scaling approach is successful.

1.1.2.2 Statistical

Weight estimation by statistical analysis relies on obtaining a numerical relationship between relevant parameters affecting the weight. By generating statistical relationships, patterns and trends can be uncovered from apparently random data. Some examples of statistical methods are tracing a regression of the weight of a major component as a function of MTOW, as a function of the component weight index, e.g. wing weight versus wing weight index; or even as a function of main weight driving parameters, e.g. fuselage weight versus cabin pressure differential.

One of the challenges with a statistical method is that it requires a large data set for any results to be considered statistically relevant. For this reason and because of the scarcity of unconventional designs, statistics cannot be applied when novel configurations are being considered. Adding to this issue, collecting data from different aircraft is not a trivial process because of non-disclosure, commercial reasons as well as aircraft part, system or component breakdown complexity.

1.1.2.3 Physics-based

A physics-based method models the physical behaviour of an aircraft for various levels of analysis. These methods are usually applied for a primary structure bearing the main loads. Secondary structure items can also be modelled physically by either considering loads separately or sizing based weight drivers beyond loads. Moreover, the secondary structure weight is of extreme importance for computing the aeroelastic loads. Lastly, systems and systems installation can also be estimated using system architecture and, again, sizing based weight drivers.

The structural model is generally: produced, loaded, analysed and then sized. An iterative approach is essential for this process: The loads themselves depend on the aircraft weight, lift and pitch coefficients, which, in turn, depend on the structural sizing. Moreover, structural optimisation is a multidisciplinary process that involves considering several load cases, failure modes and different structural solutions. Beam analysis and Finite Element based methods are examples of physics-based methods, as well as simplified loads calculations and component weight estimation using empirical equations [9, 11]. In [12], the loads calculation and structural sizing are tightly integrated into a Multidisciplinary Design Optimisation MDO. They are then combined with appropriate design criteria models in order to simultaneously consider the full set of design driving requirements within the optimisation process by determining the analytical sensitivity of each design response. In [13] an extended physics-based wing mass estimation system applicable for conventional and unconventional aircraft designs through its high flexibility, including physics-based models for secondary structures, is presented.

* * *

One of the drawbacks of component weight estimation is that, by sizing primary and secondary structures, the rest of the aircraft components are estimated by a correction factor. Unless physics-based models become complex enough to, realistically, model the aircraft as a whole, the focus will still be on working out the physics for the heaviest parts and the let the lighter parts be an after thought. One of the solutions could encompass the combination of the three methods for different components. There are still a lot of reservations when trying to apply an academic approach to a very industrial, deterministic and human problem. MDO with weight as the optimisation parameter is well researched. However, the challenge proposed in this work is to have a weight outcome that is not purely physics-based or academic, but also industrially relevant, i.e. that includes all the weight drivers in a multidisciplinary analysis, not necessarily an optimisation. Weight drivers in this case are not just physics-based, but also industrial, environmental and human impact, involved in the design process.

1.1.3 Range optimisation

Aircraft are complex systems, composed of hundreds of thousands parts, individually and collectively designed, simulated, manufactured and integrated for a proposed optimal solution. In commercial jet propulsion aviation, the optimal design is driven by the predicted revenue generated by an airline when the aircraft is in service. Airlines carry a specific payload at a set cruising speed over a limited range, such that

$$R = \frac{V}{SFC}\frac{L}{D}\ln\frac{W_i}{W_f} \tag{1.1}$$

This is known as the Breguet range equation where the range of the aircraft R is the product of its flight speed V over the specific fuel consumption SFC, lift-to-drag (L/D) ratio and initial and final aircraft weights, W_i and W_f respectively, concerning the cruise-segment mission in study [3]. Breguet range allows for a good initial estimate of the aircraft weight, particularly by breaking the mission into its several segments, such as taxi/take-off, climb, cruise, descent, loiter and land/taxi.

Range optimisation is then a multidimensional problem. There is a trade-off between having the right balance of aircraft empty weight, payload to be carried and necessary fuel weight, respectively OWE, ZFW and TOW, see Fig.1.3 [14]. The goal is to maximise jet engine efficiency for fuel consumption, optimise the aerodynamic profile for drag reduction, whilst minimising the structural weight. This trade-off is at the basis of market and economy's product placement and subsequent configurations definition and development. These proportions, together with assumptions about achievability and risk management assessments are made right at the beginning of aircraft development.

The trade-off between OWE and fuel burn is explored for a long range wide-body transonic aircraft in a multi-objective optimisation problem by Kenway [15]. A multipoint aerostructural gradient-based optimisation with hundreds of design variables, including airfoil shape, wing

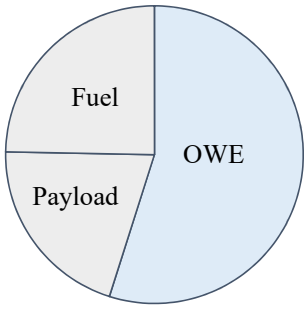

FIGURE 1.3. Proportional revenue making weight.

planform and structural thickness variables, is used to analyse two different objectives: minimum TOW and minimum fuel burn. If optimising the aerodynamics and structural sizing for minimum TOW (and MTOW), it is possible to reduce the latter by 4.2% and fuel burn by 6.6%. On the other hand, if optimising for minimum fuel burn, a reduction of 11.2% is achieved with no significant impact on TOW.

Declarations of aircraft performance are made to the market at programme launch, and, subsequently, to individual customers. From that performance assumption, together with other relevant information, a target weight is established. During programme development, if the target weight seems to be out of reach, design reconsiderations and modifications for weight saving purposes must be undertaken. Changes in design entail undesirable financial and time expenses. On the other hand, a decision not to tackle a potential weight excess compromises the aircraft mission by either reducing range or exchanging payload for fuel capacity. To summarise, accurately estimating the aircraft's definition and design solutions early in the development process, as well as managing its progress throughout, reduces the risk of late changes that can be highly detrimental to the aircraft manufacturer.

1.1.4 Phases of design

A development plan is defined in order to ensure a smooth and mature aircraft development process. The plan sequences the main phases of the design cycle and implements project milestones. At each milestone, the aircraft is assessed in terms of maturity and progress against specific requirements associated with the milestone at hand. The phases of design and milestones (grey diamonds) are represented in Fig.1.4. Each phase of design entails a unique set of activities, problems and requirements for the weight engineer to solve and meet.

Initial studies on market trends, potential business and industrial models and different configurations are carried out at the *feasibility* phase. A baseline for the project aircraft is conceived, including requirements, market and pricing positioning, working strategies and technological considerations. At the *concept* phase, the aircraft and its components become a concept design and potential suppliers and partners may be selected. Preliminary loads studies

FIGURE 1.4. Different phases of the design process and milestones. *Note*: Data from Airbus.

are carried out, performance is calculated and margins studies are taken into account for risk management, and operational considerations are analysed. The *design* phase is where design solutions arise and more detailed trade studies and changes on design solutions happen. Elements of the design are progressively frozen throughout this phase and data for manufacture is produced. The last phase before the aircraft makes its way into service is *integration and qualification*. Here, manufacturing, assembly and final component integration take place, resulting in the manufactured product. Simulation models are calibrated and certification testing and checks, including flight testing are performed. Maintenance procedures are delineated and, finally, the aircraft is ready to operate at *in-service*.

Throughout the design cycle, milestone assessments are defined to enable an efficient evaluation of the aircraft development project progress and maturity, looking at current weight estimates and foreseen changes to that estimate, against target requirements. Each milestone has a list of requirements and objectives regarding aircraft maturity, performance and trend, that need to be met. Following a milestone assessment, a decision is made on whether to proceed or to rethink some solutions and changes to the design.

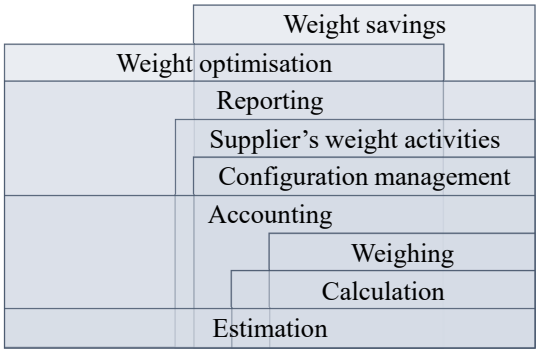

FIGURE 1.5. Weight activities throughout the phases of design. *Note*: Data from Airbus.

The aircraft's project development plan can otherwise be conceptualised as a time-frame puzzle of all the weight engineer's activities, as represented in Fig.1.5. Weight estimation is constant in all the phases of design, as well as accounting and weight reporting. Weight calculation, configuration management and saving strategies, however, are taken into account later on, at

the design and integration stages. As the design is progressively frozen, weight optimisation opportunities reduce and weight savings become more expensive, and deliverables at milestone level are smoothly reached. Consequently, weight optimisation starts at the very first estimation and stops when the design freezes.

Given that many aircraft components are outsourced, supplier or partner weight activities are closely related to the previously mentioned activities. Developing and improving on weight estimation methods and models is crucial to ensure that the calculated and weighed values closely approximate the estimations. Calculation coming from drawings of the manufactured design and weighing being the final validation of the manufactured part, calculation and weighing are progressive increases of maturity on weight knowledge.

1.1.5 Weight convergence corridor

During its development cycle, the weight of the aircraft is assessed at each milestone so that, as more parameters become fixed and more definitions of the design are established, the weight becomes more certain and converges to the desired result for achieving the expected or declared aircraft performance [2]. The weight convergence corridor allows for tracking the evolution of the weight against a target, as shown in Fig.1.7. Three types of weight are discerned: **target**, **status** and **outlook**. A description of each of them follows.

1.1.5.1 Target weight

Target weight is set as the ideal weight to ensure achieving the declared aircraft performance at product launch, and any specific guarantee made to customers. It is what the aircraft should weigh when entering into service. At the feasibility stage, weight iterations are made to establish an appropriate target. This is a complex exercise that not only demands an extensive knowledge of aircraft requirements but also an expert understanding on the weight estimation process, current aircraft weights and how these are sensitive to changes and new technologies. The target weight is first set at aircraft level and then cascaded down to lower level components. Ultimately, the components' target weights may form an element of the commercial agreement with suppliers or partners by establishing a "not to exceed" weight at component or work package level. Setting independent target weights at component level, in an early phase of design might not lead to an optimal final aircraft weight, given the interdependencies between disciplines and components. However, this effect is outside the scope of this work.

1.1.5.2 Status weight

Status weight refers to the current view of what the weight of the aircraft is, at any stage in the design process and, if nothing was to change, it is the weight the aircraft would have at the end. It is the current status of the weight of the aircraft. As the design process develops and matures, so

does the maturity of the status weight. In the early design stages, when little is known about the aircraft, the status weight is built up from weight estimation methods. As the development cycle progresses, weights are calculated from drawings and FE models. As the drawings and models mature, so does the weight knowledge. When all the parts are manufactured and ultimately weighed on a scale, the status weight takes on its final value.

1.1.5.3 Outlook weight

Outlook weight is what the aircraft is projected to weigh, at any stage in the design process, assuming certain changes to the aircraft definition will happen. These changes are under development or in study at the time the outlook weight is projected. A change can be seen as a variation in weight, either that is a potential increase or decrease. It can affect single or multiple parts of the aircraft and can amount to less than one kilogram or significant hundreds. Their weigh impact needs to be accurately estimated in order for it to be embodied into the aircraft. All the lighter parts are often forgot by physics but can easily add up to relevant weight and uncertainty values.

These variations in weight are called risks and opportunities. A risk is a potential weight increase and an opportunity is a potential weight decrease. In a weight management process, alongside the assessment of all the different parts and components that make up the final product, these variations in weight are also evaluated. They can occur for multiple reasons such as regulatory changes, trade-off design changes, the use of a new technology, etc. Opportunities are assessed in terms of their robustness and likelihood. Robustness refers to how accurate the weight value is and likelihood refers to how likely this change is to be embodied in the final design. Robustness evaluates the weight estimation method in use (the more detailed and complex the method, the more robust) in combination with the amount and maturity of the information available for the calculations, as well as which team has calculated the weight. Values supplied from vendors through weight reports and that are not double checked in house tend to be less robust. Likelihood evaluates factors such as: the recurring cost of having that change implemented; How mature the technology associated to the change is; If there are any industrial constraints at tools and machinery level, commonality with other aircraft, manufacturability, supply chain and time; If there are any operational constraints associated to airlines, maintenance, airport restrictions, reparability, etc; And finally, how far in progress this change is, that is, has the need for the change been identified, have all the impacts of the proposed change been evaluated and has the modified data been released. Given certain thresholds, opportunities are then divided into two types: A and B. Opportunities type A are robust and likely to happen and thus included in the outlook weight. Opportunities type B are either not robust enough or unlikely to happen, or both, and thus not included in the outlook weight. Risks are solely assessed in terms of their robustness because its likelihood is always considered to be 100%. This is justified by experience (once a risk is declared, it is most likely to be integrated) and by conservatism and the need

to consider the worst case scenario. However, risks have mitigations directly linked to them. A mitigation is considered to be an opportunity to alleviate the risk and therefore assessed as one.

The Outlook weight is obtained by combining the weight variation in risks and opportunities type A to the status weight. In order to illustrate how the different weights (target, status and outlook) correlate with each other and with the potential variations in weight (risks and opportunities), a concept called the weight ladder is created and represented in Fig.1.6.

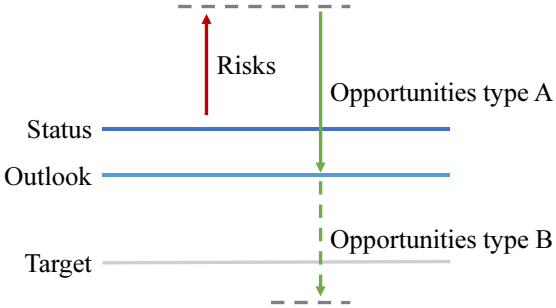

FIGURE 1.6. The Weight Ladder.

The outlook weight often provides a depiction of what the status weight is going to look like once all the predicted changes in weight are embodied and therefore help manage the design process further.

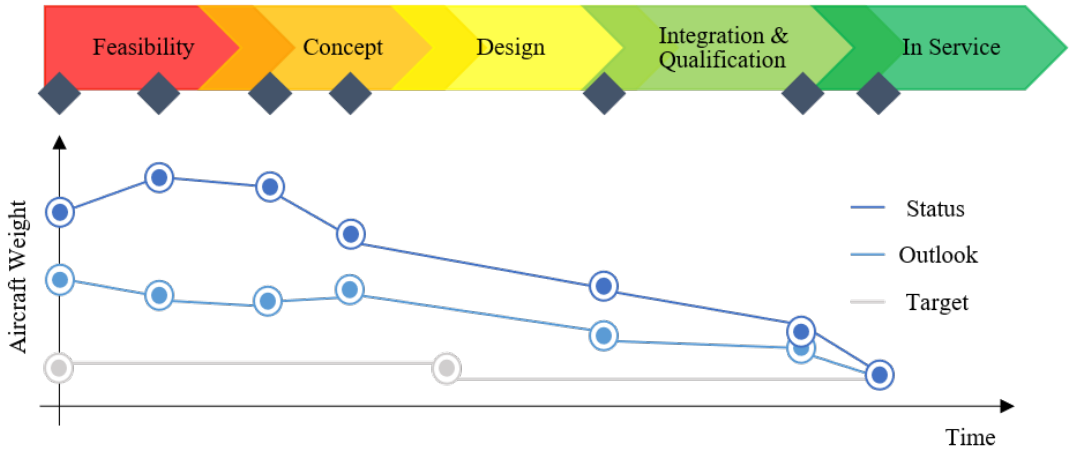

FIGURE 1.7. Representative evolution of the status, outlook and target weights, throughout the design phases, in the weight convergence corridor. As time (x-axis) progresses, and with a weight management process in place, the expectation is that the status weight will converge to outlook weight and both will converge to target weight. It is also expected that, as design optimisations and continuous technological improvements occur with time, the final aircraft weight is lower than its initially estimated value.

1.2 Uncertainty modelling, identification and backpropagation

Uncertainty can be treated as a continuum of knowledge. From what is certain to the complete unknown [16]. Within this spectrum, uncertainty is commonly separated into the categories of aleatory or epistemic.

Aleatory uncertainty is related to luck or chance of an event. It is randomness inherent to nature. It can be because the process to be modelled is not deterministic or there may be unsolvable indeterminacy in it. Aleatory uncertainty is a constant bound to the model, that is, it is not solved or lessened by the addition of new information or refinement of the existing one. **Epistemic** uncertainty is linked to lack or immaturity of information. It is the scientific uncertainty in the model, something theoretically known but not in practice. Having a large enough data set, one can express the probability of each event and, consequently, quantify the uncertainty of a problem parameter or outcome. The data set is obtained to express probabilities of events and build correlations between them. Thus overfitting or increasing the data set for any analysis will always increase accuracy, either by learning new spurious correlations or providing more evidence for the existing ones, unless the new training data is noisy. Whilst some data might be easy to capture, other, such as the failure rates of a material or component, human error or environmental effects, is more challenging.

In a weight management process, epistemic uncertainty decreases throughout the different stages of design - as information matures and design features become fixed, uncertainty related to the lack of information, and likelihood of that information changing, decreases. Aleatory uncertainty, on the other hand, is a constant throughout design - things like human error or an incorrect weight report are unknowns and random uncertainties. One can argue that the boundaries between the two uncertainty definitions are arguable, when models are found for "randomness". For example, a weight engineer's expert judgement on weight reports and past data can be used to generate a model for supplier (human) error, allowing uncertainty to be predicted and predictable.

Different types of uncertainty are quantified in different ways, usually either by the means of probability theory or interval analysis. Different methods have implications on the results and on the way uncertainty is generated, combined and quantified. More on this subject is progressively discussed on the sections below. Ferson [17] claims interval analysis should be used to propagate ignorance, and probability theory should be used to propagate variability. Hora [18] discusses the nature of the two different uncertainty types and how such classification affects the choice of input probabilities, particularly with expert elicitation. Du [19] proposes a mixed uncertainties approach and Swiler et al. [20] discusses the application of different methods (probabilistic and not) on a structural analysis problem, including the use of surrogates and margin allocation.

When modelling a complex system, such as the aircraft design process, and, more specifically, weight estimation within it, uncertainty sources can be generally described as:

- Model and numerical: When modelling a physical or deterministic process into a set of equations, these are always subject to assumptions and simplifications; Moreover, simulations in UQ or optimisation problems are often computationally expensive because of the need perform multiple runs and have a sufficient data set. The trade-off between high-fidelity models (HFM) and low fidelity, inexpensive but less accurate, models (LFM) comes with its set of implicit uncertainties. A multi-fidelity model (MFM) combines the information of multiple models with different levels of accuracy and complexity (and uncertainty), achieving accuracy at a reasonable cost [21].
- Parametric: The parameters fed into the model and its variability are deterministic values set by the user;
- Time: When setting a target weight, the duration of the development cycle and technology evolution must be considered;
- Human error: In making estimations, reporting data or communication flaws;
- Experimental: Parameters, such as material allowables, are often experimentally obtained. Experiments carry inevitable errors, both systematic and random;
- Statistical limits: Not only related to the statistical or sampling method used but also in the amount and quality of data available;
- Randomness: In the unpredictability of events;
- Behavioural elements: In the unpredictability of events.

Uncertainty refers to something involving imperfect, immature or unknown information. Uncertainty Quantification (UQ) is the science of quantifying uncertainty, both in computational modelling and real world problems. UQ considers the range of all possible scenarios associated to uncertain data and statistically describes the likelihood and/or conditional likelihood of a particular scenario happening. UQ has gained much relevance and attention in the past decade, across a variety of fields, including biology, finance, insurance, natural disasters prediction, meteorology and, certainly, engineering. Consider the uncertain input variables X. By propagating these uncertainties through a model $G(X)$, we obtain an output variable of interest $Z = G(X)$ and therefore quantify the uncertainty of a certain model response. This is the working principle of uncertainty quantification.

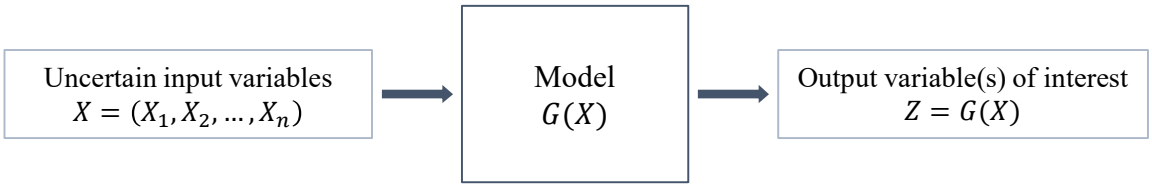

FIGURE 1.8. Uncertainty quantification.

Depending on the quality of the input data available and the nature of the analysis, UQ can

be broadly categorised into two main approaches: probabilist and non-probabilistic or possibilistic. A probabilistic approach can be described as the likelihood that a specific set of inputs, depicted as a joint probability density function and propagated throughout the model in analysis, outputs a specific model response. A possibilistic approach, on the other hand, considers only the bounds of the input variables and determines the worst-case responses of the model. These approaches are further described bellow.

1.2.1 Probabilistic uncertainty modelling and propagation

The global methodology for probabilistic uncertainty treatment, adapted from Rocquigny et al. [22] and Blanchard et al. [23], is shown in Fig.1.9.

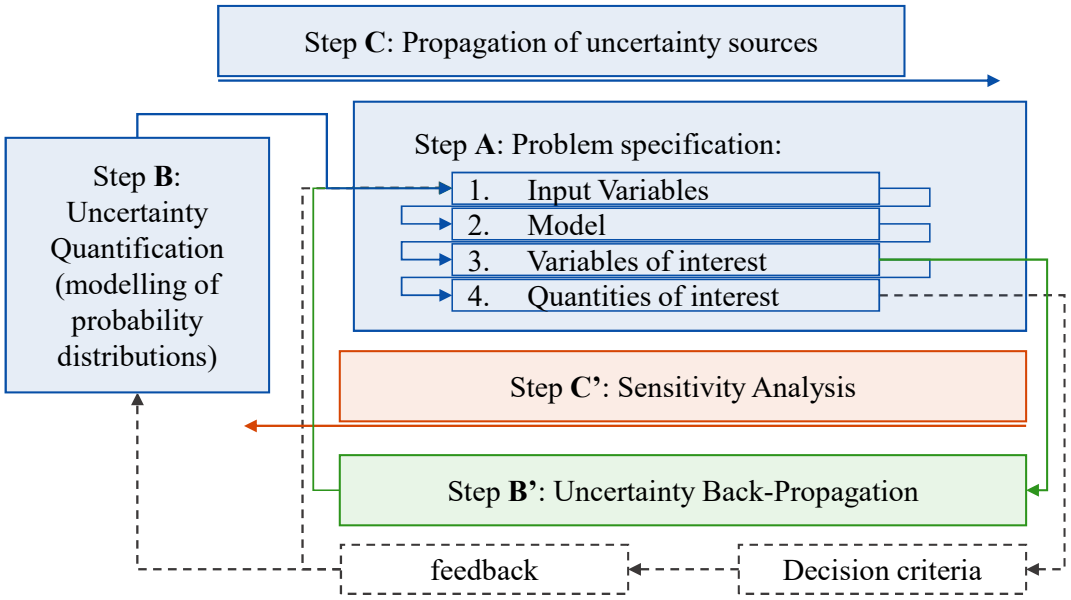

FIGURE 1.9. Flow diagram representing the different steps that constitute an uncertainty propagation and quantification analysis. Adapted from Rocquigny et al. [22] and Blanchard et al. [23].

Step **A** the uncertainty sources (input variables) are identified, the model is generated and the study's variables of interest and quantities of interest for each variable are established. In step **B**, one input variable is generated that defines a joint probability density function of the uncertain input parameters. The function is computed by defining each input's marginal distribution (a distribution type, bounds and parameters) and dependence structure via a correlation matrix. With the input variable and model defined (steps A and B), a Latin Hypercube sample is taken from the input variables distribution, and the model is evaluated for each data point, in step **C**. The variables of interest, or model's outputs, are retrieved and stored for uncertainty assessment.

The inverse quantification of outputs or uncertainty backpropagation is represented in step **B'**. Given the problem definition in step A and a specific set of experiments, the mean value

and/or uncertainty in the input variables can be obtained, for model calibration or reliability analysis. With the input variable and model defined (steps A and B), sensitivity analysis can be performed on the simulation results in step **C'**. The uncertainty sources are ranked in order of impact on the model's variables of interest and their uncertainty.

Let's now look at some of these definitions in more detail.

1.2.1.1 Input variables

The uncertain inputs are modelled through a random vector X, composed of n univariate random variables $(X_1, X_2, ..., X_n)$ linked by a dependence structure. Adequately defining the input uncertain variables, considering the nature and variability of its sources, is a key step in the uncertainty analysis process as it will impact the subsequent uncertainty propagation.

A random variable can be described as a measurable function X that can take several different values x, according to $X(w) = x$, where w is a particular event related to that variable. The Cumulative Distribution Function (CDF) is the function that relates x to the probability of X taking on a value less than or equal to x: $F_X(x) = P(X \leq x)$. For a continuous variable, the Probability Density Function (PDF) is the function that relates x to the probability that the random variable X belongs to the infinitesimal interval $[x, x+dx]$: $f_X(x)dx = P(x < X \leq x+dx)$ and thus $F_X(x) = \int_{-\infty}^{x} f_X(x)dx$, see Fig.1.10.

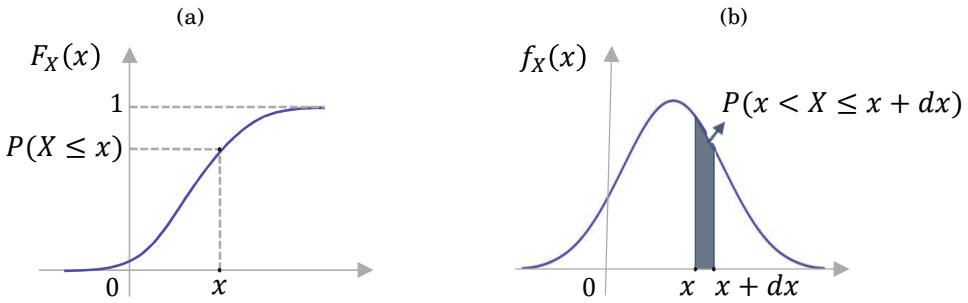

FIGURE 1.10. (a) Cumulative Distribution Function (CDF) and (b) Probability Density Function (PDF), of a generic variable X.

1.2.1.2 Variables of Interest (VoIs)

The output variable of interest Z, in this case weight and derivatives, can be formally related to a number of continuous or discrete uncertain inputs X and fixed variables d, by function G, such that

$$Z = G(X, d) \tag{1.2}$$

1.2.1.3 Quantities of Interest (QoIs)

The quantities of interest define a variable of interest and depend on the research questions and the goal of the uncertainty assessment. If a variable is defined by a probability distribution, its QoIs are features that characterise that distribution: central value, dispersion and shape. These features are called **statistical moments**.

Consider the random variable X. The expected value of X is denoted

$$E[X] = \int_{x \in X} x f_x(x) dx \tag{1.3}$$

The first statistical moment used to define the location of the central tendency of a PDF is the *mean* μ

$$\mu_X = E[X] \tag{1.4}$$

The second statistical moment is a measure of the variability of the central tendency of the PDF and is called *variance* σ^2. In other words, the variance is the average of the squared differences from μ. The standard deviation σ is simply the square root of the variance and indicates how spread out the numbers are in the distribution.

$$\sigma_X = \sqrt{Var[X]} = \sqrt{E[(X - \mu_X)^2]} \tag{1.5}$$

The third and fourth statistical moments characterise the shape of the distribution and are called *skewness* $\widetilde{\mu_3}$ and the *kurtosis* k. The skewness is a measure of the symmetry of the distribution $\delta_X = E\left[\frac{(X-\mu_X)^2}{\sigma_X^3}\right]$. Kurtosis is a measure of the flatness of the distribution $k_X = E\left[\frac{(X-\mu_X)^4}{\sigma_X^4}\right]$.

Other quantities of interest include *quantiles* and *confidence intervals*. The quantile of a probability distribution corresponds to the inverse of its cumulative function. A quantile specifies the value of a random variable for which the probability of it being less than or equal to that value is the given probability. For example, the 50% quantile corresponds to the value $q_{0.50}$ for which the probability of X being less than or equal to $q_{0.50}$ is 50%, and in this case, to the median value $F_X(\widetilde{x}) = 50\% \equiv \widetilde{x} = q_{50}$. A Confidence Interval (CI) is used to define the variability of X on a population bounded by two quantiles centred on $q_{0.50}$. The quantiles of interest for this work and the CI are shown in Fig.1.11.

1.2.1.4 Probability distributions

There are a number of distributions that can be used to define the uncertain input variables X. The continuous distribution types employed in this work, are the uniform, normal or Gaussian and Generalised Extreme Value (GEV) distributions, shown in Fig.1.12 respectively. The uniform

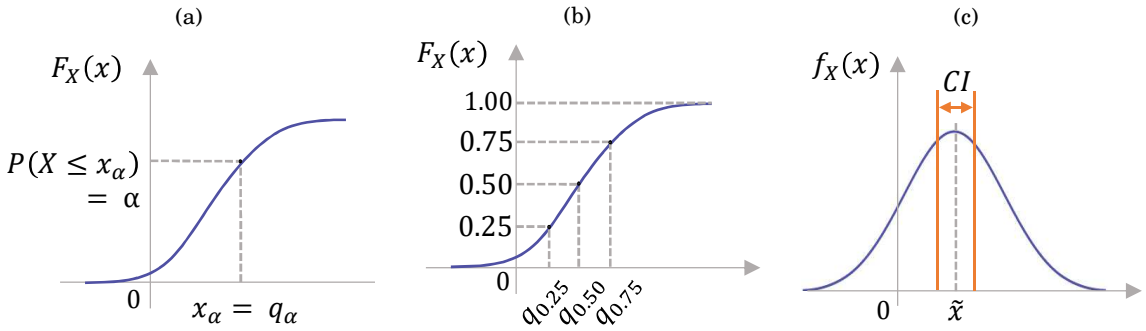

FIGURE 1.11. Some quantities of interest of a probability distribution: (a) Probability of quantile α, q_α; (b) 25%, 50% and 75% quantiles, respectively $q_{0.25}$, $q_{0.50}$ and $q_{0.75}$; (c) Confidence Interval, CI.

distribution is defined by its bounding values a and b, such that

$$X \sim U(a,b) \quad a,b \in \mathbb{R}; a < b$$
$$f_X(x) = \frac{1_{[a,b]}(x)}{b-a} = \begin{cases} cl\,\frac{1}{b-a} & \text{if } x \in [a,b] \\ 0 & \text{if } x \notin [a,b] \end{cases} \tag{1.6}$$

The normal or Gaussian distribution is defined by μ and σ, such that

$$X \sim N(\mu,\sigma) \quad \mu \in \mathbb{R}; \sigma > 0$$
$$f_X(x) = \frac{1}{\sigma\sqrt{2\pi}} e^{-\frac{(x-\mu)^2}{2\sigma^2}} \tag{1.7}$$

The GEV distribution is defined by μ (location), σ (scale) and ξ (shape), such that

$$X \sim \text{GEV}(\mu,\sigma,\xi) \quad \mu,\xi \in \mathbb{R}; \sigma > 0$$
$$s = (x-\mu)/\sigma$$
$$f_X(x) = \begin{cases} (1+\xi s)^{(-1/\xi)-1} \exp(-(1+\xi s)^{-1/\xi}) & \xi \neq 0 \\ \exp(-s)\exp(-\exp(-s)) & \xi = 0 \end{cases} \tag{1.8}$$

GEV is a family of continuous probability distributions that combines three simpler distributions into a single form. These are known as types I, II and III distributions, and correspond to the Gumbel, Frechet and Weibull extreme value distrbutions, respectively. GEV models the largest value of a long and finite set of identically distributed, independent data.

For the Gaussian distribution, 68.27% of the values are within one standard deviation, $\pm 1\sigma$, of the mean value, μ. For two standard deviations, 95.45% of the values are within $\mu \pm 2\sigma$. For and three standard deviations, $\mu \pm 3\sigma$ account for 99.73% of the values. This is illustrated in Fig.1.13.

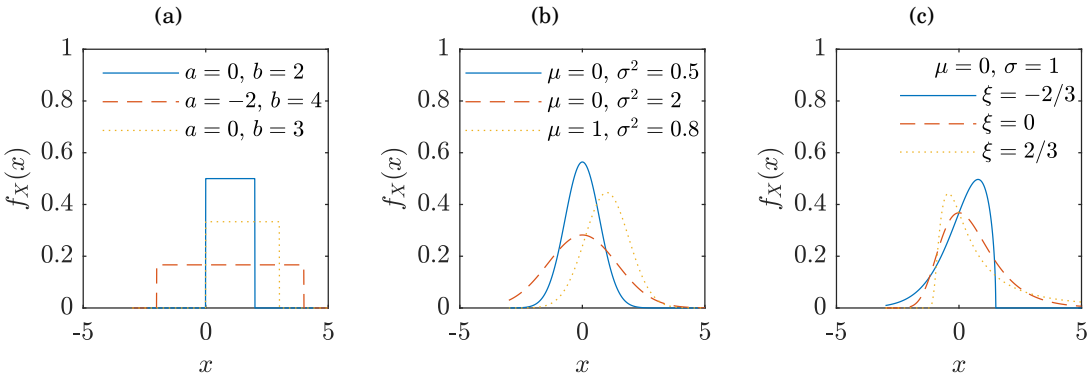

FIGURE 1.12. Univariate continuous distributions used. (a) Uniform distribution; (b) Normal or Gaussian distribution; (c) Generalised extreme value distribution.

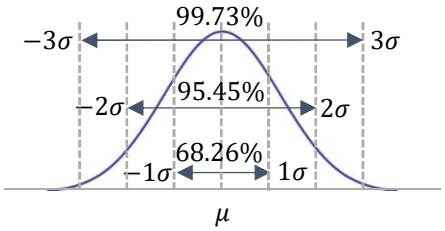

FIGURE 1.13. Normal distribution set percentage and σ deviation from μ.

1.2.1.5 Multidimensional random variables, correlation coefficients and dependence modelling with copulas

Similarly to a random variable X_i, a random vector $X = (X_1, X_2, ..., X_n)^t$ is also a measurable function. A vector is composed of n random variables and is a multidimensional random variable itself. A vector can be defined directly from its joint distribution or from a collection of marginal distributions and a copula.

The joint distribution of a random vector X is defined by its statistical moments such as the expected value, the covariance matrix and the correlation matrix. The expected value of a random vector X is the vector of the expected values of random variables that compose it. The expected value and the covariance matrix are defined as

$$E[X] = (E[X_i], i = 1, ..., n)^T \tag{1.9}$$

$$\sigma_{ij} = \text{cov.}[X_i, X_j] = E[(X_i - \mu_{X_i})(X_j - \mu_{X_j})], \text{ such that } i, j = 1, ..., n \tag{1.10}$$

The covariance is a measure of how much two variables change together and the sign of the covariance parameter indicates the tendency of the correlation between the variables. In order to interpret the magnitude of the correlation, the **Pearson's Correlation Coefficient** (PCC) is introduced as a normalised covariance, the covariance of the variables divided by the product of

their standard deviations. PCC quantifies the strength and direction of the linear relationship between two variables.

$$\rho_P(X_i, X_j) = \frac{\text{cov.}(X_i, X_j)}{\sigma_{X_i}\sigma_{X_j}} \tag{1.11}$$

quantify the strength and direction of the linear relationship between two variables. The **Spearman's Rank Correlation Coefficient** (SRCC), on the other hand, is a measure of the monotonic dependence between X_i and X_j, i.e. a measure of how well the relationship between two variables can be described by a monotonic function, i.e. a function that is entirely non-increasing or entirely non-decreasing.

$$\rho_S(X_i, X_j) = \rho_P(F_{X_i}(X_i), F_{X_j}(X_j)) \tag{1.12}$$

The linear and rank correlation matrices are then built with the correlation coefficients as indices, from PCC and SRCC respectively [24].

The marginal distributions of a vector are the probability distributions of the n random variables of X and copulas define the stochastic dependency structure between them. A copula is a joint cumulative distribution function defined on the unit cube with uniform marginal variables. The collection of the marginal distributions with the copula forms a joint distribution of the newly generated multivariate vector. At the basis of the copula formalism lies Sklar's theorem [25]:

$$F_X(x) = C(F_{X_1}(x_1), ..., F_{X_M}(x_M)) \tag{1.13}$$

In this work, Independent and Gaussian copulas are used. Using an independent copula corresponds to the case of having all statistically independent variables, i.e. $P(A \cap B) = P(A)P(B)$. The correlation matrix is equivalent to an identity matrix $\rho = I_n$ and the joint cumulative distribution function is the product of the marginal distributions. A Gaussian copula is the joint cumulative distribution function of a multivariate normal distribution, introducing a linear or rank correlation matrix calculated with Eq.1.11 or Eq.1.12, respectively [26].

1.2.1.6 Monte Carlo Simulation

Monte Carlo Simulation is a method to propagate uncertainty in a given model. It works on the principle of repeated random sampling in order to predict the probability of a given outcome. MCS takes the uncertain input variables probability distributions and randomly samples each one. It runs the model for the samples and obtains a result. This process is then repeated again and again until the results are combined to produced an estimation of the output uncertainty. Because of the randomness in the sampling method, Monte Carlo falls short when it comes to covering the entire sampling space, especially the tails of the distributions. MCS works best in fields where the input variables are random and have significant uncertainty, such as business or finance.

1.2.1.7 Latin Hypercube Sampling (LHS)

A Latin Hypercube is a method of generating near-random samples from the input variable distribution. LHS aims at spreading the sampling points evenly across the probability distribution. It is based on the latin square layout, where an $N \times N$ array is filled with N different samples, each occurring exactly once for each row and column, see Fig.1.14. A hypercube is a cube with more than three dimensions and thus latin hypercube is extended to sample from multiple dimensions [27].

LHS partitions each input variable's CDF into N equally probable intervals and a random sample is taken from each interval. For multidimensional sampling, the sample space is, similarly, partitioned into sub-spaces with equal probability and the random samples are chosen so that each subspace is sampled with the same density, such that LHS prevails [28].

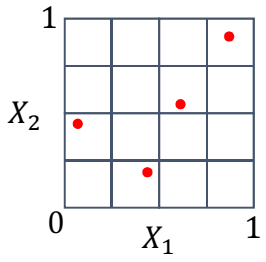

FIGURE 1.14. Two-dimensional Latin hypercube sampling in the (X_1,X_2) space; There is only one sample in each row and column.

LHS ensures the sample space is a good representation of the whole input space variability. LHS is chosen over Monte Carlo for its speed at convergence, i.e. reduced number of necessary runs for a converged result, and smoothness at representing input distributions. LHS has been proven to be advantageous for computing models where few variables are responsible for the variability of the output VoI, and neutral (offers no disadvantage) for models where copulas are widely used and many variables are important uncertainty sources. [29] discusses the efficiency of various importance sampling methods for the case of structural reliability analysis. Generally, better accuracy was obtained for LHS at half the required sample size compared to MC analysis, although exact savings are dependent on the analysis. It is also shown that the sampling direction has an impact on the results. More discussion on LHS's versus MC's can be found in [30].

1.2.1.8 Perturbation Theory

The word perturbation, or disturbance, is allusive to the essence of perturbation theory. The general approach is to start with a "simple" solution to a known problem and perturb it by adding small disturbances. The final approximate solution is achieved by correcting the "simple" solution to the perturbation results. The problem is broken into solvable and perturbative parts. The correction is then calculated, usually recursively, order-by order, such that

$$A = A_0 + \varepsilon^1 A_1 + \varepsilon^2 A_2 + ... \tag{1.14}$$

where A_0 is the simple solution and the further terms represent the deviations to that solution, constituting a series expansion in powers of a small parameter (ε) - perturbation series. The first

order perturbative correction, for instance, is $\varepsilon^1 A_1$ and the final solution is given by A.

Perturbation theory is best applied to a system that does not have a known exact solution but can be seen as a small change to a known solvable system. It is widely used across fields but takes its most advanced forms in the field of quantum mechanics.

1.2.2 Non-probabilistic uncertainty modelling and propagation

Non-probabilistic uncertainty is an umbrella term for various different methods of handling uncertainties that are not defined as probability distributions. It is also known as possibilistic uncertainty and includes approaches such as interval analysis and fuzzy logic, amongst others [31].

Possibilistic uncertainty is complementary to the probabilistic approach by handling incomplete or subjective information. Incomplete information might be due to lack of knowledge or maturity of the information, randomness or unknown factors. Possibility theory makes it easier to capture partial ignorance and is meant as a modelling tool to natural language uncertainty statements. When there is not sufficient information about the input data to build an accurate probability distribution, possibility theory is applied, where the inputs are measured in terms of their bounds of possibility [32–34].

Probabilistic methods can be used to model the different types of uncertainties, as long as there is sufficient data to build a probability distribution. Bayesian theory considers that probability is a subjective measure of the degree of belief that specific outcome will occur. These probabilities are construed based on a design of experiments and expert judgement, alluding to the fact that probability theory can be used when little is known about the input data. This partial belief representation parallels probability theory, however it can also be the basis of possibility theory. Possibilistic uncertainty can be defined quantitatively or qualitatively [35].

In possibilistic modelling, two set functions are calculated: one of possibility and one of necessity, ranging from 0 to 1. A possibility distribution is a mapping π from a set of states in the state space S, to a totally ordered scale L=[0,1]. The state of information of an agent is represented by the function π, distinguishing degrees of plausibility, such that: $\pi(s) = 0$ means that the state s is impossible and is rejected; and $\pi(s) = 1$ means that the state s is plausible or totally possible. If the state space S is exhaustive, at least one of the elements should be totally possible. Possibility is driven by minimum specificity meaning that any state that is not impossible cannot be rejected. The most specific state is the most restrictive and informative. The degree of possibility of A is defined by

$$\Pi(A) = max\{\pi(s), s \in A\} \tag{1.15}$$

whereas the necessity function, or the degree of belief in A, is defined by

$$N(A) = min\{1 - \pi(s), s \notin A\} = 1 - \Pi(\neg A) \tag{1.16}$$

The possibility degree Π evaluates to what extent A is possible given the knowledge π, while $N(A)$ evaluates the extent to which A is implied by π [31].

1.2.2.1 Interval analysis

Interval analysis or interval arithmetic is a technique used in numerical problems, to set bounds or intervals in the computations. In interval analysis, instead of representing the input variables as a single value or a probability distribution, each value is represented as a range of possibilities. For instance, instead of describing the weight of a part A as a normal distribution with mean $\mu = 20$kg and a standard deviation $\sigma = 2$kg, one can describe it as the weight of part A being between 15 to 23kg with a confidence level of 80%. Confidence level is introduced as a measure of expected probability that the solution lies within certain interval. The confidence level considers only prior estimates and denotes the system's relevant certainty, in percentage. A confidence level of 100% guarantees that the solution lies within the interval associated with that CL [36, 37].

For the generic description of UQ in Fig.1.8, the uncertain variable X is represented by an interval $[\underline{x};\overline{x}]$ that contains X. $\underline{x}$ is the minimum estimated parameter value above which the exact value X should be, depending on the interval's confidence level. $\overline{x}$ is the maximum parameter value below which the exact value X should be. Both $\underline{x}$ and $\overline{x}$ are represented by real values.

$$x = [\underline{x};\overline{x}] = \{X \in [0;1] : \underline{x} \leq X \leq \overline{x}\} \tag{1.17}$$

The midpoint of the interval is defined as

$$\mu_x = \frac{\underline{x} + \overline{x}}{2} \tag{1.18}$$

and the corresponding radius of the interval is

$$\Delta x = \frac{\overline{x} - \underline{x}}{2} \tag{1.19}$$

The interval arithmetical approach, also known as interval analysis, is defined on the standard arithmetic for addition, subtraction, multiplication and division of intervals, such that:

$$x + y = [\underline{x} + \underline{y}; \overline{x} + \overline{y}] \tag{1.20}$$

$$x - y = [\underline{x} + \overline{y}; \overline{x} + \underline{y}] \tag{1.21}$$

$$x \times y = [\underline{x} \times \underline{y}; \overline{x} \times \overline{y}] = [\min(\underline{xy}, \underline{x}\overline{y}, \overline{x}\underline{y}, \overline{xy});\ \max(\underline{xy}, \underline{x}\overline{y}, \overline{x}\underline{y}, \overline{xy})] \tag{1.22}$$

$$\frac{x}{y} = \begin{cases} x \cdot \left[\frac{1}{\overline{y}}, \frac{1}{\underline{y}}\right], & \text{if } 0 \notin Y \\ \text{undefined} & \text{if } 0 \in Y \end{cases} \tag{1.23}$$

Interval analysis is used for a variety of purposes, including to propagate precision and rounding errors in calculations and in physical and technical parameters uncertainty modelling

and propagation, when measurement errors and allowables for materials and components are often limited by computational accuracy. Uncertain interval parameters are propagated through a given model (Fig.1.8) in order to find the extreme responses of the numerical model. The set of interval parameters can be solved by directly applying interval arithmetic techniques or following a global optimisation approach [38].

Global optimisation is a branch of numerical modelling that aims to find the global minima or maxima of a model on a given set. Given a model $g(x)$, input parameters $x \in X$ and output $z \in Z$:

$$\underline{z} = \min g(x) \tag{1.24}$$

$$\overline{z} = \max g(x) \tag{1.25}$$

Generally a high computational cost is associated with global optimisation approaches, especially in engineering problems that might include millions of uncertain parameters, many of which with non linearities. Whereas local optimisation tries to find a local minima or maxima of the model, global optimisation considers the entire input parameter space and all its dimensions [39].

When the model response is deterministic and monotonic with respect to the input uncertain parameters, the Vertex method ensures an exact solution for the global optimisation problem for interval parameters. It is then considered a special case of the global optimisation approach. The vertex method builds a linear interpolation matrix between the model outputs, obtained by propagating the vertices of the hypercubic input uncertain parameter set. With these, it provides a first order response surface model approximation of the deterministic model response. For non-monotonic problems, the accuracy of this technique is greatly degraded, as the number of data points becomes insufficient to accurately model this behaviour. The computational cost of vertex methods is also exponentially increased by the number of uncertain input parameters [31, 40].

1.2.2.2 Fuzzy logic

Fuzzy logic, as possibility theory, is an approach used to handle vague, imprecise or ambiguous, linguistic information. Fuzzy sets are a more general form than intervals to describe the imprecision in real life data. Fuzzy data refers to a connected set of possible values, each of them having partial membership in the set. This means that each number in the set is attributed a weight, between 0 and 1, called a membership function. This allows for the representation of a value that is only to a certain degree member of the set. Interval analysis can be seen as a special case of the fuzzy approach where each object inside a set is assigned weight 1. Using fuzzy logic, each parameter of a model can be represented as a value, an interval, a fuzzy value or a fuzzy interval [41].

Fuzzy sets are typically represented as triangular or trapezoid-shaped curves, as each value will have a slope where the weight is increasing, a flat peak where its equal to one and another

slope where the weight decreases. They can also be represented by a sigmoid function, such as the logistic function:

$$S(x) = \frac{1}{1+e^{-x}} \tag{1.26}$$

A fuzzy set $\hat{x}$ is described by its elements x in the domain X and their respective membership functions $\mu_{\hat{x}}(x)$, such that

$$\hat{x} = \{\left(x, \mu_{\hat{x}}(x)\right) | x \in X; \mu_{\hat{x}}(x) \in [0;1]\} \tag{1.27}$$

If the membership function of $\mu_{\hat{x}}(x) = 1$, then x is certainly a member of the fuzzy set $\hat{x}$. On the other hand, if $\mu_{\hat{x}}(x) = 0$ then x is certainly not a member of $\hat{x}$. The membership is uncertain when $0 < \mu_{\hat{x}}(x) < 1$. There are a variety of different types of membership functions that can be applied in fuzzy sets, such as triangular or Gaussian. When the set is comprised of multiple parameters, a joint membership function is applied:

$$\mu_{\hat{x}}(x_1, x_2, ..., x_k) = \min(\mu_{\hat{x}}(x_1), \mu_{\hat{x}}(x_2), ..., \mu_{\hat{x}}(x_k)) \tag{1.28}$$

the membership function of a fuzzy output quantity $\hat{y}$ can be approximated by Zadeh's extension principle [42]: given a k fuzzy input parameters $\hat{x}_1$, $\hat{x}_2$, ..., $\hat{x}_k$, :

$$\mu_{\hat{y}}(y) = \begin{cases} \sup_y(\mu_{\hat{x}}(x_1, x_2, ..., x_k)), & \text{if } \exists y = m(x_1, x_2, ..., x_k) \\ 0 & \text{otherwise} \end{cases} \tag{1.29}$$

Following the extension principle and in order to compute the output quantity $\hat{y}$, solution to the fuzzy problem, several different methods have been proposed, including multidimensional optimisation, the α-cut or the transformation method. A multidimensional optimisation approach, despite its accuracy in calculations, comes at high computational expense. The α-cut method is a method used to propagate fuzzy uncertainty sets in numerical models. The fuzzy input parameters are subdivided into N_α equally spaced intervals of width $\Delta\mu = \frac{1}{N_\alpha}$. An α-cut interval contains all elements x_i that *at least* belong to $\hat{x}$ *at least* to the degree α [31]. Interval analysis is performed in each of these intervals and the smallest and largest possible solutions are found for each α level. As an extension to the Vertex method, the transformation method is introduced. Consequently, transformation has the same limitations as the Vertex method, such as it can only be applied for monotonic problems and an exponential increase in computational cost. It combines an α-cut approach with the propagation of the vertices of the hypercube input parameter set through the deterministic model.

1.2.3 Uncertainty backpropagation

Uncertainty, so far, was described as being propagated forwards through the model, by the means of probability theory. Forward propagation progresses from an input parameter uncertain

space $\mathbb{X}$ to an output distribution $f_Z(z)$. Uncertainty backpropagation, also known as uncertainty identification or inverse uncertainty propagation, moves in the reverse direction where, for given a desired output, the correspondent input subspace is sought. Backpropagation aims at estimating input parameters subspaces and is crucial for experimental design and monitoring programmes, as well as estimating input uncertainty interval bounds and correlations [43]. Recall the interval-based representation of uncertainty, described in sec.2.4.2.

In forward propagation, the input distribution or entire input parameter space, $\mathbb{X}_{\text{prior}}$, is sampled. The model runs for each sample and an output distribution is obtained. In inverse propagation, one starts by looking at the output distribution and defining an output interval of interest IoI or margin, see Fig.1.15(a). In aircraft design this is likely to be a discrepancy from the output weight to a target weight or a reliability margin. Given the newly defined output's IoI, the forward method is reverted in order to compute the input parameter sub-space that allows for that IoI, $\mathbb{X}_{\text{posterior}}$. In other words, what individual viable margins and correlations can be set at input level in order to obtain the desired IoI, see Fig.1.15(b). The objective might be to find an interval for maximum target reliability, robustness, specific performance constraints or critical and rare objective cases.

FIGURE 1.15. Uncertainty backpropagation. (a) Output probability distribution and interval of interest IoI; (b) Input parameter space $\mathbb{X}_{\text{prior}}$ and the subspace retrieved from backwards propagation of uncertainty correspondent to IoI, $\mathbb{X}_{\text{posterior}}$.

Uncertainty backpropagation in this research is made by sampling the entire input parameter space $\mathbb{X}_{\text{prior}}$, selecting the VoI and its interval of interest IoI and then collecting the subset $\mathbb{X}_{\text{posterior}}$ that have resulted from the samples in IoI. The QoIs of this subset are then analysed and conclusions are made for the specific analysis.

Surrogate models can be used to map the IoI to the $\mathbb{X}_{\text{posterior}}$. Particularly, ANNs are widely applied [44, 45].

1.2.3.1 Parallel-coordinate plots

One way to visualise sample based uncertainty backpropagation is through parallel-coordinate plots or cobweb plots. This data visualisation method, allows for quickly identifying trends and patterns across variables, as well as providing an overall map of the variance or uncertainty of each parameter, relative to another parameter sub-space [46].

The parallel-coordinate plots, as indicated by its name, plot each simulation run as a horizontal line, crossing each variable, represented in a vertical axis, at its value. The variables are displayed parallel to each other and each variable's distribution is normalised between 0 and 1 to allow for comparison.

An example is shown in Fig.1.16 where a structural sizing framework was used to run a number of simulations for different load cases. The variables displayed in the vertical axis are the load case parameters: Mach number M, altitude h, load factor n and fuel fraction f; and the obtained wing weight W_{Wing}. Each simulation is represented by one line and the simulations are coloured from blue to yellow in ascendant order of W_{Wing}.

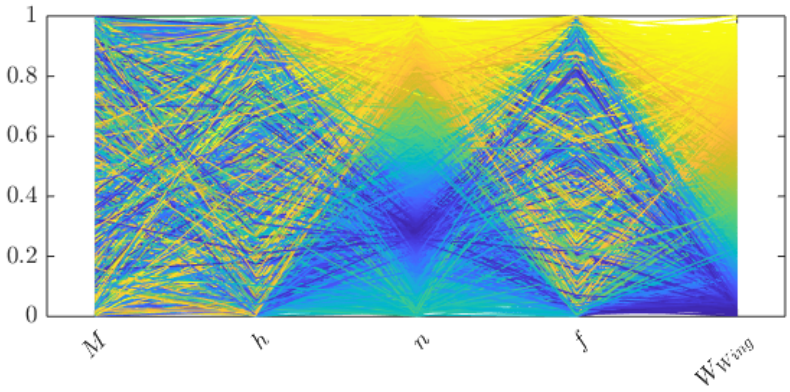

FIGURE 1.16. Parallel-coordinate plot showing the load case parameters and correspondent wing weight distributions.

Correlations between factors can be identified: If for two specific input variables, the lines follow a trend (for example if every time the first variable is high the second variable is low and vice-versa), these variables are highly correlated; If, on the other hand, for two input variables, their values are randomly scattered across their range of variability, the variables are lowly correlated. Sensitivity indices can also be predicted: If the sample lines cover the entire range of variability, sensitivity is low; Whereas if the lines cover a concentrated region, sensitivity is high [47].

Consider again the example of Fig.1.16. Knowing that the load factor n was varied between $[-1, 2.5]g$, the higher W_{Wing} (in yellow) correspond to larger n; whereas the lowest W_{Wing} (in dark blue) are a result of $n \approx 0$. In other words, the larger the absolute value of n, the larger the value for W_{Wing}. Thus, load factor n and W_{Wing} are highly correlated. On the other hand, the fuel

fraction f shows a large range of variability, indicating low correlation between f and W_{Wing}. Since the 4 load case parameters are the only input parameters to this simulation, the correlation is synonym of sensitivity. That is, W_{Wing} is highly sensitive to n and not f.

A specific parameter sub-space can be defined in order to facilitate the visualisation of certain aspects one might want to study. In the structural sizing example, some of the sizing load cases could not trim the aircraft and these are highlighted in red in Fig.1.17. This plot indicates that the events for which trim was not possible were low M, high h and high n.

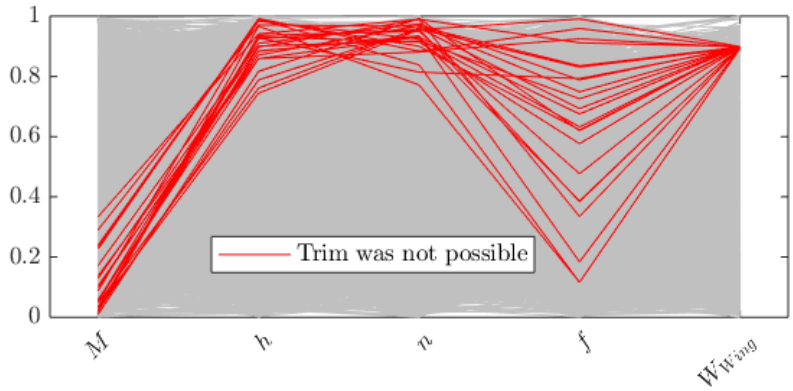

FIGURE 1.17. Parallel-coordinate plot showing the load case parameters and correspondent wing weights for which the aircraft trim was not possible.

Another example is shown in Fig.1.18, where a subset of W_{Wing} was isolated between a and b. This plot shows evidently the high sensitivity of W_{Wing} towards n, and low towards the rest of the parameters. In terms of uncertainty backpropagation, or inverse uncertainty propagation, for

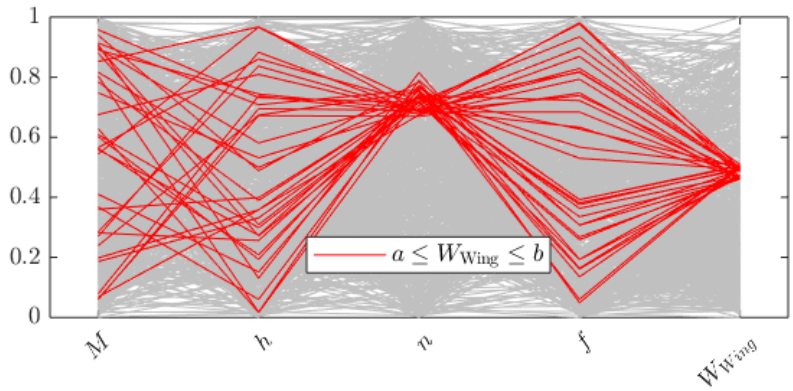

FIGURE 1.18. Parallel-coordinate plot showing an interval of interest of the wing weight distribution $[a, b]$, and the respective (driving) load case parameters.

a certain subset of the output variable, the parallel-coordinate plots allow the identification of the ranges and variabilities of the respective input variables. In the case of Fig.1.18, the interval

of interest is $IoI = [a,b]$ and the highlighted lines correspond to the specific subset $\mathbb{X}_{\text{posterior}}$ in analysis.

Cooke et al. propose an interactive version of parallel-coordinate plots in an open source software called UNINET [48]. UNINET is a stand alone program that uses Bayesian Belief Nets (BBNs) for stochastic modelling and multivariate ordinal data mining. It is designed by the Risk and Environmental modelling group at the Department of Mathematics of the Delft University of Technology, under contract with the Dutch Ministry of Transport [48]. In UNINET the user defines the random variables, by defining their marginal distributions, and a Directed Acyclic Graph DAG to capture conditional relations between them. Conditional rank correlations can be added to the DAG as probabilistic influence between parent and child. A joint PDF is built using the joint normal copula to realise any dependence relations. The PDF is sampled and analysed using MC methods. The same software is used for aircraft conceptual design exploration with two objectives in mind: identifying promising designs and accurate interval uncertainty allocation [45]. The QoIs are measured using an ANN surrogate of the simulation and it includes dependencies between the design, uncertainty and interval variables.

1.2.3.2 Bias correction and model calibration

Bias correction and model calibration are a parallel branch of uncertainty backpropagation, when the goal is to use the results of a simulation and a set of real data, to calibrate the model or the input parameter uncertainty, including its distribution types and parameters [49, 50].

Bias correction estimates the difference between real or experimental (observations) and simulated outputs (predictions). Given the differences or bias, it then calibrates the values of the uncertain input parameters to be fed to the model. A general formulation for quantifying different sources of uncertainty is

$$y^e(x) = y^m(x) + \delta(x) + \varepsilon \tag{1.30}$$

where x is a vector of the uncertain input variables, $z^e(x)$ describes the experimental output, $z^m(x)$ describes the model output, $\delta(x)$ is the bias function for model discrepancy and ε accounts for experimental error variability [51]. A representation of a bias correction and model calibration study is shown in Fig.1.19. The confidence intervals CI are provided as the quantification of uncertainty for the model. The aim is to calibrate the input parameter space or the model itself so that the predictions and CIs fit and comprise the observations.

Bayarri et al. [52] uses this approach to quantify different multiple uncertainty sources, as well as to update validation assessments once more information is simulated or observed and becomes available and makes predictions about untested data. Li et al. [53] proposes a methodology to quantify uncertainty in the input parameters by performing bias correction, model calibration, validation and SA at different levels of model complexity. Wong et al. [54] suggests a frequentist solution to this method. Patelli et al. [55] apply stochastic model updating techniques to the DLR AIRMOD structure.

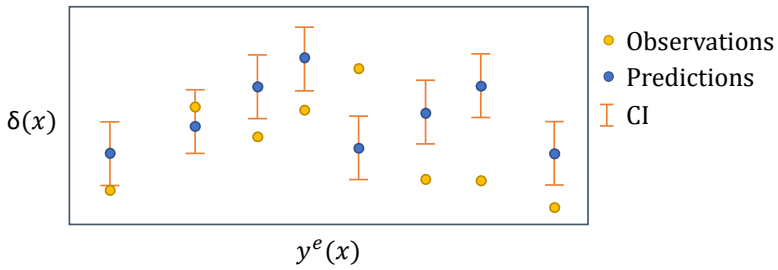

FIGURE 1.19. Bias correction and model calibration.

1.2.4 Sensitivity Analysis (SA)

Reconsider the mathematical model $G(X,d)$, dependent on a set of input variables described by a random vector X, declared in sec.1.2.1.2. The aim of sensitivity analysis is to describe how the variability of the model response $Z = G(X)$ is affected by the variability of each input variable. In other words, SA investigates how the variation in the output Z can be associated to variations in the different uncertain input factors $(X_1, X_2, ..., X_n)$ [56].

There are several different methods and methodologies used to perform SA. In order to understand which one suits each case best, it is important to understand the problem specification at hand and what the purpose of the analysis is. Some definitions on the latter follow [47, 57].

- **Purpose**
  SA has three main purposes: model reduction, importance ranking and mapping. Model reduction aims at identifying which input variables are negligible and therefore can be disregarded when running the simulation. Importance ranking, or factor prioritisation, lists the input variables in order of influence on the model's response, allowing for building dependence structures between output and input variables and spot important correlations between the two. Mapping is the process of determining which subsets of values or regions within the input variables distributions are contributing significantly to the output variability or uncertainty or subsets of output values of major impact.
- **Type**
  SA methods can be local or global. Local sensitivity methods look at partial derivatives of the output z relative to variations of the input factor around a nominal value $\overline{x}$. Global sensitivity methods take into account the whole input domain. For global SA the user needs to define the whole input variability space and, for local methods, the nominal value needs to be defined. Local methods are more likely to experience errors [58].
- **Sampling strategy**
  Input random variables can be evaluated and sampled One-At-a-Time OAT or All-At-a-Time AAT. In OAT design, the variables are all kept at their nominal values except for one that is varying. The process is then repeated for all other variables. In AAT sampling, all the input variables are varying simultaneously. AAT considers different combinations of

variations of the input variables, within their variability space. Both OAT and AAT account for the input's impact on the output's variability but AAT also accounts for correlations between inputs. Local methods use OAT samples whereas global methods can use either OAT or AAT samples [59].

- **Computational expense**
  Different SA methods require different number of model evaluations to be applied. These are dependent on the number of uncertain input parameters n.
- **Results**
  The results of a SA test can be evaluated quantitatively or qualitatively. Qualitative SA refers to methods where conclusions can be drawn by visual inspection, e.g. scattered plots, and quantitative SA refers to attributing sensitivity indices to each input variable.

After understanding the model and the problem, the purpose of the sensitivity analysis, the computational and time resources and how the results are intended, a specific method for SA is adopted.

1.2.4.1 Standardised Regression Coefficients (SRC)

Standardised Regression Coefficients or Standardised Rank Regression Coefficients (SRC and SRRC) are a SA global technique that makes use of AAT samples, consistent with the input variables definition and sampling strategy used [60]. The regression coefficients are indicative of the inputs' global impact on the model and aim at ranking inputs in order of impact on the outputs' uncertainty to allow for discerning and understanding uncertainty drivers and prioritising efforts. If the relationship between input and output is strongly nonlinear or non monotonic, the SRC method may be inadequate. The number of model evaluations available for each analysis' application was $5000n$. SRC allows for quantitative, via sensitivity indices, and qualitative, via bar and regression line plots, evaluation of the results.

The sensitivity indices SI are a by-product of the regression analysis applied to the input to output LH sample set. If the relationship between Xi and Z is linear, the regression takes the form $Z = a_i + b_i X_i$, and the SI is the linear least squares estimate of the regression coefficient b_i.

To be able to evaluate parameters with different units of measure and relative magnitudes, a standardisation process is warranted. The standardisation is applied by transforming the ratio of the parameter's standard deviation σ to its mean μ and $b'_i = b_i \cdot \frac{\sigma_{X_i}}{\sigma_Z}$.

SRRC is calculated by performing regression analysis to rank-transformed samples, i.e. to a sample set that was transformed for a perfect fit to a uniform distribution.

1.2.5 Surrogate modelling

For complex engineering design models, a single simulation may take minutes, hours or even days to run. Design optimisation, design space exploration, uncertainty propagation and sensitivity analysis are tasks that require hundreds, thousands or even millions of evaluations, which

makes direct sampling from simulations extremely costly. In many problems the output is also deterministic, meaning that rerunning the model for the same inputs would result in the same outputs. Consequently, the idea of building a surrogate of a simulation model was introduced in the 1980s by [61].

A surrogate model, metamodel or emulator, is an approximation model that mimics the behaviour of the simulation at a reduced computational expense. It works in a black-box, bottom-up approach, by taking the inputs and outputs and generating a map between them. The metamodel does not look at the simulation and the physics behind it. For this reason, the choice of the data set used to train and validate the emulator is an important step in the process.

The first step to building a surrogate model is to choose its type. Different methods will work best for different cases and this depends on the input-to-output response surface (linear/nonlinear, monotonic/non-monotonic, etc), computational resources at the start (design of experiments' size and quality) and accuracy required. The design of experiments is divided into a training set and a validation set. The surrogate is first generated using the training set and then evaluated against a validation set. The process is repeated until the desired level of accuracy is obtained [62].

A number of surrogate model approaches have been developed and studied over the past few years and the ones relevant to this work are generally described below [63]:

- **Polynomial Chaos (PC)** is a method in which the input to output relationship is fitted via a family of orthogonal polynomials. PC expansions can be intrusive via the Galerkin projection or Non-Intrusive (NIPC) using the Least-square approximation or a non-intrusive spectral projection [64].
  PC was first introduced by Wiener [65] to model Gaussian random variables using Hermite polynomials. It was then extended by Xiu and Karniadakis in [66] to different probability distributions using different polynomials such as Laguerre, Jacobi, Legendre for the continuous distributions gamma, beta and uniform, respectively. Multivariate distributions can be modelled by multivariate polynomials [62]. and UQ on random processes and simulations can be done with the use of PC expansions [67, 68].
- **Gaussian Process (GP)** is an extension of the Gaussian distribution. GP assumes that the function that models the output of the simulation $f(x)$, is marginally normally distributed for each data point $f(x_i)$ [69]. The regression line crossing all the data points is the mean value of each normal distribution and the uncertainty in the fit corresponds to the 95% confidence intervals of the distributions (see Fig.1.20). The further away from any two data points, the largest the uncertainty. Similarly, increasing the training data, approximates $f(x)$ to the true function. GP's uncertainty increases rapidly for critical or boundary values of the data, if trying to extrapolate information outside the data. The statistical theory and mathematical background can be found in [70–72].
- **Artificial Neural Networks (ANNs)** are data processing modelling tools inspired by biological neural networks. Similarly to biological neurons, ANNs have artificial neurons

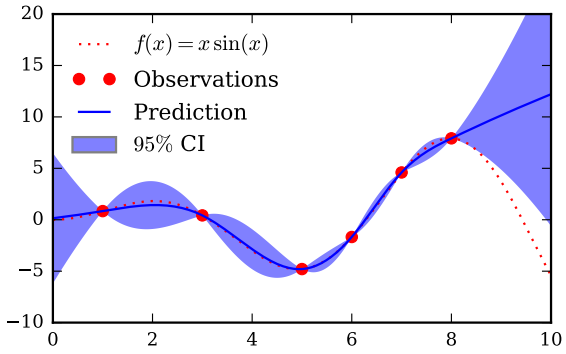

FIGURE 1.20. Gaussian process regression fit example for non-noisy data [73].

in hidden layers, capable of processing highly parallel, nonlinear computations. ANNs function without any prior knowledge about the inputs. Instead, they learn the inputs' characteristics by processing the data in cycles (or layers) in different neurons. Each neuron is attributed a weight that is adjusted once, and if, more data is used to train the network, i.e. they learn from experience. The output is then generated by a nonlinear function of the sum of its inputs. ANNs are powerful tools that provide practically accurate solutions and are capable of dealing with nonlinearities in the data, are computationally inexpensive (fast processing due to high parallelism), learn and adapt to new data and can be applied to unknown, black-box type of problems [74]. ANNs can be used for a variety of data driven problems, including uncertainty backpropagation in [44, 75], discussed in sec.1.2.3.

1.3 Literature review on uncertainty quantification in the aircraft design

Uncertainty in the aircraft design process has been a topic much explored in recent years, both in academia and in industry. Applications of uncertainty quantification in aeroelasticity studies consider uncertainty in aircraft design and structural sizing, including weight considerations, aircraft Life-Cycle Cost (LCC) and its environmental impact and aeroelastic stability and aerodynamic characteristics.

1.3.1 Uncertainty in the aircraft development plan - The weight uncertainty pyramid

As the aircraft design cycle evolves, knowledge increases and information matures. An uncertainty pyramid representing the different genus of uncertainties at each phase of design is shown in Fig.1.21. Climbing the pyramid symbolises progression in the aircraft design cycle [2].

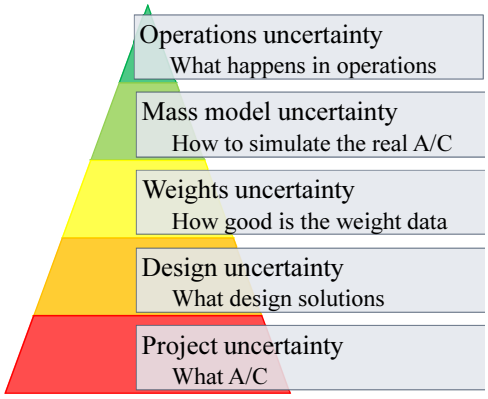

FIGURE 1.21. The uncertainty pyramid and types of uncertainty.

In the early stages of design, or at the bottom of the pyramid is project uncertainty. The aircraft is being conceptualised and the uncertainty is present in all model parameters. Trades regarding range, payload, fuel and costs, as well as major configuration principles such as taking a conventional tail aft design approach or a design that would push the physics boundaries differently, e.g., canard, three surface aircraft, flying wing, etc, are considered. One level above there is design uncertainty. This is where more detailed trades and changes happen and the design is iteratively optimised. Parameter variability is a big source of uncertainty at this stage. Once the major design variables are fixed and the final product is subject to fewer significant changes, efforts are focused on securing the best weight maturity or lowest weights uncertainty. Components are being manufactured, tested, qualified and integrated. A significant portion of the aircraft components are outsourced either to suppliers or partners and, when this is the case, the weight engineer relies on reported weight data. Thus, good reports and communication are essential at this stage. As data gets reported, it is fed into all simulations and eventually testing the aircraft - mass model uncertainty. These simulations are computer based and thus, subject to modelling uncertainty. The results of testing are used to validate and, if needed, to calibrate models. To simulate an aircraft, many mathematical models, simplifications, approximations and assumptions are made. Finally, there is operations uncertainty, accounting for how airlines operate the aircraft. Airlines set their own operational margins due to their variabilities in operations. Manufacturers set certification limits which cannot be exceeded, by considering loadability and stability studies, depending on the payload's mass, c.g., mission, etc.

While the sources of uncertainty in the different stages of the aircraft development plan have been widely identified, these are not physically modelled, quantified, propagated and accounted for in the decision making process in a systematic and streamlined way.

1.3.2 Uncertainty in the weight convergence corridor

In the early phases, the status weight is likely to have some distance from the target weight and potentially the outlook weight only demonstrates partial convergence. Programme decisions may be taken to set the target below the current view of status weight, with the assumption that efficient weight solutions will be developed and weight optimisation technologies will be matured soon enough to be embodied into the aircraft. Additionally, relying on historical statistics to estimate a preliminary status weight is potentially over conservative, given the advancements in aircraft performance, particularly the proportion of payload versus fuel burn. Thus, the expectation is that, with a weight management process in place, the status weight will converge to outlook weight as changes are progressively embodied and that outlook and hence status weight will reach the target.

In [76], [77] and [78], the need to incorporate physics-based models to conceptual and preliminary design of unconventional and larger aircraft configurations is evaluated. For these unconventional aircraft, statistical data and empirical formulas are not sufficiently reliable, and physics is needed to account for negative aeroelastic effects, such as increased drag at cruising speed. These detailed models are only identified at a later stage and can then cause considerable changes in structural design and subsequently on the weight distribution. Generally, the reliance on models and simulations to predict the response of unconventional configurations is apparent, due to lack of engineering experience of likely behaviour.

As explained with the uncertainty pyramid, a number of factors can influence the weight convergence corridor, including a combination of uncertainty in what will happen as the aircraft develops and uncertainty in the accuracy of information on both inputs to and outputs from the weights process, :

- Accuracy of estimation methods and means of application;
- Maturity of the aircraft definition;
- Technology choices and maturities;
- Aircraft performance targets;
- Accuracy of 3D modelling and manufacture;
- Accuracy of weighing equipment.

Both the status and outlook weights carry uncertainty and are, therefore, represented by uncertainty bounds, i.e. are assumed to vary around a nominal value to account for error dispersion, as represented in Fig.1.22.

Throughout the convergence corridor and the phases of design, at each milestone assessment, requirements have to be met for the aircraft project development to be considered mature enough to progress to the next milestone. Weight maturity is a proxy for the uncertainty band around the nominal weight value. A maturity assessment, including the uncertainty band and the distance between the nominal weight (status and/or outlook) to the target weight, is available at industrial

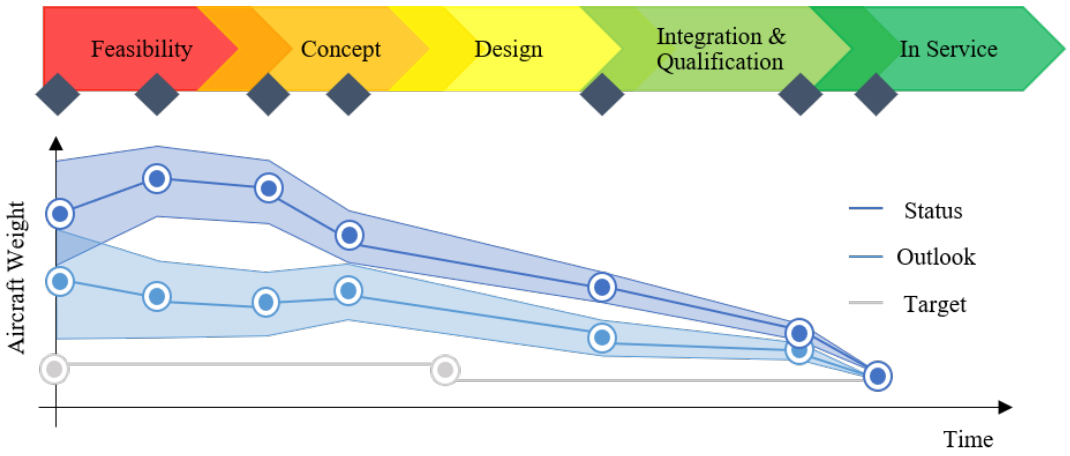

FIGURE 1.22. Representative evolution of the status, outlook and target weights in the weight convergence corridor, and respective (status and outlook) uncertainty bounds. As time (x-axis) progresses, and with a weight management process in place, the expectation is that both the status and the outlook weights' uncertainty will decrease. Target weight is a nominal target that might suffer revaluations during the design process but it is not assessed in terms of its uncertainty.

milestones.

A conceptual way to represent the different weights and their uncertainty bounds throughout the aircraft design process has been defined as the weight convergence corridor. Whilst conceptually proposed, the weight convergence corridor is yet to be defined physically as a framework or a tool.

1.3.3 Aircraft design, wing structural sizing and weight

Three methods of probabilistic uncertainty propagation and quantification were introduced to the field of aircraft analysis in conceptual design [79]. The method of moments, Monte Carlo simulation, and a non gradient simulation search method are applied to an aircraft analysis and conceptual design program to demonstrate design under uncertainty. For this effect, a mission analysis implementation known as the Flight Optimization System (FLOPS) was successfully augmented with approximations to the first-order and second-moment probabilistic uncertainty propagation. Two design variables: the aircraft's Thrust T and the wing's surface area S_w, were assumed uncertain in two separate cases: a subsonic and a supersonic transport design. The variables were assumed independent and normally distributed around a mean value. For the subsonic case, input uncertainties of 5% and 10% of the mean value were considered, as well as increasing amounts of required constraint satisfaction. The weight increase was proportional to both increasing amounts of uncertainty and to increasing amounts of constraint satisfaction specified for the optimisation. For the subsonic transport design problem, the output PDF

distributions are non normal in shape, indicating a nonlinear response from the code for which the method of moments is known to be inaccurate.

The method of moments is used to compute the design space with probabilistic, uncertain, normally distributed, independent, T and S_w, constrained by an upper limit approach speed (constraint 5) and a lower limit on missed approach climb gradient (constraint 2), on Fig.1.23. Three robust optimisation points are shown for reliability indices of $\beta = 1\sigma$, $\beta = 2\sigma$ and $\beta = 3\sigma$. It is concluded that weight increases proportionally to both increases of uncertainty (5% and 10% considered) and confidence level.

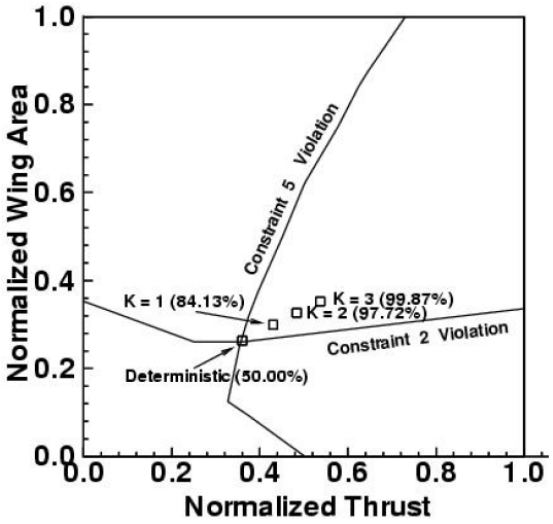

FIGURE 1.23. Design points and active constraint boundaries for deterministic and robust optimisation, $2\sigma = 5\%$.

The simulation research method (SSM) is used to determine the weight distribution for this aircraft. SSM allows for the identification of the most probable point (mpp) and the calculation of reliability and sensitivity data for non differential discontinuous problems. The weight output PDF showed a non normal in shape distribution, shown in Fig.1.24, suggesting the results obtained with the method of moments might be inaccurate.

The same analysis as the method of moments, was performed with a 5000 sample MCS for a supersonic transport aircraft. MC was the chosen method in this case because the output shown PDFs that are non normal in shape, indicating nonlinearity in the model's response, for which the method of moments is inaccurate.

Large failure rates are retrieved from discontinuities in the model and no conclusions are drawn from the sensitivity results, except that 3 distinct regions in the design space are identified: both negative sensitivity indices SI, positive for T (Thrust) and negative for S_w and negative for both. Multidisciplinary analysis based on an integrated model for aircraft wing design, with subsequent single and multi-objective wing design is demonstrated in [80]. A similar

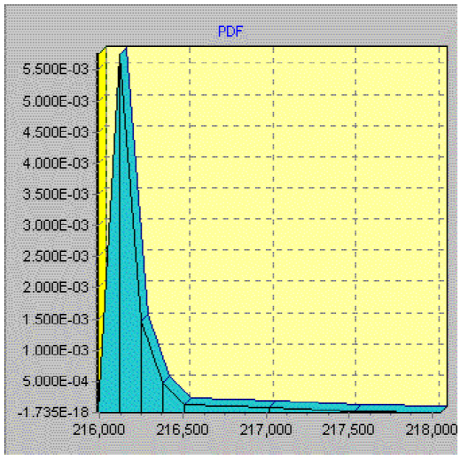

FIGURE 1.24. Aircraft gross weight distribution for the two variable (T and S_w) deterministic design case with $2\sigma = 5\%$.

multidisciplinary analysis was deployed in a multi-objective Pareto front optimisation, with the goal of studying aircraft range and fuel efficiency in [81], ultimately aiding aircraft design. In [82], aircraft preliminary design is analysed using multi-objective optimisation, in a multi-physics simulation, aiming to search very large regions of the design space.

Studies the effect of (1) the use of safety factors (2) conservative material properties and (3) final component certification tests (executed to reduce stress and material uncertainties for given critical loads due to inaccurate structural models); on the probability of failure (P_f) of a structural component are performed in [83]. The methodology is tested in an unstiffened panel design under uniaxial loads for yield strength. Analytical calculations and MCS were applied to study both the variability in geometry, loads and material properties of the panel, as well as uncertainties in the methodologies themselves, by treating each one as a random variable. This work sheds a light on the impact of 3 different safety measures, individually as well as combined, in the probability of structural failure. It was found that in some situations, larger uncertainty variability in the analytical models reduces the P_f if, and only if, certification tests are conducted.

Probabilistic structural design is proposed in [84], using the probability of structural failure for design optimisation. By Federal Aviation Administration FAA regulations, providing statistical characteristics of the failure stresses is a requirement. Therefore, the inverse problem is proposed where a probability distribution of the failure stresses is an input to the structural design optimisation. When optimising the design for minimum weight and a safety level of 1.5 (unchanged), it was found that, by redistributing components' weights, and consequently redistributing the safety factor, a reduction in weight is possible. On the other hand, when optimising for minimum probability of failure and keeping the overall weight unchanged, but still redistributing the structural component weight, the P_f can also be reduced.

The impact of disciplinary uncertainty in aerodynamics, propulsion and weights' metrics on

aircraft conceptual design is examined in [85]. Pareto frontiers are used to explore the trade space in a bi-objective optimisation: reliability and robustness. On the one hand, balanced multi-performance metrics are sought after, and, on the other, robust to system-level-losses designs are preferred.

A framework was developed in [86] that implements reliability based design optimisation methods, namely reliability index approach and performance measure approach, to compensate for the discrepancies associated with the low fidelity analysis commonly employed in conceptual design. It yields that the optimised designs are less likely to fail to meet any performance requirement when re-evaluated at a later stage with higher fidelity methods. A clear trade-off between robustness and reliability in design is observed. This method models uncertainties from a historical database of different commercial aircraft parameters, using uniform and normal probability distributions.

An exhaustive uncertainty quantification analysis of the structural sizing of a simplified half wing model is presented in [87]. The wing model produced in ANSYS is a half wing-box, shell only structure, clamped at the root as illustrated in Fig.1.25. The uncertain input variables considered are the wing span, root chord and thickness of the shell, web and flanges. Both the PDF and CDF

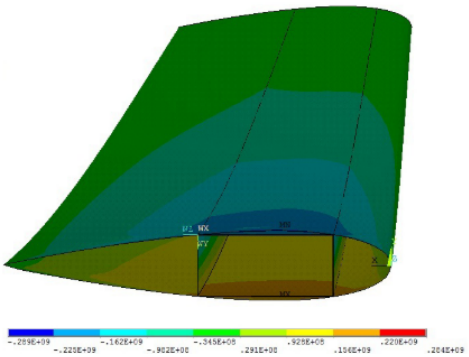

FIGURE 1.25. Stress distribution deterministic output results on a half wing-box shell only simplified model [87].

of the maximum displacement at the tip and maximum and minimum stress are analysed. Three different methods are used and compared: MCS, LHS and the Perturbation Method PM. They all generate similar results but MC's computational cost is of 598×1, when compared to PM, whereas LHS's is 58×1.

A method for determining the wing weight of an aircraft featuring the accuracy of a physics-based model and the ease-to-use and speed of a handbook equation is computed in [88]. It combines a beam model, a vortex lattice model and empiric equations into a centralised approach, i.e. the three methods derive their input data from the same geometric definition by introducing a correction function for a variable with physical dimensions. The sensitivities of different methods are compared in this study.

A probabilistic method for reliable and robust optimisation of an aircraft design at conceptual design stage is developed in [89]. Similarly to [86], uncertainties in both model and design are considered and these are modelled by an adaptive normal law strategy, in order to fit a historical database and adjusted depending on the available information at the current point of the optimisation process. This allows for taking into account that uncertainty increases when statistical data is scarce but decreases with the amount of information available.

A new wing-box structural sizing and load estimation methods have been developed by analytical derivation of the airfoil effective distance parameter. They allow for quantifying the effect of many detailed design choices, such as airfoil shape and spars position on the wing weight. The framework is described in [90] and its application is demonstrated in [91].

Corman proposes a method [92] to more efficiently identify the critical load cases for a reference aircraft wing and reduce the computational expense of propagating uncertainties for each case. This is achieved through adaptive sampling of the loading conditions' space with the use of a Kriging-based sequential routine. When compared to the benchmark exhaustive approach, the success rate sr of identifying the critical loading condition is of sr = 81% and 79% for reliability indices of $\beta = 50\%$ and 75% respectively. However, this method falls short at larger reliability indices, e.g. for $\beta = 95\%$, sr = 47%.

Uncertainty is considered for conceptual design of derivative aircraft from an existing one in [93]. The proposed derivative example used the altitude range of operation as the uncertain variable, in order to consider the change from a small piston engine to a turbocharged engine for high altitude. Fuzzy logic in the form of possibility-based design optimisation PBDO is considered to perform the analysis. PBDO addresses uncertainty in design variables and parameters when the data available is insufficient to calculate a PDF. Fuzzy operations are simpler than probability based methods and fuzzy variables are easier to define. Two cases were analysed: one where all the design variables are considered and the second were three main variables are fixed, to reduce the development and manufacturing costs of a derivative aircraft. Both optimised designs show better stability characteristics and performance (rate of climb). The performance analysis results show little error when compared to real flight data from the target aircraft and suggest a generalised applicability of the method to other types of engineering with the benefit of time and effort savings.

Uncertainty in the aircraft design, wing structural sizing and weight has been widely explored in academia, especially in conceptual design. Several different methods for probabilistic uncertainty quantification are explored and reliable and robust optimised design solutions are sought. However, the methodologies do not take into account sources of uncertainty such as human error or regulatory changes, nor do they account for the passing of time and the evolution of uncertainty when design decisions start becoming permanent. They do not consider the translation of these results into a framework that can overlook the whole process and be the basis for managerial decisions, including the representation of uncertainty through physical modelling.

1.3.4 Aircraft Life-Cycle Cost (LCC) and environmental impact

Aircraft operational, life-cycle cost (LCC) and managerial issues have also been tackled with uncertainty assessment. A methodology is developed in [94] for commercial aircraft conceptual design that, not only identifies the concept's viability, but also minimises its LCC, i.e. weighing operation and maintenance costs against manufacturing costs. The probabilistic robust design and uncertainty modelling of a supersonic transport aircraft, including LCC analysis is explored in [95]. A Multidisciplinary design optimisation of a large civil aircraft wing, for minimum manufacturing costs as primary objective is described in [96]. In [97], expert judgement is combined via Dempster-Shafer theory to estimate maintenance time during wartime operations. A review of uncertainty modelling in LCC in broad engineering applications, including the aerospace sector, is presented in [98]. The environmental impact of an aircraft, particularly its emissions [99] and noise nuisance [100] are estimated with the use of uncertainty quantification methods. A global inventory of emissions is produced and the departure procedure's optimisation for maximum air quality is generated.

Whilst outside the scope of the physical modelling of the aircraft, the aircraft life-cycle cost and the environmental impacts of commercial aircraft have been explored in isolation. Having them considered in a more holistic approach of aircraft design is missing from literature.

1.3.5 Aerodynamics and aeroelasticity

Many successful applications for both robust and reliable optimisation techniques are described below, for aircraft structural design related topics, including aerodynamics and aeroelasticity analysis.

Following [101] where the probabilistic response of a nonlinear panel in supersonic flow is examined and [102] where the integration of aeroservoelastic uncertain systems, structural variations (including structural mass) and control synthesis methods are unified for mapping flutter boundaries in a three-dimensional uncertainty space, the subject of uncertainty quantification in aeroelastic stability, including problems like flutter speed, Limit Cycle Oscillation LCOs and robust or reliable design optimisation, is described and reviewed in [103]. The impact of geometric uncertainties on the aerodynamic loads of a vertical stabiliser under dynamic manoeuvres [104] and airfoil aerodynamic characteristics [105] is explored. A PCE was built as a surrogate model for uncertainty quantification and Sobol analysis was used for sensitivity. Uncertainty quantification in high-fidelity CFD simulations, employing PC methods is introduced in [106, 107]. A response surface method is later used to surrogate a CFD model to evaluate the impact of flight velocities on a flapping wing [108]. In [109], a NIPC based stochastic expansion approach is applied to robust aerodynamic optimisation under mixed (aleatory (Mach number) and epistemic (turbulence model)) uncertainties. In [110], a metallic wing's aeroelastic stability (critical flutter speed) with uncertain structural mass is analysed with PCE and Fuzzy Analysis. Time-varying, correlated gust loads of a civil jet airliner are plotted against each other in a

convex hull in [111], in an effort to determine the aeroelastic critical conditions. In [112, 113], PCE and fuzzy logic are used to predict at what dynamic pressure flutter occurs, by varying fuel load and consequently structural weight. The concern that novel aircraft configurations push nonlinear behaviour beyond levels at which current tools operate induces the need to explore aeroelastic stability in different ways, namely the use of UQ to measure the impact of parametric uncertainties in airfoil LCO [114].

Interesting developments in the uncertainty analysis of composite wings: [115] applies MCS and PCE on a flutter model, for variations on the material properties, fiber-direction angle and ply thickness of a composite wing configuration and proceeds to determine the optimal robust design for minimum probability of failure due to flutter. The same two methods were employed and contrasted in [116] for the prediction of the uncertainty bounds of frequency response functions, extracted from a composite wing aircraft FEM with uncertain material properties. Similarly, in [117] PCE is used to study the impact of uncertain material properties and severity of damage on the aeroelastic stability and dynamic response of a FEM composite wing model, particularly critical flutter speeds. Scarth models the impact of uncertainty in the ply orientation angles of composite laminate wings on its aeroeloastic stability. A PCE surrogate model is used in [118] and in [119, 120] a Gaussian process surrogate model is used and the research is focused on 1) reliability based design for minimum probability of failure and 2) a robust design for a trade-off between the mean and standard deviation of the instability speed.

Similar to the aircraft structural sizing and life-cycle analysis, UQ in aerodynamics and aeroelastic studies is primarily applied in optimisation studies and for specific problems. They are not considered in conjunction with all the other disciplines in aircraft design.

1.4 Aims and Objectives

Robust and reliability-based design optimisation have been widely applied to: aircraft design, particularly wing structural sizing; aircraft operations, maintenance and manufacturing costs; aircraft emissions and noise nuisance; or aerodynamic and aeroelasticity problems. While these topics have been considered individually, they have not been considered combined. Considering uncertainty in the structural design with other aspects of the weight management process, such as human factors, costs, technological advancements, or environmental restrictions, would allow for a complete understanding of the process. The analysis in this thesis centres around weight because it is the figure of merit of the design process. The aim is not to deliver an optimised solution for aircraft weight or performance. Rather, it is to build understanding on what are the weight uncertainty drivers, what is the impact of design variables and decisions on weight and how can the overall process of aircraft design be improved and modelled with this information.

With this in mind, the aim of this thesis is to demonstrate how uncertainty quantification can be incorporated into the weight management process. Three main objectives are identified:

1. **Analyse historical weight management data.**
   The industrial weight management and uncertainty assessment processes are reviewed and validated, and areas for improvement and sensitivities are identified. Historical weight data is then used to understand variations in weight throughout the design process, sources of uncertainty, identify trends and analyse the predictability of weight information.
2. **Model the weight estimation process for uncertainty quantification.**
   In order to understand uncertainty and its impacts on the weight estimation process as well as the accuracy of the weight figures, a baseline weight estimation model is developed that provides the large database for UQ. Through aircraft configuration studies and design exploration, the sources and multi-disciplinary drivers and dependencies of uncertainty can be understood.
3. **Establish a physical basis for a proposed weight convergence corridor.**
   The weight convergence corridor is a framework that allows for the weight and its uncertainty to be tracked throughout the aircraft design process. It allows for uncertainty to be quantified at any stage in the design, robust and risky areas of design to be flagged and estimations to converged to a proposed target result.

1.5 Layout

In chapter 2, the industrial scenario is introduced. First, the available capabilities for uncertainty and risk assessment in the aircraft design process are described, tested and validated with different software, and areas for improvement are identified. With the latter in mind, some methodologies are explored with the aim to introduce them to the industrial context, such as probabilistic margin setting and dependence modelling.

Exploratory data analysis is introduced in chapter 3. The global challenge of digital transformation, aiming to integrate digital technology and data flow across all areas of business, in order to enhance processes and products, is layed out for the topic of aircraft design. For an industry involving many partners, standardising all input information can be a challenge and EDA applied to weight reporting is investigated. Moreover, the application of data visualisation methods and machine learning techniques such as clustering, into aircraft historical data is shown.

The need for a tool that allowed to produced the necessary data to wrap uncertainty quantification and sensitivity analysis methods around, culminates in chapter 4. A physics-based framework that emulates the weight convergence corridor for an aircraft wing is developed and is here described. It combines a traditional wing-box sizing method for primary weight with alternative methods for secondary weight.

The results of forward propagation of uncertainty through the framework developed, are presented in chapter 5. These are divided in primary structure (wing-box geometries) and

secondary structure uncertainties. For the primary structure, the wing-box sizing routine is analysed: propagation of uncertainty from aerodynamic loads, to stress and sizing (and weight). uncertainty in the stress allowable (material properties) of the wing-box and stress constraints are considered. Lastly, adding uncertainty to an external weight, in this case the engine, is demonstrated. For the secondary structure, the impact of the variability in the input parameters to the final component and wing weights are studied. The effects of an uncertain secondary structure weight, on the primary structure of the wing is also examined.

Reliability-based analysis are pictured in chapter 6, using the secondary weight uncertainty as a test case. First, a reliability level β is set for the wing weight and the P_f set values are evaluated. Then, a new wing target weight is sought. Using neural networks to propagate uncertainty backwards through the sizing model, the input distributions that allow for reaching the wing weight target are obtained. Finally, the weight convergence corridor is depicted. Using the same target weight and the results obtained for the inputs, the evolution of the design features and resultant weights through the aircraft design process are assessed, against and with the goal of converging to the proposed target.

Conclusions drawn from this work, its scientific novelty and framing in the current state-of-the-art context are presented in chapter 7. Final observations and remarks on the topic of uncertainty assessment on aircraft weight engineering, as well as future work suggestions are also listed.

1.6 Publications

There are three publications arising from this work, listed below:

- *"Uncertainty Modelling in a Wing Weight Convergence Simulation Framework"*
  Presented at the 77th Society of Allied Weight Engineers (SAWE) International Conference on Mass Properties Engineering, held in Irving, Texas, USA, in May 2018.
- *"Development of a WingWeight Convergence Simulation including Uncertainty Modelling and Sensitivity Analysis"*
  Presented at the American Institute of Aeronautics and Astronautics (AIAA) Science and Technology Forum and Exposition (SciTech) held in Kissimmee, Florida, USA, in January 2018.
  Awarded best student paper presentation.
- *"Uncertainty propagation in aircraft weight management process"*
  by Teresa Reis and J.E.Cooper.
  Under preparation.

The following publication has received contribution from the author, related to work presented in this thesis:

- *"A Deceptively Simple Method for Uncertainty Quantification and Management at AIRBUS"* by Dorota Kurowicka, Judi Cheeseman, Teresa Reis, Sanjiv Sharma, Roger Cooke, Sankaran Mahadevan, Tom Zang, Jimmy Tai and Dimitri Mavris.
  Under review.

CHAPTER 2

INDUSTRIAL SCENARIO

This project was initially proposed and developed in partnership with industry. For this reason, time is spent understanding and studying the industrial processes and means, as well as areas for improvement. The present chapter aims at presenting the reader with the findings of this learning, including the exploration of different techniques and software in well established pieces of a streamlined process. It has helped direct the course of this PhD and establish its core research questions.

2.1 Review of the current weight estimation and management process

Industrially or in practice, the weight estimation and uncertainty assessment process can be described simplistically as a step-by-step operation represented in Fig.2.1.

The components' and overall aircraft weights are evaluated in a weights' convergence corridor against a target weight and target requirement margins for uncertainty. The corridor allows for tracking the weights' evolution in time. For more information on the weights' corridor, the types of weight and weight estimation methods, refer back to sec.1.1.5.

Throughout the design cycle and the different phases of design, some key information regarding the aircraft's constituent parts that is relevant to the weights' process, is kept on a mass properties database. This includes information about the part itself, its weight, position in the aircraft, material, etc. Furthermore, the database records the component's history, that is, all the entries registered or changes it has gone through. More details are described in sec.2.1.1.

At each milestone assessment, specific requirements have to be met for the design to be considered mature enough and the development process to continue. Using the mass properties

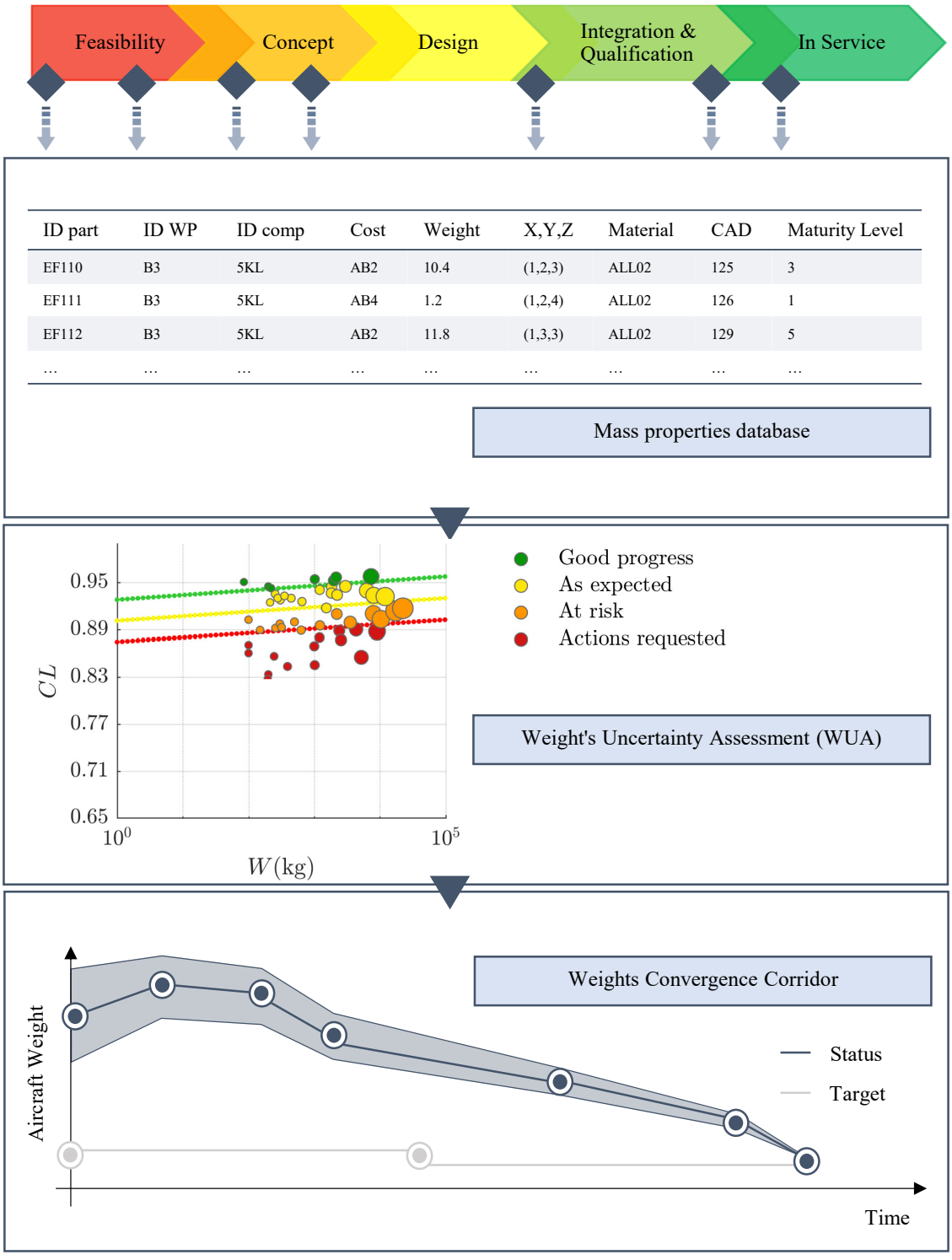

FIGURE 2.1. Representative flow diagram of a typical industrial uncertainty assessment approach for weight estimation in the aircraft design process.

database, components weights are estimated in a variety of ways [2], and their uncertainty is assessed in an internally developed methodology and tool WUA, described in sec.2.1.2.

2.1.1 Mass properties database

The mass properties database encloses all the weight information for a specific aircraft programme, including

- Identification codes;
  - Individual part code;
  - Work-Package (WP) code;
  - Component code;
  - Cost code for costing analysis.
- Weight in kg;
- Maturity level;
- (X,Y,Z) position in the aircraft;
- Material data;
- CAD model drawing number;
- Modifications' history;
- Responsible team/vendor.

Each entry refers to a specific aircraft part, and it can go as low level as nuts and fasteners. Associated with each part, the identification codes allow the weight engineer to arrange the data into different groups, such as higher level components and WPs, and enable different views on the data to be generated for different interests. As an example, consider the wingtip to be a WP, its covers to be a component and the panels, fasteners and brackets the lower level parts. The part's data is updated when and/or if there is progression or regression in its development, a change in design or a new vendor weight statement reported.

It can also refer to smaller additions or modifications to an existing aircraft that do not change its standard and can be seen as an evolution from the previous one, as a consequence of a constantly developing industry. Whichever the case, identification codes are again used to categorise derivations in aircraft. This allows to isolate and treat each aircraft separately, but also, if a modification occurs in a part involving several different aircraft, one entry will reflect that effect in all the derivatives.

2.1.2 Weight Uncertainty Assessment (WUA) method

This section describes the methodology and associated tool that allows the weight engineer to deliver an objective assessment about the weights' uncertainty.

The goal with an uncertainty assessment, is to make a judgement on the robustness of the weight, considering the information available about it, see sec.2.1.2.1. Specifically, a confidence

level CL is to be estimated and the weight defined probabilistically as a normal distribution with parameters:

$$\mu = W \qquad \sigma = \frac{W \times (1 - \mathrm{CL})}{2} \tag{2.1}$$

W being its nominal value. A dispersion of 2σ around its nominal value $\mu = W$ is assumed, meaning that 95.44% of the weight observations will be within $\mu \pm 2\sigma$. This is a typical assumption for error dispersion.

Normal distributions are elected for their many valuable qualities in analytic calculations. For example, any linear combination of a fixed set of normal deviations is a normal deviation. Propagation of uncertainty, least squares fitting, and standard regression coefficients can be derived analytically when the relevant inputs are normally distributed. Given the nature of the input/outputs being analysed in this work, i.e. weight, the normal distributions are truncated at 0 (zero), such that weight cannot take a negative value. The input distributions are truncated, i.e. restricted to positive values, and the density function is re-normalised so that the integral over that range is 1, i.e. the area under the PDF is 1.

After all the weights have been defined as normal distributions, a Monte Carlo simulation using 5000 sample points is run to integrate all the lower level parts and obtain a global expected figure at WP or aircraft level.

The weights in WUA can be assessed at different levels of granularity - part, component, WP level or even the full aircraft weight's uncertainty can be assessed as one. When retrieving the weights from the database for assessment, these can be grouped together in different ways by using the ID codes to cluster the data. After clustering for the intended aircraft and level, the weights are summed and fed to WUA.

2.1.2.1 Calculating the Confidence Level (CL)

The CL calculation is a 2-step process: The first step is to assess the weight in terms of its maturity, resulting in an initial CL_m; The second step is an evaluation of various other parameters that act as degrading factors, f_d, to the initial CL_m.

Maturity of the weight is related to the weight estimation method used, as well as its nominal value W. WEMs are broadly categorised as scaling, statistical or physics based [2] (see sec.1.1.2), but can be further broken down in order to fit the industrial context and different levels of software complexity, for instance, the weight can be

- estimated by expert elicitation;
- supplied from reported/vendor data;
- scaled from a different aircraft programme;
- obtained statistically or with an empirical equation;
- analytically calculated, from various different software;

– supported by CAD data;
– weighed on a scale.

Once a maturity level is established for each component, a correspondent reliability level β, dependent not only on the maturity but also on the nominal weight value, needs also to be established, see Fig.2.2.

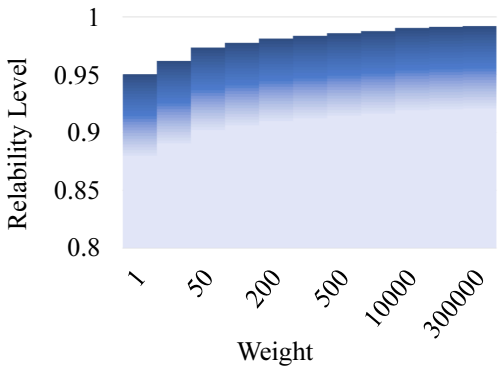

FIGURE 2.2. Weight (in kg) group VS. reliability level.

Consider a continuum of weight values being discretised into weight groups corresponding to a certain amount of kilograms (x-axis in Fig.2.2), e.g. group A is a weight between 1 and 10kg and group B between 10 and 50kg. Tracing a vertical line from the x value correspondent to the components' weight group, the reliability band is also a discretisation of its n levels of maturity. The shadow illustrates the maturity level - the darker the more mature. The correspondent β (y-axis in Fig.2.2) is retrieved once the estimated maturity level is reached within the band.

Qualitatively, if two components weigh the same but are calculated with different methods, the more mature the method, the higher the reliability level. Similarly, if the components are calculated using the same method but one is heavier than the other, the latter will have a higher β. The current values used in WUA for reliability are regressed from reference tolerance values approved internally, estimated from past evidence and expert judgement. The reason why heavier weight groups are more reliable than lighter weight groups is because it is assumed that when a heavy weight is assessed, it means that it is composed of several different parts, some of which are significantly heavier than others. Heavier parts are percentually less uncertain than lighter parts and heavier parts suppress the lighter ones.

CL_m can then be calculated using

$$\mathrm{CL}_m = \frac{\sum_{i=1}^{n} W_i \times \beta_i}{W_{TOTAL}} \tag{2.2}$$

where i corresponds to the different parts or components in analysis at different levels of maturity, n being its maximum level, and β the reliability level.

The second step to calculating the final CL looks at various other information such as robustness, complexity and documentation surrounding the weight data that describes the design solution. This information does not concern so much the weight but more so the maturity of the design and its likelihood to change over time. Weight is more than a representation of this change, it is also a consequence of it.

Robustness evaluates the source of the weight calculation (vendor, risk-sharing partner or internal), the quality of the inputs and weight reports and whether or not these have been validated by a mass properties engineer. Additionally, robustness classifies the quality of the loads and loadability information, if applicable. **Complexity** analyses the technology of the component in terms of its certification and levels of development and usage. It also looks at how many interfaces, meaning how many other parts and components this is touching. This is because changes or variations on components with more interfacing parts will have greater proliferating effects, and, generally, there is an added element of risk and uncertainty. Probabilistically, this can be dealt with using copulas in the input variables' definition in order to represent dependencies between them. Lastly, complexity also evaluates the information on the drawings and materials. **Documentation** reviews all the documentation's availability and completeness for a particular component, concerning its definition, requirements and design manuals and principles.

All these factors are broken down into different levels of maturity and rates $0 \leq f_d \leq 1$, obtained from expert elicitation, are attributed to each one, resulting in f_{d_r} for robustness, f_{d_c} for complexity and f_{d_d} for documentation. For example, f_{d_r} will be attributed a ratio from 0 to 1 depending on how available and complete the information to perform a weight calculation is. The final confidence level CL is obtained with

$$\mathrm{CL} = (\mathrm{CL}_m \times f_{d_r}) \times f_{d_c} \times f_{d_d} \tag{2.3}$$

With CL and employing the equations in Eqs.2.1, μ and σ are calculated and the weight's normal distribution is defined.

Example 1. Consider the example of a component weighing 153kg, 10kg of which are at level 2 of maturity, 120kg at level 4 and 23kg at level 5, assuming $n = 6$. Values for β_i are extracted from Fig.2.2, assume $\beta_2 = 0.92$, $\beta_4 = 0.96$, $\beta_5 = 0.95$.

TABLE 2.1. Example of a component weight, totalling 153kg, being discretised into maturity levels ML $i = 1,2,...,6$: $W_{\mathrm{ML2}} = 10kg$, $W_{\mathrm{ML4}} = 120kg$ and $W_{\mathrm{ML5}} = 23kg$; and the correspondent reliability levels β_i, obtained from Fig.2.2, taking into account ML and W_i.

ML	1	2	3	4	5	6
W_i	0	10	0	120	23	0
β_i	0	0.92	0	0.96	0.95	0

CL_m is calculated with $\mathrm{CL}_m = (10 \times 0.92 + 120 \times 0.96 + 23 \times 0.95)/153 = 0.9559$. For simplicity,

assume $f_{d_r} = f_{d_c} = f_{d_d} = 97.50\%$, and $CL = 0.9559 \times 0.9750^3 = 88.60\%$ holds. Finally, $\mu = 153$kg, $\sigma = 153 \times (1 - 0.8860)/2 = 8.72$kg for this component.

2.1.2.2 Monte Carlo analysis

Once all the weights are defined as normal distributions with parameters μ and σ, a Monte Carlo analysis is performed in each one and 5000 random numbers are generated for each weight. Summing the weights, 5000 sample points of the overall weight is achieved, allowing to define it, likewise, as a normal distribution. The Cumulative Distribution Function (CDF) of the overall weight is plotted and three points are distinguished: the best view at 5% probability, the most likely at 50% and the worst case weight at 95%. An example follows.

Example 1. (continued) Consider now that the component in the previous example is being assessed with 4 other. Their weights and CLs are as follows.

TABLE 2.2. Previous component detailed in Tab.2.1, A, is assessed with four other: B, C, D and E. Their confidence levels CL(%) have all been obtained and are also listed below.

	W(kg)	CL(%)
A	153	88.60
B	30	92.40
C	400	96.90
D	1550	91.80
E	9000	97.00

The first data visualisation aid is shown in Fig.2.3 where W is plotted against CL. Every circle represents a different component and the bigger the circle, the heavier the component. The colours represent their status: for lower CL, red and orange represent actions needed and components at risk; for higher CL yellow and green represent as expected and good progresses. The plot aims at facilitating the visualisation of the overall higher-level-product status and of the components that are at risk and need to be closely monitored or redesigned, helping to communicate uncertainty in a more practical form.

The three green, yellow and red dotted lines that delimit the status of a component, are determined by the phase of design of the aircraft or WP in analysis. In Fig.2.3(a), the aircraft is still at a preliminary stage in design, whereas in Fig.2.3(b) the aircraft is further into the design progress. The confidence bands get narrower as the design cycle progresses.

With MC analysis, the overall weight of the component based assessment in Fig.2.3(b), is obtained: $\mu = 11131.91$kg and $\sigma = 147.60$. Its CDF is shown in Fig.2.4 and the best case, most likely and worst case weights are distinguished. The most likely scenario ($P = 50\%$), correspondent to the median ($\tilde{x} = 11130.63$kg) of the distribution, is 11131.11kg. The best case scenario ($P = 5\%$) is

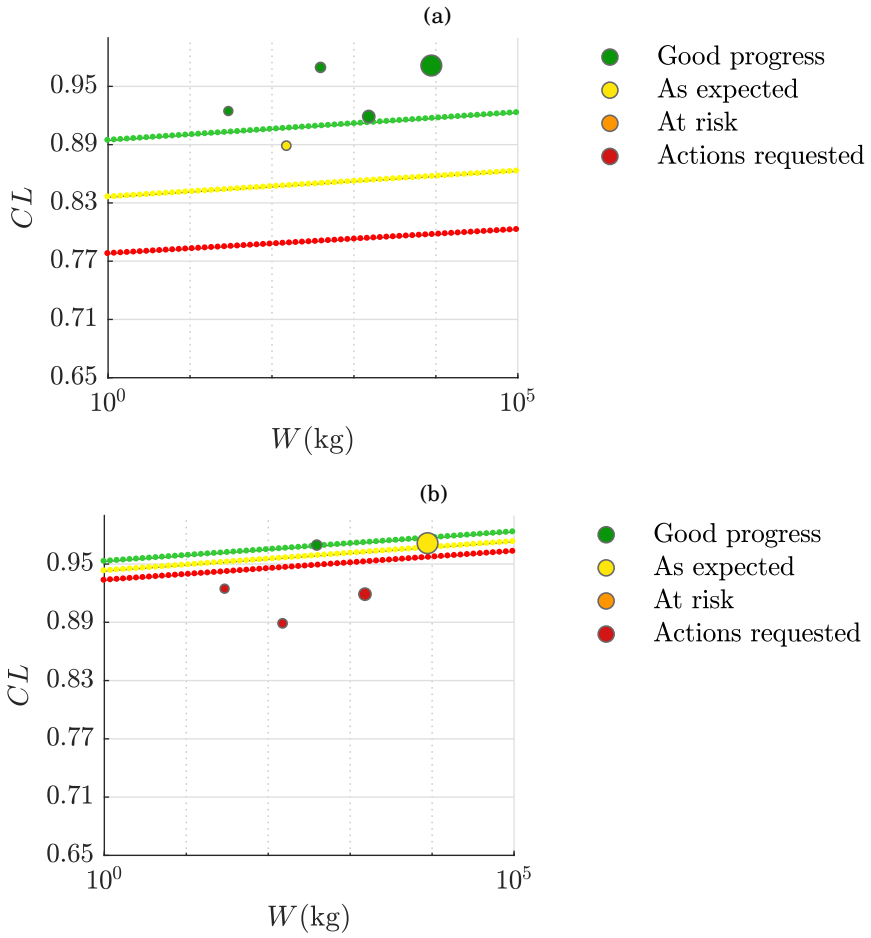

FIGURE 2.3. WUA's uncertainty assessment: component weight VS. confidence level, applied to the 5 work-packages example in Tab.2.2. (a) At a preliminary stage in the design process; (b) At a later stage in the design process.

10896.89kg, 234.20kg lighter than the mean, and the worst case scenario ($P = 95\%$) is 11371.23kg, 240.10kg heavier than the mean.

2.2 Testing and validating the Weight Uncertainty Assessment (WUA) method

In this section, replicas of the WUA tool in MATLAB, integrating UQLab and in UNINET are presented. These replicas were built for the purpose of understanding the two frameworks used: UQLab and UNINET, and explore what methodologies they could offer, as well as understanding WUA itself. They were also used to validate WUA results and served as a base for academic publishing.

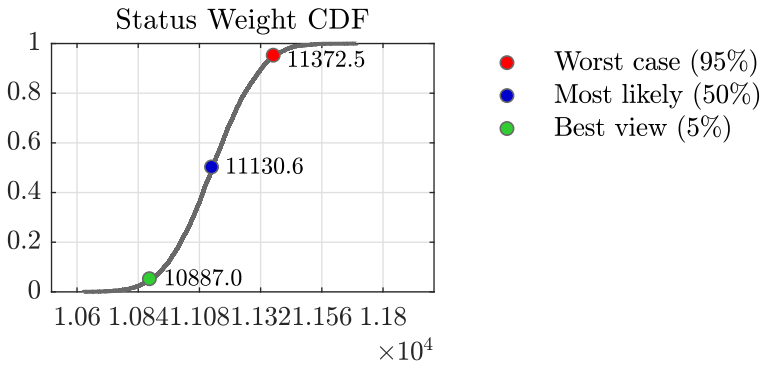

FIGURE 2.4. WUA's resulting total status weight CDF, at a later stage in the design process, computed from Fig.2.3(b).

2.2.1 WUA in MATLAB

A fully working framework for WUA in MATLAB is produced in order to replace the working tool. MATLAB is a standard platform optimised for solving engineering and scientific problems. It is the world's most used language for computational mathematics. Every software mentioned in this report is either MATLAB-based or has MATLAB wrappers. Producing a MATLAB version of this tool allows for it to be integrated with other software and enhanced with new methodologies more easily. Examples of methodologies (and respective tools) to potentially integrate or run in parallel with WUA are: Uncertainty Quantification (UQLab), sensitivity analysis (SAFE or UQLab), reliability analysis (UQLab), conditional probability for dependence modelling (UNINET) and expert elicitation (EXCALIBUR).

For the purposes of publication, the previous plots in *Example 1*: Fig.2.3 and Fig.2.4 were obtained already using the MATLAB replica of WUA. A second test case of 50 WPs composing the whole aircraft, including wing and wingtip, leading and trailing edges, fin, tailplane, fuselage, nose gear, main gear, air conditioning, power units and systems, is plotted in Fig.2.5. The CDF of the total aircraft weight is plotted in Fig.2.6. Since this test case mimics a realistic scenario for a specific aircraft programme, in this phase in the development process, the aircraft's most likely weight is of 148343.7kg, a worst case of 151001.80kg, a best case of 145628.10kg, and an average uncertainty of $u = 2\sigma = 3$t.

2.2.2 WUA in UQLab

UQLab is a MATLAB-based uncertainty quantification (UQ) framework. It offers several built-in methods and algorithms for UQ, such as MC simulation, Latin Hypercube Sampling (LHS), Polynomial Chaos Expansion (PCE) and Sensitivity Analysis (SA). In order to facilitate the understanding of the tool, as well as testing and validating the WUA methodology, WUA is replicated using UQLab and some results are presented below.

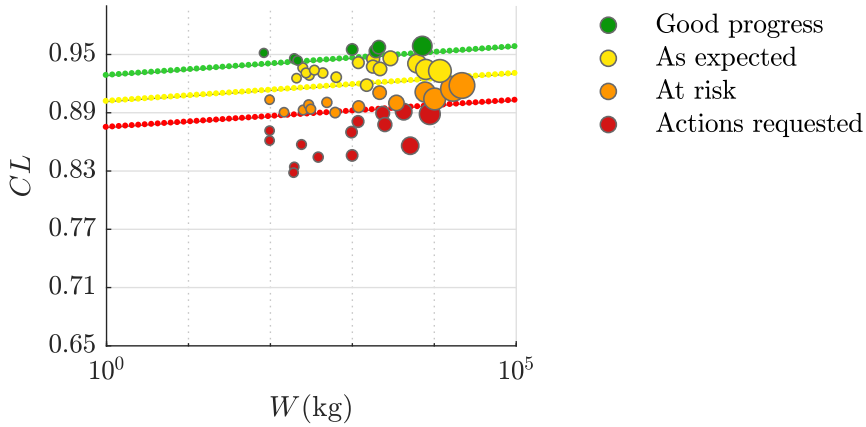

FIGURE 2.5. WUA's uncertainty assessment: component weight VS. confidence level, applied to a 50 work-packages test case representing the whole aircraft.

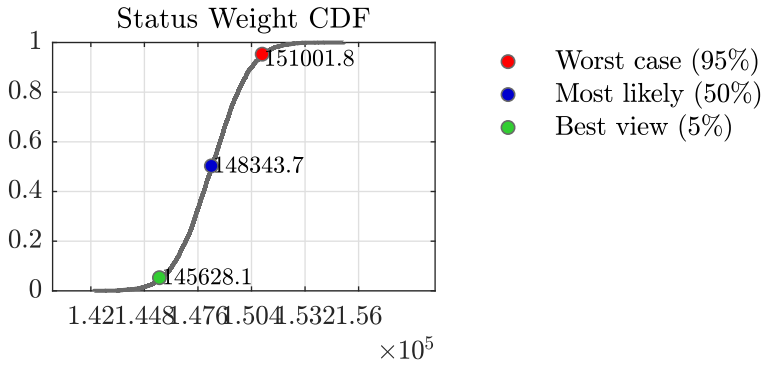

FIGURE 2.6. WUA's resulting total status weight CDF applied to the 50 work-packages test case representing the whole aircraft and computed from Fig.2.5; The weight values for the worst case (95%), most likely (50%) and "best view" (5%) scenarios are also represented.

The software is tested on the previous *Example 1*, W and CLs listed in Tab.2.2. Running a 5000 loop MC simulation with UQLab, the overall weight CDF is obtained. The absolute and relative errors, ϵ and η respectively, between the results from WUA and UQLab, are presented in Tab.2.3. This analysis allowed to validate the industrial tool.

TABLE 2.3. Comparison between WUA and UQLab worst case (95% or $q_{0.95}$), most likely (50% or $q_{0.50}$) and best view (5% or $q_{0.05}$) weights, obtained from MC simulation.

	WUA (kg)	UQLab (kg)	ϵ (kg)	η (%)
Worst case 95%	11371	11381.05	-10.05	-0.09
Most likely 50%	11131	11134.15	-3.15	-0.03
Best view 5%	10896	10886.75	9.25	0.09

2.2.3 WUA in UNINET

Similarly to what is done with UQLab in the previous section, a UNINET replica of the WUA is built. Using the same *Example 1*, W and CLs listed in Tab.2.2, the BBN in Fig.2.7(a) is built. Its CDF is represented in Fig.2.7(b).

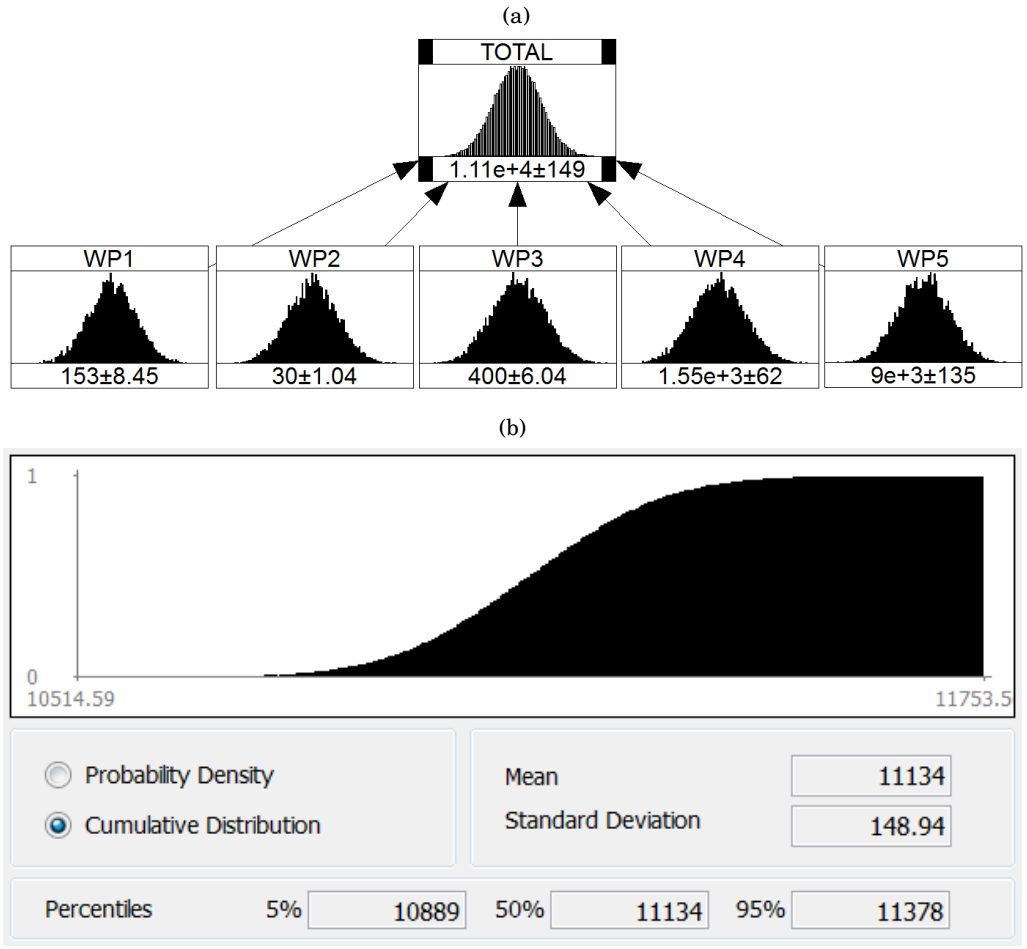

FIGURE 2.7. UNINET's uncertainty assessment using a Bayesian belief net, applied to the 5 work-packages example in Tab.2.2. (a) Bayesian belief net for WP 1 to 5 and their weight sum (total); (b) The total weight CDF, μ, σ, $q_0.05$, $q_0.50$ and $q_0.95$, equivalent to "best view" (5%), most likely (50%) and worst case (95%).

The absolute and relative errors, ϵ and η respectively, are listed in Tab.2.4. Once again, the sampling strategy is MC and the small errors can be attributed to the random nature of it and WUA is validated. A larger sampler size of 50,000 samples was evaluated and produced relative errors in the same order of magnitude as the ones in the table.

TABLE 2.4. Comparison between WUA and UNINET worst case (95% or $q_{0.95}$), most likely (50% or $q_{0.50}$) and best view (5% or $q_{0.05}$) weights, obtained from MC simulation.

	WUA (kg)	UNINET (kg)	ϵ (kg)	η (%)
Worst case 95%	11371	11378	-6.77	-0.06
Most likely 50%	11131	11132	-0.89	-0.01
Best view 5%	10896	10884	12.89	0.12

2.3 Areas for improvement in the uncertainty assessment process

In this section, some remarks, comments and suggestions are made concerning the current methodology for uncertainty quantification in the aircraft weight estimation process.

2.3.1 Solicited review

The Smith Institute for industrial mathematics and systems engineering was commissioned to provide an "independent review and enhancement of weight estimation methods for aircraft weight outlook" [121]. Scoped to the relevance for this work, comments and suggestions retrieved from the report are listed below.

1. When the aircraft has several of the same component, it is not correct to make independent assessments for each of them. This will tend to reduce the standard deviation of the distribution from what it should be. Instead, one assessment of one component should be made and then that same value used x amount of times (x being the amount of the same components) in the aircraft to produce the MC estimate of the total weight.
2. The descriptions of the 5%, 50% and 95% points in the cumulative distribution as "Best view", "Most likely" and "Worst case" could be misleading. The percentage values should always be included when describing what these values represent, e.g. "Best view (5%)", "Most likely (50%)", "Worst case (95%)".

2.3.2 Author's review

Adding to the Smith Institute's remarks, additional opinions of the author for improvements on the existing methodology for weight uncertainty estimation and assessment are considered.

1. The values shown in Fig.2.2 were obtained from scaling of reference values for tolerance requirements, past evidence and expert elicitation. Tolerance references and reliability levels are not necessarily equivalent, and a direct relation between the two could be misleading. Statistical evidence or physics based methods corroborating and/or estimating the levels of reliability should be sourced. Additionally, continuous calibration, testing and

validation should be provided, when different aircraft programmes launch and new weight assessments are produced.

2. When assessing the weight of one component, the weight can be divided into levels of maturity. However, for the rest of the assessment, the weight engineer considers the component as a whole. Assuming the component can be broken down into lower level parts, similarly to discretising the levels of maturity when assessing the initial CL_m, the method could also discretise the rating system for robustness, complexity and documentation when estimating f_{d_r}, f_{d_c} and f_{d_d}. Alternatively, the rating step could account for fractions of the total W, e.g. for the topic of validation, 50% of the weight is validated internally, 30% is validated externally and 20% is not validated.
3. The data fields assessment (robustness, complexity and documentation) have a set of possible answers, and therefore possible rates, and these may not encompass all that is behind the makings of a component. Converting the rating system to a probabilistic or other continuous assessment setting could be beneficial.
4. Still on the topic of the rating system, the specific values for the rates were conjectured by experts' opinion. There are several methods in the literature exploring the measurement and combination of experts' opinions in a more streamlined and robust manner, see sec.2.4. Incorporating these methods onto WUA could be considered.
5. The weights are defined as a normal or Gaussian probability distribution, though alternative distributions could provide a more accurate representation of the weight of a component. Monitoring the design process and weight fluctuations of different components could provide valuable insight into what type of distribution to use, if components can be clustered into different distribution types and if these prevail for different aircraft programmes. The same could be done for the robustness, complexity and documentation assessment presented in 3.
6. A dependence structure in the context of weight uncertainty analysis entails that a percentage of the uncertainty is shared or evolves in a theoretically predictable manner because of the way components are interconnected. These connections can be physical or, rather, connections can arise from components being outsourced, reported or manufactured by the same vendor, using the same material or simply by being judged by the same expert. The topic of components' dependency is incorporated by adding a data field regarding the number of interfaces. However, when adding the different components through MC analysis, the variables (components' weights) are assumed independent. A dependence structure that accounts for the various data fields being judged and rated could be established. The intended purpose of the assessing the number of interfaces a component has is to evaluate its complexity, and a dependency via interconnectivity is a consequence of this.

2.4 Expert elicitation

Expert elicitation refers to a combination of experts' judgements on the uncertainty of a VoI, on their specific area of knowledge. It ranges from an undocumented opinion to a formal process of gathering judgements in a survey or census and have this reviewed and processed. The goal is to combine experts' judgements into a good probability assessor and reach a rational and general consensus [122].

2.4.1 Structured Expert Judgement (SEJ) classical model

SEJ's classical model is proposed by Cooke in [123]. This method combines expert's unknown judgements, taking into account the expert's personal performance score, evaluated with training questions (known judgements).

Similarly to the training and validation sets in surrogate models, experts are first asked to estimate the quantiles of known VoIs' uncertainty distributions q_i, including $q_{0.05}$, $q_{0.50}$ and $q_{0.95}$. This is called the seed set. To calculate the expert's personal performance score, two factors are evaluated in their judgements: accuracy and precision. Accuracy, or Calibration C, is evaluated by the probability of falsely rejecting the statistical hypothesis. Precision, or Informativeness I, is evaluated by the ability to concentrate a high probability in small intervals. For each expert$j$, the weight from scores is obtained from

$$W_j = C_j * I_j \tag{2.4}$$

and is averaged over the entire set of seeds or known training questions. With the weight of each expert W_j, the final quantiles Q_k for an unknown VoI are

$$Q_k = \sum_j W_j * q_k \tag{2.5}$$

An example of the application of the Cooke method is represented in Fig.2.8. In it, 11 experts were solicited to estimate how long an old earth dam could withstand a leak. In the upper part of the box, the experts are represented by a number (1 to 11) followed by their estimate. The triangle represents $q_{0.50}$, whereas the line limits represent $q_{0.05}$ and $q_{0.95}$, also known as the credible limit where there is 90% probability of the estimate, in this case time, falling into this range. The lower part of the box represents the combined judgements' solutions. The first line represents a combination of the quantiles for all experts, not taking into account the experts' performance scores. And the second line accounts for the experts' performance scores, in a performance-weighted solution. In the first case, the dam was most likely to withstand a leak for 157h, whereas for the performance-based solution this was estimated at 1665h, 1508h more or 1060% more.

This method can be applied using EXCALIBUR (EXpert CALIBRation). EXCALIBUR is a Windows open-source program that allows parametric and quantile input from experts for

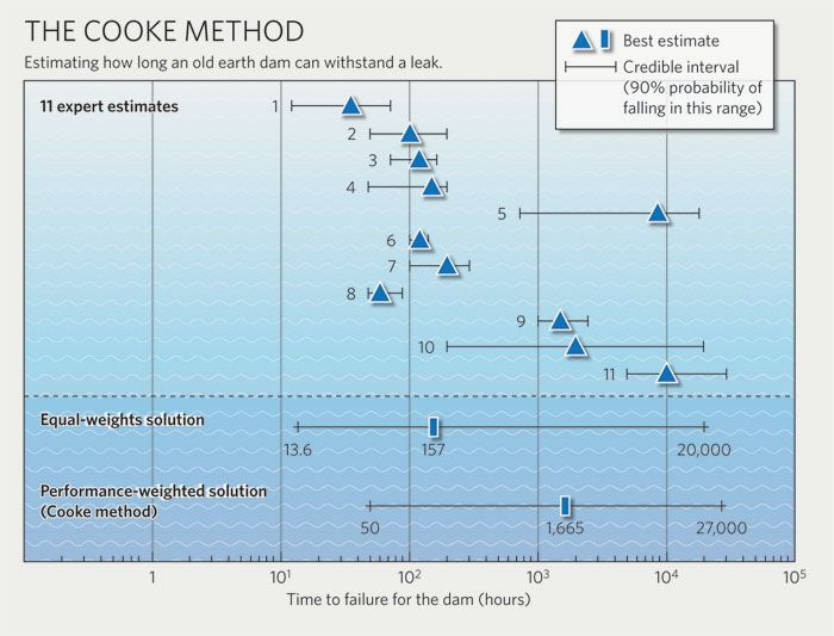

FIGURE 2.8. Application of the Cooke method to an example of estimating how long an old earth dam could withstand a leak [124].

continuous uncertain quantities and uses the combination approaches described above to integrate experts' opinions into one joint PDF of the VoI. Applications of the classical method can be consulted in [124, 125].

2.4.2 Dempster-Shafer Theory (DST)

Another method for combining expert's judgements is the Dempster-Shafer Theory. DST can be regarded as a generalisation of probability theory where probabilities are assigned to sets or intervals as opposed to singleton events. The Dempster-Shafer combination rule assumes that all sources of data are independent. In this case, the experts' judgements are independent from one another. This theory is based on the following three equations: the basic probability assignment (bpa) Eq.2.6, Belief Eq.2.7 and Plausibility Eq.2.8:

$$\begin{aligned} & m : \mathrm{P}(X) \rightarrow [0,1] \\ & m(\varnothing) = 0 \\ & \textstyle\sum_{A \in P(X)} m(A) = 1 \end{aligned} \tag{2.6}$$

$$Bel(A) = \sum_{B|B \subseteq A} m(B) \tag{2.7}$$

$$Pl(A) = \sum_{B|B \cap A \neq \varnothing} m(B) \tag{2.8}$$

where $\varnothing$ is the empty set and $m(A)$ is the bpa. As the data and its uncertainty is discrete and interval-valued, beliefs and plausibilities are non-additive, i.e. their sum is not 1 necessarily.

In other words, it is assumed that the experts do not know everything and the sum of the probabilities attributed to the intervals, likewise, is not necessarily 1. Belief and plausibility can be derived by one another and interpreted as shown in Fig.2.9. Belief is the contrary of doubt and the lower bound to the confidence interval of the uncertainty of a specific set of events A. Plausibility is the contrary of disbelief or $Pl(A) = 1 - Bel(\overline{B})$ and the upper bound to the confidence interval [126].

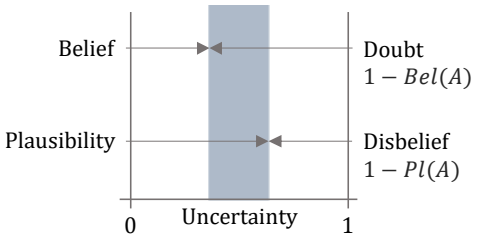

FIGURE 2.9. The concepts of belief and plausibility, and their interpretation in terms of uncertainty [126].

Assuming $m_1(A)$ and $m_2(A)$ are two bpas from two independent experts, DST combines them into a new Basic Belief Assignment (BBA) by applying the Dempster-Shafer rule [127]:

$$m_{12}(A) = \frac{\sum_{B \cap C = A} m_1(B) m_2(C)}{1 - K} \text{ when } A \neq \varnothing \tag{2.9}$$

$$\text{where } K = \sum_{B \cap C = \varnothing} m_1(B) m_2(C) \tag{2.10}$$

An example of the application of this method on aircraft maintenance times uncertainty assessment is detailed in [97].

2.4.3 Including expert elicitation methods

Following from the suggestion included in the previous list (item 4) to include experts' elicitation expert elicitation techniques into WUA, efforts were made towards that. A first study was done evaluating vendor's performance through expert elicitation and the set of questions enumerated below was assembled for this purpose.

1. Deadlines: How good is the vendor at meeting deadlines?
2. Communication/Relationship: How responsive is the vendor? How is the relationship with the vendor?
3. Transparency: How transparent is the vendor at communicating risks to weight?
4. Past history: Is this a new or experienced vendor?
5. Completeness: How complete are the reports?
6. Maturity: How mature is the information reported?

The theory used to combine experts' judgements was the Dempster-Shafer evidence theory [127]. The possibility of using EXCALIBUR and have it running in parallel with WUA was also discussed. EXCALIBR (from EXpert CALIBRation) is a software package for structured expert judgement elicitation using Cooke's classical model [123]. It allows the user to input experts' quantile assessments and parameters, and combine their assessments based on equal weights, user weights, and expert performance-based weights.

2.5 Probabilistic Margin Setting (PMS)

The Probabilistic Margin Setting (PMS) approach is introduced as a way to assign margins and reliability factors to components in order to allow for multidisciplinary optimisation. In aircraft weight estimation, the output Z is usually the weight of a specific aircraft part, component or WP. A reliability level β can be attributed to Z. Let's assume Z is the weight of the wing and $\beta = 0.95$. This means the weight of the wing has to be known with 95% certainty. H is the weight margin (+/-kg) obtained for β where H_β = Z_β - Z_μ. Z_β is then the weight value not to exceed or the target weight for the wing. H is the weight margin for increases to the current status weight Z_μ. This method is called Probabilistic Margin Setting.

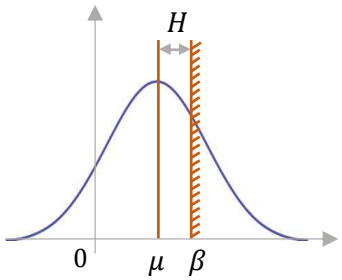

FIGURE 2.10. Reliability level β and margin H in a normal distribution, for probabilistic margin setting.

Consider now the global scenario where Z is the aircraft's overall weight. Having a set target weight, β can be obtained for which Z_β = W_{target}. This allows to conclude how reliable the current weight is. H corresponds to the difference between status and target weight and the global margin. X_m corresponds to the weight of a specific component m. β_m can be optimised and therefore H_m so that the sum of all X_m's would create a PDF for Z so that Z_β = W_{target} and β corresponds to a desirable reliability level.

Raymer's conceptual design equations [3] were used to demonstrate this approach and, as an example, its equation for wing weight is presented below.

$$W_{\text{wing}} = k_{\text{w}} \times (\text{MTOW} \times N_{\text{z}})^{u_{w1}} S_{\text{w}}{}^{u_{w2}} A^{u_{w3}} (t/c)_{\text{root}}^{-0.4} \times (1+\lambda)^{0.1} (\cos\Lambda)^{-1.0} S_{\text{csw}}^{0.1} \tag{2.11}$$

where $MTOW$ is the Maximum Take-Off Weight, N_z is the ultimate load factor (1.5× limit load factor), S_w is the trapezoidal wing area, A is the Aspect Ratio, $(t/c)_{root}$ is the thickness to chord ratio at the root of the wing, λ is the taper ratio, Λ is the wing sweep, is the wing's sweep angle and S_{csw} is the control surface area (wing-mounted). The physical parameters are assumed constant and the technology factor k_w and the uncertain parameters $u_{w_i}, i = 1,2,3$ are the uncertain variables of the equation. k_w and u_{w_i} are based on a statistical regression weighting from a historical data sample of design parameters and wing weights. The factor k_w can simplistically be seen as a way of measuring the impact of changes from the historical knowledge. Both uncertainty variables are represented by probability distributions: k_w is assumed to be a uniform distribution within its range and u_{w_i} a triangular distribution between 95% and 105% of its nominal value. It then goes on to calculating the total PDF for the wing weight by sampling the uncertain variables. Using the values listed in Tab.2.5, the PDF obtained for the wing weight is shown in Fig.2.11.

TABLE 2.5. Detailed parameter listing for Raymer's W_{Wing}, in Eq.2.11.

Design Parameter	Value
MTOW	174446.5 lbs
N_z	3.75 [-]
S_w	1393.12 sq ft
A	9.56 [-]
$(t/c)_{root}$	0.1208 [-]
λ	0.270 [-]
Λ	25.33°
S_{csw}	300.0 sq ft

Variable	Nominal value
k_w	0.0055
u_{w1}	0.557
u_{w2}	0.649
u_{w3}	0.500

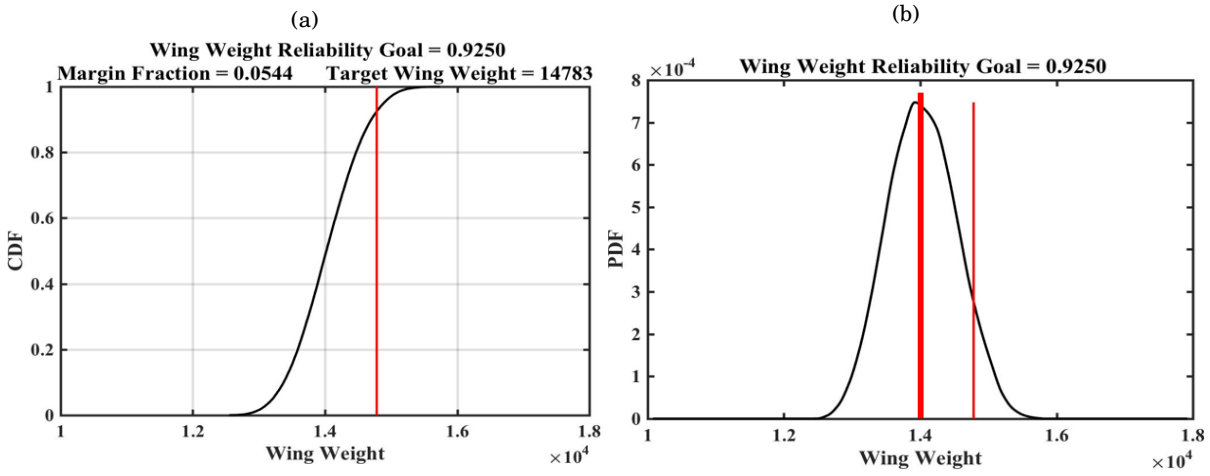

FIGURE 2.11. Raymer's W_{Wing} for probabilistic margin setting. (a) Cumulative distribution function (CDF); (b) Probability density function (PDF).

The goal is to assess how these parameters and their distribution functions can affect the final weight of the wing. Having a set target weight or a reliability level for the weight of the wing, a visual representation of the obtained weight margin is achieved. In the example of Tab.2.5, the weight margin obtained is $H_{\text{wing}} = 783\text{lbs}$, as shown in Eqs.2.12.

$$\begin{aligned} W_{\text{wing},\,\beta=92.5\%} &= 14783\text{lbs} \\ \mu_{\text{wing}} &= 14000\text{lbs} \\ H_{\text{wing}} &= 783\text{lbs} \end{aligned} \tag{2.12}$$

The final distribution is obtained by sample based conditioning of the Bayes Belief Net built for the wing weight using UNINET. The same methodology was applied to the fuselage:

$$W_{\text{fus}} = k_{\text{f}} \times (\text{MTOW} \times N_z)^{u_{\text{f1}}} L_{\text{f}}{}^{u_{\text{f2}}} S_{\text{f}}{}^{u_{\text{f3}}} (1+K_{\text{ws}})^{u_{\text{f4}}} L/D^{u_{\text{f5}}} \times C_f \tag{2.13}$$

where L_{f} is the fuselage structural length, D_{f} is the fuselage structural depth, S_{f} is the fuselage wetted area, $K_{\text{ws}} = 0.75(1+2\lambda)/(1+\lambda) \times (b_w \tan(\lambda/\Lambda))$, b_w is the wing span and C_{f} is a coefficient related to the number of cargo doors and fuselage landing gear mountings. The physical parameters are assumed constant and the technology factor k_f and the uncertain parameters $u_{\text{f}_i}, i = 1,...,5$ are the uncertain variables of the equation.

TABLE 2.6. Detailed parameter listing for Raymer's W_{fus}, in Eq.2.13.

Design Parameter	Value
MTOW	174446.5 lbs
N_z	3.75 [-]
L_{f}	124.75 ft
D_{f}	13.17 ft
S_{f}	4302.57 ft^2
K_{ws}	0.3861355 [-]
C_f	1.254400 [-]

Variable	Nominal value
k_{f}	0.328
u_{f1}	0.5
u_{f2}	0.25
u_{f3}	0.302
u_{f4}	0.04
u_{f5}	0.1

And the landing gear:

$$W_{\text{lg}} = k_l \times W_{\text{lg}_{\text{ref}}}{}^{u_{\text{l1}}} L_{\text{mlg}}{}^{u_{\text{l2}}} V_{\text{stall}}{}^{u_{\text{l3}}} C_{\text{lg}_{\text{m}}} + C_{\text{lg}_{\text{n}}} \tag{2.14}$$

where $W_{\text{lg}_{\text{ref}}}$ is the landing gear reference gross weight, L_{mlg} is the main landing gear structural length, V_{stall} is the stall speed, $C_{\text{lg}_{\text{n}}}$ is a coefficient accounting for various parameters characterizing the landing gear, such as the number of main gear shock struts and main wheels, and $C_{\text{lg}_{\text{n}}}$ is the nose landing gear weight, assumed constant. The physical parameters are assumed constant and the technology factor k_l and the uncertain parameters $u_{\text{l}_i}, i = 1,2,3$ are the uncertain variables of the equation.

TABLE 2.7. Detailed parameter listing for Raymer's W_{lg}, in Eq.2.14.

Design Parameter	Value
$W_{lg_{ref}}$	145890.2 lbs
L_{mlg}	80.0 ft
V_{stall}	194.1 ft/s
C_{lg_m}	1.221150 [-]
C_{lg_n}	685.8955 lbs

Variable	Nominal value
k_l	0.0106
u_{l1}	0.888
u_{l2}	0.4
u_{l3}	0.1

The final total weight BBN is shown in Fig.2.12. All the equations and parameters used above

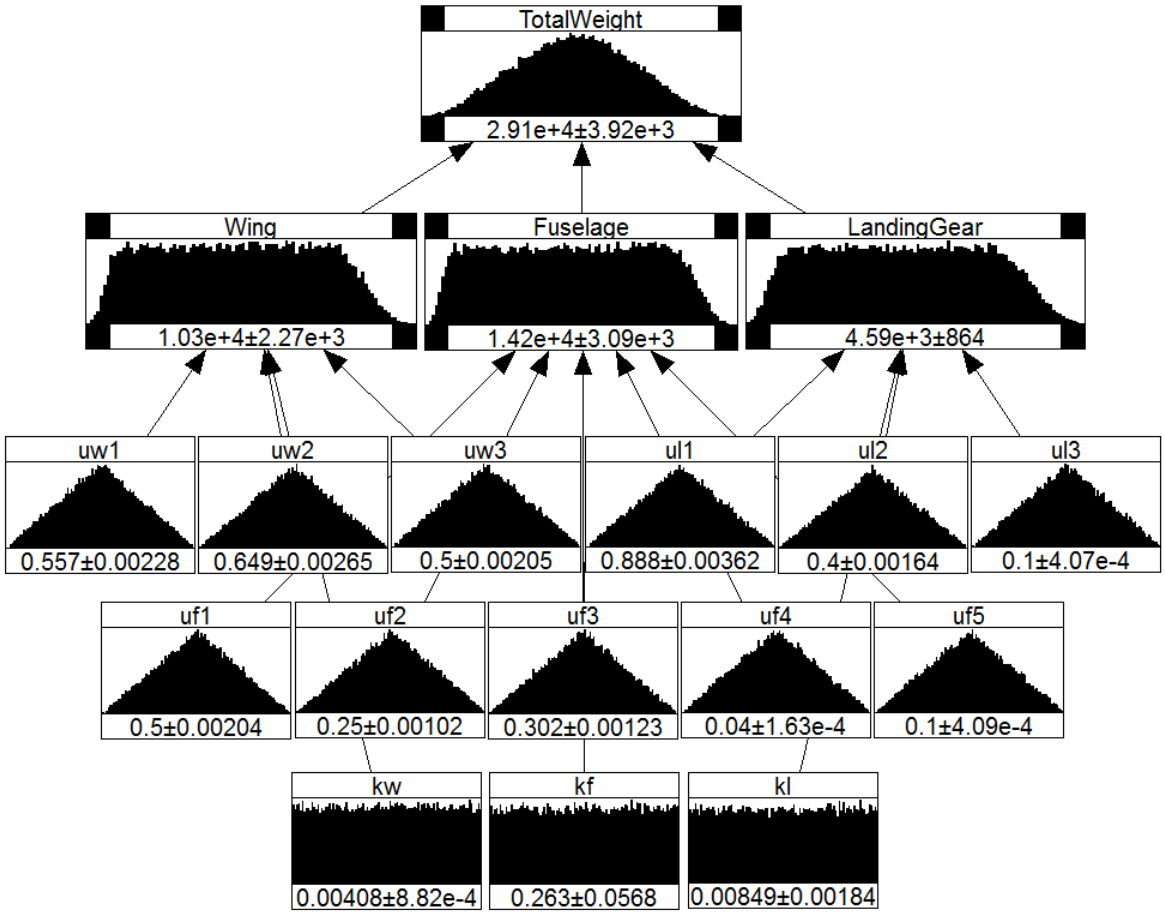

FIGURE 2.12. Bayesian belief net for the wing, fuselage and landing gear weights and their sum, total weight, in UNINET.

are detailed in Raymer [3], pages 403-407.

2.6 Dependence modelling

Considering the multidisciplinary complex machine that is an aircraft and considering its large number of interfacing and correlated components and weight drivers, it is expected that a dependency grid will have a significant impact on the probabilistic propagation of uncertainties.

For that reason, and following the PMS method, efforts are steered towards modelling dependence and studying its impact on the final weight distribution. The aim with dependence modelling is to capture relationships between components that may drive other components' designs and weights in convergent or divergent ways, e.g. environmental regulations demanding for the introduction of significant engine design adaptations and a series of chain reaction changes following in the wing design. In early design phases these dependencies could be established based on some sensitivity modelling. In later phases, many of the parameters which were open in the early phases have been frozen so dependencies are potentially less physics driven but more industrial process driven. One way of posing the question of dependency is by the use of conditional probabilities: Consider two components A_1 and A_2. Given that the weight of component A_1 has changed, what is the probability of the weight of component A_2 changing? Or, given that the uncertainty in the weight of component A_1 changed, what is the probability of the uncertainty of the weight of component A_2 changing?

Conditional probabilities can be modelled in UNINET by defining a conditional probability table for each node. The conditional probability table defines the distribution over that node's possible values, conditional on each possible combination of values of its parents' nodes [45, 48]. UNINET will then produce a correlation matrix for the whole BBN that is used in a copula when calculating the joint probability distribution. Alternatively, the correlation or dependence matrix can be built manually, via expert elicitation, statistical evidence or other methods. The dependence matrix of n random variables $A1, A2, ..., An$ is the $n \times n$ matrix whose i, j entry is $P(Ai|Aj)$. The values in the matrix need to be adjusted so that the matrix becomes symmetric and positive-semi-definite. The final matrix is introduced in UNINET and the conditional probability tables are computed.

The dependency modelling was tested in *Example 1*, where 5 components (A,B,C,D and E) constitute the whole unit in analysis. The independent BBN for this example is illustrated in Fig.2.7 and the final distribution's parameters for the overall weight are μ = 11134kg and σ = 148.94kg. These values are the baseline reference for studying dependence incorporation. The correlation matrix of the BBN is:

$$\begin{bmatrix} 1 & \delta_{AB} & \delta_{AC} & \delta_{AD} & \delta_{AE} \\ \delta_{BA} & 1 & \delta_{BC} & \delta_{BD} & \delta_{BE} \\ \delta_{CA} & \delta_{CB} & 1 & \delta_{CD} & \delta_{CE} \\ \delta_{DA} & \delta_{DB} & \delta_{DC} & 1 & \delta_{DE} \\ \delta_{EA} & \delta_{EB} & \delta_{EC} & \delta_{ED} & 1 \end{bmatrix} = \begin{bmatrix} 1 & P(A|B) & P(A|C) & P(A|D) & P(A|E) \\ P(B|A) & 1 & P(B|C) & P(B|D) & P(B|E) \\ P(C|A) & P(C|B) & 1 & P(C|D) & P(C|E) \\ P(D|A) & P(D|B) & P(D|C) & 1 & P(D|E) \\ P(E|A) & P(E|B) & P(E|C) & P(E|D) & 1 \end{bmatrix}$$

The dependence variable $\delta \in [-1, 1]$ can take any of the following 3 values: $\delta = 0.1$ for low dependence, $\delta = 0.5$ for moderate dependence and $\delta = 0.8$ for strong dependence (for independence, $\delta = 0.0$). Three scenarios were considered where all the components have the same level of dependence between them. In the first scenario the components are all low correlated and $\delta_{ij} = 0.1$. Then, the components are all moderately correlated and $\delta_{ij} = 0.5$. Finally, the components are all assumed strongly correlated and $\delta_{ij} = 0.8$. The results are listed in Tab.2.8.

TABLE 2.8. The impact of adding dependence between component weights when building the joint PDF for the total weight. The component weights used as example come listed in Tab.2.2.

	$\lvert\mu\rvert$	$\lvert\sigma\rvert$	$\lvert\mu\rvert$ (%)	$\lvert\sigma\rvert$ (%)
Independent $\delta = 0.0$	11134	148.94	-	-
Low correlation $\delta = 0.1$	11134	155.43	0.00	4.36
Medium correlation $\delta = 0.5$	11133	185.36	0.01	24.45
Strong correlation $\delta = 0.9$	11133	206.60	0.01	38.71

For the case where all the components are assumed strongly dependent, σ is ~40% bigger than the independent scenario. Although unlikely, the consequence of this case is significant. On the other hand, if all the components belong to the same WP, they are likely to be low correlated at a minimum. The low correlation can result in an impact on results of ~4%. Although smaller in consequence, its likelihood is significant. The methodology is generic enough that it can be applied at any level within or between WPs. The one varying input would be the dependence matrix.

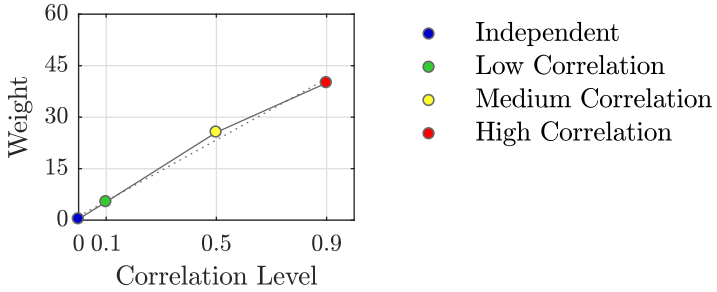

FIGURE 2.13. Correlation level VS. weight's standard deviation; σ grows quasi linearly with correlation coefficient.

Whilst μ remains equivalent, σ increases quasi linearly with the strength of the correlation between variables and its linear regression is traced in Fig.2.13.

* * *

A method for capturing dependence automatically is also developed. The methodology measures similarities between assessments. Consider two WPs are being assessed in WUA. If their weights, confidence levels and ratings change, in time, in a similar manner they are assumed to be

correlated and therefore dependent. Percentage changes are measured and compared WP to WP and a dependence matrix is built. This method was experimented with but results were inconclusive. Had there been more data to measure correlations and in project and design phases, the methodology could be a matter for further exploration. However, in weights, modelling and operations phases, many other factors come into play in the weights process and expert elicitation becomes a more reliable source of information for dependence.

2.7 Summary

In this chapter, the processes and methodologies in place for weight estimation and management in industry, including the mass properties database structure, the Weight's Uncertainty Assessment (WUA) method and the weight convergence corridor, are defined. A representative flow diagram of a typical industrial uncertainty assessment is delineated. The same processes were recreated, tested and validated using academically available software, such as MATLAB, UQLab and UNINET. The results obtained, with the different software, were analysed for relative and absolute error, respective to the industrial software. The values for error are within the margin for randomness associated with MCS, and, therefore, validation was successful.

After studying the state-of-the-art and recreating and testing the software, areas for improvement, for the processes in place, were identified. Within those, three were analysed: including expert elicitation techniques to quantify the human factor uncertainty; Introducing probabilistic margin setting as a technique to achieve the available input variability from a desired reliability or weight target; and dependence modelling as a way to incorporate component correlations when propagating uncertainties.

Exploratory data analysis on aircraft weight data, specifically the database used in the weight estimation and management process, follows.

CHAPTER 3

EXPLORATORY DATA ANALYSIS (EDA) ON AIRCRAFT WEIGHT DATA

Exploratory Data Analysis (EDA) aims at analysing data sets and identifying their main characteristics. EDA does not require formal modelling or applied statistics and is often purely visual. It is seen as a first approach into revealing the data's potential for capturing correlations and patterns, predicting events, or supporting empirical equations.

3.1 Digital transformation

Digital Transformation (DT) is one of the biggest challenges manufacturing industries currently face. DT aims at creating value in products and improving processes by integrating digital technology into all areas of business. It not only changes how value is delivered to customers but it can also have a societal impact, e.g. climate action pushing for greener aircraft which in turn can revolutionise the industry. Businesses and organisations are required to shift culturally into a new era of digital continuity, where outdated regulations, increased customer expectations, volatile markets and cultural transformations set the pace for industry renovation. Digitisation can provide unparalleled advantages to a business, by creating value in products and improving processes' efficiency, making use of data that is already being produced and used within the industry. On the other hand, DT is also seen as a major source of risk. Particularly, when an industry is connected to a number of different manufacturers, vendors and partners, ensuring data continuity across all, whilst guaranteeing the required level of data security is the biggest setback to DT.

The first step into the process of DT is to map data flow across the industry. Recall the weights' pyramid in sec.1.3.1 - a hierarchical representation of the different phases of design and the uncertainty sources in each one. With this and the DT challenge in mind, a data flowchart for the

weight's process was generated and is shown in Fig.3.1.

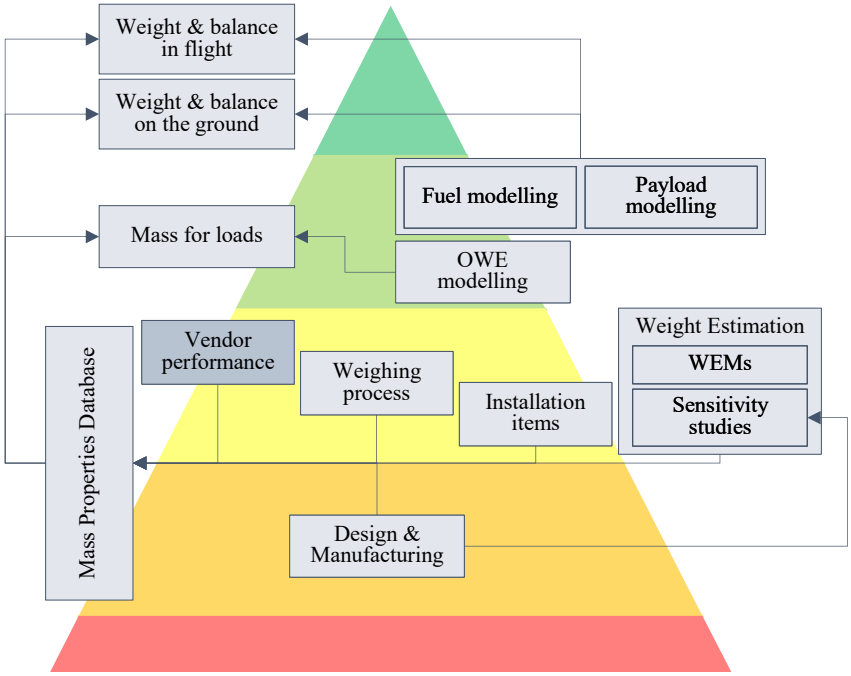

FIGURE 3.1. Weights' process digital transformation data flow diagram.

Where data is flowing, uncertainty is also flowing and propagating through the different phases: project, design, weights, modelling and operations uncertainty. The DT flowchart is then used as a parallel basis for uncertainty quantification. A deeper understanding of each individual field in Fig.3.1, including how they operate, what are the respective uncertainty sources, how uncertainty levels are changing and defining criteria to predict changes, is crucial. Secondly, defining a method that translates this knowledge into meaningful information to program and at industry level is another key area for investigation.

Vendor performance was chosen as the first field to be explored.

3.1.1 Vendor performance

Vendor performance relates to quality of reported data. Because aircraft have a significant percentage of its components outsourced, having good quality reports is essential for a smooth convergence to a target weight. Similar to the information that the database provides, the weight report provides, amongst other things, the part's names, weights, maturity levels and total component weight. Consider, once again, the component in *Example 1*, listed in Tab.2.1. A partner's weight report would include some extra information as shown in Tab.3.1.

TABLE 3.1. Example of a vendor's weight report of component A, detailed in Tab.2.1.

Maturity	Weight	Total weight (kg)	Review
1	0	153	1
2	10	153	1
3	0	153	1
4	120	153	1
5	23	153	1
6	0	153	1

After collecting the history of reports, Fig.3.2 is produced that shows the evolution of weight in maturity level, throughout reports.

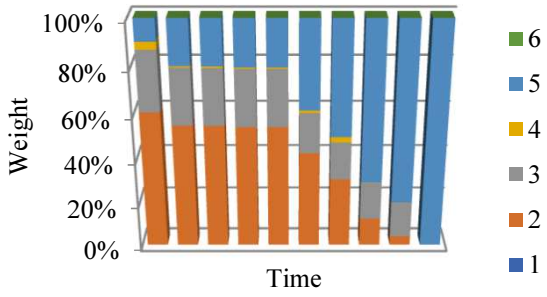

FIGURE 3.2. Total fastener's status weight and maturity level evolution.

A test case of a collection of weight reports from a specific vendor was analysed using the MATLAB's neural network toolbox for the purposes of pattern recognition and clustering. The results were inconsistent and inconclusive. This, allied with the fact that there is no standardised way of reporting data, implying that each vendor would have to be considered separately, made any automatic way of extracting information rather difficult. Data would need specific pre-processing and expert judgement to be made ready for analysis. And even then, being able to obtain enough data corroborating the same hypothesis so it could constitute statistical evidence, was not possible. For these reasons, a decision was made to discontinue the vendor performance assessment.

3.2 Machine learning on aircraft weight data

One way of studying uncertainty is to look at past data and gather enough statistical evidence to build and support potential correlations, patterns, trends or even empirical equations. After learning about the industrial process of weight estimation and management within aircraft design, researching ways of incorporating uncertainty into large, complex models and getting involved in different on-going projects, their avenues of exploration and inputs, a first step into machine learning from aircraft past data is made.

The idea here is to take the mass properties database and extract all the information concerning a specific WP. Because, industrially, WPs are assigned to separate design teams and vendors, decomposing the problem into WPs was intelligible. Then, the evolution of each data field is analysed against time (one frozen database entry is one point in time) for each part constituent of that WP. This is done in efforts to retrieve such patterns, relationships and/or clusters of information, either among data fields or parts.

The results shown refer to one specific WP containing 2 sub-WPs and 60 individual parts, and the two data fields in analysis are weight and maturity level. Consider that, for example, the WP corresponds to the wing, the 2 sub-WPs correspond to the primary and secondary structures of the wing, and the 60 individual parts include all the skins, spars, ribs, leading and trailing edge devices, etc. Time 1 to 11 in the plots (see, for example, Fig.3.3), correspond to weight report numbers. With a weight management process in place, every x number of weeks, the weight data is assessed. Time 1 corresponds to the first weight report submitted and so on, until the most recent report number 12.

3.2.1 Weight evolution

The first data field to be analysed is the weight evolution of the WP, shown in Fig.3.3. Every line (and colour) represents a different part of the WP and every dot is a frozen weight report. The weight is presented in percentage of the total WP weight. As mentioned at the start, 60 parts are analysed in this study, but only a smaller number seems to be shown. This is because several parts have very small weight (in %) are overlapped close to 0 (zero) weight.

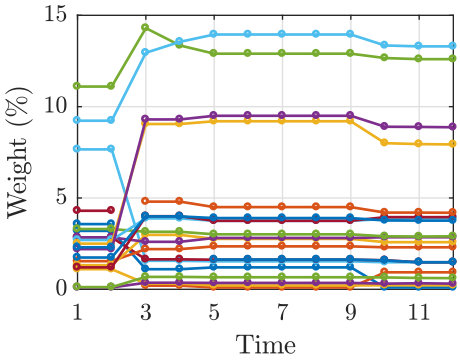

FIGURE 3.3. Weight reports' absolute weight evolution.

From weight reports 2 to 3, big weight fluctuations occur for a significant number of the parts. This can be explained by changes in the identification codes, specifically the denomination code. It might be that the component being plotted in the beginning of a line is not the same as the one in the end, because their denomination codes were altered in procedures, sometime in between weight reports 2 and 3. The denomination code change was not, however, generalised for all parts nor WPs or aircraft.

The parts do not suffer any other major weight fluctuations and, when they do, these seem to happen at the same time. Besides 2 to 3, from 9 to 10, a number of parts mainly decrease in weight. Changes in weight happening at the same time is a strong indication of the dependencies between different parts, especially within the same WP. Further, the weight being a percentage weight adds to that effect.

If data analysis to the mass properties database is to be considered and carried forward in the future, there needs to be an industrial concern with standardisation and consistency of denomination codes and granularity of parts and WPs.

3.2.2 Maturity level evolution

Similarly to the weights' evolution, the maturity level evolution of the WP is shown in Fig.3.4. Maturity is here are discretised into $n \geq 4$ levels.

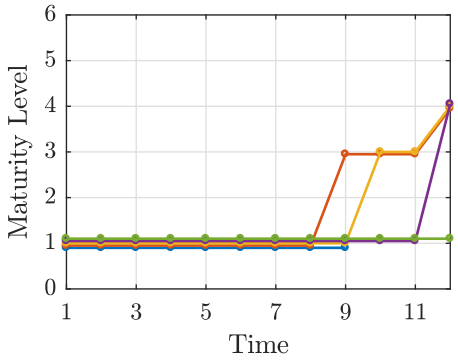

FIGURE 3.4. Weight reports' maturity level evolution.

Only after weight report 8, changes in maturity are reported, despite weight fluctuations happening before that. None of the parts was ever at level 2 of maturity and it might be that the level is not applicable in this case. The maximum ML reached was 4. Three research questions that follow are: are the data fields rightly defined, discretised and up-to-date; what is driving the changes in ML; can the data fields be clustered so that one cluster represents data fields with consistent inverse or direct correlations.

3.2.3 Clustering

Clustering or cluster analysis is the collection of data objects or cases into relative groups called clusters, when there is no prior knowledge about the group for any object - it is known as unsupervised classification. Objects within the same cluster are similar to one another and dissimilar to the objects in other clusters. Clustering is also known as classification analysis or numerical taxonomy.

Depending on the data set at hand and the intention of the analysis, there are a number different clustering algorithms to choose from. These differ in their setting of grouping parameter(s),

such as distance between cluster objects, density of objects in the data space or data statistical distribution. Four popular cluster analysis algorithms include: centroid-based clustering, distribution-based clustering, density-based clustering and hierarchical clustering.

Centroid-based clustering fixes the number of clusters to k clusters, finds the k central vectors, which may or may not be members of the data set, and organises the data by assigning each point to its nearest k centre. K-means is the most commonly used centroid based clustering algorithm, in which the data is assigned to the cluster with the nearest mean. Distribution-based clustering assumes the data set is composed of distributions, such as a normal distributions. The furthest away from the cluster centre, the lesser the probability that a data point belongs to that distribution. Density-based clustering defines areas, with no particular shape, of high density of data points. Points that are outside of these areas are considered outliers and are excluded from the analysis. Finally, hierarchical clustering, also known as connectivity-based clustering, is set on the core idea that a data point is more related to another one closer to it than to one further away. An extensive and comprehensive survey of clustering algorithms can be found in [128].

After plotting the weight and maturity level evolution, the idea of clustering parts emerged. Clustering aims at finding correlations between parts or data fields as well as facilitate the processing of data, once, and if, the entire aircraft is to be analysed. Two clustering algorithms are proposed and results are shown for each of them. The clustering algorithms applied are different than the standard ones mentioned above and were developed by the author. This is because the purposes of the clustering were very specific to the data available and problems. The clusters intended to agglomerate parts by looking at different types of data and using different clustering methods for each data field, some of which unquantifiable. Because of time and computational expense at fitting and choosing the right clustering parameters required by pre-defined algorithms, and for the purpose of the exploratory data analysis intended, the custom algorithms described below are used.

3.2.3.1 Variations in the same data fields at the same time

The first clustering technique groups individual parts whose data fields change at the same time, independently from if the change is effectively the same. Consider two different parts A and B and a data field on the mass properties database (see sec.2.1.1), X. A and B belong to the same cluster if, for any X, all the changes that occur for both parts in X, if any, occur at the same time (in between the same two weight reports). In other words, looking at the entire database time-line, the same data fields change in between the same two weight reports. The change itself can be different, e.g. an increase/decrease in weight or maturity level.

An example of this type of cluster is represented in Fig.3.5. From 9 to 10, changes in the position, material and drawings of the parts changed for all. From 10 to 11, the maturity level changed again for all the items.

It was concluded that this technique was clustering parts that were very similar in nature,

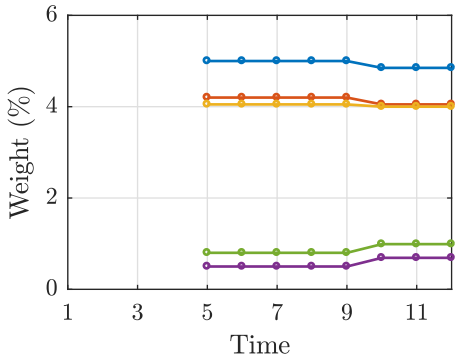

FIGURE 3.5. Clustering parts using the variations in the same data fields, at the same time, approach.

e.g. a group of fasteners or a group of butt-straps, and there is a potential for an additional identification code to arise from this clustering technique.

3.2.3.2 Absolute percentile variations for each time-step

The second clustering technique groups individual parts whose data fields evolve absolutely and percentually similarly. Consider again two different parts A and B and a data field on the mass properties database X that is measurable (see sec.2.1.1), e.g. weight or maturity level.

A and B belong to the same cluster if, for one specific X, all the changes that happen for both parts in X, if any, are absolutely and percentually similar, i.e. if a certain threshold of dissimilarity is not surpassed. In other words, this approach looks at comparing A and B's percentage decrease or increase in the same data field, for each weight report. This can be done using just one data field, e.g. weight, or more than one and the percentage values are added.

One of the clusters obtained by this method, using the evolution in weight alone to measure correlation between parts, is shown in Fig.3.6. Let us name the parts in this cluster A, B, C, D and E, from top to bottom, A being the green line and E the orange. The similarity in the shape of the lines are visible, even if dealing with parts with different percentage weights. Contrary to the previous cluster in Fig.3.5, parts A to E are of different types, including buttstraps, ribs, a panel and spar. Using this technique could help identify specific punctual dependencies between parts, respective to each WP or location within the WP.

This methodology was created in an attempt to capture dependencies or correlations between parts so that a dependence structure could be incorporated to WUA. The weight engineer would have to look at enough clusters that are produced with this methodology and see if the results are a good representation of what a dynamic correlation matrix would look like. This was out of the reach for this PhD.

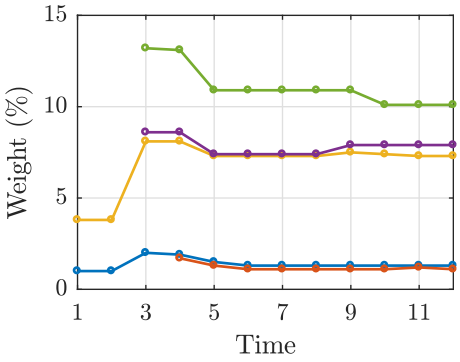

FIGURE 3.6. Clustering parts using the absolute percentile variations, for each time-step, approach.

3.2.4 Uncertainty bands

For each weight report and each individual component, the correspondent maturity level and weight are retrieved from the weight's database, fed into WUA (in sec.2.1.2) and an uncertainty band is produced. The uncertainty band is a proxy for a confidence interval around that weight.

The plots in Fig.3.7 and Fig.3.8 illustrate the uncertainty bands obtained for two different components of the WP. The blue lines represent weight evolution and the red lines are the uncertainty bands. Both parts are plotted twice, one is the "Best Case Scenario" (BCS) and the second the "Worst Case Scenario" (WCS). The BCS is when the ratings in WUA are maximum and therefore the confidence level initially obtained by the maturity assessment is not degraded: $f_{d_r} = f_{d_c} = f_{d_d} = 1$ and $\text{CL} = \text{CL}_m$. The WCS is when all the ratings in WUA are at their minimum value and therefore C_m is the degraded at its maximum.

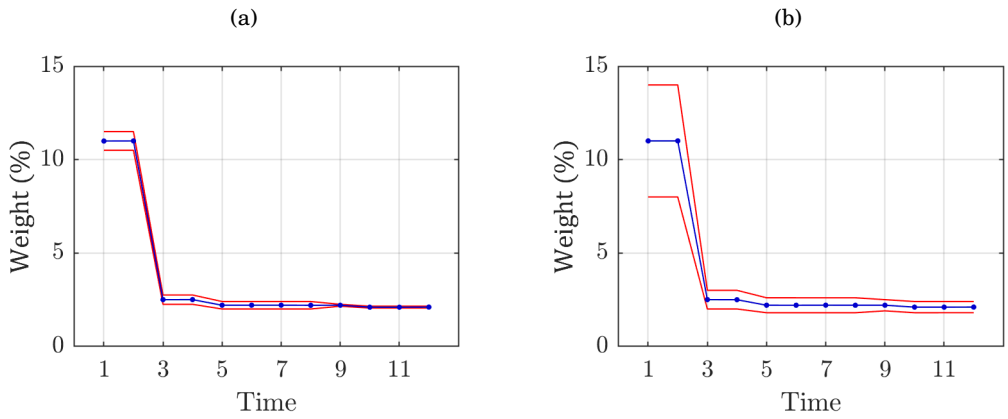

FIGURE 3.7. WUA's uncertainty band for part A. (a) Best case scenario; (b) Worst case scenario.

The aim of this study is to visually understand what is being captured by the confidence levels on WUA and, more specifically, if the bands are capturing all the fluctuations in weight

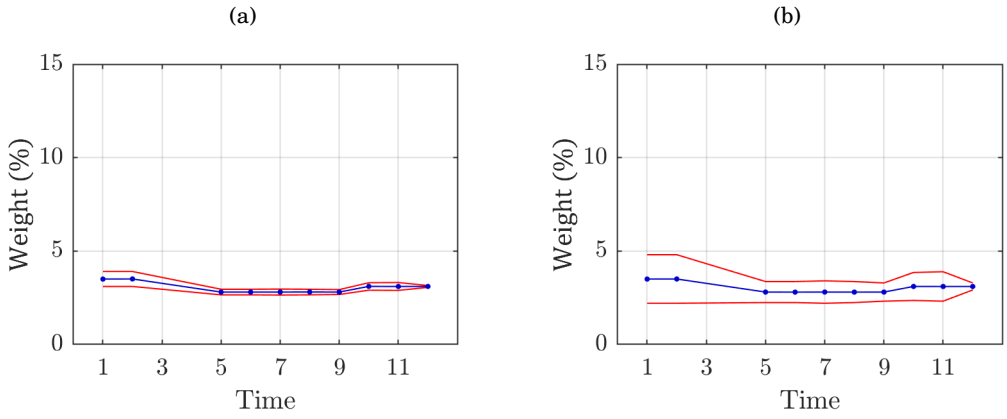

FIGURE 3.8. WUA's uncertainty band for part B. (a) Best case scenario; (b) Worst case scenario.

throughout the consecutive weight reports. Moreover, it allows for a visual perception of how under or over confidently uncertainty (or the confidence intervals) is being quantified.

In Fig.3.8(b), all changes in weight are captured by the uncertainty band but the same does not happen in any of the other cases. This illustrated the need to reassess uncertainty every time a weight report is frozen. Alternatively, the WUA methodology could be made more conservative but that would then have adverse effects on the milestone requirement margin assessment. Back propagating uncertainties from the database would be a way to calibrate the tool and, specifically, the reliability levels used to calculate the maturity's assessment confidence level C_m, shown in Fig.2.2.

3.2.5 WUA's granularity

The last item in the data analysis section aims to study the impact of using different component-level granularity (individual parts, sub-WP and WP) in the overall weight assessment for the current methodology WUA. The table in Tab.3.2 lists the results of the overall weight's μ and σ for three different cases. In the first case, the WP is decomposed into its lowest-level individual parts and the 60 variables are assessed independently. In the second case, the WP is decomposed into a sub-level of WPs (sub-WP) and the 2 variables are assessed independently. Finally, the WP is assessed as 1 variable in WUA, i.e. WP-level assessment. The results for the BCS and WCS are listed in Tab.3.2.

As expected, σ is significantly lower for BCS than it is for WCS. The more parts the WP is broken down into, the smaller the uncertainty, even if the weight adds up to the same amount. Assessing the individual parts might not be a viable option but it reduces the standard deviation on the final result which in turn reduces uncertainty. Understanding which σ or uncertainty corresponds to an accurate representation of reality and, therefore, determining the granularity

TABLE 3.2. The impact of the weights' granularity level when building the joint PDF for the total weight: assessing individual parts separately (60 input variables), sub-work-packages or components (2 input variables), and WPs (1 input variable).

		BCS		WCS	
		μ(%)	σ(%)	μ(%)	σ(%)
Granularity level	Individual parts (60 vars)	98.45	0.97	98.46	4.26
	sub-WP (2 vars)	98.48	2.37	98.45	10.81
	WP (1 var)	98.51	3.09	100.00	13.90

level WUA should be assessed at is imperative, as it can cause significant discrepancies in uncertainty of up to ~9.64%.

3.3 Summary

Exploratory data analysis is performed on weight data in the aircraft design process.

First, the digital transformation industrial challenge is introduced. Digital technology integration consists of having a standardised, connected and continuous flow of data between all disciplines in the industrial context, aiming to improve product and processes efficiency. A data flow diagram of the weight engineering behind the aircraft design process is delineated. One of the areas identified in the diagram is vendor performance. In an industry that relies on partners for products manufacturing or testing, it is imperative that the reporting and feedback complies with the digital transformation requirements. Some EDA was performed on a set of weight reports detailing maturity level and correspondent weight fraction, total weight and review number, amongst other data. For a number of reasons, including scarcity and dispersion of reports, non-standardisation of their format, lack of information reported as well as lack of validation of its quality, this analysis was inconclusive and discontinued.

Because weight reports from partners were inconclusive, the internal mass properties database, or internal weight data collection, was explored. The database contains all the weight information for a specific aircraft programme, including identification codes, weight, maturity level, position in the aircraft, etc., see sec.2.1.1. Machine learning techniques were applied to the data with the purpose of: finding correlations between data fields, particularly correlations between weight fluctuations and other data fields, namely maturity level; and clustering components or aircraft parts with similar weight changes or changes in other data fields. Lastly, the in place weight's uncertainty assessment (WUA) method, see sec.2.1.2, was tested for its uncertainty bands and if these were, in fact, capturing the weight variations reported throughout.

Two main issues were found with the employment of machine learning techniques on the weights' database. The first one being that a lot of the identification codes for aircraft parts, components, WPs or costs, were inconsistent. The historical data collected listed identification codes that were dependent on the aircraft programme or even the weight engineer in charge at

the time. The second issue was, and still is, that there are simply not enough different aircraft being produced, that warrant a set of data big enough for statistical evidence. The need to have a framework that emulates the aircraft design and sizing process and the weight convergence corridor, became indisputable.

CHAPTER 4

WEIGHT CONVERGENCE SIMULATION (WEICOS) FRAMEWORK

The framework developed for the ultimate purpose of tracking weight probabilistically in the convergence corridor of aircraft design is named WeiCoS, the WEIght COnvergence Simulation. WeiCoS enables structural sizing exploration and design sensitivities analysis, including their impact on aircraft weights. Instead of inspecting past aircraft data for trends and patterns, WeiCoS allows for generating new data, including aerodynamic loads, wing-box stress analysis, sizing data and a weight function based approach for secondary structure, and perform probabilistic uncertainty and sensitivity studies on the results.

A flow diagram of WeiCoS is shown in Fig.4.1, illustrating how the framework works and the interaction between its different modules. It combines a probabilistic uncertainty quantification wrapper (outside dashed box) around a traditional wing-box sizing routine for the primary structure of a wing and an alternative weight model for the secondary structure (inside dashed box). A detailed description of the wing-box sizing routine is available in sec.4.1 and the uncertainty wrapper is described in sec.4.2.

WeiCoS allows the user to define the input parameters to the sizing routine as either a probability distribution or a constant value. Input parameters include planform geometries, material properties, sizing load cases, among others. It then samples the distributions and runs the sizing for each sample, extracting in each run the resulting loads envelopes, stress analysis results and converged weights.

Depending on the analysis intended, a different set of parameters is varied and specific probability distributions are chosen. Depending on how far down the weight convergence corridor the analysis is "located", the variability, i.e. the distributions parameters, will get respectively wider or narrower. Post processing the results involves fitting the output data to a distribution and analysing its QoI's for the purpose of UQ. Moreover, sensitivity analysis on all input-to-

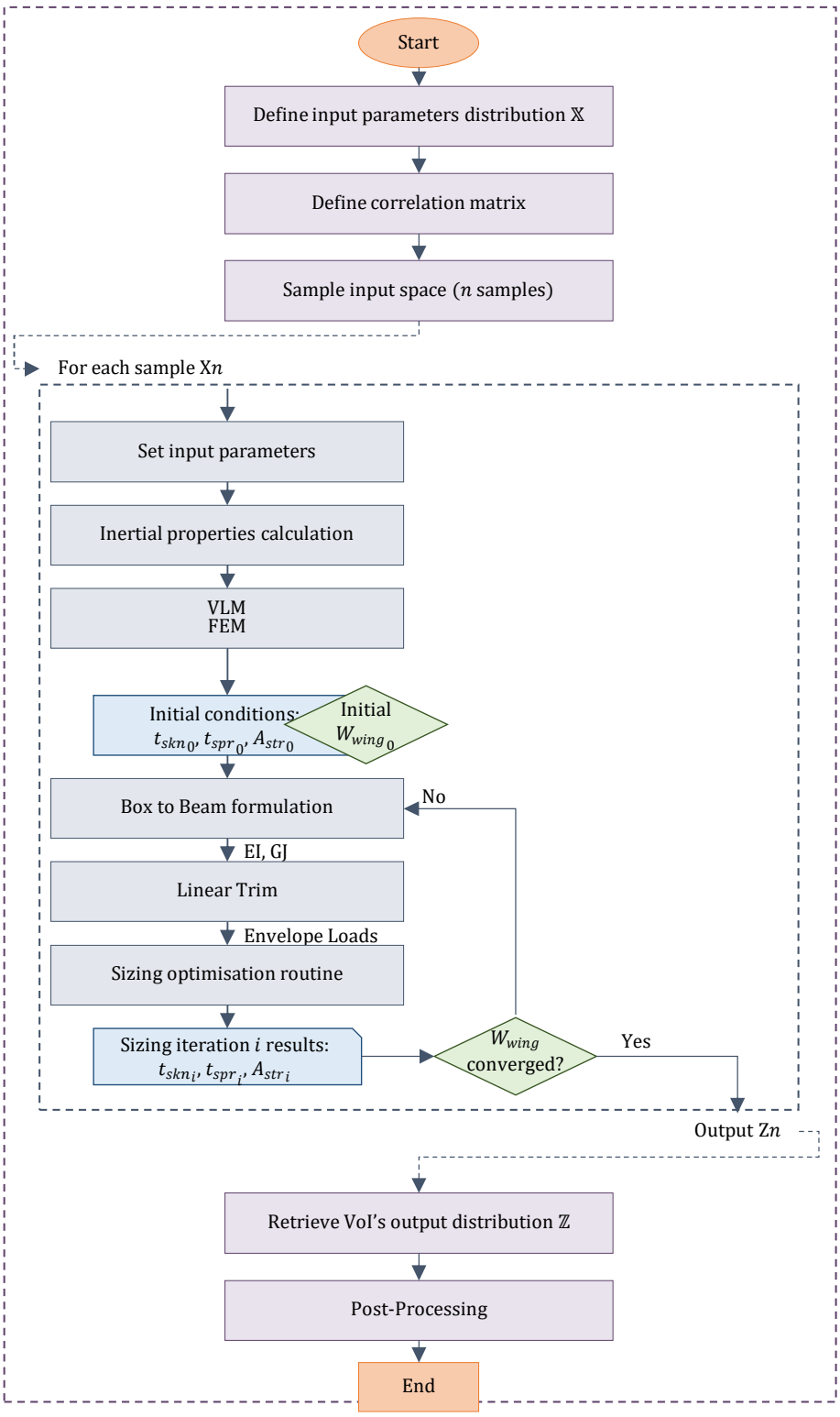

FIGURE 4.1. WEIght COnvergence Simulation (WeiCoS) framework flow diagram.

output variables (inside and outside the sizing routine) is performed, allowing to extract some conclusions. Further, back-propagating the results of a case where the full input parameter scope $\mathbb{X}_{prior}$ is varying, setting the target reliability margin or IoI for final aircraft weight at that particular stage in the design process, and ultimately analysing the sub-margins of the posterior input space $\mathbb{X}_{posterior}$, see sec.1.2.3.

4.1 Wing-box linear static aeroelastic sizing framework

The wing-box linear static aeroelastic sizing framework is described here. Its flow diagram is shown in Fig.4.2. The purpose of this framework is to extract the results of a sizing routine for each sample of input parameters defined. These include aeroelastic envelope loads, stress and sizing, including converged weights of each wing-box section.

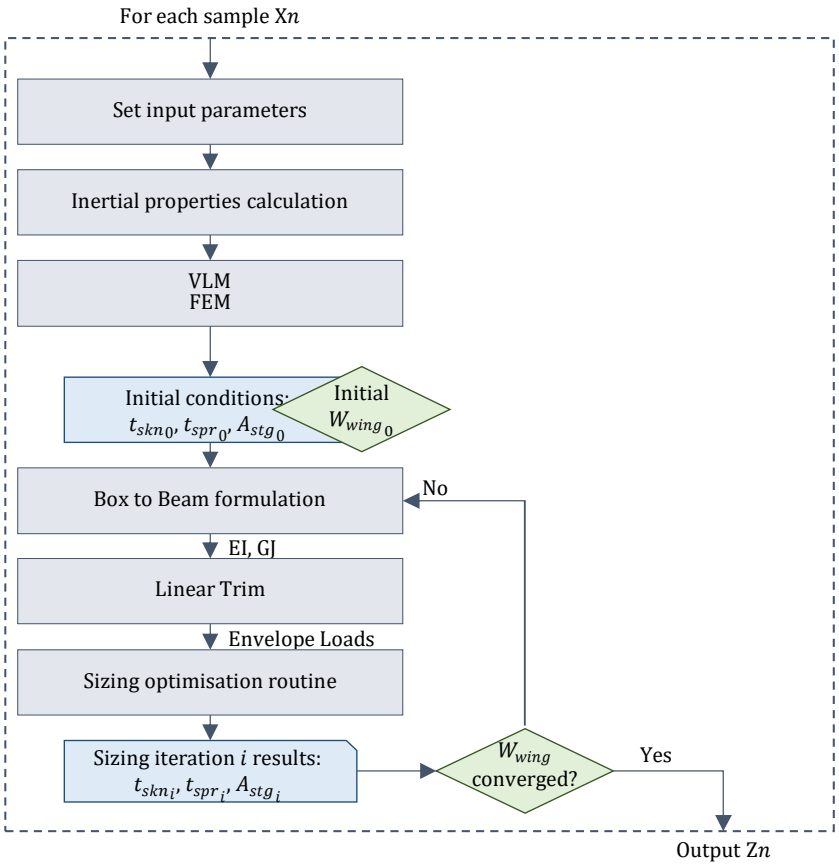

FIGURE 4.2. WeiCoS' wing-box linear static aeroelastic sizing flow diagram.

First, the wing-box section geometries (skins, spars and stringers), ribs and material properties are defined in sec.4.1.1. Next, the input parameters that fully define the aeroelastic model are detailed in sec.4.1.2. These include: planform geometry and aircraft model, including landing gear, engine and pylon and fuselage specifications, as well as general fixed aircraft weight assumptions

such as fuel weight, payload and MTOW. The secondary weight model and model parameters are presented in sec.4.1.3. And finally, the sizing optimisation parameters including the stress analysis formulae and the load cases for sizing (flight conditions and load factors) are defined in sec.4.1.4.2. A safety margin of SF= 1.5 is used throughout.

The sizing is limited to the wing-box skins, spars and stringers and the sizing varies the mass and stiffness of these parts, while keeping the rest of the aircraft's mass constant. Thus, the mass of the empennage and fuselage is kept constant and not included in the sizing, however, it is included in the overall aircraft trim analysis. The second step, after defining the input parameters, is to calculate the inertial properties of the fuselage, pylon and engines, payload and landing gear, and transfer these properties to a beam formulation of the wing in the form of lumped masses. These masses are expressed by a 6×6 matrix and have an associated structural node. The initial estimation of MTOW is then used to calculate the secondary structure weight. The secondary structure weight, as well as the fuel weight, are expressed as lumped masses and distributed spanwise over the structural nodes of the wing. Their weights are distributed throughout the nodes according to the fraction of internal volume of each wing-box (and respective node) over the total internal volume of the wing-boxes combined. Pylon and landing gear attachments to the wing and ribs weight are also expressed as lumped masses and placed on specific locations along the wing span, relatively to the aircraft model and further detailed in the sections below. The MTOW is kept constant for sizing, excepting the wing weight.

An initial condition for t_{skn_0}, t_{spr_0} and A_{stg_0} is defined and these, along with the lumped masses previously specified, allow to reduce the wing-box formulation to a beam formulation, where mass and stiffness matrices describe each beam element. The load cases are then used in a linear trim analysis and enveloped for sizing. The sizing is done through an optimisation routine that takes the enveloped loads and calculates the stress in each beam element, given its material properties and stress and minimum thickness constraints. The optimiser calculates the new t_{skn}, t_{spr} and A_{stg} for the objective of minimum overall weight of the wing. Each wing-box is sized discretely or separately, for wing-box specific calculated stress constraints and global minimum values for geometries' thickness. However, they are analysed collectively to deliver the minimum wing weight overall. The sum of the weight of the wing-boxes corresponds to the total primary wing weight. The section geometries are updated in the box formulation and the whole process geometry is repeated until the wing weight converges. The load cases used in the sizing are listed in Tab.4.8.

The sizing framework used in this work was adopted from Calderon et al. in [129]. For a full description of its beam and static aeroelastic modelling formulations, as well as the stress formulae used to size each individual wing-box section, please refer to the given reference.

4.1.1 Wing-box section geometries

The wing is discretised into a consecutive series of wing-boxes (see Fig.4.3) that are sized in the sizing optimisation module, described in Sec.4.1.4. In it, the aerodynamic loads are taken and used to calculate the stresses in each section. The material properties, minimum thickness and stress constraints need to be satisfied for each box. The optimiser calculates the skin thickness, spar thickness and stringers area for minimum overall weight of the wing, under the specified constraints. That corresponds to t_{skn}, t_{spr} and A_{stg} respectively, shown in Fig.4.4. Both upper and lower skins, as well as front and rear spars are assumed identical. The z-stringers geometry is fully defined by A_{stg}, where $A_{\text{stg}} = 3t_{\text{stg}}d$ and $t_{\text{stg}} = 0.12d$ and the stringer pitch is SP = 0.24 m. The chord of each box c_{box}, as well as the height of the spars h_{spr} are fixed.

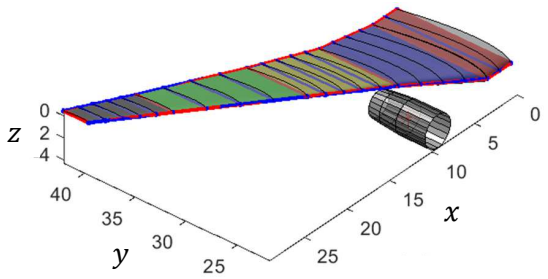

FIGURE 4.3. XRF-1 wing-box model adaptation.

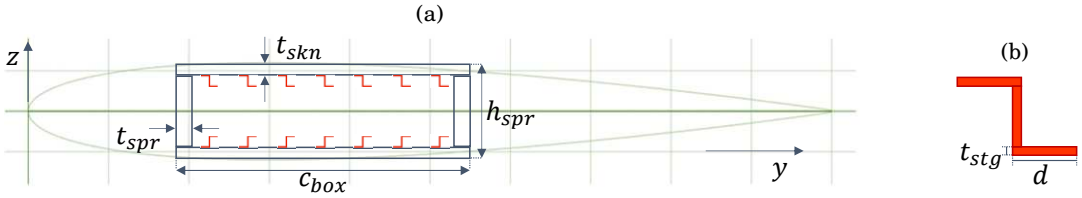

FIGURE 4.4. Wing-box configuration used in the sizing optimisation: airfoil cross-section geometry. (a) Wing-box geometry: skins thickness (t_{skn}) and box chord length (c_{box}) and spars thickness (t_{spr}) and box height (h_{spr}); (b) Z-stringer geometry: $A_{\text{stg}} = 3t_{\text{stg}}d$ and $t_{\text{stg}} = 0.12d$.

The distributions of the box chord c_{box}, the height of the spars h_{spr} and the length of the wing-box sections l_{box}, along the span of the wing, are shown in Fig.4.5. The vertical dotted lines across these plots represent the wing-box sections length, so it is noticeable the direct correlation between the spacing of the vertical lines and the y-value for l_{box} in Fig.4.5(c). The wing is divided into 20 sections. The wing-box sections are not equally spaced, instead the length of each section follows the wing sectioning illustrated in Fig.4.3. The chord of each box and height of the spars decreases almost linearly from the root to the tip of the wing, as shown in Fig.4.5(a) and (b),

respectively.

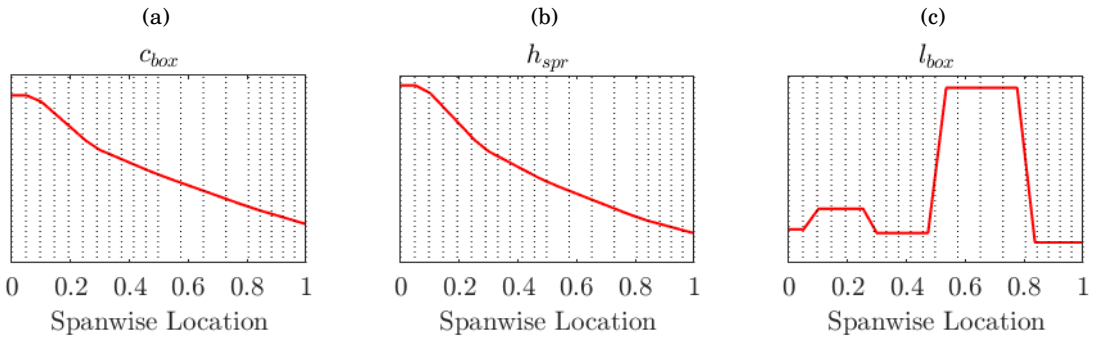

FIGURE 4.5. Wing-box geometric properties' spanwise distribution. (a) Box chord, c_{box}; (b) Box (or spar) height, h_{spr}; (c) Box length, l_{box}.

4.1.1.1 Ribs

Although the wing-box sizing is restricted to the skins, spars and stringers, the ribs' weight is considered for the calculation of the aerodynamic loads. The rib pitch is RP= 0.65 m, resulting in 46 ribs. A RP of 0.65m is chosen for similarity with equivalent deployed aircraft models. The ribs are created by diving the wing span in the number of ribs and spacing these out throughout it, iterating through the kinks. The wing-box sectional area is calculated for each rib, according to its location in the span, and the density is constant throughout. The weight of the ribs is then calculated by multiplying rib density, sectional area and thickness of the rib. The ribs' thickness was adapted from a rib thickness spanwise profile plot, from a similar aircraft model. The spanwise distribution of the ribs' weight, (consecutive lumped masses), is represented in Fig.4.6. The size of each circle corresponds to the thickness of the rib.

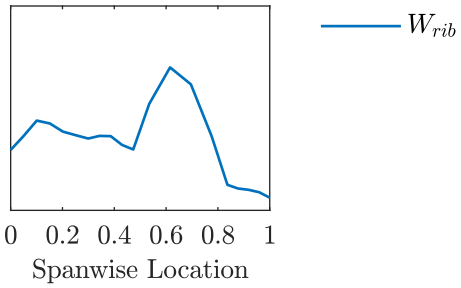

FIGURE 4.6. Ribs weight W_{rib}. W_{rib} varies throughout the span of the wing (x-axis). This is related to the wings structural components and localised necessary rib thickness. The ribs thickness profile was adapted from a similar aircraft model.

4.1.1.2 Material properties

The wing is metallic and the aluminium used for the calculations has its properties listed in Tab.4.1.

TABLE 4.1. Aluminium 6061-T6/651 material properties.

Aluminum	Young's modulus, E	Density, ρ	Poisson's ratio, ν	Tensile strength, σ_{allow}
6061-T6/651	68.9 GPa	$2.90 g/cm^3$	0.33	0.276 GPa

4.1.2 Planform geometry and baseline aircraft model, including engine, landing gear, fuselage and fixed aircraft weights

The baseline aircraft model used in this work is the XRF-1: an industrial standard multidisciplinary research test case, representing a typical configuration for a long range wide body aircraft, shown in Fig.4.7. XRF-1 helps bridge the gap between academia and industry and engage research, development and demonstration of capabilities and technologies, relevant to both. Such as the implementation of a MDO process for vehicle system integration [130], automated sizing of a composite wing [131] or a gradient-free optimisation algorithm for minimum fuel burn [1].

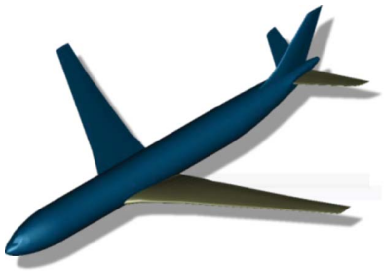

FIGURE 4.7. XRF-1 model configuration, from Gortz et al. [1].

The planform geometry parameters needed to fully define the model for the sizing routine are listed in Tab.4.2, where the values for the XRF-1 are also specified. The quarter chord sweep ($\Lambda_{c/4}$) is the the angle between the wing quarter chord line and the aircraft centreline. The dihedral angle (Γ) is the upward angle from horizontal of the wings. The taper ratio (λ) is the ratio of the root and tip chord lengths of the wing. The thickness-to-chord ratio (t/c) is the ratio between the maximum vertical thickness (t) of a wing and its chord (c). The dihedral angle, taper and thickness-to-chord ratios are given in root-to-tip wing sections, see Fig.4.3 for the different coloured wing sections. The half wing span b_{st} is 29m, the wing chord length c_{st} is 11.2m and the wing surface area S_{st} is 362m^2. The front spar is located at $0.14c_{\text{st}}$ and the rear spar at $0.64c_{\text{st}}$.

TABLE 4.2. XRF-1 wing-box model parameters.

Quarter chord sweep angle	$\Lambda_{c/4}$	29.73 deg
Dihedral	Γ	[0;4.77;4.58;4.58;4.58] deg
Taper ratio	λ	[1;0.69;0.77;0.62;0.68]
Thickness-to-chord ratio	t/c	[0.153;0.153;0.143;0.132;0.116;0.108]
Half wing span	b_{st}	29 m
Mean aerodynamic chord	c_{st}	11.2 m
Wing surface area	S_{st}	362 m^2
Front spar	f_{spr}	0.14
Rear spar	a_{spr}	0.64

4.1.2.1 Aircraft design weights

The aircraft design weights used in the sizing are listed in Tab.4.3 including MTOW, payload and fuel weight. MTOW is kept constant, excepting the wing weight. The payload, fuel weight and an initial assumption of wing weight are subtracted from the MTOW, generating the constant weight used for aircraft trim. The initial assumption for wing weight was obtained for a maximum load case design, no uncertainty simulation. It was iteratively corrected, until the initial wing weight subtracted from MTOW matched the wing weight obtained from in the sizing. The initial assumption for MTOW is used for the calculation of the secondary structure weight. The aircraft is sized for half full tank of fuel and full payload. The fuel weight is distributed along the span of the wing, in the form of lumped masses, according to the internal volume ratio of each wing-box, in order to be accounted for when calculating the aircraft loads.

TABLE 4.3. General aircraft weight assumptions.

MTOW	245000kg
Payload	65000kg
Fuel Weight	60500kg

4.1.2.2 Fuselage

The fuselage is treated as a rigid body with translational and rotational inertial properties, defined by its length and diameter:

TABLE 4.4. Fuselage simplified geometry parameters.

Fuselage length	l_{fus}	65 m
Fuselage diameter	d_{fus}	6 m

4.1.2.3 Engine, pylon & pylon attachment

The engine is modelled onto the wing as a 3 section cylindrical geometry of length 5.8m, The first section has a constant radius of 1.5m and the two remaining sections' radius decreases linearly from 1.5m to 1.35m and 1.35m to 1.2m, respectively. It's located at 9.3m spanwise from the root of the wing and weighs 8694.9kg.

The pylon attachment weight is treated as a lumped mass with a 6×6 mass matrix and associated beam structural node, which, in this case, is the node closest to its position $[x, y, z]_{pya}$ in the wing. This weight is accounted for in the linear trim for the aerodynamic loads. The lumped masses for both the engine and pylon and pylon attachment, are shown in Fig.4.8 for the case of 20 wing-box sections and 21 structural beam nodes.

TABLE 4.5. Engine and pylon weights and geometry parameters.

Engine weight	W_{eng}	8695 kg
Pylon weight	W_{pyl}	1689 kg
Engine and pylon location	$[x, y, z]_{\text{eng+pyl}}$	[28.3;9.3;−1.7] m
Pylon attachment weight	W_{pya}	420 kg
Pylon attachment location	$[x, y, z]_{\text{pya}}$	[25.3;9.3;−1.4] m

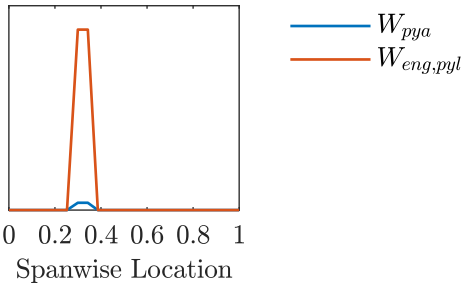

FIGURE 4.8. Engine & pylon weight and pylon wing attachment weight, respectively $W_{\text{eng,pyl}}$ and W_{pya}. Over the wing span (x-axis), $W_{\text{eng,pyl}}$ and W_{pya} masses are located between 20 and 40% of the span.

4.1.2.4 Landing Gear (LG) & LG attachments

The LG and its attachments' weights are differentiated from the aircraft mass that is kept constant, for the purpose of including these weights in the aerodynamic loads calculation. The total weight of the LG and its attachments, for half aircraft (one wing), are listed in Tab.4.6. From these, an assumption is made that 50% of the weight is supported by the fuselage and the other 50% is supported by the wing. Next, in order to allocate the lumped masses into the wing structural beam nodes, two separate parts are distinguished: 80% of the mass is distributed evenly across the initial 14% nodes, and the other 20% is distributed evenly across the 20% of the

wing nodes after the initial 14%. The resulting nodal distribution of the LG and LG attachment weights, spanwise, is shown in Fig.4.9.

TABLE 4.6. Landing gear weights.

LG weight	W_{lg}	$4500kg$
LG attachment weight	W_{lga}	$2150kg$

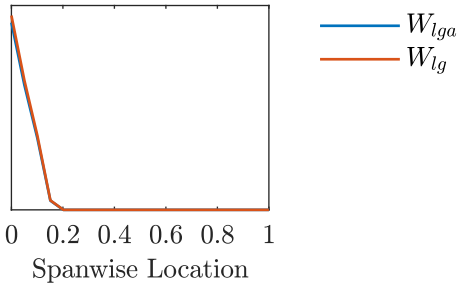

FIGURE 4.9. Landing Gear weight and LG attachment weight, respectively W_{lg} and W_{lga}. Over the wing span (x-axis), W_{lg} and W_{lga} masses are located at the root of the wing.

4.1.3 Secondary structure

The secondary structure corresponds to the wing components located in front of the front spar f_{spr} and behind the rear spar a_{spr}. These components are generally categorised as fixed and movable (high lift or flight control) leading and trailing edge devices and, depending on their complexity, typically amount up to 35% of the overall weight of the wing. The secondary weight cannot be sized in the same manner as the primary structure for the fact that there are different design loads and requirements driving the complexity of simulating the design solution and reflecting the correct weight drivers. For this reason, most published methods are based on statistical evidence, basic geometric assumptions and functional parameters as input. Although the parameters are physics-based, the physical sensitivities are not necessarily explicitly or even correctly represented by the formulations.

The secondary weight structures are grouped as Fixed Leading Edge (FLE) sec.4.1.3.1, Movable Leading Edge (MLE) sec.4.1.3.2, Fixed Trailing Edge (FTE) sec.4.1.3.3 and Movable Trailing Edge (MTE) sec.4.1.3.4 devices and miscellaneous items (misc) sec.4.1.3.5. The equations used to model the secondary devices weight are empirically obtained, from physics and statistics based equations, derived from aluminium alloy civil aircraft structures, from Torenbeek [132]. A reference aircraft is used for its statistical baseline and the reference values used are:

The reference specific weight $\Omega_{\text{ref}} = 56Nm^{-2}$ is defined as the hypothetical weight of a thin section constructed from two aluminium alloy skins with $1mm$ thickness each [132]. The

TABLE 4.7. Reference aircraft parameters.

Specific weight	Ω_{ref}	$56Nm^{-2}$
Surface area for normalisation	S_{ref}	$10m^2$
Dynamic pressure	q_{ref}	30^3Pa
MTOW	W_{ref}	10^6kg
Wing span	b_{ref}	$50m$
Wingtip length	l_{ref}	$5m$

secondary structures are then assumed to be lifting surfaces with a comparable geometry to the same $1mm$ section and so are their weights. The specific weight Ω is defined as the weight of the structure divided by its surface area in plan view, normalised by the reference surface area $S_{ref} = 10m^2$.

4.1.3.1 Fixed Leading Edge (FLE)

The FLE refers to the structural elements located in front of the front spar, f_{spr}, or, in the case of the wing-box geometry, in front of the box, excluding all parts that are movable. Typically, the FLE amounts to 4% to 7% of the total weight of the wing and it is designed to carry the aerodynamic surface pressure and fill the gap between the wing-box and the movable parts. It has a range of differing design and hence weight drivers such as access requirements, cost, maintenance and bird strike. The equations used to calculate the weight of the FLE are:

$$\Omega_{\text{fle}} = 3.15 \cdot k_{\text{fle}} \cdot \Omega_{\text{ref}} \left(\frac{q_{\text{D}}}{q_{\text{ref}}}\right)^{0.25} \left(\frac{\text{MTOW} \cdot b_{\text{st}}}{W_{\text{ref}} \cdot b_{\text{ref}}}\right)^{0.145} \tag{4.1}$$

$$l_{\text{fle}} = \frac{b_{\text{st}}}{cos(\Lambda_{c/4})} \tag{4.2}$$

$$d_{\text{fle}} = c_{\text{st}} \cdot f_{\text{spr}} \tag{4.3}$$

$$W_{\text{fle}} = \Omega_{\text{fle}} \times (l_{\text{fle}} \cdot d_{\text{fle}}) \tag{4.4}$$

The FLE specific weight, Ω_{fle}, is obtained by Eq.4.1, where $k_{\text{fle}} = 1.3$ is a factor that accounts for the strengthening necessary to support slats, and q_{D} is the dynamic pressure. Some assumptions are made about the in-plan view geometry of the FLE, where its length, l_{fle}, and depth, d_{fle}, are given respectively by Eq.4.2 and Eq.4.3. All the rest of the function parameters can be extracted from Tab.4.2 and Tab.4.7. The weight of the FLE structure W_{fle} is then obtained via Eq.4.4, that multiplies its in plan surface area by its specific weight. In wing-box sizing, if all other aircraft planform geometry parameters fixed, the FLE is highly dependable on the position of the front spar, f_{spr}.

4.1.3.2 Movable Leading Edge (MLE)

The MLE accounts for LE high-lift devices such as slats, weighing typically up to 5% of the total weight of the wing. The slats weight equation described below includes its panel structure,

supports and tracks, but excludes slat actuation.

$$l_{\text{sla}} = \frac{k_{l_{\text{sla}}} \cdot b_{\text{st}}}{cos(\Lambda_{c/4})} \tag{4.5}$$

$$d_{\text{sla}} = c_{\text{st}} \cdot k_{d_{\text{sla}}} \tag{4.6}$$

$$\Omega_{\text{sla}} = 4.83 \cdot \Omega_{\text{ref}} \left(\frac{l_{\text{sla}} \cdot d_{\text{sla}}}{S_{\text{ref}}} \right)^{0.183} \tag{4.7}$$

$$W_{\text{mle}} = \Omega_{\text{sla}} \times (l_{\text{mle}} \cdot d_{\text{mle}}) \tag{4.8}$$

The specific weight of the slats, Ω_{sla}, refers to the plan view area when the slats are retracted. For that reason, the geometric parameters used to describe the slats area l_{sla} and l_{sla}, takes this into account and uses factors $k_{l_{\text{sla}}}$ and $k_{d_{\text{sla}}}$ to portion the FLE area. Chordwise, slats usually occupy 15% to 20% of the clean wing (retracted state) planform, i.e. $k_{d_{\text{sla}}} \approx [0.15; 0.20]$, and not over the full wing span, i.e. $k_{l_{\text{sla}}} \approx [0.80; 0.95]$.

4.1.3.3 Fixed Trailing Edge (FTE)

The FTE refers to the structural elements behind the rear spar, a_{spr}, or, in the case of the wing-box geometry, after the box, excluding all movable devices such as trailing edge flaps and controls, spoilers and lift dumpers. Typically, the FTE amounts to up to 8% of the total weight of the wing and it consists of ribs supporting control surface hinges, intermediate supports for flaps and potentially part of the undercarriage support structure, skin panels and auxiliary beams.The equations used to calculate the weight of the FTE, considering it is supporting single-slotted flaps, ailerons and spoilers, are:

$$\Omega_{\text{fte}} = 2.6 \cdot \Omega_{\text{ref}} \left(\frac{\text{MTOW} \cdot b_{\text{st}}}{W_{\text{ref}} \cdot b_{\text{ref}}} \right)^{0.0544} \tag{4.9}$$

$$l_{\text{fte}} = \frac{(b_{\text{st}} - c_{\text{st}} \cdot sin(\Lambda_{c/4}))}{cos(\Lambda_{c/4})} \tag{4.10}$$

$$d_{\text{fte}} = c_{\text{st}} \cdot (1 - a_{\text{spr}}) \tag{4.11}$$

$$W_{\text{fte}} = \Omega_{\text{fte}} \times (l_{\text{fte}} \cdot d_{\text{fte}}) \tag{4.12}$$

The FTE in planview length, l_{fte}, and depth, d_{fte}, are calculated with Eq.4.10 and Eq.4.11. All the rest of the function parameters can be extracted from Tab.4.2 and Tab.4.7. The weight of the FTE structure W_{fte} is then obtained via Eq.4.12, that multiplies its in planform surface area by its specific weight, Ω_{fte}, from Eq.4.9. Similarly to the FLE, if all other aircraft planform geometry parameters fixed, the FTE is highly dependable on the position of the rear spar, a_{spr}.

4.1.3.4 Movable Trailing Edge (MTE)

The MTE devices include TE flaps and flight control devices such as ailerons and spoilers:

$$[S_{\text{fla}};\ S_{\text{ail}};\ S_{\text{spo}}] = S_{\text{st}} \cdot [k_{S_{\text{fla}}};\ k_{S_{\text{ail}}};\ k_{S_{\text{spo}}}] \tag{4.13}$$

$$\Omega_{\text{fla}} = 1.7 \cdot k_{\text{sup}} \cdot k_{\text{slot}} \cdot \Omega_{\text{ref}} \cdot \left[1 + \left(\frac{\text{MTOW}}{W_{\text{ref}}}\right)^{0.35}\right] \tag{4.14}$$

$$\Omega_{\text{ail}} = 3.0 \cdot \Omega_{\text{ref}} \cdot k_{\text{bal}} \cdot \left(\frac{S_{\text{ail}}}{S_{\text{ref}}}\right)^{0.044} \tag{4.15}$$

$$\Omega_{\text{spo}} = 2.2 \cdot \Omega_{\text{ref}} \cdot \left(\frac{S_{\text{spo}}}{S_{\text{ref}}}\right)^{0.032} \tag{4.16}$$

The flaps' specific weight, Ω_{fla}, is calculated with Eq.4.14, where $k_{\text{sup}} = 1.2$ to account for link/track end supports and $k_{\text{slot}} = 1$ for single-slotted flaps. The ailerons' specific weight, Ω_{ail}, is calculated with Eq.4.15, where $k_{\text{bal}} = 1.54$; to account for mass-balanced ailerons. Lastly, the spoilers' specific weight, Ω_{spo}, is calculated with Eq.4.16.

$$[W_{\text{fla}};\ W_{\text{ail}};\ W_{\text{spo}}] = [\Omega_{\text{fla}};\ \Omega_{\text{ail}};\ \Omega_{\text{spo}}] \cdot [S_{\text{fla}};\ S_{\text{ail}};\ S_{\text{spo}}] \tag{4.17}$$

$$W_{\text{mte}} = W_{\text{fla}} + W_{\text{ail}} + W_{\text{spo}} \tag{4.18}$$

The areas of the three MTE structures are a fraction of the wing surface area S_{st}, obtained by using factors $k_{S_{\text{fla}}}$, $k_{S_{\text{ail}}}$ and $k_{S_{\text{spo}}}$ for flaps, ailerons and spoilers respectively. The weight of each one is calculated by multiplying its correspondent specific weight by its area. The weight of the MTE structure, W_{mte}, is the sum of the three weights.

4.1.3.5 Miscellaneous (Misc)

Miscellaneous items represent a wide variety of components, typically paint, fuel tank sealant, fairings, jacking fittings, rivets, nuts and bolts and wing tips. Generally, if not enough data is available to estimate these items, the miscellaneous items can be accounted for by multiplying the secondary weight by a factor of 1.1. WeiCoS considers the wingtip, paint and fairings:

$$W_{\text{wtip}} = 150 \cdot \left(\frac{\text{MTOW}}{W_{\text{ref}}}\right)^{0.67} \tag{4.19}$$

$$W_{\text{paint}} = t_{\text{paint}} \cdot \rho_{\text{paint}} \left(k_{S_{\text{paint}}} \cdot S_{\text{st}}\right) \tag{4.20}$$

$$W_{\text{fairings}} = k_{W_{\text{fairings}}} \cdot W_{\text{wing}} \tag{4.21}$$

$$W_{\text{misc}} = W_{\text{paint}} + W_{\text{fairings}} + W_{\text{wtip}} \tag{4.22}$$

Considering a traditionally tapered wing, Eq.4.19 is suggested as a statistical depiction of the wingtip weight W_{wtip}, consisting of its components, attachments and provisions for lights. Paint weight is estimated by multiplying the paint's thickness, t_{paint}, by its density, ρ_{paint}, and surface area, in Eq.4.20. Typically, for painting of airplane exterior surfaces, its thickness varies from 0.0889 to 0.1397 mm [133]. The paint density is fixed at $\rho_{\text{paint}} = 1$. The surface area is a product of

the wing's surface area S_{st} multiplied by a factor $k_{S_{\text{paint}}}$. Fairings weight typically ranges between 1% and 5% of the wing weight, depending on the configuration of the wing's wheel wells. The weight of the fairings is then estimated as the wing weight W_{wing} multiplied by a factor $k_{W_{\text{fairings}}}$. W_{wing} is here pre-obtained iteratively, using the maximum load factor sizing case and keeping all the rest of the uncertain input parameters at its nominal value, and fixed. The weight of the miscellaneous items W_{misc} is given by the sum of the three miscellaneous weights described.

* * *

The initial assumption for MTOW is used to estimate the weight of the secondary structure. When wing weight is varying, the final MTOW is likely to change. However, this change in MTOW is not considered to recalculate the secondary structure weight. Any change in MTOW is typically handled by adjusting payload and fuel weights and, therefore, not updating the MTOW when the wing weight is varying is justified. The total secondary weight is distributed across the wing span, according to the ratio of internal volume of each wing-box and the total internal volume of the wing.

4.1.4 Sizing optimisation

An initial condition for the thickness of the skins and spars, as well as the area of the stringers is set, respectively t_{skn_0}, t_{spr_0} and A_{stg_0}, and the initial weight of the wing, W_{Wing_0}, is calculated. This initial wing-box geometry allows for a reduction of the box to a beam formulation, assigning mass and stiffness matrices to each beam element. The ultimate load case and the beam formulation are used in a linear trim analysis and the resulting aircraft loads are enveloped for the sizing optimisation routine.

The aerodynamic loads are then used in the sizing optimisation. The optimisation looks for thickness of skins, spars and stringers (t_{skn}, t_{spr} and A_{stg}), such that the aerodynamic loads are sustained, the stress constraints are satisfied, and the wing weight is minimum. For more details on the sizing optimisation, please refer to Sec.A.

Sequential quadratic programming (SQP) is the method chosen for the optimisation, an iterative method used for constrained nonlinear optimisation problems (NLP). The optimisation problem is defined by its objective function $f(x)$, equalities $c(x)$ and inequalities $b(x)$, as well as the suitable lower (x_l) and upper(x_u) bounds of the design variables, such that

$$\begin{aligned} &\min_x f(x), \quad x \in \mathbb{R} \\ &c(x) = 0 \\ &b(x) \geq 0 \\ &x_l \leq x \leq x_u \end{aligned} \tag{4.23}$$

SQP works by sequentially solving quadratic programming (QP) sub-problems. The NLP is modelled for a given iterate x^k, $k \in \mathbb{N}_0$, for which it is solved. That solution is then used to

construct a new iterate x^{k+1}. The sequence of sub-problems is done in such a way that it converges to a local minimum x^* as $k \to \infty$.

The objective for the sizing optimisation is minimum total wing weight:

$$\min \quad \left(W_{\text{Wing}} = \sum_i \left(\left(\rho_{\text{skn}} * A_{\text{spr}_i} + \rho_{\text{spr}} * A_{\text{skn}_i} + \rho_{\text{stg}} * A_{\text{stg}_i} \right) l_{\text{box}_i} \right) \right) \tag{4.24}$$

where i corresponds the i-th wing-box section and A corresponds to the area of the skins, spars and stringers:

$$A_{\text{skn}} = 2(t_{\text{skn}} c_{\text{box}}) \tag{4.25}$$

$$A_{\text{spr}} = 2\left(t_{\text{spr}} \left(h_{\text{spr}} - 2t_{\text{skn}}\right)\right) \tag{4.26}$$

$$A_{\text{stg}} = 25 {t_{\text{stg}}}^2 \tag{4.27}$$

The design variables being optimised are t_{skn}, t_{spr} and t_{stg}. There is no upper bound (x_u) to the variables but there is a lower bound (x_l), i.e. minimum thickness, applied as described in Eq.4.28. There are no equalities in this optimisation, and the inequalities $b(x) \geq 0$ correspond to the stress constraints described in Eqs.4.29-4.37. The fixed parameters are c_{box}, l_{box} and h_{spr}, defined for each wing-box as shown in Fig.4.5.

The loop of retrieving the enveloped loads, calculating the stress in each wing box section and estimating new section geometries for the skins, spars and stringers is illustrated in Fig.4.10. The loop, and overall sizing routine, runs until W_{Wing} and W_{Wing_0} converge and the final configuration for the wing-box sections is obtained.

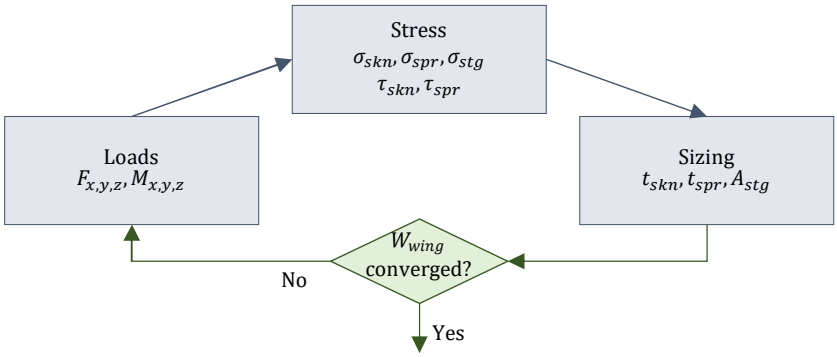

FIGURE 4.10. WeiCoS' sizing optimisation loop: loads, stress and sizing for minimum wing weight.

4.1.4.1 Stress analysis

The stress formulae used for each wing-box section in Fig.4.4, in the sizing optimisation routine, is here summarised. The full description of the stress analysis formulae is presented in Appendix A

and in Calderon et al. [129]. The assumption is made that the top and bottom skins are equivalent in thickness, as well as the front and rear spar.

The stress constraints imposed in the sizing optimisation routine include material strength constraints, buckling and skin-stringer flexural instability, as well as the minimum values for thickness of the skins, spars and stringers, imposed at the start of the optimisation.

The minimum values for skin spar and stringers thickness are represented by

$$[t_{\text{skn}}; t_{\text{spr}}; A_{\text{stg}}] \geq [t_{\text{skn}_{\text{min}}}; t_{\text{spr}_{\text{min}}}; A_{\text{stg}_{\text{min}}}] \tag{4.28}$$

where the stringer thickness is describable by its area by $A_{\text{stg}} = 25 {t_{\text{stg}}}^2$.

The bending stresses of the skins, spars and stringers, and the shear stresses of the skins and spars constrain the wing-box sizing as follows:

$$\frac{[\sigma_{\text{skn}}; \sigma_{\text{spr}}; \sigma_{\text{stg}}]}{\sigma_{\text{allow}}} \leq 1 \tag{4.29}$$

$$\frac{[\tau_{\text{skn}}; \tau_{\text{spr}}]}{\tau_{\text{allow}}} \leq 1 \tag{4.30}$$

Using the Von Mises Yield Criterion, the bending and shear stresses above are combined for the skins and spars material strength, resulting in the second set of constraints for the optimisation

$$\frac{\sigma^{v}_{\text{skn}}}{\sigma_{\text{allow}}} \leq 1 \tag{4.31}$$

$$\frac{\sigma^{v}_{\text{spr}}}{\sigma_{\text{allow}}} \leq 1 \tag{4.32}$$

The next set of constraints used are buckling constraints, including skin buckling from the principal stress formulation

$$\sigma_P = 1 - \frac{2}{\frac{\sigma_{\text{skn}_{\text{b}}}}{\sigma_{\text{skn}_{\text{cri}}}} + \sqrt{\frac{\sigma^2_{\text{skn}_{\text{b}}}}{\sigma_{\text{skn}_{\text{cri}}}} + 4\frac{\tau^2_{\text{skn}_{\text{b}}}}{\tau_{\text{skn}_{\text{cri}}}}}} \leq 1 \tag{4.33}$$

stringer local buckling

$$\frac{\sigma_{\text{stg}}}{\sigma_{\text{cc}}} \leq 1 \tag{4.34}$$

and column buckling of the skin-stringer panel

$$\frac{\sigma_{\text{stg}}}{\sigma_{\text{col}}} \leq 1 \tag{4.35}$$

The Farrar's efficiency factor, accounting for a pure flexural instability of the skin-stringer panel yields the constraint

$$N = \frac{1}{2} \cdot \frac{F_z}{\text{NS} \cdot d} \tag{4.36}$$

$$F = 0.95 \cdot \sqrt{\frac{N \cdot E}{\text{RP}}} \cdot \sigma_{\text{allow}} \leq 1 \tag{4.37}$$

4.1.4.2 Load cases for sizing

The load case parameters for the aircraft sizing include the flight conditions: Mach number M, altitude h, the fuel fraction f and the load factor n. The fuel fraction corresponds to the fraction of fuel weight necessary for a respective mission in analysis and therefore loaded onto the wings and consumed. Both the flight conditions and the load factor are varied using a uniform distribution to achieve the critical load case, which translates to the maximum value for each parameter, in Load Case 1.

TABLE 4.8. Load cases used for sizing and cruise condition.

Load Case	Mach Number, M	Altitude (FL), h	Load Factor (g), n	Fuel Fraction, f
1	0.87	470	2.5	1.00
Cruise	0.83	430	1.0	0.50

Industrially, the load analysis for sizing is an exhaustive and extremely computationally expensive process where hundreds of thousands of load cases are tested for a variety of scenarios. In this work, load case "cruise" is used to trim the aircraft whereas load case "1" stands for the maximum load case scenario. The load cases used for the sizing in this work are obtained probabilistically to mimic the cumbersome industrial process. Each load case parameter is defined as a probability distribution, bounded by its maximum loading case "1". Latin Hypercube Sampling is used to propagate the uncertainty through the model, towards the sizing and weight results.

4.2 Uncertainty modelling and propagation

Uncertainty is included in the framework as illustrated in Fig.4.11. In the previous section sec.4.1, a description of the aircraft sizer is presented, including its different modules and inputs. This was the starting point to define the input parameters that were going to be made uncertain, considering the analysis intended. All the parameters in purple in the previous section are the input parameters to the model. These include the load case parameters, the material's stress allowable $\sigma_{\max}$, several secondary structure parameters, including the location of the front and rear spar and the punctual weights (lumped masses) of the engine and pylon.

Conditional on the analysis at hand, the uncertain input parameters are set aside and defined either as a uniform or a Gaussian distribution. A correlation matrix is defined for the input space that allows the sampling to be done in a particular dependent manner. That is, if design variables are dependent on one another this is captured by using a linear correlation matrix copula in the computation of the joint probability distribution, see sec.4.2.2. The number of samples n is chosen and a LHS sampling method is performed. For each sample of inputs X_n, the aircraft is sized and the outputs of interest are retrieved Z_n. After running n times, the output distributions $\mathbb{Z}$ can

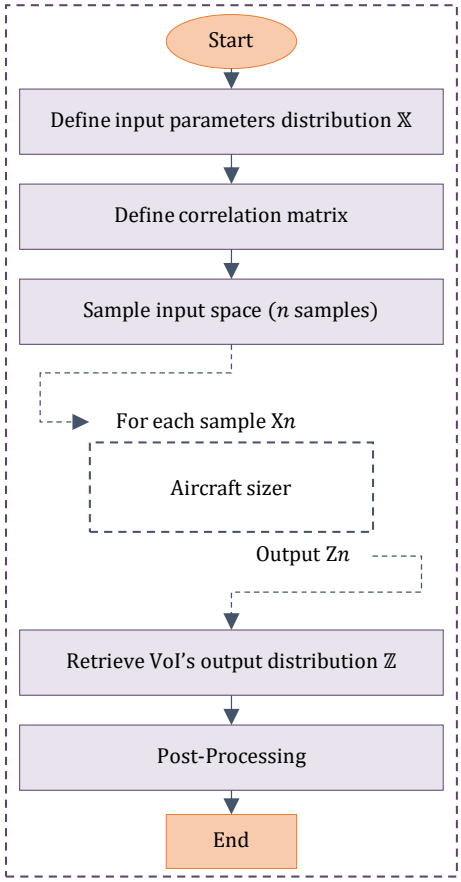

FIGURE 4.11. WeiCoS' uncertainty modelling and propagation flow diagram.

be defined and its $QoIs$ obtained. Post processing looks at performing percentile and visual UQ, sensitivity studies, and backward uncertainty propagation.

4.2.1 Input parameters distribution $\mathbb{X}$

The framework allows the user to define the input parameters distributions as a variety of different distributions, e.g. uniform, Gaussian, Lognormal, Gumbel, Exponential, Beta, Gamma, Triangular, Weibull, among others. For the purpose of this work, only two distributions were used: the uniform and the Gaussian distribution. These are fully described in sec.1.2.1.4. The uniform distribution is used for the case where there are two values the variable can vary between, and the goal of the analysis is to study what are the effects of each one of those values. It is almost taking a possibilistic interval approach to a probabilistic framework. The Gaussian distribution is used if the uncertainty is aleatory around a predicted nominal value. When this is the case a Confidence Level (CL) for the variable in question, x, is considered. The Gaussian distribution parameters are defined as follows:

$$\mu = \text{nominal value} = x \tag{4.38}$$

$$\sigma = \frac{(1 - CL) \cdot x}{2} \tag{4.39}$$

It is assumed that the uncertainty shows a dispersion of 2σ, which means that it is within the $\pm 2\sigma$ interval around the nominal value, with a probability of $95,45\%$, from Fig.1.13.

$$u = 2\sigma \tag{4.40}$$

$$P = 95.45\% \tag{4.41}$$

4.2.2 Correlation matrices

The multivariate input joint PDF is obtained with the copula formalism, as described in sec.1.2.1. For the case of independent variables, an independent copula is used. For the case of dependencies, the Gaussian copula is used when a dependency or correlation between variables needs to be maintained.

One of the uncertainty forward propagation analysis present in this document in sec.5.1.2, introduces uncertainty around the nominal value for the loads envelopes, fed directly to the sizing routine described in sec.4.1.4. After the critical loading case and correspondent critical loads envelopes are obtained, these critical values are varied around its mean by the means of a Gaussian distribution. Since the wing-box model is computed in discrete spanwise sections, the loads, stresses and sizing parameters are, likewise, treated discretely (per section). It was then necessary that, when the critical load case is treated as uncertain, the spanwise correlations remain. In this way, the correct wing loading is obtained. This is illustrated in Fig.4.12 where the vertical shear force in Fig.4.12(a), the bending moment in Fig.4.12(b) and the torque in Fig.4.12(c) envelopes are compared for the three different cases of sampling the enveloped loads as independent, linear or rank correlated.

The first plot for each aircraft load corresponds to the case where, when sampling the loads from the Gaussian distribution, an independent copula was used. The second and third plots correspond to using linear and rank correlation Gaussian copulas, respectively. The colours of the lines in all plots are randomly assigned, but each colour corresponds to one sample and therefore one run of the sizing optimisation loop. The independent case assumes that the loads are not correlated spanwise or between each other and the resulting wing loading envelope obtained presents peaks and does not correspond to any real loading scenario. Using a linear and rank correlations, on the other hand, allows for the spanwise load distribution to maintain the shape of what a single output (for a single load case scenario) would be. That is, the spanwise interdependencies between wing sections are maintained when sampling using one of these copulas. The rank correlation measures the monotonic dependence between the different variables being sampled. Because it is not necessarily true that the correlations between different aerodynamic loads are monotonic, the linear case was chosen. The linear and rank correlation

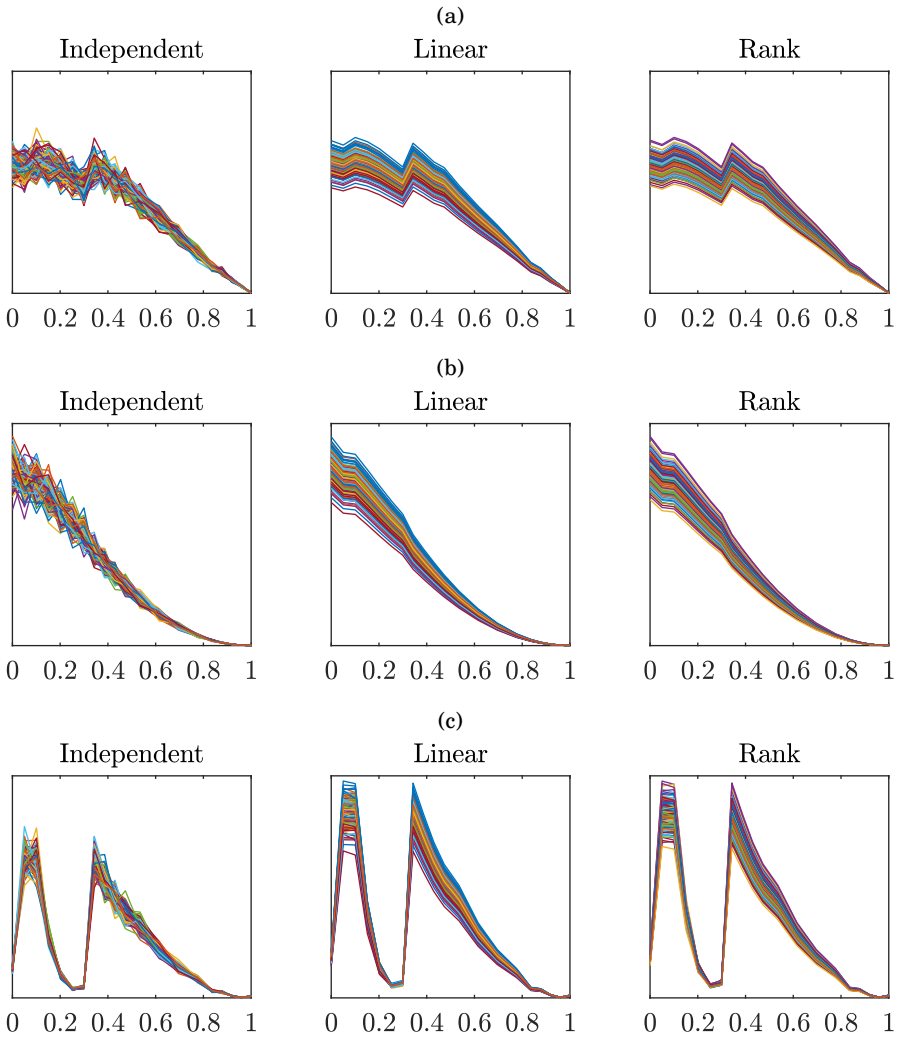

FIGURE 4.12. Internal aerodynamic loads envelopes: (a) Shear force; (b) Bending moment; (c) Torque. The input variable that defines a load envelope is, in reality, a multivariate input, one value per wing-box section. In order to sample the multivariate, so that the loads maintain its envelope shape, the correlations between spanwise load values need to be defined using the copula formalism. The first column shows sampling using an independent copula (no correlation); the second column uses a linear correlation matrix (PCC); and the third column shows samples using a rank correlation matrix (SRCC).

matrices are obtained by varying the load case parameters uniformly and extracting the loads envelopes correlations. These plots are illustrative of the influence of the correlation between inputs. The correlation matrices used in the analysis were built using 10000 load samples.

4.2.3 Sampling and post processing

A user defined number of samples is taken from the joint distribution using Latin Hypercube Sampling. LHS spreads the sample points evenly across all possible values and is more efficient than MC sampling in a large range of conditions, see sec.1.2.1.7. The sizing routine runs in a loop, one sample at a time, producing in the end a multivariate random output vector that is later processed for extracting patterns and trends, computing the input to output curve fit, and general statistical measures on all variables of interest.

Most academic research, on aircraft robust design optimisation RBO or reliability-based design optimisation RBDO, is processed using a surrogate model, usually PCE, to emulate the model and obtain results in a computationally cheaper manner, see sec.1.3. Because the goal with this work was to study the computations within the sizing and conclude on how uncertainty is propagated between different disciplines or components, throughout the whole process and for different uncertain scenarios, the decision to compute the results using LH sampling alone, with no use of a surrogate model, was made. This allows for extracting the variables of interest at different stages in the sizing process in WeiCoS, represented in Fig.4.1. Moreover, using LHS in a Monte Carlo simulation can account for nonlinearities and discontinuities in the sizing, whilst reducing variance, compared with random sampling.

Computationally, generating all the surrogate models for the different uncertain scenarios tested was comparable to running WeiCoS for each sample.

The post processing is divided in two main pieces: forward and backward propagation, respectively presented and described in 5 and 6. These include plots of the different variables of interest, such as loads, stress and sizing parameters, spanwise dispersion of uncertainty for different scenarios of input uncertainty. Sensitivity indices for each case, using standardised regression coefficients, see sec.1.2.4.1. Progressing in the weight convergence corridor translates to higher confidence level in the input parameters, narrowing uncertainty. The relationship between confidence levels and uncertainty is computed.

Backward propagation of uncertainty is done by inverting the WeiCoS simulation. Uncertainty is introduced to all input parameters in WeiCos (structural design variables) and the correspondent component, wing and final aircraft weights are obtained. The samples are then used in the reverse order to generate an artificial neural network that emulates the reverse structural sizing model. The new inputs to the reverse model are aircraft weights and the outputs are the design input parameters. By limiting the component or wing weights to a reliability level, a target weight, or both, the design parameters variability and dispersion can be obtained. Ultimately, the decisions in the design process can be made more informedly. The surrogate allows for quickly computing the probabilistic margins of each input and their combinations (the posterior input space), for different reliability levels. Parallel-coordinate plots are widely explored in the process.

4.3 Summary

A framework was developed to perform uncertainty quantification and sensitivity studies on weight estimation in wing design. The framework, named WeiCoS, combines a traditional wing-box, linear static, aeroelastic sizing routine for the primary structure, with empirically obtained equations, from physics and statistics based, for the secondary structure. The wing sizing is used as a representative test case, that could be added to, and scaled up, for the entire aircraft.

WeiCoS allows the user to define a variety of design variables as a probability distribution. As the aircraft design process evolves, design decisions are progressively embodied into the aircraft and uncertainty on the correspondent design variables decreases. In WeiCoS, this translates to defining the input probability distributions, specifically their standard deviation (assumed $u = 2\sigma$), accordingly. As information and design mature, confidence levels become higher and uncertainty narrows. Eventually, WeiCoS generated weights will be replaced with weights of designed parts, with ever increasing levels of maturity.

Once the input variables are defined, as well as a potential copula, a joint probability distribution is computed. Using LHS, n data points are collected from the latter distribution and MCS is run on the wing sizing. The wing-box geometries being sized are skins, stringers and spars. And the secondary structure accounts for fixed and movable, leading and trailing edge, sections and miscellaneous items. External weights are added to the wing beam formulation as lumped masses, including fuselage, pylon and engines, payload and landing gear.

WeiCoS is built as a way of simulating the weight data that could not be obtained historically for uncertainty studies. The framework represents the physics based model behind the weight estimation of an aircraft, taking into account the structural sizing and aeroelastic effects. It is a crude and simplistic representation of the sizing of an aircraft and the physics behind its design. The objective of this work, however, is to demonstrate how uncertainty can be integrated into the weight management process and deliver valuable information for it. WeiCoS is here a baseline to showcase the capability to draw dependencies between components and disciplines from UQ, to propagate uncertainty through to component weight versus total weight result, what is driving the uncertainty and what it is most sensitive to.

In the following section, uncertainty will be propagated forward through the model, including: uncertainty at each step of the sizing routine; uncertainty on aerodynamic loads; uncertainty in the stress constraints applied in the sizing; uncertainty in the material properties of the wing-box; uncertainty on an external mass, such as the engine; and uncertainty on the secondary weight and its effect on the primary weight.

CHAPTER 5

WING WEIGHT UNCERTAINTY BREAKDOWN

In this chapter, a full analysis on the uncertainty and variability of the weight convergence corridor is presented. WeiCoS is the framework used for the analysis and, therefore, the results presented here are an outcome of its modules and formulae. The sizing of the aircraft is restricted to the wing and the wing elements are divided into three main sections, governing the subsequent chapter sections: the primary weight in sec.5.1, the secondary weight in sec.5.2 and the wing attachments.

The primary weight makes for 64% of the weight of the entire wing. Primary structure consists of covers (skins and stringers), spars and ribs, i.e. with the exception of the ribs that are a fixed value, the primary structure consists of the elements being sized in the wing-box sizing routine. The covers are about 44% of the weight of the wing, the spars are about 12% and the ribs 9%, as listed below. An additional module could be integrated to the sizing to replace the fixed ribs with an empirical sizing model.

TABLE 5.1. Wing's primary weight breakdown.

Covers	Skins	44.01%	33.83%
	Stringers		10.17%
Spars		12.01%	
Ribs		8.50%	
Primary weight total		64.52%	

These values are validated against the results in [131] where the same aircraft baseline model is used and the wing mass components are discretised: 68% of the wing weight is attributed to the skins and stringers, in comparison to 64% in [131]; 19% of the weight attributed to the front

and rear spars, whereas 21% corresponds to the front, middle and rear spars weight in [131]; As for the ribs, 13% of the wing weight is attributed to the ribs, in comparison to 15% in [131], see Fig.5.1

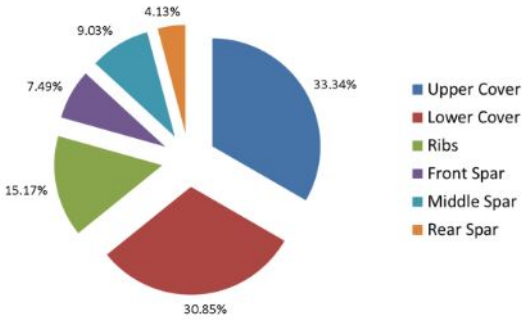

FIGURE 5.1. Share of wing-box assemblies on total wing-box mass (%), from [131]

The secondary weight consists of the leading and trailing edges, LE and TE respectively, fixed and movable parts, and miscellaneous items. The LE makes up around 11% of the weight of the wing, the TE is 16% and the miscellaneous items are slightly more than 1%. The detailed percentile weight breakdown is listed below. The total secondary weight of the wing model in use and according to WeiCoS is 28%.

TABLE 5.2. Wing's secondary weight breakdown.

Leading Edge	fixed	10.84%	2.82%
	movables		8.02%
Trailing Edge	fixed	16.17%	7.36%
	movables		8.81%
Miscellaneous		1.18%	
Secondary weight total		28.19%	

The secondary weight breakdown is validated against the values presented in [132], where the total secondary weight is believed to contribute up to 35% to the wing weight (28% in WeiCoS), the leading edge to weigh between 9-12% of the total wing (11% in WeiCos), the trailing edge to weigh around 20% (16% in WeicoS) and the rest 3-6% to be attributed to the miscellaneous items (1% in WeiCoS).

Lastly and for the calculation of the internal loads, the attachments to the wing are also considered as integral part of the wing weight. These are the pylon (Fig.4.8) and landing gear attachments (Fig.4.9) and the values for their weights is fixed throughout the sizing routine. As listed below, the landing gear attachment makes for 6% of the wing weight and the pylon attachment 1%. These values were validated against historical (industrial) weight data.

TABLE 5.3. Wing's attachments weight breakdown.

Landing gear	6.10%
Pylon	1.19%
Attachments weight total	7.29%

* * *

This chapter presents the results from the analysis of the primary (sec.5.1) and secondary (sec.5.2) weights when subjected to uncertain inputs.In this model, the attachments are constant with fixed weights and will not be included in the uncertainty analysis. In reality, they would also be subject to variation.

5.1 Primary weight

Regarding primary structure, the goal was to vary the input parameters related to the sizing of the wing and identifying the propagation of variability in the weight convergence. First, the wing-box structural sizing routine is evaluated, including variability on load case parameters, internal loads, stress, sizing and finally weight of the different wing-box elements. Then, the stress analysis was considered by adding uncertainty to the stress allowable of the wing box components and assessing the uncertainty on the sizing and weight of the wing. Moreover, a study was done on the activation and deactivation of the stress constraints involved in the sizing optimisation and conclusions regarding the sensitivity of the process to each constraint were drawn. Lastly, uncertainty about the weight of the engine is examined. The engine is an element that is external to the wing but its inertial properties are used in the calculation of the internal loads, which are inputs to the wing-box sizing process.

5.1.1 Structural sizing routine

The first set of analyses done to the framework aims at investigating the impact of the external loading conditions to the internal loads and subsequent stresses, wing-box sizing parameters, including thickness of the skins, stringers and spars, and weights. For this, the load case parameters that define the different mission segments of the aircraft's total flight are varied probabilistically. All the values for the internal loads, stress, sizing and weights are normalised.

5.1.1.1 Load cases

The Mach number M, altitude h, load factor n and fuel fraction f, are the four load case parameters used in WeiCoS. A particular combination of these 4 parameters defines a particular load case, i.e. a particular segment or condition the aircraft can find itself in during its mission. The internal

loads envelopes are calculated for each load case, i.e. $|F_x|$, $|F_y|$, $|F_z|$, $|M_x|$, $|M_y|$ and $|M_z|$, and the maximum for each one is taken as critical and fed to the sizer.

Instead of varying the load cases punctually for a particular scenario, the load case parameters were varied probabilistically, in order to fully understand the sensitivities of the structural sizing routine. A uniform distribution defines each parameter between its operational lower and upper bounds, listed in Tab.5.4. A uniform distribution was introduced so that any value in between the operational bounds would have an equal probability of being sampled. This allows for any loading case scenario to be represented, mimicking the industrial process of running the thousands of different scenarios punctually. A 10000 points LHS is taken from the input distributions defined and WeiCoS runs for each sample. The loads, stresses, sizing parameters and weights are recovered for each sample. The number of samples was chosen given the nature of the study: sensitivity analysis is to be performed on the data obtained and an all at once sampling strategy is performed for global methods, particularly through the means of Standardised Regression Coefficients (SRC). To perform this analysis, $1000x$ sample points are required, x being the number of uncertain input variables [47]. In this case, the number of uncertain variables is 4 therefore > 4000 samples are required. For the purpose of a reasonable trade-off between accuracy of results and computational expense, 10000 samples are drawn.

$$\text{Load cases:} \quad X \sim \mathcal{U}(a,b), \qquad X = (M,h,n,f) \tag{5.1}$$

TABLE 5.4. Load case parameters variation.

Mach number	M	[0.5; 0.9]
Altitude	h	[0;45000]ft
Load factor	n	[-1;2.5]g
Fuel fraction	f	[0;1]

The uniform distributions are shown in Fig.5.2, diagonally from left to right. The rest of the plots are the scattered samples of the two load cases intersecting for every run of the sizing framework (one run is one dot). The samples are colour mapped, from blue to yellow, in ascendant order of total wing weight. For the plots where the load factor n is involved, the ascendant blue to yellow dots are clear. This means that there is a clear correlation between the load factor n and the total wing weight: an increasing load factor results in a higher wing weight. The same cannot be concluded for the rest of the parameters, indicating that n is the parameter contributing the most, almost single handily, for the variability of the wing weight. The critical load case, for which the wing weight is maximum, was found to correspond, for this particular sample size, to the maximum load factor and altitude, but not necessarily Mach number or fuel fraction. Due to the fact that a linear static sizing routine is in use, the maximum output corresponds to a combination of the maximum inputs, should the sample size be infinite. The fact that M and f are

not the clear maximum for the sample size used, is an indication of them having lower sensitivity indices than the load factor and altitude.

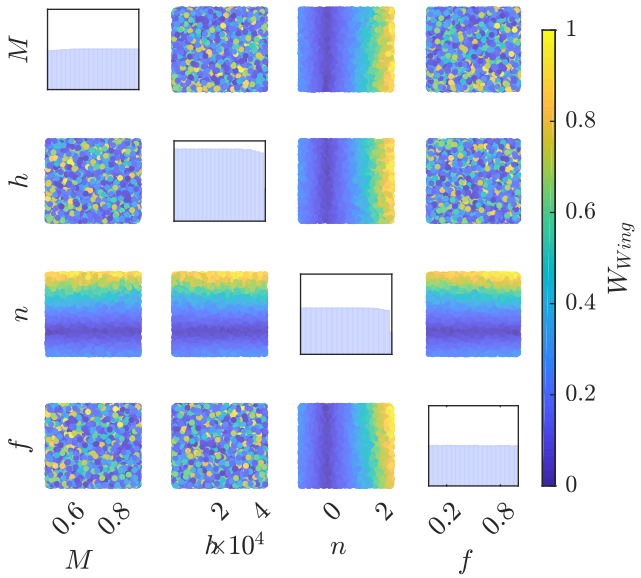

FIGURE 5.2. Load case input parameters distributions, from Tab.5.4

It is important to also mention that the aircraft did not trim for some of the sample points and a linear correlation matrix was used as a Gaussian copula, with the values

$$\mathrm{CI}(M,h,n,f) = \begin{bmatrix} 1 & 0.11 & 0.10 & 0.02 \\ 0.11 & 1 & -0.21 & -0.01 \\ 0.10 & -0.21 & 1 & -0.04 \\ 0.02 & -0.01 & -0.04 & 1 \end{bmatrix} \tag{5.2}$$

The correlation matrix imposes a relationship between M, h and n, so that: for high altitude and load factors, M cannot be low, i.e. the aircraft's speed needs to be above a certain threshold. This correlation matrix adds some constraints to the load case parameters so that the unrealistic conditions causing the failure to trim the aircraft are avoided. This is illustrated in Fig.5.3, where the normalised load case parameters and total wing weight are plotted in a parallel-coordinate plot. Each line represents one sample or one run, and the lines in grey are trim cases and the lines in red are load cases for which the aircraft did not trim.

5.1.1.2 Internal loads

The internal loads resulting from the input probability distribution imposed to the load case parameters are shown in Fig.5.4 and their envelope, or the absolute load, in Fig.5.5. Again, the samples are colour mapped and it can be seen that the dark blue correspondent to $n = 0$ will, as expected result in the case of $F_z = M_y = M_x = 0$. The x-axis corresponds to the spanwise axis (y-axis in Fig.4.3), through each wing box section. F_x corresponds to the wing's axial shear, F_y is the

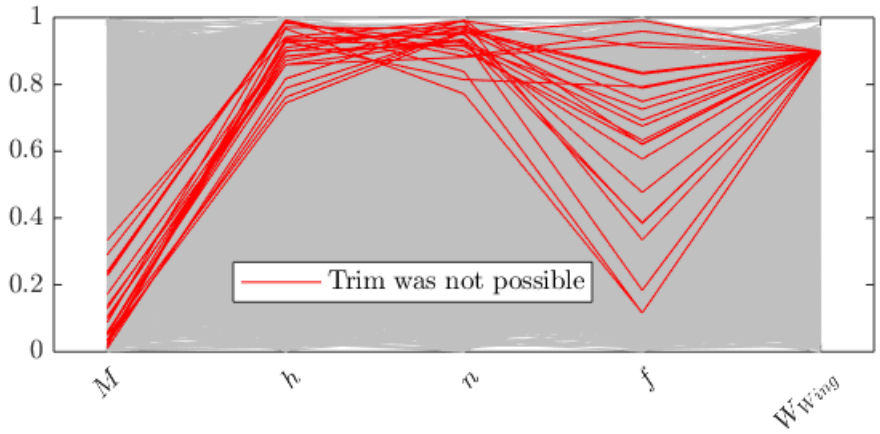

FIGURE 5.3. Parallel-coordinate plot showing the load case parameters and correspondent wing weights for which the aircraft trim was not possible.

horizontal shear, F_z is the vertical shear, M_x is the torque, M_y is the out-of-plane bending moment and M_z is the in-plane bending moment. The red line (or sample), represents the critical case for which the total wing weight is maximum. The two kinks noticeable in the plots, particularly in Fig.5.4(d) and Fig.5.5(d), correspond to the landing gear and engine, respectively. The kinks are the locations where a local vertical shear is introduced. The lumped masses of these two elements and respective attachments are represented in Fig.4.8 and Fig.4.9.

The envelopes or absolute loads in Fig.5.5 are represented in scale to each other, using the same y-axis for the forces and the same y-axis for the moments. In this manner, the impact the different forces and moments on the stress and sizing becomes visible and the comparison between them is facilitated. The wing's axial and vertical shear, respectively $|F_x|$ and $|F_z|$, are generally, spanwise, greater than the horizontal shear $|F_y|$. The out-of-plane bending moment $|M_y|$ is greater than the torque or in-plane bending moment, respectively $|M_x|$ and $|M_z|$.

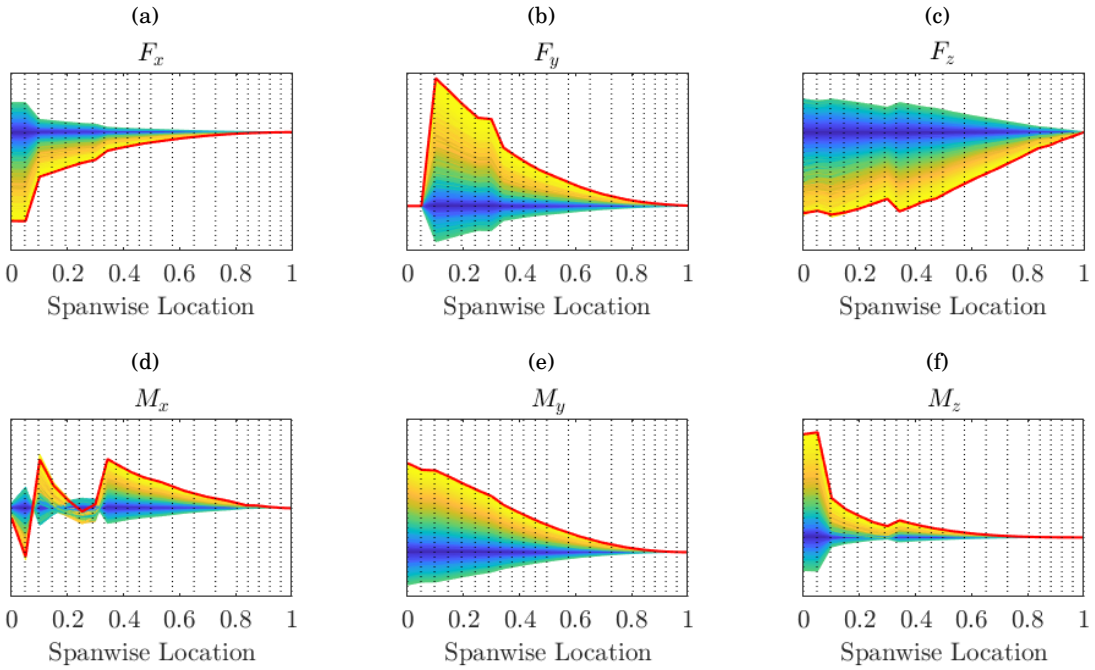

FIGURE 5.4. Internal loads spanwise distribution. (a) Axial shear; (b) Horizontal shear; (c) Vertical shear; (d) Torque; (e) Out-of-plane bending moment; (c) In-plane bending moment.

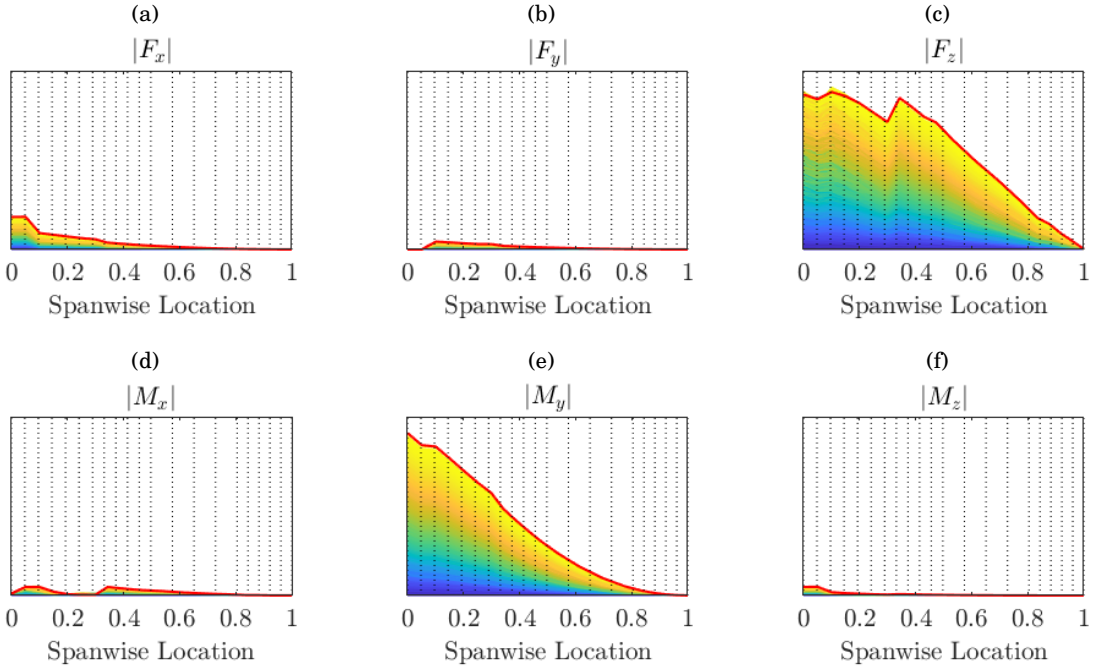

FIGURE 5.5. Internal loads envelope spanwise distribution. (a) Axial shear; (b) Horizontal shear; (c) Vertical shear; (d) Torque; (e) Out-of-plane bending moment; (c) In-plane bending moment.

The results for the aerodynamic loads obtained are compared to the results obtained using the trim analysis on a different aircraft model in [129], see Fig.5.6. The aircraft model correspondent to Fig.5.6 does not account for ribs and landing gear weight, hence the discrepancies in the distributions, particularly noticeable in the Torque (M_x) and in-plane bending moment (M_z). The out-of-plane bending moment M_y shows a similar pattern to the one on Fig.5.6.

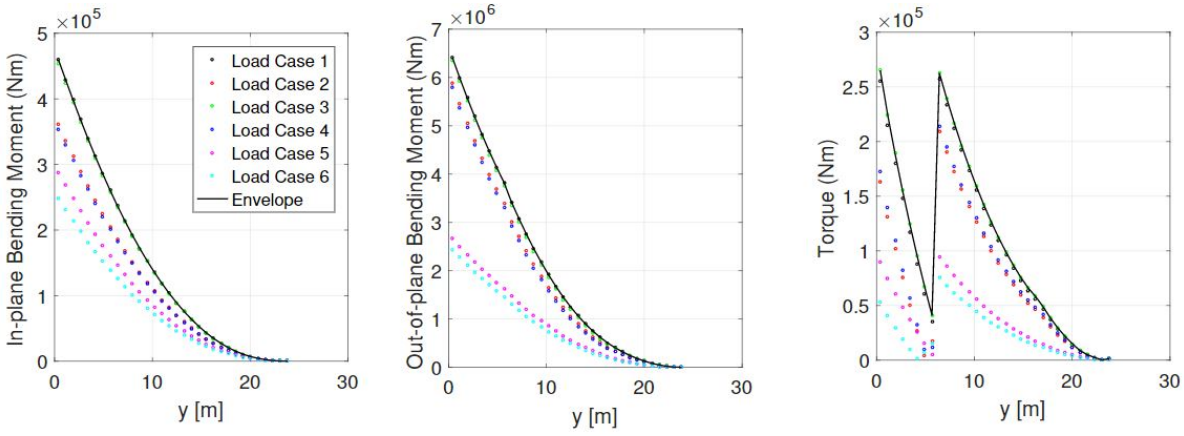

FIGURE 5.6. Internal moments distribution, for an aircraft model with AR=18, from [129]

The XRF-1 aircraft model is sized in [1] and the in-plane bending moment is shown in Fig.5.7. Unlike the previous aircraft model, the landing gear weight impact is noticeable in Fig.5.7 and compareable to the results obtained by WeiCoS and shown in Fig.5.5(e).

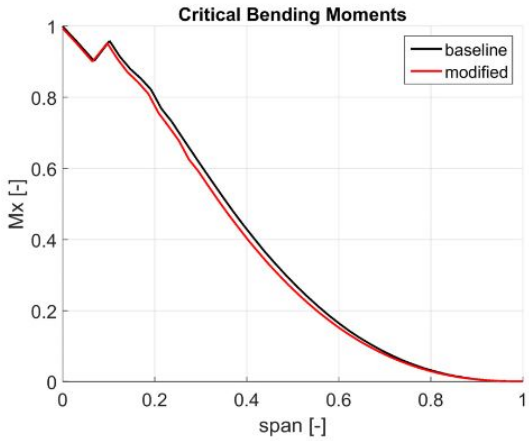

FIGURE 5.7. Integrated critical wing out-of-plane bending moment for the baseline aircraft model XRF-1 and a modified model, from [1].

5.1.1.3 Stress

After obtaining the internal loads, including forces and moments, for each wing-box section, the stress analysis described in Appendix A is performed. The stress is carried by the different wing-box sections, spanwise, and therefore higher loaded sections will have to carry higher stress levels and be sized accordingly. The straight red line running across all the plots represents the bending and shear stress allowable.

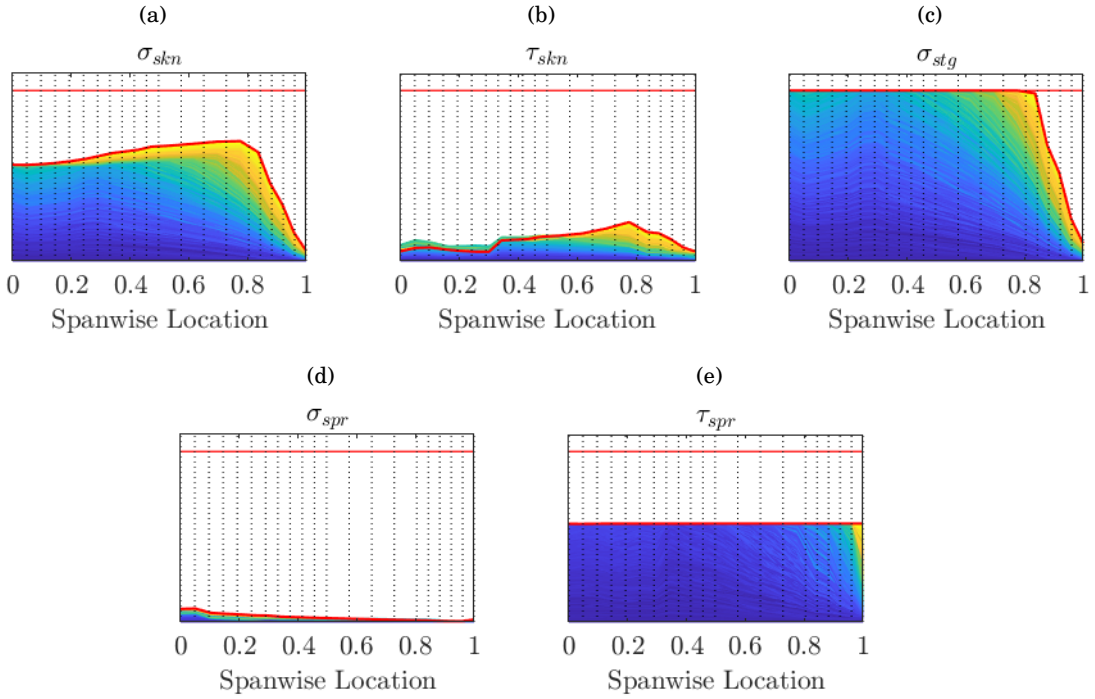

FIGURE 5.8. Wing-box elements' (skins, stringers and spars) stress spanwise distribution. (a) Skins bending stress; (b) Skins shear stress; (c) Stringers bending stress; (d) Spars bending stress; (e) Spars shear stress.

Regarding the covers (skins and stringers) section, the out-of-plane bending moment $|M_y|$ and vertical shear $|F_z|$ are the stress main drivers and, as a result, the bending stress is much higher than the shear stress, see Figs.5.8(a), 5.8(b) and 5.8(c). The skin to stringer constraints, including the Farrar's efficiency factor, are making so that the stringers stress is, spanwise, generally higher than the skins. For the critical case, the stringers bending stress is at its allowable level for over 80% of the span of the wing. For the same 80% span and critical case, the skins stress starts at a margin from its allowable and gradually increases until plateauing at its allowable.

Regarding the spars, the bending stress is driven by $|F_y|$ and $|M_z|$, whilst shear stress is driven by $|F_z|$, $|M_x|$ and $|F_y|$. $|F_z|$ dominates and the shear stress is then greater than the bending stress, see Figs.5.8(d) and 5.8(e). The spar shear stress plateaus at its constrained maximum very quickly or for lower overall wing weights.

The structural optimisation and the stress constraints drive the stress to its maximum constrained level very quickly, i.e., only for minimum values of its sizing parameters (blue area on Fig.5.9) there is a variation on the stress of the different sections. For higher wing weights, the thickness of the sections increase for the maximum constrained stress, consequently minimum sizing and weight.

5.1.1.4 Sizing

The sizing parameters defined for the wing-box are the skin thickness t_{skn}, spar thickness t_{spr} and stringers area A_{stg} (which can be directly correlated to the stringers thickness by $A_{\text{stg}} = 3t_{\text{stg}}d$ and $t_{\text{stg}} = 0.12d$. In WeiCoS, the sizing routine calculates the skin and spar thickness of each wing-box. Within the same wing-box however, the upper and lower skins, as well as the front and rear spars are identical. There is a lower bound to these parameters but not an upper one. The way these are obtained is by the sizing routine finds the combination of skins, stringers and spars weight, that will provide the minimum overall wing weight, but withstand the bending and shear stresses and stress constraints each is facing.

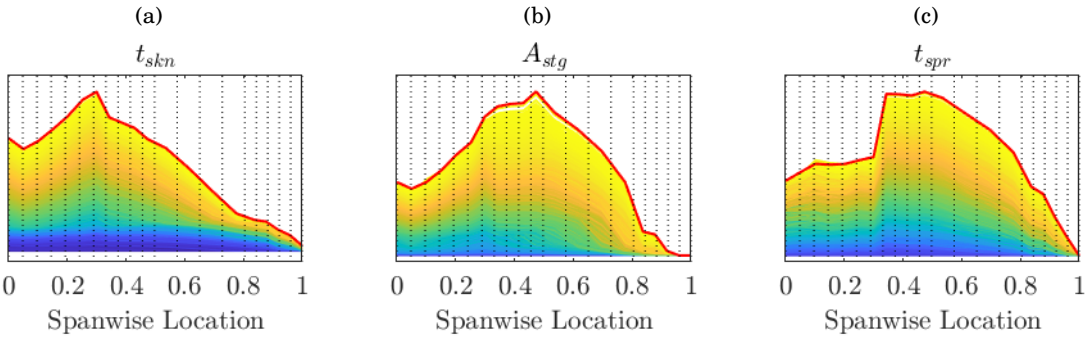

FIGURE 5.9. Wing-box elements sizing spanwise distribution. (a) Skins thickness; (b) Stringers area ($A_{\text{stg}} = 25t_{\text{stg}}^2$); (c) Spars thickness.

The sizing distributions for the uniformly distributed set of load case parameters are shown in Fig.5.9. The horizontal line at the bottom represents the minimum thickness imposed on the wing-box parameters. As shown, and recalling Fig.5.8, the skin thickness follows the same trend of the skins and stringers bending stress, reaching its peak where the blue lines in the stress tend upwards. The stringers thickness continues to increase until around 50% of the span where the length of the each wing-box section also increases, see Fig.4.5(c). The loads are distributed over a larger area and the stress the stringers are under starts decreasing, and so does its thickness (or Area). The spars thickness, on the other hand, has a significant increase where the engine is located, see Fig.4.8. After that, it decreases non-linearly until the tip of the wing. The plots for the skins, stringers and spars thickness are not on the same scale of magnitude.

5.1.1.5 Weight

After the sizing optimisation loop, the final sizing of the structural elements is obtained. Having this, as well as the wing-box dimensions, the weights for the skins, stringers and spars are obtained. These are shown in Fig.5.10. The plots for the skins, stringers and spars weight are on the same scale of magnitude.

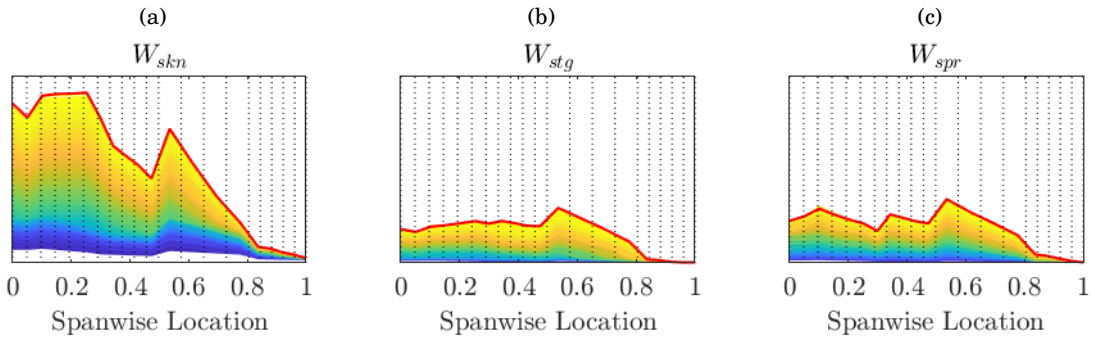

FIGURE 5.10. Wing-box elements weights spanwise distribution. (a) Skins weight; (b) Stringers weight; (c) Spars weight.

As for the thickness, the skins weight follows the same two peaks where the length of each wing box section, l_{box}, also peaks, see Fig.4.5(c). The stringers follow a similar trend where their weight increases where the length of the sections is bigger and therefore the stringers are longer and heavier. The spars weight increases, at first, at around 30% of the span, where the engine is located. After the that a second increase happens with l_{box}.

The skins weight distribution is compared to the one obtained in [1] for validation, shown in Fig.5.11. The same aircraft model (XRF-1) is used. There s a kink in the trend of the distribution at around 0.4 of the span, justified by the ribs mass distribution. The same later kinks are observed in WeiCoS, driven by the weigh-box sectioning and the ribs mass. In Fig.5.11 only the upper skin weight is considered, unlike WeiCoS, that considers upper and lower skins equivalent. For this reason, the distribution differs closer to the root of the wing.

The total wing weight W_{Wing} follows the same fluctuations as mentioned before, mostly due to the change in l_{box}. Its distribution is shown in Fig.5.12. The fixed leading edge FLE is the only secondary weight structure that varies in weight when varying the load case parameters. This is because the FLE is dependent on the dynamic pressure q_{D} , which, in turn, is a function of the Mach number and altitude via

$$q_{\text{D}} = \frac{1}{2}\rho u^2, \tag{5.3}$$

where ρ is obtained from interpolation of tabled values for altitude and correspondent atmospheric pressure;

$$u = M\sqrt{\gamma R T}; \tag{5.4}$$

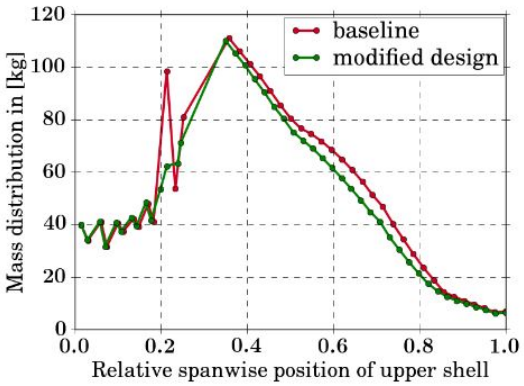

FIGURE 5.11. Upper wing skin mass distribution for the baseline aircraft model XRF-1 and a modified model, from [1].

and

$$T[K] = \begin{cases} 288.2 \cdot \frac{71.5h}{11000}, & \text{for } h < 11000m \\ 216.7, & \text{for } h \geq 11000m \end{cases}$$

Its distribution of different weight values, for each wing-box section, is shown in Fig.5.13. The FLE weight does not follow the same colour scheme as the total wing weight and it is, instead, random. This is explained by the low sensitivity of the W_{Wing} to the Mach and altitude parameters, shown in Fig.5.15. The secondary structure weight is calculated for the aircraft. It is then distributed over the wings as a function of the volume fraction of each wing-box section, given the total volume of all wing-box sections. For this reason the shape of the spanwise distribution of W_{fle} is equivalent to the product of c_{box}, h_{spr} and l_{box}, shown in Fig.4.5.

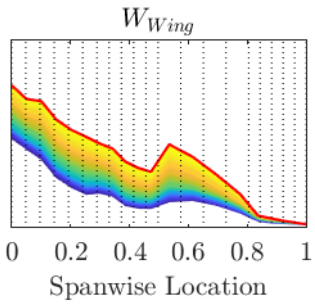

FIGURE 5.12. Total wing weight spanwise distribution.

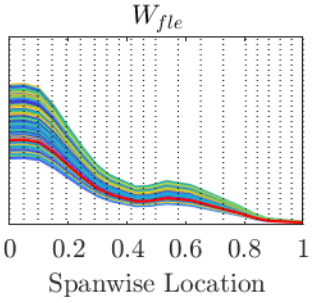

FIGURE 5.13. Fixed leading edge (fle) weight spanwise distribution.

5.1.1.6 Sensitivity Analysis (SA) on sizing optimisation

Using the Spearman's rank correlation, the sensitivity indices for the weights are obtained. The standard regression coefficients indices (SRCI) for the weight of the skins (W_{skn}), stringers (W_{stg})

and spars (W_{spr}) are shown and listed in Fig.5.14. The load factor n is the main contributor for the variation on any of the weights with SRCI = 0.85/0.86. The fuel fraction f is the second input parameter to which the weights are more sensitive and the Mach number M has an inverse correlation to the sizing and weights, with all the indices below zero.

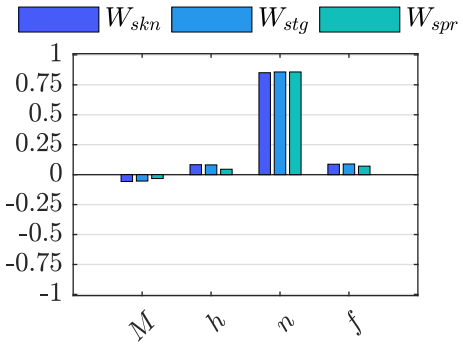

	W_{skn}	W_{stg}	W_{spr}
M	-0.06	-0.05	-0.03
h	0.08	0.08	0.05
n	0.85	0.86	0.86
f	0.09	0.09	0.07

FIGURE 5.14. Sensitivity indices (SRCI) of the wing-box elements (skins, stringers and spars) weights, towards the load case parameters.

The standard regression coefficients indices (SRCI) for the weight of the FLE (W_{fle}) and total wing (W_{Wing}) are shown and listed in Fig.5.15. The load factor n is the main contributor for the W_{Wing}'s variability with a 0.86 correlation index. As previously mentioned, the W_{fle} varies with the dynamic pressure, a function of Mach and altitude. Therefore, the correlation indices of M and h, to the variability of W_{fle}, are, respectively, 0.52 and -0.85. The temperature (up to 11 km) and density of the atmosphere decrease with altitude, and, therefore, the dynamic pressure q_D decreases with the increase in altitude.

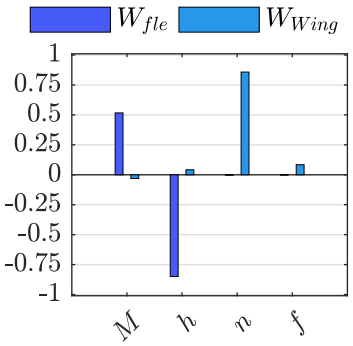

	W_{fle}	W_{Wing}
M	0.52	-0.03
h	-0.85	0.04
n	0.00	0.86
f	0.00	0.08

FIGURE 5.15. Sensitivity indices (SRCI) of the total wing weight and the fle weight, towards the load case parameters.

* * *

From this point forward, the critical load case is used for all calculations.

5.1.2 Varying loads envelopes around its critical value

A study was done on varying the loads envelopes around its critical value, i.e. around its maximum value, corresponding to the critical load case (red lines in Fig.5.5). Using Eqs.4.38, 4.39 and 4.40, the nominal value is the respective critical load for each spanwise location x. A normal distribution is used to define the loads variability and confidence levels of 99, 95 and 85% are analysed, i.e. $2\sigma = x[1,5,15]\%$.

$$\begin{aligned} &\text{Loads envelopes:} \quad X \sim \mathcal{N}(\mu,\sigma^2), \\ &\qquad\qquad\qquad\quad X = (F_x,F_y,F_z,M_x,M_y,M_z) \\ &\qquad\qquad\qquad\quad \mu = \text{critical load} \\ &\qquad\qquad\qquad\quad 2\sigma = [5,10,15]\% \end{aligned} \tag{5.5}$$

The distributions and corresponding uncertainty of 18 parameters, including stress, sizing and weight of the wing-box sections are obtained. The first information to be analysed was the linearity of the different confidence levels CLs. The uncertainty defined by 2σ of the input ($2\sigma = [1,5,15]\%x$) versus the output parameters is shown in Fig.5.16. Each colour in the plot represents a different parameter and linearity between different uncertainty levels is visually determined. Next, a quantification of this linearity is presented. The coefficient of determination,

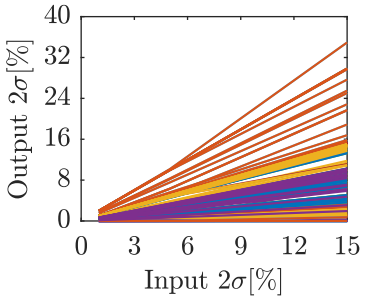

FIGURE 5.16. Input to output uncertainty (2σ) regression.

R^2 is a measure of how well a model can predict the data which, in this case, because the models built are linear regressions between the 3 points at different CLs, R^2 is used to measure their linearity. R^2 ranges between 0 and 1 and the higher it is, the higher the linearity. Consider the output parameters to be represented by y and $\hat{y}_i$ represents the calculated values of y and $\overline{y_i}$ is the mean of y. R^2 is defined as

$$R^2 = 1 - \frac{\sum_{i=1}^{n}(y_i - \hat{y}_i)^2}{\sum_{i=1}^{n}(y_i - \overline{y_i})^2} = 0.959 \tag{5.6}$$

The average linearity for all the parameters analysed is quantified at 0.959. For this reason, from this point forward, only the distributions for $2\sigma = 5\%$ are shown. For any desired distinct input uncertainty level, the output uncertainty is directly proportional to the one of $2\sigma = 5\%$.

The uncertainty on the stress, sizing and weight of the wing's primary structure was evaluated for a variation of 5% around the critical loads.

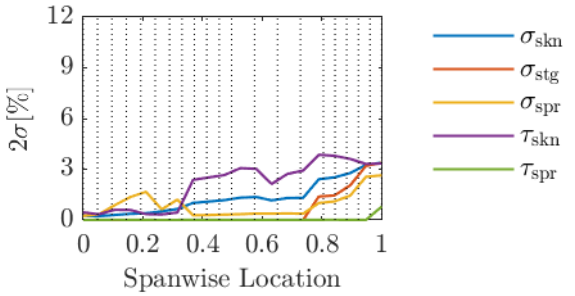

FIGURE 5.17. Spanwise distribution of the stress uncertainty, for the different wing-box elements.

The first plot, in Fig.5.17, depicts the uncertainty on the different stress elements of the wing-box. For an input uncertainty of $u = 5\%$ on the loads, the mean value (spanwise) of the different stress elements are: $\overline{u}_{\sigma_{skn}} = 1.34\%$, $\overline{u}_{\sigma_{stg}} = 0.89\%$, $\overline{u}_{\sigma_{spr}} = 0.89\%$, $\overline{u}_{\tau_{skn}} = 2.12\%$ and $\overline{u}_{\tau_{spr}} = 0.04\%$. Recalling the covers stress critical cases, see Fig.5.8, the uncertainty on the stringers is null until ~75% of the span because the stringers stress was at its allowable level up until this point. That is, for any variation around the nominal load value, the stringers stress will continue to be at its maximum level: no variation and therefore no uncertainty. The stringers will vary in size but and so that their stress is always at critical level. The optimisation for minimum wing weight favours the stringers for being less heavy, when distributing the loads between skins and stringers. Moreover, the Farrar's efficiency factor, a stress constraint detailed in sec.4.1.4.1 and analysed below, assumes a structural efficiency of 95% for the skin-stringer panel, which is another contributor to the inaccurate distribution of the wing loading. In reality, the skins should be bearing most of the load and a load redistribution factor or additional studies on the Farrar's efficiency factor are suggested, if to integrate in an increased complexity scenario.

Recall the spars stress critical stress in Fig.5.8. Similarly to the stringers, the spars shear stress was at its maximum level for ~95% of the span, the same location where uncertainty goes grows from 0 to 0.79%. In sum, in WeiCoS, stress uncertainty is correlated to the margin between the critical case and its allowable level, which might not necessarily be representative of reality. In any case, the maximum stress uncertainty obtained is for τ_{skn} and it is of 3.86%. For this reason, a general trend of increasing standard deviation of the stress components at the tip of the wing is noticeable. The stress constraints and the fact that the wing-box sections closer to the root are bigger (larger c_{box} and h_{spr}), suggest that the stress in these sections is kept at a more stable valuable for the different loading scenarios, it is less uncertain.

The next plot, in Fig.5.18, depicts the uncertainty on the different sizing elements of the wing-box. For an input uncertainty of $u = 5\%$ on the loads, the mean value (spanwise) of the sizing elements are: $\overline{u}_{t_{skn}} = 3.05\%$, $\overline{u}_{A_{stg}} = 7.12\%$ and $\overline{u}_{t_{spr}} = 5.04\%$. The uncertainty on the spars

sizing is $u_{t_{spr}} \approx 5\%$ at any spanwise location, the same percentage as its input uncertainty. Skins are less affected by the uncertainty on loads, reaching a minimum value of $\min(u_{t_{skn}}) = 1.25\%$. The stringers are the elements that are most affected by the variability on the loads, leading to up to $\max(u_{A_{stg}}) = 10.14\%$.

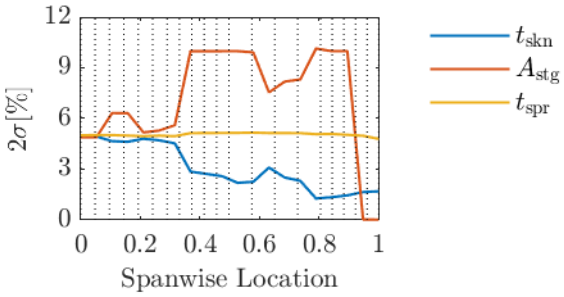

FIGURE 5.18. Spanwise distribution of the sizing parameters uncertainty, for the different wing-box elements.

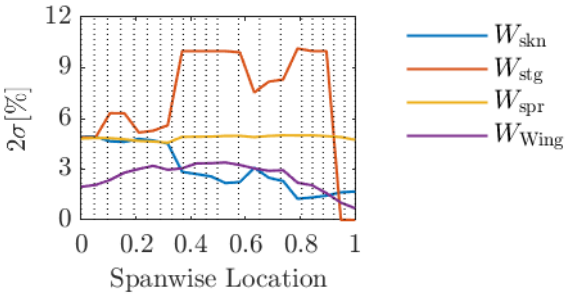

FIGURE 5.19. Spanwise distribution of the weights' uncertainty, for the different wing-box elements and total wing.

Finally, the plot in Fig.5.19, depicts the uncertainty on the different weight elements of the wing-box, as well as the total wing weight uncertainty. For an input uncertainty of $u = 5\%$ on the loads, the mean value (spanwise) of the weight elements are: $\overline{u}_{W_{skn}} = 3.05\%$, $\overline{u}_{W_{stg}} = 7.12\%$ and $\overline{u}_{W_{spr}} = 4.87\%$. Because c_{box}, h_{spr} and l_{box} are fixed, the uncertainty on the weight of each wing-box element (skins, stringers and spars) is the same as the sizing uncertainty, by

$$W_{box} = [(2c_{box}t_{skn}) + (2nb_{stg}A_{stg}) + (2(h_{spr} - 2t_{skn})t_{spr})] \cdot l_{box} \cdot \rho \tag{5.7}$$

where nb_{stg} is the number of stringers on each skin, dependent on the stringer pitch (SP = 0.24m) and the c_{box}; ρ is taken from Tab.4.1.

The total wing weight has an average value of $\overline{u}_{W_{Wing}} = 2.56\%$, maximum of $\max(u_{W_{Wing}}) = 3.40\%$ and minimum of $\min(u_{W_{Wing}}) = 0.69\%$ at the tip of the wing. Overall, one can assume the average uncertainty on the final wing weight to be half of the uncertainty on the loads.

5.1.3 Stress allowable uncertainty

The next analysis presented focuses on varying the stress allowable (σ_{allow}) of the wing-box material, the aluminium described in Tab.4.1. The analysis considers adding uncertainty to the the material properties, particularly the tensile yield strength, and quantify the effect on the weight of the wing.

A Gaussian (or normal) distribution was built to define σ_{allow}, with $\mu = 276$MPa, the tensile yield strength's nominal value, and CL = 0.85. The 5% and 95% quantiles are $q_{0.05} = 242$MPa and $q_{0.95} = 310$MPa, respectively, and, the latter, corresponds to its tabled tensile ultimate strength,

σ_{ult}. The distribution is shown in Fig.5.20, the mean μ is represented in dark blue, and the quantiles $q_{0.05}$, $q_{0.50}$ and $q_{0.95}$ in green, cyan blue and red, respectively. The three quantiles are monitored through the uncertainty propagation on the new distribution of weights obtained.

$$\text{Stress allowable:} \quad \sigma_{\text{allow}} \sim \mathcal{N}(\mu, \sigma^2) \qquad \mu = 276MPa,\ 2\sigma = 15\% \tag{5.8}$$

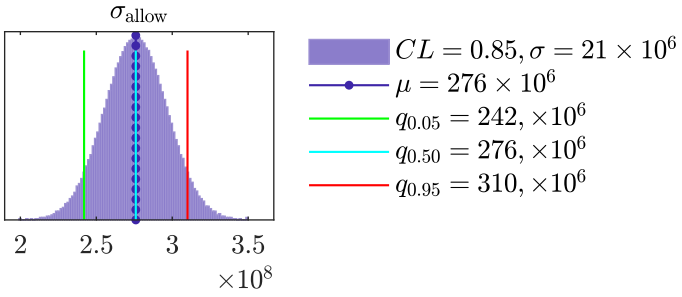

FIGURE 5.20. Wing-box stress allowable normal distribution and its 5, 50 and 95% quantiles.

The weights' distributions of the skins, stringers, spars and total wing, obtained with varying the stress allowable, are shown in Fig.5.21. These distributions take on a new shape, non-normal, and a GEV distribution can be fitted into the data. The statistical moments defining a GEV are μ, σ and the skewness $\widetilde{\mu_3}$. For an input uncertainty of $u(\sigma_{\text{allow}}) = 15\%$, $2\sigma(\sigma_{\text{allow}}) = 0.15x$, the values obtained are listed in Tab.5.5.

The maxima of the GEV distribution is depicted in the plots (μ), as well as the prior quantiles of $q_{0.05} = 242$MPa, $q_{0.50} = 276$MPa and $q_{0.95} = 310$MPa. Note that the 50% quantile corresponds to the critical load case, i.e. no uncertainty in the stress allowable.

TABLE 5.5. GEV's standard deviation σ and skewness $\widetilde{\mu_3}$ for input σ_{allow} and outputs W_{skn}, W_{stg}, W_{spr} and W_{Wing}.

	σ_{allow}	W_{skn}	W_{stg}	W_{spr}	W_{Wing}
σ	0.075	0.043	0.173	0.084	0.048
$\widetilde{\mu_3}$	0	-1.20	0.25	-0.10	-0.11

If the stress allowable is bigger, the weight generally decreases, and, likewise, if the stress margin tightens, the sizing, and consequently weight, will increase. Material properties, test results, safety factors, margins, etc., are all limiting factors in this analysis. The percent decrease or increase in weight, with the baseline being $q_{0.50} = 276$MPa, is tabled in Tab.5.6. For all the wing-box elements, covers, spars and overall wing, the new μ taken from fitting the data points to a GEV distribution is lower than the nominal case. For the skins its -1.27%, the stringers -6.02%, spars -3.01% and total wing of -1.76% lower. Except for W_{skn}, the absolute percent difference

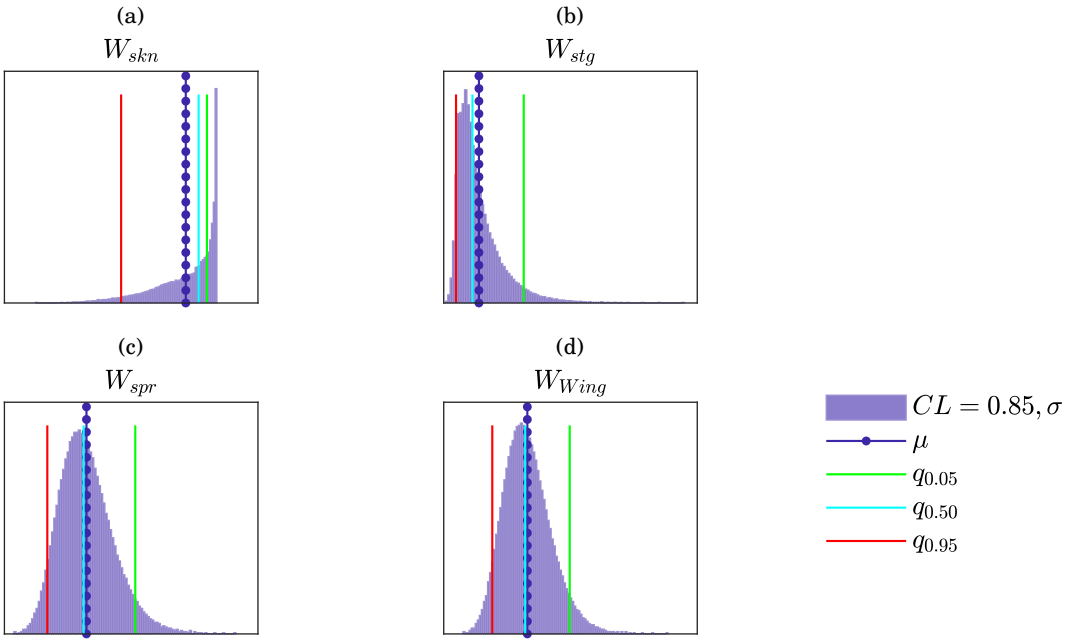

FIGURE 5.21. Wing-box elements and total wing weight distributions, including their 5, 50 and 95% quantiles, for the σ_{allow} variation. (a) Skins weight; (b) Stringers weight; (c) Spars weight; (d) Total wing weight.

between the weight values for $q_{0.50}$ to $q_{0.05}$ are bigger than for $q_{0.50}$ to $q_{0.95}$. This means that decreasing the stress allowable has a bigger effect on the (increasing) weight of the wing. In the case of W_{skn}, the skins' shear stress τ_{skn} is generally decreasing with an increasing stress allowable and is causing the sizing of the wing to be non-monotonic. If the tensile ultimate strength was taken as the stress allowable for the wing-box, one could observe a decrease of 7.31% on the weight of the wing, being that most of the effect would be beared by the stringers, with a 21.20% weight decrease.

TABLE 5.6. Deviation (%) of μ, $q_{0.05}$ and $q_{0.95}$, from the $q_{0.50}$ baseline. E.g. For σ_{allow}: $[q_{0.05}, q_{0.50} = \mu, q_{0.95}]$=[242,276,310] MPa; Thus $\frac{(\mu - q_{0.50})}{q_{0.50}} = 0.00$, $\frac{(q_{0.05} - q_{0.50})}{q_{0.50}} = -0.1232$ and $\frac{(q_{0.95} - q_{0.50})}{q_{0.50}} = 0.1232$.

	σ_{allow}	W_{skn}	W_{stg}	W_{spr}	W_{Wing}
μ (%)	0.00	-1.27	-6.02	-3.01	-1.76
$q_{0.05}$ (%)	-12.32	1.04	66.21	17.77	9.90
$q_{0.95}$ (%)	12.32	-9.65	-21.20	-12.50	-7.31

Looking at Fig.5.22, W_{skn} increases for an increasing stress allowable up until $\sigma_{\text{allow}} \approx$ 255.08MPa where it then decreases quasi-linearly. For all the other weights: W_{stg}, W_{spr} and

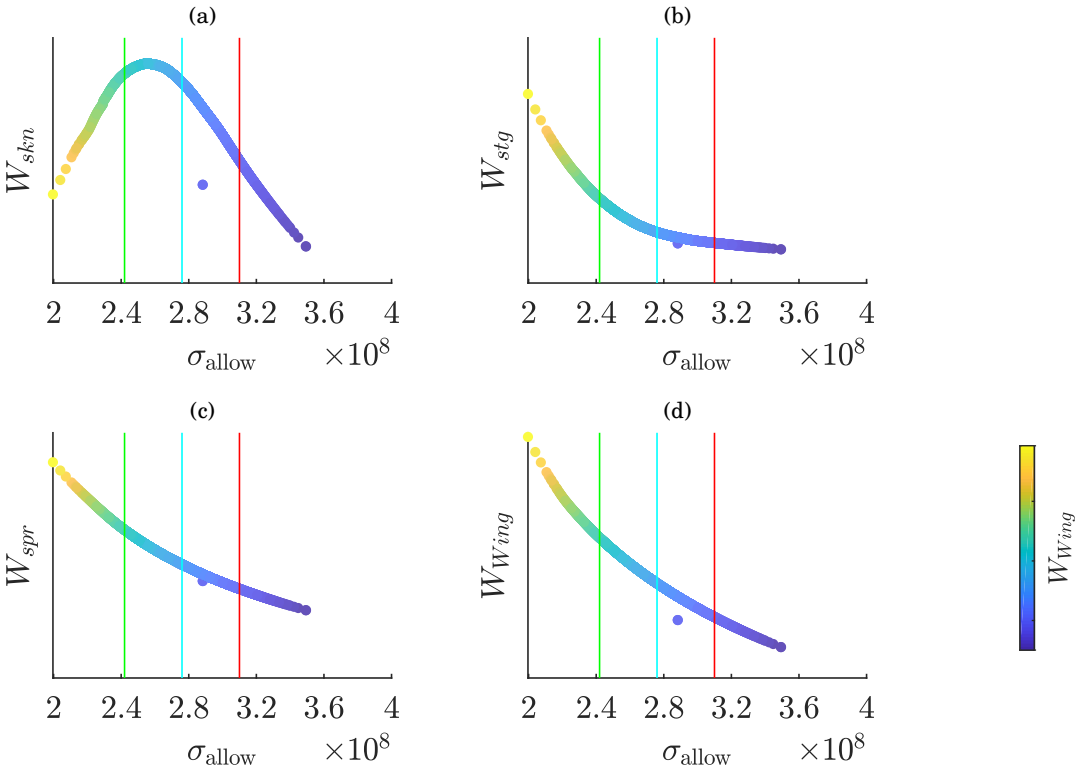

FIGURE 5.22. Wing-box elements and total wing weights VS. stress allowable, coloured by ascendant wing weight. (a) Skins weight; (b) Stringers weight; (c) Spars weight; (d) Total wing weight.

W_{Wing}, the weight decreases monotonically, non-linearly with the stress allowable, being that the curves are steeper for the first half of smaller stress allowable. This means that decreasing the stress allowable incurs more variability in the (increasing) weight of the wing. The three quantiles $q_{0.05}$, $q_{0.50}$ and $q_{0.95}$ from σ_{allow}'s distribution, are also represented in the green, cyan blue and red vertical lines, respectively.

To check if there are specific locations in the span of the wing where uncertainty is more prevalent, or, in other words, areas in the span that are more (or less) sensitive to variations, in this case, of the stress allowable of the wing-box, the graphics in Fig.5.23 are presented. The spanwise weight fluctuations are similar to the ones obtained in the load case parameters distributions, see Fig.5.10, and the reasons why the fluctuations are this way can be consulted in the previous section. The uncertainties (2σ from a fitted GEV distribution) for W_{Wing}, relative to the μ value at each span location, are listed in Tab.5.7. The uncertainty does not only depend on the nominal value of the weight for a specific wing-box, but also from the indirect influence the sizing and external elements have on the wing.

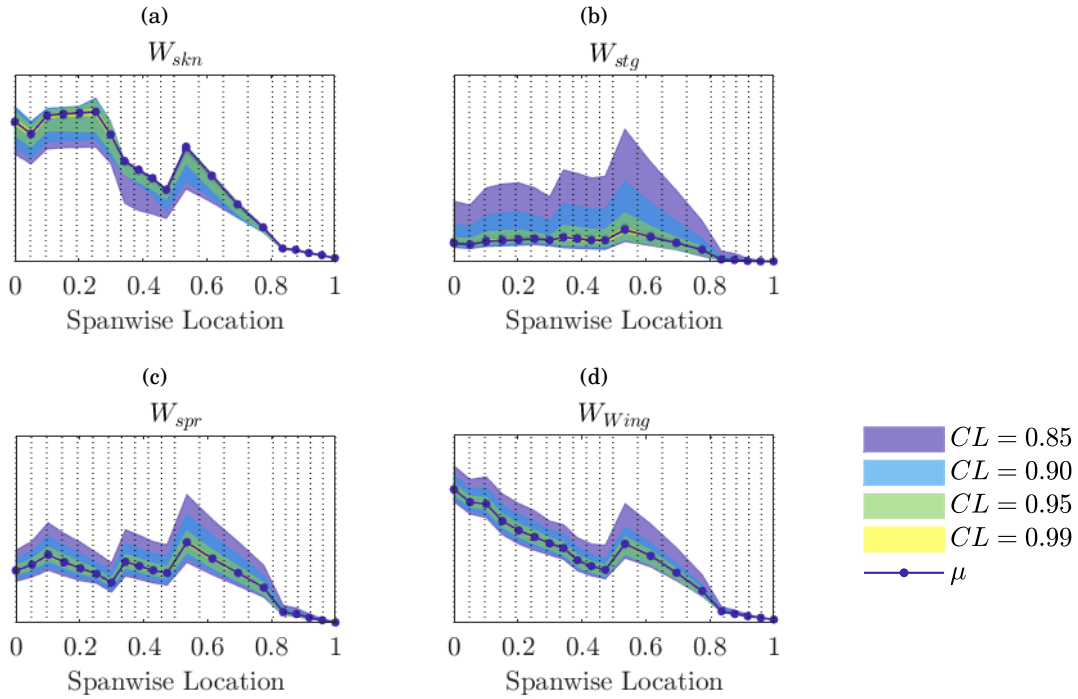

FIGURE 5.23. Weights' spanwise distribution, for different Confidence Levels (CL) of stress allowable. (a) Skins weight; (b) Stringers weight; (c) Spars weight; (d) Total wing weight.

TABLE 5.7. W_{Wing}'s spanwise uncertainty (2σ from a fitted GEV distribution) relative to the μ value for the specific span location.

1	3	5	7	9	10	12	14	16	18	20
6.32	7.96	10.20	10.14	11.93	12.12	12.55	11.16	7.64	5.28	0.92

The weight of the skins, W_{skn} in Fig.5.23(a), stringers, W_{stg} in Fig.5.23(b) and spars, W_{spr} in Fig.5.23(c) are in the same scale of magnitude, contrary to the total weight of the wing, W_{Wing} in Fig.5.23(d). As aforementioned and with the exception of W_{skn}, the uncertainty, depicted by the shadowed area surrounding the mean value μ, is bigger for higher weight values. That is, a lower stress allowable induces more uncertainty or variability on weight. It is also apparent that W_{stg} is the most sensitive element to an uncertain σ_{allow}.

Results were additionally retrieved for CL = 0.90, CL = 0.95 and CL = 0.99. Following the same criteria as before for quantifying linearity between different CL's, see Eq.5.6, the coefficient of determination R^2 is quantified at 0.972 overall. For W_{Wing}, specifically, it is 0.998. This means that all the uncertainty and the new GEV weight distributions obtained for CL = 0.85, can be scaled directly for different CL values.

5.1.4 Stress constraints

Carrying on the topic of stress and stress analysis, this section delves into the stress constraints action on the sizing optimisation process. The goal with this analysis is to check what constraints are activated when sizing the wing for the critical load case, provide insights into the sensitivity of the wing weight to the constraints used in WeiCoS, and help understand the stress distributions in sec.5.1.1.3.

$$\text{Stress constraints:} \quad X \sim [0,1], \quad X = (b_1, b_2, ..., b_{11}) \tag{5.9}$$

TABLE 5.8. Stress Constraints - sizing optimisation inequalities.

b_1	b_2	b_3	b_4	b_5	b_6
$\sigma_{skn}/\sigma_{allow}$	$\sigma_{spr}/\sigma_{allow}$	$\sigma_{stg}/\sigma_{allow}$	τ_{skn}/τ_{allow}	τ_{spr}/τ_{allow}	$\sigma^{v}_{skn}/\sigma_{allow}$
b_7	b_8	b_9	b_{10}	b_{11}	
$\sigma^{v}_{spr}/\sigma_{allow}$	σ_P	σ_{stg}/σ_{cc}	$\sigma_{stg}/\sigma_{col}$	F	

The constraints are nonlinear inequalities that the optimisation needs to satisfy for $cin(x) \leq 1$. The full description of the stress analysis, including the stress constraints, can be consulted in sec.4.1.4.1 and further detail regarding specific formulae is given in Appendix A. The constraints range between 0 and 1, with the exception of the skin buckling principle stress σ_P that can take any number up to 1, and are activated when at 1. Fig.5.24 shows the constraints behaviour, along the wing span, for the 7 iterations it took for the sizing optimisation to converge.

The first and last iteration lines are the only visible ones, indicating that the sizing optimisation converged very quickly after the first iteration for what would be the final stress constraints activation status. Numbering the plots from left to right, top to bottom, the first three plots of stress constraints is related to the skins' bending and shear stress ($\sigma_{skn}/\sigma_{allow}$ and τ_{skn}/τ_{allow}), and the combination of the two through the Von Mises Yield Criterion (σ^{v}_{skn}). These resemble the skins' stress distribution in sec.5.1.1.3 and the constraints are never activated. Equivalently, plots five to seven depict the spars' bending and shear stress constraints ($\sigma_{spr}/\sigma_{allow}$ and τ_{spr}/τ_{allow}) and the Von Mises stress constraint (σ^{v}_{spr}). In this case, the Von Mises stress constraint is activated throughout the whole wing span. Revisiting the spar's shear stress distribution τ_{spr} in sec.5.1.1.3, the latter is cut-off at a maximum that is lower than the stress allowable τ_{allow}. This maximum is now justified as its Von Mises stress. Similarly, the stringers bending stress is cut off at its allowable level with the constraint $\sigma_{stg}/\sigma_{allow}$. This is active until about 80% of the span, as demonstrated previously in the stringers stress distribution.

Minimum thickness are required for skins, stringers and spars: $t_{min_{skn}}$, $A_{min_{stg}}$ and $t_{min_{spr}}$. The constraints in this case only take values 0 or 1: when the calculated thickness is below the minimum, the constraint is activated (1); otherwise the constraint is 0. The stringers are the only

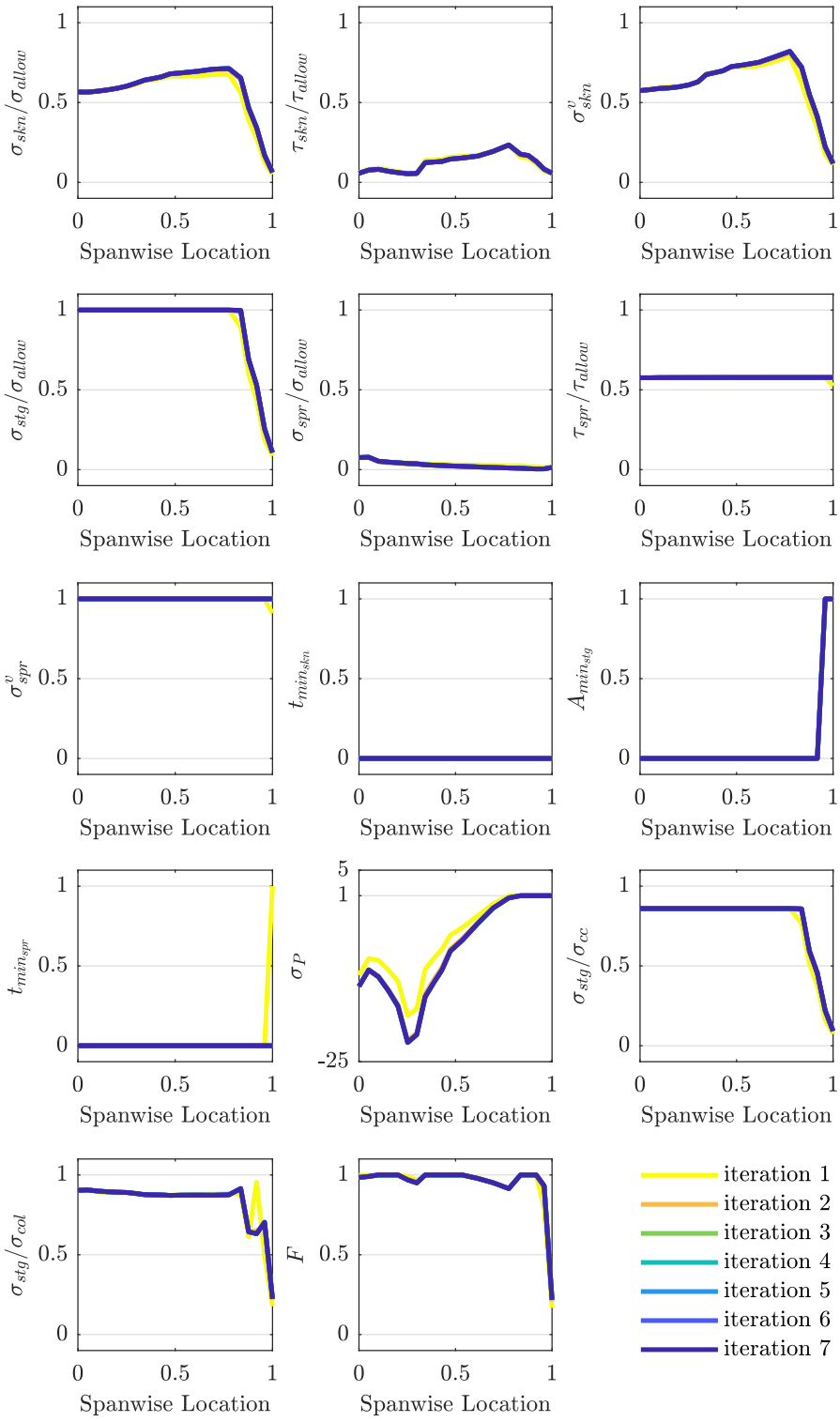

FIGURE 5.24. Stress Constraints activation plots, for each iteration of the sizing optimisation.

element where its thickness minimum requirement is activated, at the very tip of the wing, when σ_{stg} significantly drops. The principle stress formulation is used to account for skin buckling σ_P and it becomes active from around 80% of the span, where tip deflection becomes a concern for buckling. Both the constraints for stringer buckling ($\sigma_{\text{stg}}/\sigma_{\text{cc}}$) as well as column buckling of the skin-stringer panel ($\sigma_{\text{stg}}/\sigma_{\text{col}}$) are never activated but the stresses are close to 1. Finally, the Farrar's efficiency factor F is generally activated throughout the whole span. This means that the failure stress of the skin-stringer panel, accounting for its structural efficiency of 95%, is at its allowable level for a great part of the wing span.

Next, the Spearman's rank correlation between the stress constraints activation and the W_{skn}, W_{stg}, W_{spr} and W_{Wing} is calculated. The sizing optimisation ran for $1000x$, x being the number of stress constraints used, in this case $x = 11$. The number of samples was chosen given the nature of the study, as previously done: the SRC method applied requires the number of samples to be $> 1000x$ [47]. In each run, a randomiser outputs a sequence of 11 numbers, one or zero, e.g. $[0,0,1,0,1,0,1,0,1,1,0]$. The constraints are used in the sizing optimisation if 1, and not used if 0. The constraints for the required minimum thickness of each wing-box element are not in analysis as these are always in use. By running WeiCoS for different combinations of constraints used in the sizing, the sensitivity of the weights to each constraint is achieved. The Standard Regression Coefficients Indices (SRCIs) range from -1 to 1: the magnitude indicates the strength of the correlation; The positive or negative sign indicates if the constraint is directly or inversely proportional to the weight variation, respectively. The skins' weight, shown in Fig.5.25, is most

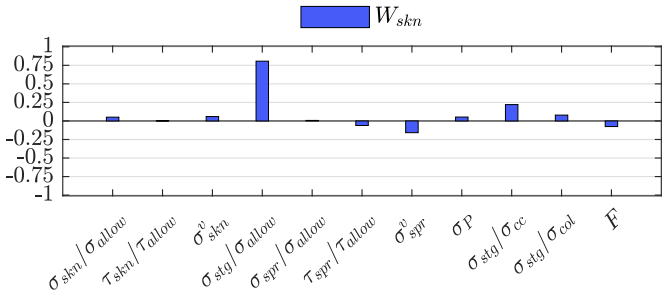

W_{skn}			
$\sigma_{\text{stg}}/\sigma_{\text{allow}}$	0.81	$\sigma^{\text{v}}_{\text{skn}}$	0.06
$\sigma_{\text{stg}}/\sigma_{\text{cc}}$	0.22	σ_{P}	0.05
$\sigma^{\text{v}}_{\text{spr}}$	-0.16	$\sigma_{\text{skn}}/\sigma_{\text{allow}}$	0.05
$\sigma_{\text{stg}}/\sigma_{\text{col}}$	0.08	$\sigma_{\text{spr}}/\sigma_{\text{allow}}$	0.01
F	-0.08	$\tau_{\text{skn}}/\tau_{\text{allow}}$	0.00
$\tau_{\text{spr}}/\tau_{\text{allow}}$	-0.06		

FIGURE 5.25. Sensitivity indices (SRCI) of the skins weight, towards stress constraints.

sensitive to $\sigma_{\text{stg}}/\sigma_{\text{allow}}$ with $SRCI = 0.81$, followed by $\sigma_{\text{stg}}/\sigma_{\text{cc}}$ with 0.22 and $\sigma^{\text{v}}_{\text{spr}}$ with -0.16. This is indicative of the influence the sizing of the stringers has on W_{skn}. As previously discussed, in the primary weight stress distribution, the skin stress does not reach its maximum or critical level at any point in the span. On the other hand, the stringers stress is at its critical level throughout most of it, and so is the spar's shear stress. For that reason, any variation on the stringers or spars constraints has a bigger influence on the variation of the skins' weight.

The stringers' weight, shown in Fig.5.26, is most sensitive to $\sigma_{\text{stg}}/\sigma_{\text{col}}$ with $SRCI = 0.58$, followed by F with 0.22 and $\sigma_{\text{stg}}/\sigma_{\text{cc}}$ with 0.17. The driving constraints for W_{stg} are the stringers

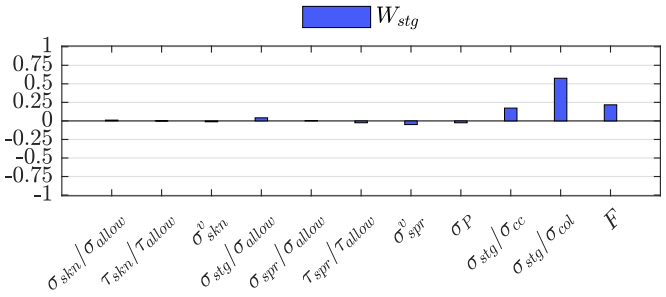

W_{stg}			
$\sigma_{stg}/\sigma_{col}$	0.58	τ_{spr}/τ_{allow}	-0.03
F	0.22	σ^{v}_{skn}	-0.01
σ_{stg}/σ_{cc}	0.17	$\sigma_{skn}/\sigma_{allow}$	0.01
σ^{v}_{spr}	-0.05	$\sigma_{spr}/\sigma_{allow}$	0.00
$\sigma_{stg}/\sigma_{allow}$	0.04	τ_{skn}/τ_{allow}	0.00
σ_P	-0.03		

FIGURE 5.26. Sensitivity indices (SRCI) of the stringers weight, towards stress constraints.

buckling and the skin-stringer panel column buckling stresses.

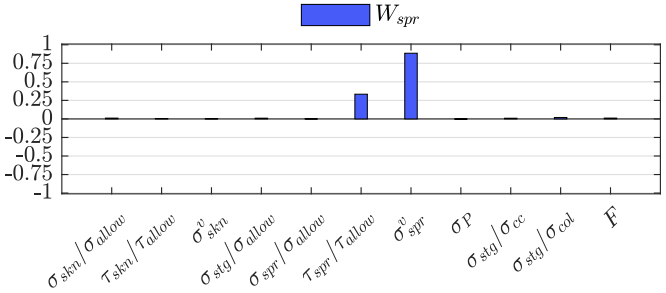

W_{spr}			
σ^{v}_{spr}	0.89	σ_{stg}/σ_{cc}	0.01
τ_{spr}/τ_{allow}	0.33	τ_{skn}/τ_{allow}	0.00
$\sigma_{stg}/\sigma_{col}$	0.02	σ^{v}_{skn}	0.00
F	0.01	σ_P	0.00
$\sigma_{skn}/\sigma_{allow}$	0.01	$\sigma_{spr}/\sigma_{allow}$	0.00
$\sigma_{stg}/\sigma_{allow}$	0.01		

FIGURE 5.27. Sensitivity indices (SRCI) of the spars weight, towards stress constraints.

The spars' weight, shown in Fig.5.27, is most sensitive to σ^{v}_{spr} with $SRCI = 0.89$, followed by τ_{spr}/τ_{allow} with 0.33. W_{spr} is highly dependent on the direct spar stress constraints, especially its Von Mises stress that, when in use, is active throughout the whole span. The shear stress constraint is limiting the τ_{spr}.

Finally, the total wing's weight, shown in Fig.5.27, is most sensitive to $\sigma_{stg}/\sigma_{allow}$ with $SRCI = 0.65$ followed by σ^{v}_{spr} with 0.34, $\sigma_{stg}/\sigma_{col}$ with 0.27, σ_{stg}/σ_{cc} with 0.24 and τ_{spr}/τ_{allow} with 0.12. The variation on the wing weight is most sensitive to stringers and spars weight. The stringers on the other hand have a big influence on the sizing of the skins, whereas the spars stress constraints are mostly driving variations on spar weight.

Additional tests are possible and advisable where, for a specific stress constraints combination, the specific weight variation and wing-box stress distribution are examined, as well as, what constraints become active for different combinations of constraints in use.

The same set of data, correspondent to sizing the wing $1000x$ times, each time using a different set of constraints in its sizing and x being the maximum number of constraints (11 in this case), is analysed using parallel-coordinate plots (for reference, see sec.1.2.3.1). Results for

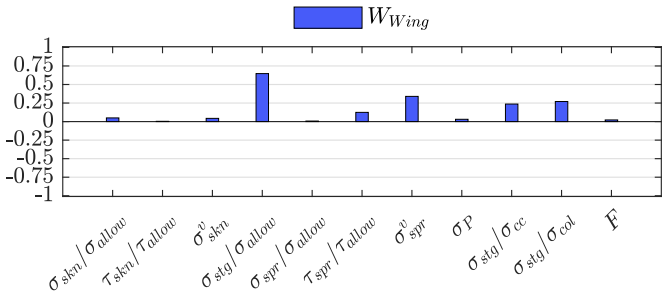

W_{Wing}			
$\sigma_{\text{stg}}/\sigma_{\text{allow}}$	0.65	$\sigma^{\text{v}}_{\text{skn}}$	0.04
$\sigma^{\text{v}}_{\text{spr}}$	0.34	σ_{P}	0.03
$\sigma_{\text{stg}}/\sigma_{\text{col}}$	0.27	F	0.02
$\sigma_{\text{stg}}/\sigma_{\text{cc}}$	0.24	$\sigma_{\text{spr}}/\sigma_{\text{allow}}$	0.01
$\tau_{\text{spr}}/\tau_{\text{allow}}$	0.12	$\tau_{\text{skn}}/\tau_{\text{allow}}$	0.00
$\sigma_{\text{skn}}/\sigma_{\text{allow}}$	0.05		

FIGURE 5.28. Sensitivity indices (SRCI) of the total wing weight, towards stress constraints.

having all the constraints in use or no constraints in use as well as for maximum and minimum wing weight are shown.

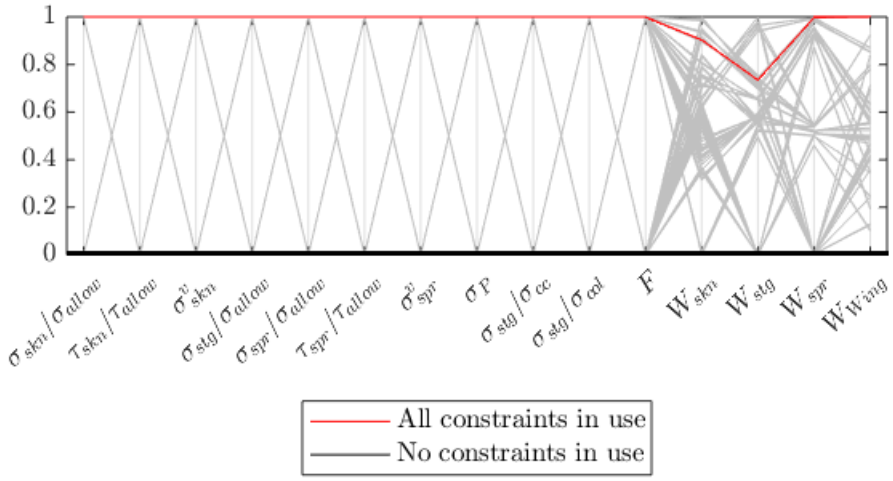

FIGURE 5.29. Parallel-coordinate plot showing the stress constraints and primary and wing weights for which all the constraint are in use and none of the constraints are in use.

The first parallel-coordinate plot is presented in Fig.5.29. In grey, all the runs in this analysis are depicted, including the combinations of using (at 1) or not using (at 0) a specific constraint, as well as the normalised weights for the skins, stringers, spars and total wing, obtained for a given set of constraints in use. Two lines are distinguished: in red, the runs correspondent to having all the constraints in use; and, in black, the runs correspondent to having no constraints to the sizing, except for the minimum requirements for thickness. As visually identifiable, and

as expected, using all the stress constraints in the sizing results in the maximum wing weight. Equivalently, using no stress constraints in the sizing results in the minimum wing weight, with a difference between the two of 54%.

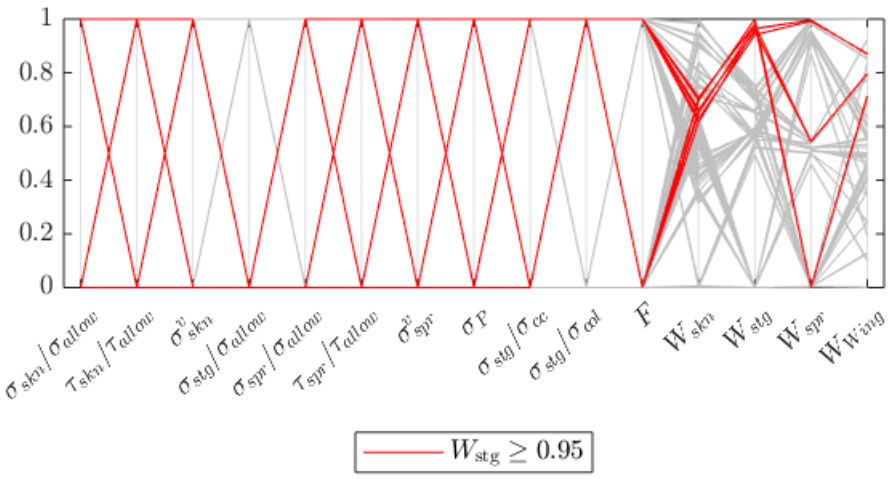

FIGURE 5.30. Parallel-coordinate plot showing the stress constraints and primary and wing weights for which the normalised stringers weight is $W_{stg} \geq 0.95$.

For the black case, the minimum wing weight also corresponds to the minimum weight for the wing-box components. Differently, the maximum wing weight does not correspond to the maximum W_{skn} or W_{stg}. The latter was investigated using the same method and the higher values for W_{stg} highlighted in red in Fig.5.30. One can obtain the higher values for W_{stg} by always using the column buckling constraint ($\sigma_{stg}/\sigma_{col}$) and not using the stringer's stress allowable constraint ($\sigma_{stg}/\sigma_{allow}$). This will drive W_{skn} down which ultimately results in a lower W_{Wing}.

The maximum wing weight was then obtained for having all of the stress constraints in use. However, not all of the constraints are active when they are in use, see Fig.5.24, and, for this reason, the next analysis captures all the stress constraint combinations that culminate in the highest W_{Wing} values. Equivalently, results for minimum weight are also obtained. Both are shown in Fig.5.31.

For maximum weight, the stringer's allowable ($\sigma_{stg}/\sigma_{allow}$), the Von Mises spars' (σ^{v}_{spr}), the skin buckling (σ_P) and the column buckling ($\sigma_{stg}/\sigma_{col}$) stress constraints, and the Farrar's efficiency factor F have to be always in use. These correspond to the constraints with higher activation values, being that only $\sigma_{stg}/\sigma_{col}$ is not active for the critical load case, see Fig.5.24. W_{Wing} is independent of all other stress constraints and, thus, all combinations, of using them or not, will result in the same (maximum) value of W_{Wing}. For minimum weight, the spars' stress allowable constraint ($\sigma_{spr}/\sigma_{allow}$) is the only constraint that, in use or not, the same (minimum)

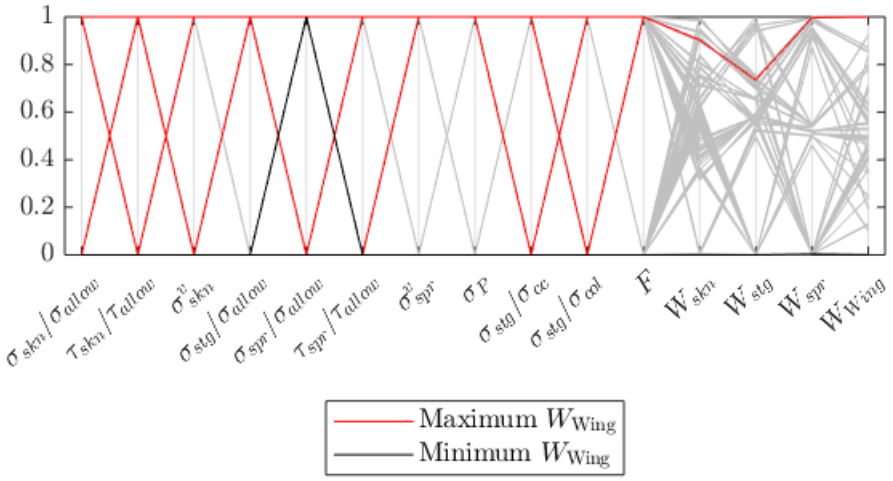

FIGURE 5.31. Parallel-coordinate plot showing the stress constraints and primary and wing weights for which the wing weight is maximum (in red) and minimum (in black).

weight value of W_{Wing} is obtained.

5.1.5 Engine & pylon

In this analysis, the idea to vary the weight of the wing's engine and pylon is tested. The engine and pylon here represent any external weight that is added to the wing in the form of a lumped mass, i.e. calculating the inertial properties of given mass, transfer these properties to the beam formulation of the wing with a mass matrix, and associating it with a structural node. Considering the aircraft is at a phase in the design process when the specific engine model has not yet been decided, by adding uncertainty to the engine and pylon's weight in WeiCoS and/or its geometric elements, the wing's weight and all the factors and components that take part in its sizing can be studied probabilistically. For this analysis, the CL of the weight of the engine and pylon ($W_{\text{eng,pyl}}$) is assumed $CL = 0.85$.

$$\begin{aligned} &\text{Engine \& Pylon weight:} \quad X \sim \mathcal{N}(\mu, \sigma^2), \\ &\qquad\qquad\qquad\qquad\quad X = W_{\text{eng,pyl}} \\ &\qquad\qquad\qquad\qquad\quad \mu = \text{nominal } W_{\text{eng,pyl}},\ 2\sigma = 15\% \end{aligned} \tag{5.10}$$

The engine and pylon's weights are distributed over two different structural nodes, see Fig.4.8. In this analysis they are considered and varied together. The variation of this weight is depicted in Fig.5.32(a), for $u = 0.15$: the dashed line is the μ value for the weight distributed over the structural nodes along the span of the wing (x-axis); the two vertical red lines represent the beam

where the two nodes where the engine is located; and the shaded area represents the $u = 2\sigma$ around the μ value for the weight.

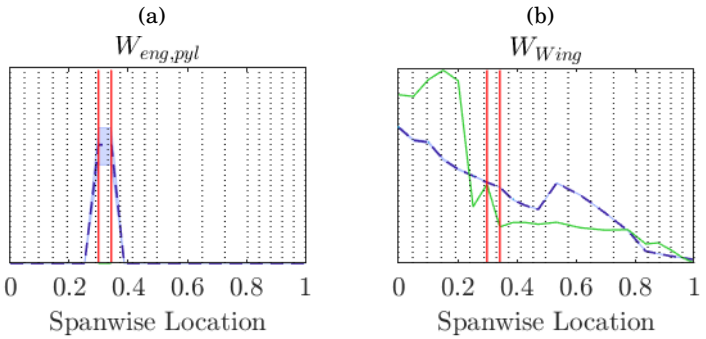

FIGURE 5.32. (a) Engine and pylon's varying weight. (b) Resultant wing weight variation. For each wing-box spanwise location: the dashed line represents the mean value μ; the shaded area around it represents its uncertainty 2σ; and the green line represents the normalised uncertainty 2σ[%] (in weight percentage). The red vertical lines identify the location of the engine on the wing span.

The W_{Wing} is represented in Fig.5.32(b) and the location of the engine nodes is again plotted as the red vertical lines. The green line represents the normalised uncertainty, in weight percentage, 2σ[%] distribution across the span of the wing. Given a 15% uncertainty on $W_{\text{eng,pyl}}$, the uncertainty on W_{Wing} is, on average, of 0.34%, with a maximum of 0.87% and minimum of 0.04% at the tip.

The breakdown of its effect on the loads, sizing and weight of the specific wing-box elements is presented below these lines. The vertical shear $|F_z|$, torque $|M_x|$ and bending moment $|M_y|$ are

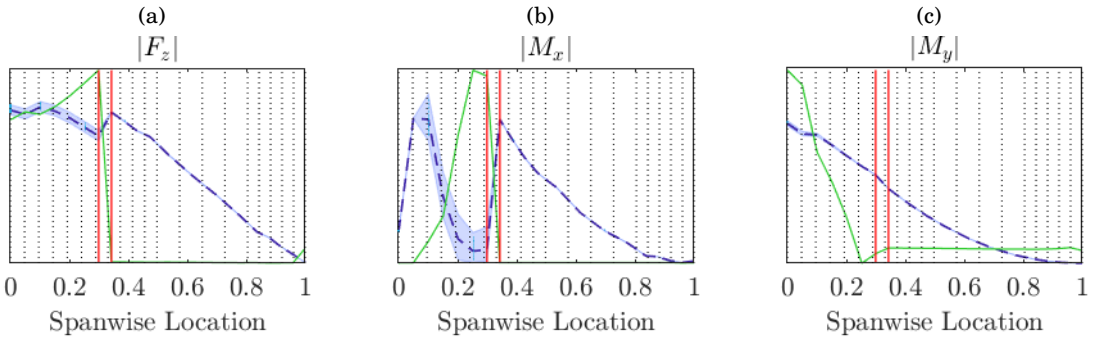

FIGURE 5.33. Internal loads envelope spanwise variation, resultant from an uncertain engine and pylon's weight. (a) Vertical shear; (b) Torque; (c) Out-of-plane bending moment.

plotted in Fig.5.33. The torque, followed by the vertical shear are the most affected aerodynamic loads, particularly at the nodes to the root of the wing, from the location of the engine. The torque

has an average uncertainty of 21.54% across the wing span, with a maximum of 143.03% and minimum of 0.04% at the tip. The vertical shear has an average uncertainty of 1.47% across the wing span, with a maximum of 4.17% and minimum of 0.31%.

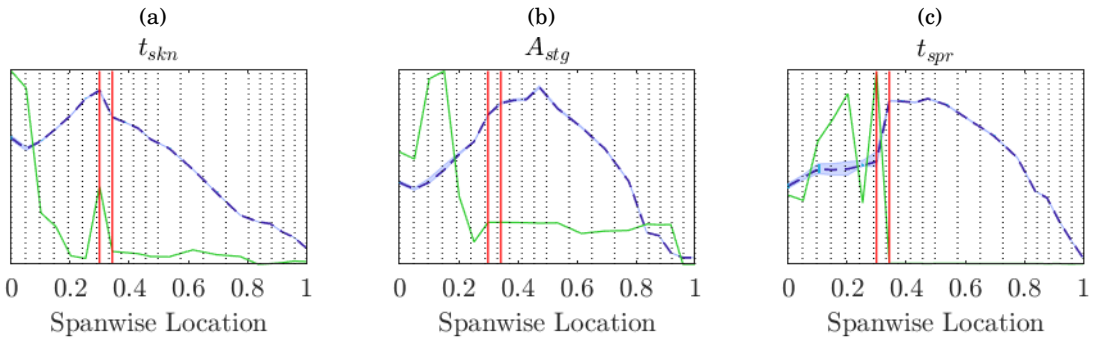

FIGURE 5.34. Wing-box elements sizing spanwise variation, resultant from an uncertain engine and pylon's weight. (a) Skins thickness; (b) Stringers area; (c) Spars thickness.

The thickness of the skins and spars and area of the stringers are plotted in Fig.5.34. The thickness of the spars is the most sensitive to the uncertainty on the engine weight, with an average uncertainty itself of $\overline{u}(t_{\text{spr}}) = 1.95\%$ and maximum of 8.01%. Comparatively, $\overline{u}(t_{\text{skn}}) = 0.34$ and maximum of 1.66% and $\overline{u}(A_{\text{stg}}) = 0.90\%$ and maximum of 3.01%.

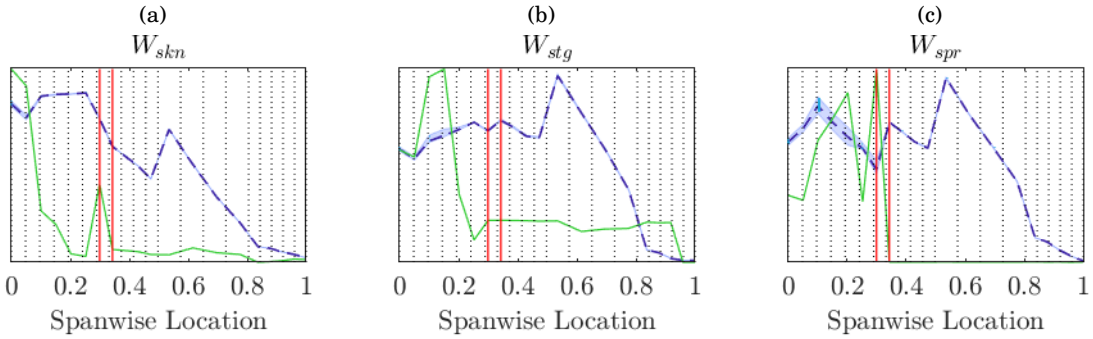

FIGURE 5.35. Wing-box elements weights spanwise variation, resultant from an uncertain engine and pylon's weight. (a) Skins weight; (b) Stringers weight; (c) Spars weight.

The weight of the skins, stringers and spars for $u(W_{\text{eng,pyl}}) = 0.15$ is plotted in Fig.5.34. Similarly to the sizing, the weight of the spars is the most sensitive to the uncertainty on the engine weight, with an average uncertainty itself of $\overline{u}(W_{\text{spr}}) = 1.95\%$ and maximum of 8.07%. Comparatively, $\overline{u}(W_{\text{skn}}) = 0.34\%$ and maximum of 1.66% and $\overline{u}(W_{\text{stg}}) = 0.90\%$ and maximum of 3.01%.

A variation on any lumped mass, in WeiCoS, is translated to a variation in the global wing loading. The local effects of the lumped mass variation are therefore not completely captured by its global integration. Empirically obtained weight functions or knowledge-based factors could be added to the framework in order to account for local effects on the sizing of the covers and spars.

5.2 Secondary weight

After breaking down the uncertainty on the primary wing-box structure, the secondary structure follows. The loads driving the secondary structure weight are different from those of the primary structure. In the early phases of design, sizing the secondary structure using physics-based methods is a task of great complexity and the inputs to these methods have large amounts of uncertainty. For these reasons, the equations used to model these devices are obtained empirically, from statistical evidence. MTOW is used for secondary weight calculation as a scale factor, unlike the functional physical role it has for the primary weight and the aerodynamic loads. In WeiCoS, the secondary weight formulae is derived from metallic civil aircraft structures data, taken from Torenbeek [132]. The formulae is fully detailed in sec.4.1.3, including the distinction of the uncertain input parameters, in purple.

The secondary structure's devices are organised into fixed and movable leading edge devices (FLE and MLE), fixed and movable trailing edge devices (FTE and MTE) and miscellaneous items. Uncertainty in the secondary devices' input parameters is propagated through and quantified at the secondary weights' level (W_{fle}, W_{mle}, W_{fte}, W_{mte} and W_{misc}). Additionally, the effects of this uncertainty on the primary wing-box weight (W_{skn}, W_{stg}, W_{spr}) is also analysed, as well as the total wing weight (W_{Wing}). The wing sizing was run $1000x$ times, x being the number of uncertain input parameters, discriminated below.

5.2.1 Leading Edge (LE)

The LE structure represents all the wing elements located forward to the front spar. In this analysis, the uncertain input parameter to the FLE structure is the front spar location in chordwise percentage, f_{spr}. For the MLE devices, two uncertainty factors are considered, one concerning the length and the other one the depth of the parts, $k_{l_{\text{mle}}}$ and $k_{d_{\text{mle}}}$ respectively.

The front spar is assumed to be located, throughout the whole span, at the mean location of 13.99% of the chord and so will the FLE also be located at. The MLE structure, namely the slats, is typically located between 15 and 20% of the chord of the wing and over around 90% of the span. Using Eqs.4.38, 4.39 and 4.40, f_{spr} and $k_{l_{\text{mle}}}$ are defined by two normal probability distributions, with CL= 0.85 and bounding values described as follows. For f_{spr}: $\mu = 0.1399$ and $x \in [0.10, 0.20]$; whereas for $k_{l_{\text{mle}}}$: $\mu = 0.9$ and $x \in [0.70, 0.95]$. A uniform distribution is used to define $k_{d_{\text{mle}}}$, with

parameters $a = 0.15$ and $b = 0.20$.

$$
\begin{aligned}
& f_{\text{spr}} \sim \mathcal{N}(\mu, \sigma) \\
& \mu = 0.1399,\ 2\sigma = 15\% \\
& \text{bounded by:} \quad f_{\text{spr}} \in [0.10, 0.20]
\end{aligned}
\tag{5.11}
$$

$$
\begin{aligned}
& k_{l_{\text{mle}}} \sim \mathcal{N}(\mu, \sigma) \\
& \mu = 0.9,\ 2\sigma = 15\% \\
& \text{bounded by:} \quad k_{l_{\text{mle}}} \in [0.70, 0.95]
\end{aligned}
\tag{5.12}
$$

$$
\begin{aligned}
& k_{d_{\text{mle}}} \sim \mathcal{U}(a, b) \\
& a = 0.15,\ b = 0.20
\end{aligned}
\tag{5.13}
$$

The input distributions as well as their relation to one another and the total wing weight are shown in Fig.5.36. Each dot corresponds to one sample of the distribution, and the colours of the dots are mapped from lower to higher W_{Wing} obtained, from blue to yellow, as indicated by the colour bar on the right of the plot. The higher values for wing weight are obtained for lower values of f_{spr} and higher values of $k_{l_{\text{mle}}}$ and $k_{d_{\text{mle}}}$. This is because, for lower values of f_{spr}, even though W_{fle} decreases, c_{box} increases, making the primary weight, and consequently W_{Wing}, increase.

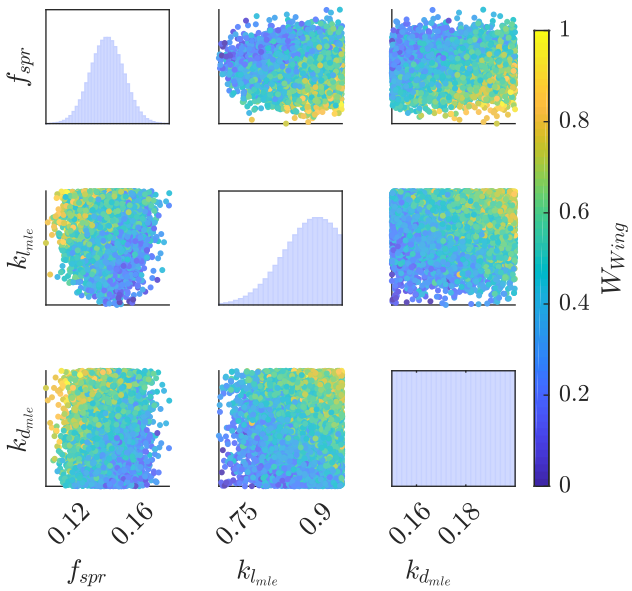

FIGURE 5.36. Leading edge weight input parameters distributions.

The obtained spanwise weight distribution for the FLE and MLE is shown in Fig.5.37. The plots show the μ value for the weight as the dashed line and the uncertainty around μ, 2σ, as the blue shaded area around the dashed line. Specific nodal weight distributions, i.e. uncertainty distributions for specific wing-box weights, are shown throughout the spanwise

overall distribution, in the style of bar histograms. The secondary weights are calculated for one

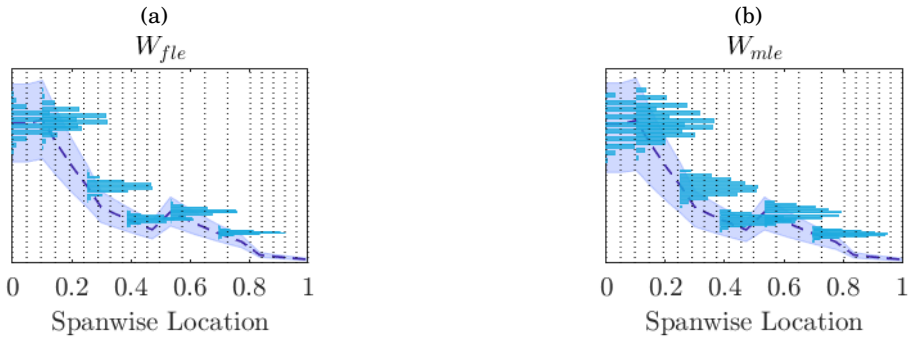

FIGURE 5.37. Leading edge weights spanwise variation, resultant from uncertain secondary weight inputs: (a) FLE Weight; (b) MLE weight. For each wing-box spanwise location: the dashed line represents the mean value μ; and the shaded area around it represents its uncertainty 2σ. The horizontal blue histograms represent the individual distributions at a specific wing-box location.

wing and then distributed over its span following a wing-box volume fraction scale factor, i.e. the ratio of volume of one wing-box to the total volume of all boxes is used to allocate a lumped mass to each structural node. For that reason, also the uncertainty is proportional to the volume of the wing-box and consistent spanwise as a weight percentage. Over the span of the wing, the FLE weight has an average uncertainty of 15.21%, linear to the input uncertainty, and the MLE weight of 23.60%.

5.2.2 Trailing Edge (TE)

Equivalently to the LE, the TE structure represents all the wing elements located to the aft of the rear spar and, the uncertain input parameter to the FTE structure is the aft spar location in chordwise percentage, a_{spr}. The MTE devices include the flaps, ailerons and spoilers and their associated uncertain input parameters are area scale factors k_S, between the area of each component and the wing area. Respectively: $k_{S_{\text{flap}}}$, $k_{S_{\text{ail}}}$ and $k_{S_{\text{spoi}}}$.

The aft spar is assumed to be located, throughout the whole span, at the mean location of 64.22% of the chord of the wing. From Torenbeek, the flaps' total nested area can be estimated at about 18% of the wing planform area. The area of the ailerons, in the neutral position, varies between 3 and 5% and the spoilers' may amount to about 4% of the gross wing area [132]. Using Eqs.4.38, 4.39 and 4.40, a_{spr}, $k_{S_{\text{flap}}}$ and $k_{S_{\text{spoi}}}$ are defined by normal probability distributions, with CL= 0.85 and μ and bounding values described as follows. For a_{spr}: $\mu = 0.6422$ and $x \in [0.60, 0.70]$; for $k_{S_{\text{flap}}}$: $\mu = 0.18$ and $x \in [0.15, 0.21]$; and for $k_{S_{\text{spoi}}}$: $\mu = 0.04$ and $x \in [0.00, 0.05]$. A uniform

distribution is used to define $k_{S_{\text{ail}}}$ with parameters $a = 0.03$ and $b = 0.05$.

$$
\begin{aligned}
& a_{\text{spr}} \sim \mathcal{N}(\mu, \sigma) \\
& \mu = 0.6422,\ 2\sigma = 15\% \\
& \text{bounded by:} \quad f_{\text{spr}} \in [0.60, 0.70]
\end{aligned} \tag{5.14}
$$

$$
\begin{aligned}
& k_{S_{\text{flap}}} \sim \mathcal{N}(\mu, \sigma) \\
& \mu = 0.18,\ 2\sigma = 15\% \\
& \text{bounded by:} \quad k_{l_{\text{mle}}} \in [0.15, 0.21]
\end{aligned} \tag{5.15}
$$

$$
\begin{aligned}
& k_{S_{\text{spoi}}} \sim \mathcal{N}(\mu, \sigma) \\
& \mu = 0.04,\ 2\sigma = 15\% \\
& \text{bounded by:} \quad k_{l_{\text{mle}}} \in [0.00, 0.05]
\end{aligned} \tag{5.16}
$$

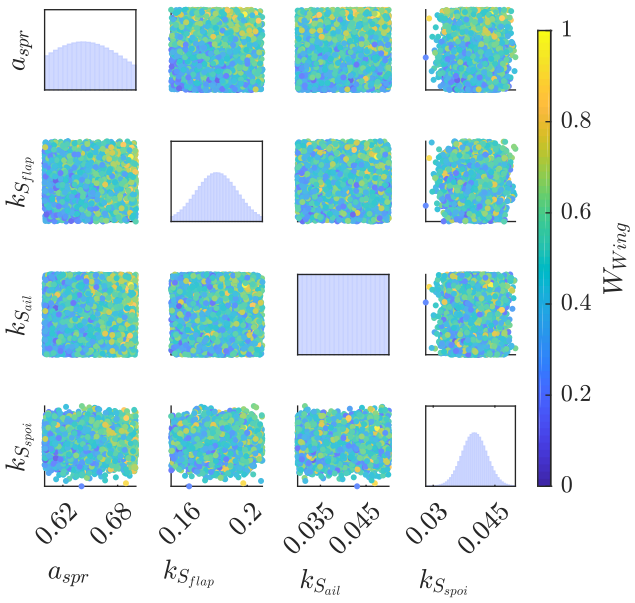

FIGURE 5.38. Trailing edge weight input parameters distributions.

The input distributions as well as their relation to one another and the total wing weight are shown in Fig.5.38. Each dot corresponds to one sample of the distribution, and the color of the dots are mapped from lower to higher W_{Wing} obtained, from blue to yellow, as indicated by the colorbar on the right of the plot. The W_{te}'s input parameters show less of a correlation to the W_{Wing} than the W_{le}, i.e. the different colour sample points (dots) are more scattered over the distributions. Despite this, it is still noticeable that the higher values for W_{Wing} (yellow dots) are obtained for higher values of a_{spr}. This is because, for bigger a_{spr}, even though W_{fte} decreases, c_{box} increases, making the primary weight, and consequently W_{Wing}, increase.

The correlation between the front and rear spar locations, f_{spr} and a_{spr}, the consequent size of the wing-box, c_{box}, and the final wing weight W_{Wing}, is shown in Fig.5.39(a). As explained before,

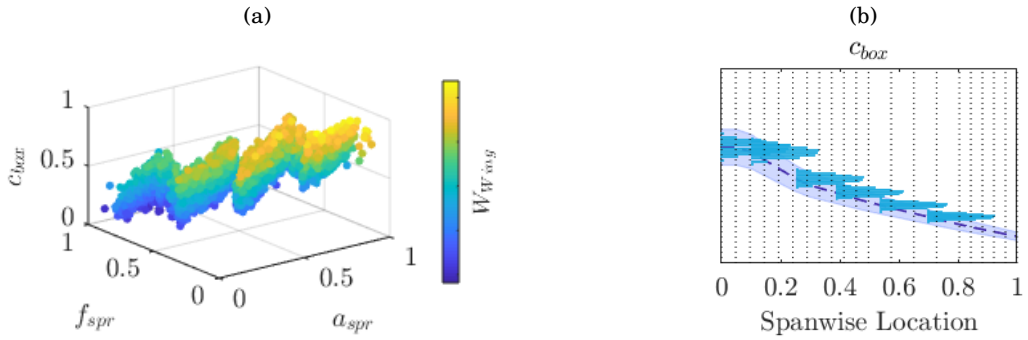

FIGURE 5.39. (a) Correlation between the location of the front and aft spars (respectively f_{spr} and a_{spr}) and the wing-box chord (c_{box}), coloured by ascendant wing weight. (b) Wing-box chord variation, resultant from varying f_{spr} and a_{spr}.

the combination of small f_{spr} and big a_{spr} result in larger wing-boxes that in turn result in higher W_{Wing}. The spanwise distribution of c_{box} is shown in Fig.5.39(b), with an 11.34% variation around its nominal value, resultant of $f_{\text{spr}} = 0.1399$ and $a_{\text{spr}} = 0.6422$.

The obtained spanwise weight distribution for the FTE and MTE is shown in Fig.5.40. The plots show the μ value for the weight as the dashed line and the uncertainty around μ, 2σ, as the blue shaded area around the dashed line. Specific nodal weight distributions, i.e. uncertainty distributions for specific wing-box weights, are shown throughout the spanwise overall distribution, in the style of bar histograms.

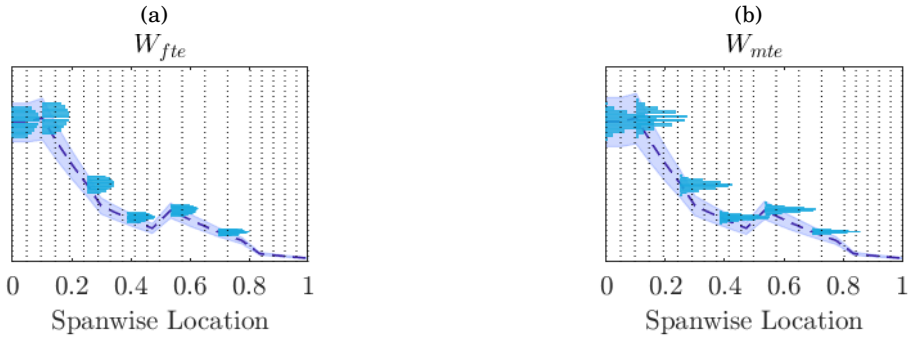

FIGURE 5.40. Trailing edge weights spanwise variation, resultant from uncertain secondary weight inputs. (a) FTE weight; (b) MTE weight.

The secondary weights are calculated for one wing and then distributed over its span following a wing-box volume fraction scale factor, i.e. the ratio of volume of one wing-box to the total volume of all boxes is used to allocate a lumped mass to each structural node. For that reason, also the uncertainty is proportional to the volume of the wing-box and consistent spanwise as a weight percentage. Over the span of the wing, the FTE weight has an average uncertainty of 15.49%,

linear to the input uncertainty, and the MTE weight of 11.64%.

5.2.3 Miscellaneous

The miscellaneous items category represents various scattered, usually small, wing components. In WeiCos, W_{misc} accounts for the weight of the paint, over the wing of the aircraft, the wingtip and fairings. The uncertain input parameters in their equations are the thickness and area factor of the paint (scale factor from the wing's planform area), t_{paint} and $k_{S_{\text{paint}}}$, and, for the fairings, $k_{W_{\text{fai}}}$ is a weight scale factor from W_{Wing}, which is assumed fixed, taken from the critical load case scenario, with no uncertainty added. The wingtip is sized for a reference aircraft and remains constant in this analysis, i.e. has no uncertain inputs to it.

The thickness of the paint work varies from 0.0889 to 0.1397mm (from Hansen, [133]) and the area factor is justified by the folds and intricacies of the external wing components that are painted. Fairings, on the other hand, can amount to anywhere from 1 to about 5% of the wing weight. All the uncertain input parameters are defined using normal probability distributions (recall Eqs.4.38, 4.39 and 4.40), with CL= 0.85 and μ and bounding values described as follows. For t_{paint}: $\mu = 0.1143$ and $x \in [0.0889, 0.1397]$; for $k_{S_{\text{paint}}}$: $\mu = 1$ and $x \in [1,2]$; and for $k_{W_{\text{fai}}}$: $\mu = 0.009$ and $x \in [0.005, 0.05]$.

$$
\begin{aligned}
& t_{\text{paint}} \sim \mathcal{N}(\mu, \sigma) \\
& \mu = 0.1143,\ 2\sigma = 15\% \\
& \text{bounded by:} \quad f_{\text{spr}} \in [0.0889, 0.1397]
\end{aligned}
\tag{5.17}
$$

$$
\begin{aligned}
& k_{S_{\text{paint}}} \sim \mathcal{N}(\mu, \sigma) \\
& \mu = 1,\ 2\sigma = 15\% \\
& \text{bounded by:} \quad k_{l_{\text{mle}}} \in [1,2]
\end{aligned}
\tag{5.18}
$$

$$
\begin{aligned}
& k_{W_{\text{fai}}} \sim \mathcal{N}(\mu, \sigma) \\
& \mu = 0.009,\ 2\sigma = 15\% \\
& \text{bounded by:} \quad k_{l_{\text{mle}}} \in [0.005, 0.05]
\end{aligned}
\tag{5.19}
$$

The input distributions as well as their relation to one another and the total wing weight are shown in Fig.5.41. Each dot corresponds to one sample of the distribution, and the color of the dots are mapped from lower to higher W_{Wing} obtained, from blue to yellow, as indicated by the colorbar on the right of the plot. Unlike the leading and trailing edges, none of the miscellaneous weight input parameters show any clear correlation with the W_{Wing}, which indicates an insensitivity of the final weight to any changes in this W_{misc}. This means that the effects of any variations in W_{misc} are outweighed by variations in W_{le} or W_{te}.

The obtained spanwise weight distribution for the W_{misc} is shown in Fig.5.42. The plots show the μ value for the weight as the dashed line and the uncertainty around μ, 2σ, as the blue shaded area around the dashed line. Unlike the previous weight distributions, the uncertainty

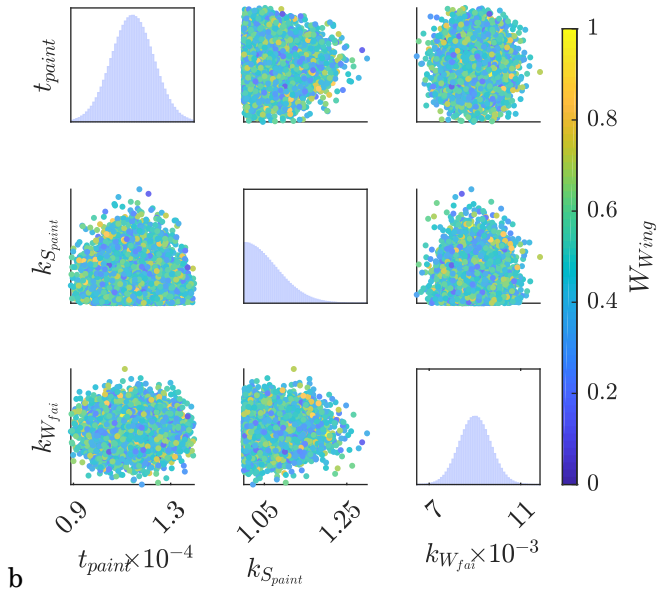

FIGURE 5.41. Miscellaneous weight input parameters distributions.

bound around the nominal miscellaneous items weight is very small and the shaded area barely distinguishable. Specific nodal weight distributions, i.e. uncertainty distributions for specific wing-box weights, are shown throughout the spanwise overall distribution, in the style of bar histograms.

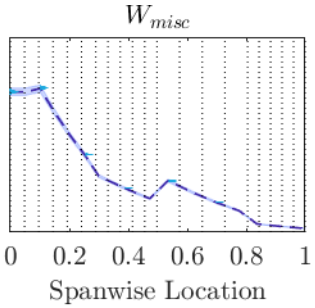

FIGURE 5.42. Miscellaneous weight spanwise variation, resultant from uncertain secondary weight inputs.

The miscellaneous weight is calculated for one wing and then distributed over its span following a wing-box volume fraction scale factor, i.e. the ratio of volume of one wing-box to the total volume of all boxes is used to allocate a lumped mass to each structural node. For that reason, also the uncertainty is proportional to the volume of the wing-box and consistent spanwise as a weight percentage. Over the span of the wing, W_{misc} has an average uncertainty of 1.85%, much lower than the previous weights. This can be explained by the fact that a big component of this weight is fixed, the wingtip weight W_{Wtip}.

5.2.4 Effects on primary weight

The secondary structure is introduced to the wing's beam formulation as lumped masses. Varying the secondary weight has, therefore, an effect on the aircraft loads calculated for the primary weight's wing-box sizing. Additionally, varying the extension of the fixed LE and TE, by varying the location of the front and rear spars, will affect the wing-box's chord length (c_{box}) and consequently introduce uncertainty on the sizing process, see Fig.5.39. In this section, the effect of varying the secondary weight input parameters on the wing's primary weight is discussed.

The obtained spanwise weight distribution for the skins W_{skn}, stringers W_{stg} and spars W_{spr} is pictured in Fig.5.43, and the total wing weight distribution in Fig.5.44. The plots show the μ value for the weight as the dashed line and the uncertainty around μ, 2σ, as the blue shaded area around the dashed line. Specific nodal weight distributions, i.e. uncertainty distributions for specific wing-box weights, are shown throughout the spanwise overall distribution, in the style of bar histograms. The W_{skn} has an average uncertainty of 9.08%, with a maximum of 16.89%

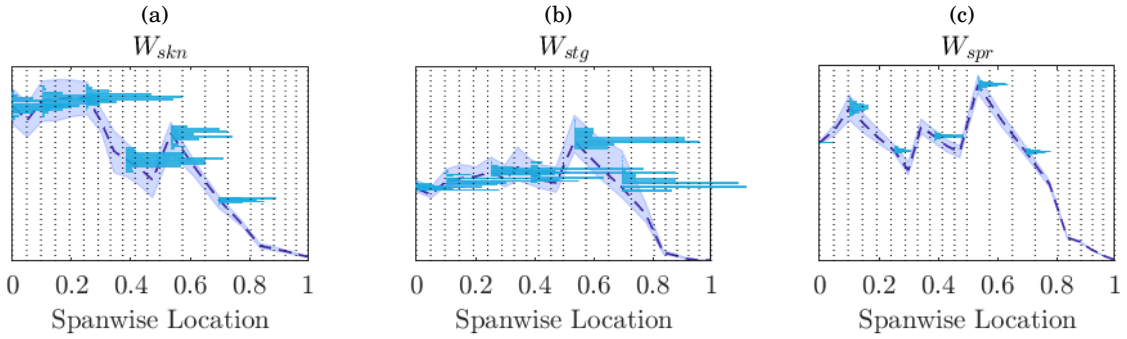

FIGURE 5.43. Wing-box elements weights spanwise variation, resultant from uncertain secondary weight inputs. (a) Skins weight; (b) Stringers weight; (c) Spars weight.

and minimum of 4.58%. The W_{stg} has an average uncertainty of 10.54%, with a maximum of 18.05% and minimum of 5.42%. The W_{spr} has an average uncertainty of 3.12%, with a maximum of 5.81% and minimum of 3.12%. The skins and stringers are more sensitive to the secondary weight uncertainty, which, again, is justified by the variation in c_{box}. This appears to be more prevalent for wing-boxes located at 30% of the span or over. The spars, on the other hand, are only affected by the uncertainty propagated to the aircraft loads, which is, on average, of 3.12%.

The W_{Wing} has an average uncertainty of 3.22%, with a maximum of 5.80% and minimum of 2.43%. Given that the secondary weight amounts to about 30% of the wing weight (see Tab.5.2), a variation on the secondary weight of generally 15%, results in an average of 3% uncertainty on the final wing weight.

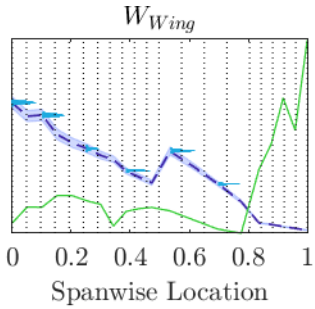

FIGURE 5.44. Total wing weight spanwise variation, resultant from uncertain secondary weight inputs.

5.2.5 Sensitivity Analysis (SA) on secondary structure weight

The standard regression coefficients indices (SRCI) are obtained for the secondary weight uncertainty. First, the W_{fle}, W_{mle} and the total LE structure weight W_{le} are analysed against its uncertain input parameters, shown in Fig.5.45. As expected, the W_{fle} is independent from $k_{l_{\text{mle}}}$ and $k_{d_{\text{mle}}}$, and owes all its sensitivity to f_{spr}. The W_{mle} is more sensitive to $k_{d_{\text{mle}}}$, with SRCI = 0.83, than to $k_{l_{\text{mle}}}$, with SRCI = 0.57. Combined, the LE weight is more sensitive to $k_{d_{\text{mle}}}$ with SRCI = 0.81, followed by $k_{l_{\text{mle}}}$ with SRCI = 0.55 and finally f_{spr} with SRCI = 0.22.

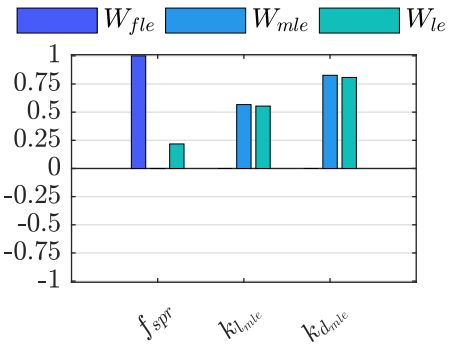

	W_{fle}	W_{mle}	W_{le}
f_{spr}	1.00	0.00	0.22
$k_{l_{\text{mle}}}$	0.00	0.57	0.55
$k_{d_{\text{mle}}}$	0.00	0.83	0.81

FIGURE 5.45. Sensitivity indices (SRCI) of the leading edge structures' (fixed and movable) weights, towards their input variables.

Additionally, W_{le} is more sensitive to W_{mle}, with SRCI = 0.98, than to W_{fle}, with SRCI = 0.22.

Next, the W_{fte}, W_{mte} and the total TE structure weight W_{te} are analysed against its uncertain input parameters, shown in Fig.5.47. Again, and as expected, the W_{fte} is entirely dependent on a_{spr}, but this time the correlation is negative SRCI = -1. This is because the further to the rear the aft spar is, and therefore the bigger c_{box} is, the smaller the FTE structure. W_{mte} is more sensitive to $k_{S_{\text{flap}}}$ with SRCI = 0.81, followed by $k_{S_{\text{ail}}}$ with SRCI = 0.56 and, finally, $k_{S_{\text{spoil}}}$ with SRCI = 0.14. This sensitivity order can be correlated to the relative size of these devices and therefore their impact on the weight of the MTE structure. Combined, the TE weight is more

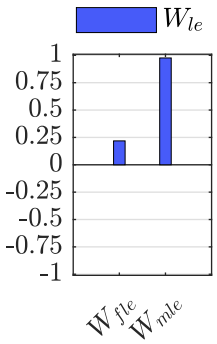

	W_{le}
W_{fle}	0.22
W_{mle}	0.98

FIGURE 5.46. Sensitivity indices (SRCI) of the leading edge weight, towards their structures' (fixed and movable) weights.

sensitive to a_{spr} with SRCI = −0.88, followed by $k_{S_{\text{flap}}}$ with SRCI = 0.38, $k_{S_{\text{ail}}}$ with SRCI = 0.27, and $k_{S_{\text{spoil}}}$ with SRCI = 0.06.

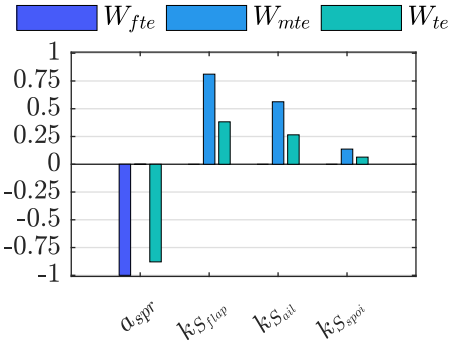

	W_{fte}	W_{mte}	W_{te}
a_{spr}	-1.00	0.00	-0.88
$k_{S_{\text{flap}}}$	0.00	0.81	0.38
$k_{S_{\text{ail}}}$	0.00	0.56	0.27
$k_{S_{\text{spoi}}}$	0.00	0.14	0.06

FIGURE 5.47. Sensitivity indices (SRCI) of the trailing edge structures' (fixed and movable) weights, towards their input variables.

Additionally, W_{te} is more sensitive to W_{fte}, with SRCI = 0.88, than to W_{mte}, with SRCI = 0.47.

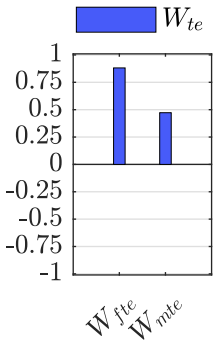

	W_{te}
W_{fte}	0.88
W_{mte}	0.47

FIGURE 5.48. Sensitivity indices (SRCI) of the trailing edge weight, towards their structures' (fixed and movable) weights.

The miscellaneous items weight is most sensitive to the thickness of the paint (t_{paint}) with SRCI = 1, and the rest of the input parameters are negligible, shown in Fig.5.49.

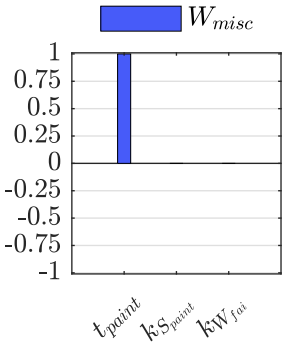

	W_{misc}
t_{paint}	1.00
$k_{S_{\text{paint}}}$	0.00
$k_{W_{\text{fai}}}$	0.00

FIGURE 5.49. Sensitivity indices (SRCI) of the miscellaneous items' weight, towards their input variables.

5.2.5.1 Effects on primary weight

Flaps, slats, FLE and FTE are driven by the high lift performance requirements of the wing. At the same time, varying the secondary weight input parameters impacts the aircraft loads used for primary wing sizing. Two of these parameters - front and rear spar location - will directly impact the ratio of fixed leading and trailing edges to wing-box structural sizes. Although this parameter is in reality defined very early in the design process, it is used in this analysis as a test case parameter to showcase the complex interdependencies between all the disciplines, computations and components involved in the total wing, and ultimately aircraft, sizing.

The sensitivity indices (SRCI) of the wing-box weights (W_{skn}, W_{stg} and W_{spr}) and total wing weight (W_{Wing}), towards the secondary weight inputs, are shown and listed in Fig.5.50. The inputs with higher impact on primary component weights are f_{spr} and a_{spr}, as predicted. For the total W_{Wing} however, the MLE and MTE parameters, such as $k_{\text{l}_{\text{mle}}}$, $k_{\text{d}_{\text{mle}}}$, $k_{\text{S}_{\text{flap}}}$ and $k_{\text{S}_{\text{ail}}}$, have a comparable effect to the one driven by the variation of f_{spr} and a_{spr} and therefore in primary weight.

The sensitivity indices (SRCI) of the wing-box weights (W_{skn}, W_{stg} and W_{spr}) and total wing weight (W_{Wing}), towards the secondary weight components, are shown and listed in Fig.5.51. W_{Wing} is more sensitive to W_{mle}, with SRCI = 0.76, followed by W_{fte} and W_{fle}, with SRCI = −0.45 and SRCI = −0.41 and finally W_{mte}, with SRCI = −0.24. W_{misc} has a negligible impact on all of the weights.

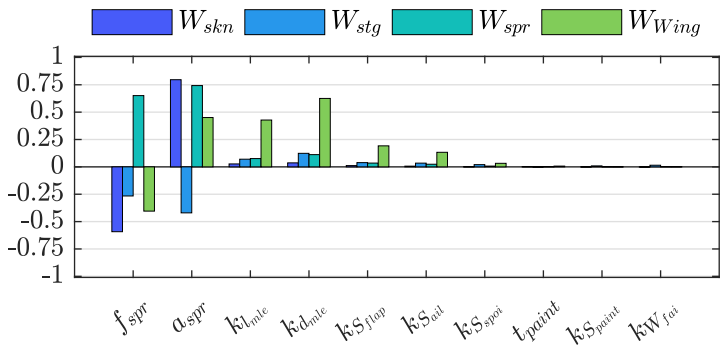

	W_{skn}	W_{stg}	W_{spr}	W_{Wing}
f_{spr}	-0.59	-0.27	0.65	-0.40
a_{spr}	0.80	-0.42	0.74	0.45
$k_{l_{\text{mle}}}$	0.03	0.07	0.08	0.43
$k_{d_{\text{mle}}}$	0.04	0.12	0.11	0.63
$k_{S_{\text{flap}}}$	0.01	0.04	0.03	0.19
$k_{S_{\text{ail}}}$	0.01	0.03	0.02	0.13
$k_{S_{\text{spoi}}}$	0.00	0.02	0.01	0.03
t_{paint}	0.00	0.00	0.00	0.01
$k_{S_{\text{paint}}}$	0.00	0.01	0.00	0.00
$k_{W_{\text{fai}}}$	0.00	0.02	0.00	0.00

FIGURE 5.50. Sensitivity indices (SRCI) of the wing-box elements (skins, stringers and spars) weights, towards the secondary structure weights input variables.

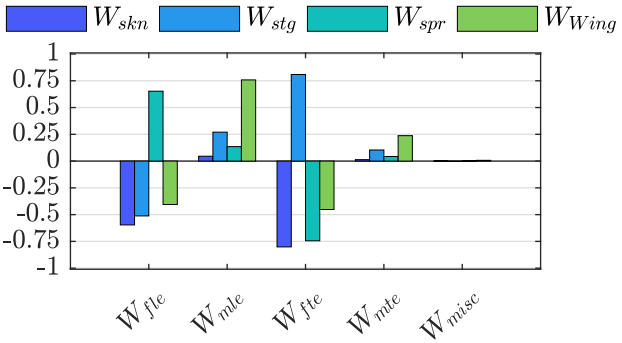

	W_{skn}	W_{stg}	W_{spr}	W_{Wing}
W_{fle}	-0.60	-0.51	0.65	-0.41
W_{mle}	0.05	0.27	0.14	0.76
W_{fte}	-0.80	0.81	-0.74	-0.45
W_{mte}	0.01	0.10	0.04	0.24
W_{misc}	0.00	0.00	0.00	0.00

FIGURE 5.51. Sensitivity indices (SRCI) of the wing-box elements (skins, stringers and spars) weights, towards the secondary structure weights.

5.3 Summary

A series of different uncertainty analysis were performed in WeiCoS. The first set of analysis is targeting the primary wing-box structure, particularly the skins, stringers and spars, and aims at understanding structural sizing routine sensitivities.

- The load case parameters, including Mach number M, altitude h, load factor n and fuel fraction f were varied around its operational (flight mission) lower and upper bounds. The aircraft could not trim for specific cases of the load case parameters, particularly for high h and n, and low M, and a correlation matrix was imposed to the input distribution.
  The aircraft loads, stress, sizing parameters and weights' spanwise distributions were obtained. A spanwise analysis was done to understand the sizing obtained for each wing-box section, including wing-box geometric properties, the stress at each wing-box and the sizing optimisation algorithm: the stringers and spars shear stress, σ_{stg} and τ_{spr}, are at its maximum constrained stress allowable for most of the wing span sections.
  The secondary structure component FLE is dependent on the dynamic pressure q_{D} a function on M and h and therefore also varies with the load case parameters variation. The sensitivity of the weights to the load case parameters is found: SRCI(W_{Wing}) is 0.86 for n and negligible for the rest; as for the FLE: SRCI(W_{fle}) is 0.52 for M and -0.85 for h. The load factor is the main contributor to the sensitivities in the sizing routine, except for the case of the FLE weight. Because the sizing is linear static, the critical load case corresponds to the combination for the maximum M, h, n and f.

- The aerodynamic loads are varied around its nominal critical value for $u = 2\sigma = x[1,5,15]\%$. For the three cases of uncertainty, the results were proven to be directly scalable, by a coefficient of determination $R^2 = 0.959$. For $u = 5\%$, the mean value of uncertainty (averaging for all the wing-box sections): for stress is $\overline{u}_{\sigma_{\mathrm{skn}}} = 1.34\%$, $\overline{u}_{\sigma_{\mathrm{stg}}} = 0.89\%$, $\overline{u}_{\sigma_{\mathrm{spr}}} = 0.89\%$, $\overline{u}_{\tau_{\mathrm{skn}}} = 2.12\%$ and $\overline{u}_{\tau_{\mathrm{spr}}} = 0.04\%$; for sizing is $\overline{u}_{t_{\mathrm{skn}}} = 3.05\%$, $\overline{u}_{A_{\mathrm{stg}}} = 7.12\%$ and $\overline{u}_{t_{\mathrm{spr}}} = 5.04\%$; and for weight is $\overline{u}_{W_{\mathrm{skn}}} = 3.05\%$, $\overline{u}_{W_{\mathrm{stg}}} = 7.12\%$, $\overline{u}_{W_{\mathrm{spr}}} = 4.87\%$ and, finally, for the weight of the wing $\overline{u}_{W_{\mathrm{Wing}}} = 2.56\%$. Because of scalability, if for $u = 5\% \equiv \overline{u}(W_{\mathrm{Wing}}) = 2.56\%$, for $u = 1\% \equiv \overline{u}(W_{\mathrm{Wing}}) = 0.51\%$, for example. Spanwise, loads uncertainty has different impacts on different sections of the wing for the different elements.

- Uncertainty in the material properties of the wing-box, particularly uncertainty in the tensile yield strength σ_{allow}, is analysed and the effect on the weight of the wing is quantified. A normal distribution is defined for which $\mu = 276$MPa and $u = 2\sigma = 15\%$, and the quantiles $[q_{0.05}, q_{0.95}] = [242,310]$MPa are identified. As expected, for decreasing values of σ_{allow}, the wing weights increase, and vice versa. For example, for $q_{0.05} \equiv \sigma_{\mathrm{allow}} = 242$MPa: $W_{\mathrm{skn}} = +1.04\%$; $W_{\mathrm{stg}} = +66.21\%$; $W_{\mathrm{spr}} = +17.77\%$ and $W_{\mathrm{Wing}} = +9.90\%$. As seen before, the stringers and spars stress are at their maximum constrained allowable level for most of the

wing span and therefore these elements are the most affected ones in a decrease in σ_{allow}. Moreover, the spars and wing's distributions are quasi-normal in shape whereas the skins and stringers' are more skewed: $\xi(W_{\text{skn}}) = -1.20$ and $\xi(W_{\text{stg}}) = 0.25$, see Fig.5.21.
The spanwise distribution of uncertainty of the weights is also obtained for different levels of input uncertainty: $u(\sigma_{\text{allow}}) = [1, 5, 10, 15]\%$, see Fig.5.23. Following the same criteria for scalability, the overall weights were proven to be directly scalable for different uncertainty levels, with $R^2 = 0.972$. This means that, for $u(\sigma_{\text{allow}}) = [1, 5, 10, 15]\%$, $\overline{u}(W_{\text{Wing}}) = [0.57, 2.87, 5.73, 8.6]\%$.

- The stress constraints activation and its effect on sizing is explored. The constraints used in the stress analysis are detailed in Appendix A. The activated constraints are: stringers allowable stress $\sigma_{\text{stg}}/\sigma_{\text{allow}}$, minimum imposed stringers' Area $A^{\text{stg}}_{\text{min}}$, Von Mises stress for spars $\sigma^{\text{v}}_{\text{spr}}$, the principal stress σ_{P} and the Farrar's efficiency factor F.
The sensitivity of the weight to the stress constraints is quantified: W_{Wing} is most sensitive to $\sigma_{\text{stg}}/\sigma_{\text{allow}}$ with SRCI=0.65, $\sigma^{\text{v}}_{\text{spr}}$ with SRCI= 0.34, the column buckling constraint for the skin-stringer panel $\sigma_{\text{stg}}/\sigma_{\text{col}}$ with SRCI= 0.27 and the stringer's crippling stress $\sigma_{\text{stg}}/\sigma_{\text{cc}}$ with SRCI= 0.24.

- The engine and pylon weight ($W_{\text{eng,pyl}}$) was varied around its nominal baseline value, to account for measure the impact of different engine configurations on the wing's structural sizing. For $u(W_{\text{eng,pyl}}) = 15\%$: The Torque $|M_x|$, followed by the vertical shear $|F_z|$ are the most impacted aerodynamic loads with $\overline{u}(|M_x|) = 21.54\%$ and $\overline{u}(|F_z|) = 1.47\%$; the variation on the primary structure weights yields $\overline{u}(W_{\text{skn}}) = 0.34\%$, $\overline{u}(W_{\text{stg}}) = 0.90\%$ and $\overline{u}(W_{\text{spr}}) = 1.95\%$; and the total wing weight $\overline{u}(W_{\text{Wing}}) = 0.34\%$, with a maximum of $u_{\text{max}}(W_{\text{Wing}}) = 0.87\%$ towards the root of the wing and minimum $u_{\text{min}}(W_{\text{Wing}}) = 0.04\%$ at the tip.
$W_{\text{eng,pyl}}$ is located at around 0.3 of the wing span, $b_{\text{ep}} = 0.3b_{\text{st}}$. Despite this, uncertainty in sizing and wing elements weight is carried through the whole span, being more prominent at wing-box sections from the root of the wing until b_{ep}. The lumped masses affect the wing loading and, therefore, uncertainty is not localised. Local effects can be captured and further explored by incorporating empirically obtained weight functions or knowledge-based factors into the framework.

The first set of analysis is targeting the secondary structure and the results are divided by Leading Edge (LE), Trailing Edge (TE), miscellaneous items (misc), the effect of the secondary structure weight uncertainty on the primary structure and sensitivity analysis.

- The LE uncertain input parameters are the location of the front spar f_{spr} and the length and depth of the movable LE, respectively $k_{l_{\text{mle}}}$ and $k_{d_{\text{mle}}}$. f_{spr} and $k_{l_{\text{mle}}}$ are defined by normal probability distributions, with $u = 15\%$ and μ and bounding parameters as follows: for f_{spr}, $\mu = 0.14$ and $x \in [0.10, 0.20]$; for $k_{l_{\text{mle}}}$: $\mu = 0.9$ and $x \in [0.70, 0.95]$. A uniform distribution is

used to define $k_{d_{\text{mle}}}$, with parameters $a = 0.15$ and $b = 0.20$.
Over the span of the wing, $\overline{u}(W_{\text{fle}}) = 15.21\%$, proportionate to the input uncertainty, and $\overline{u}(W_{\text{mle}}) = 23.60\%$.

- The TE uncertain input parameters are the location of the aft spar a_{spr} and the area factors for the flaps, ailerons and spoilers, respectively $k_{S_{\text{flap}}}$, $k_{S_{\text{ail}}}$ and $k_{S_{\text{spoi}}}$. a_{spr}, $k_{S_{\text{flap}}}$ and $k_{S_{\text{spoi}}}$ are defined by normal probability distributions, with $u = 15\%$ and μ and bounding parameters as follows: for a_{spr}, $\mu = 0.64$ and $x \in [0.60, 0.70]$; for $k_{S_{\text{flap}}}$: $\mu = 0.18$ and $x \in [0.15, 0.21]$; and for $k_{S_{\text{spoi}}}$: $\mu = 0.04$ and $x \in [0.00, 0.05]$. A uniform distribution is used to define $k_{S_{\text{ail}}}$, with parameters $a = 0.03$ and $b = 0.05$.
  Over the span of the wing, $\overline{u}(W_{\text{fte}}) = 15.49\%$, proportionate to the input uncertainty, and $\overline{u}(W_{\text{mte}}) = 11.64\%$.

- The miscellaneous items account for wing paint, wingtip and fairings. Its uncertain input parameters are the paint's thickness and area factor, respectively t_{paint} and $k_{S_{\text{paint}}}$, and a weight factor for the fairings $k_{W_{\text{fai}}}$. All three are defined by normal probability distributions, with $u = 15\%$ and μ and bounding parameters as follows: for t_{paint}, $\mu = 0.1143$ and $x \in [0.0889, 0.1397]$; for $k_{S_{\text{paint}}}$: $\mu = 1$ and $x \in [1, 2]$; and for $k_{W_{\text{fai}}}$: $\mu = 0.009$ and $x \in [0.005, 0.05]$.
  Over the span of the wing, $\overline{u}(W_{\text{misc}}) = 1.85\%$, much lower than the previous weights uncertainty, justified by a big component of this weight being fixed, the wingtip weight W_{Wtip}.

- Varying the secondary structure weight has an effect on the primary structure sizing, as a result of varying the aerodynamic loads and the spar's locations, f_{spr} and a_{spr}, and therefore the wing-box geometry. This uncertainty introduced on the primary structure is quantified: $\overline{u}(W_{\text{skn}}) = 9.08\%$, $\overline{u}(W_{\text{stg}}) = 10.54\%$ and $\overline{u}(W_{\text{spr}}) = 3.12\%$.
  The secondary weight amounts to about 30% of the wing weight, a variation on the secondary weight of 15%, results in $\overline{u}(W_{\text{Wing}}) = 3.22\%$.

- The weights' sensitivity towards the secondary structure uncertain inputs is quantified and W_{Wing} is most sensitive to $k_{d_{\text{mle}}}$, followed by a_{spr}, $k_{l_{\text{mle}}}$ and f_{spr}, with respective SRCIs= $[0.65, 0.45, 0.43, -0.40]$.
  In terms of weight: W_{Wing} is most sensitive to W_{mle}, followed by W_{fte}, W_{fle}, W_{mte} and finally W_{misc}, with respective SRCIs= $[0.76, -0.45, -0.41, 0.24, 0.00]$.

CHAPTER 6

RELIABILITY-BASED UNCERTAINTY BACKPROPAGATION AND THE WEIGHT CONVERGENCE CORRIDOR

Reliability-based analysis is crucial for project milestones assessment. In weight engineering, for instance, at the milestone, target weights as well as reliability levels are sought. In this chapter, a reliability level is set for the total wing weight in 6.2.1. The input variability that corresponds to the respective probability of failure is analysed. Note that, in this case, the probability of failure corresponds to failure to meet the desired target weight with desired reliability level. Then, a new target weight with the same reliability level is defined in 6.2.2. For the desired target weight and reliability level, the correspondent input probability distributions are obtained using uncertainty backpropagation by the means of artificial neural networks. ANNs are chosen for their ability to handle highly parallel nonlinear computations, without the need for any prior knowledge about the inputs. In pair with these reasons, time and computational expenses were constrained for this exercise, and ANNs capability to deliver quality results under these circumstances was key. Finally, the evolution of the design variables and correspondent weights, through the design process, is shown, i.e. the weight convergence corridor, in 6.2.3. As information matures and design features become fixed, uncertainty decreases. Moreover, with a weight management process in place, the expectation is that the status weight will converge to the desired target weight, as changes are progressively embodied into the aircraft.

6.1 Robust and reliability-based design optimisation

Robustness aims at making a product's performance as insensitive to variations as possible, whether these are production tolerances, parametric uncertainties, model or numerical sensitivities or other. Robust design does not try to reduce uncertainty, instead it computes specific values

for the design variables such that the final product's performance's robustness is maximum. In other words, it optimises the design variables, taking into account its equality and inequality constraints. Model uncertainty is analysed in [134] where the robust design is optimised for two objectives: to minimise the impact of the model's uncertainty and to minimise the variation impact of the design variables (sensitivity analysis).

A review of the different approaches to robust design optimisation is presented in [135], including non-probabilistic or deterministic, mathematical programming methods, and probabilistic, stochastic programming methods. The deterministic approach considers nominal values for the design variables and the stochastic approach considers variations on design variables [136]. The use of stochastic expansion methods, namely the Polynomial Chaos Expansion PCE and Stochastic Collocation SC, for robust design under uncertainties is explored in [137] for global and local sampling of the uncertain variables.

Multidisciplinary Design Optimisation (MDO) is the systematic approach to optimise complex problems involving a number of interacting disciplines such as aircraft and spacecraft design, and industrial manufacturing applications [138]. The disciplines involved in aircraft design are previously shown in Fig.1.1: mission requirements and performance, structural sizing, aerodynamics, loads and loadability studies, geometry, materials, systems, manufacturing and cost. Weight is a variable that has an impact on all the disciplines driving the aircraft design and vice-versa. For that reason, weight has the potential to reduce the dimensionality of a MDO problem to a multiple constraint, uni-disciplinary one. A decoupled Individual Discipline Feasible/Polynomial Chaos formulation is proposed in [139] for MDO, said to ensure the system's multidisciplinary physical feasibility for the whole uncertain design space. It works by iteratively computing surrogate models of the functional coupling relations between disciplines.

Reliability aims at making a product perform its intended function for a desired probability of success. It informs the user how likely the product is not to fail. Whereas robust design aims at optimising the design for stability under uncertainty, reliability-based design (RBD) provides the range of the design space for which the desired reliability level is achieved. Similarly to robust design, often reliable design uses a performance function to predict failure. Consider the performance function $g(X)$, the probability of failure is given by $P_f = Pg(X) < 0$. The respective reliability or probability of success is then $\beta = 1 - P_f$. This approach is called performance-based design [140].

Reliability-Based Design Optimisation (RBDO) is often associated with uncertainty backpropagation problems (see sec.1.2.3) [44, 141]. Working from a target reliability level β, RBD inverts the simulation to compute the design options that hold β. Moreover, it is crucial to evaluate the trade-off costs between the design options. Whether these are costs associated with product development, performance and/or robustness. RBD Optimisation (RBDO) is the optimisation method that minimises the cost function in use for a reliable design [142].

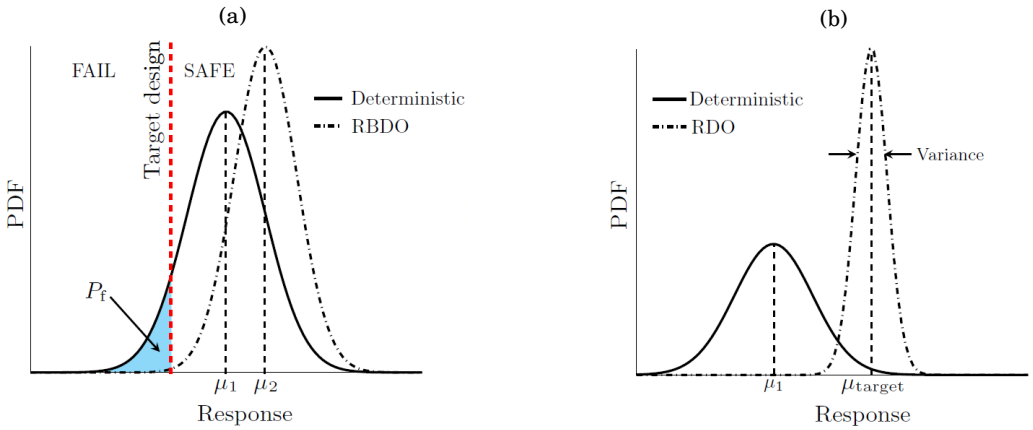

FIGURE 6.1. Variations in the PDFs of a generic design response due to (a) Reliability-Based Design Optimisation (RBDO) and (b) Robust Design Optimisation (RDO); RDO minimises the standard deviation of the response around a target mean value, whilst RBDO minimises P_f.

Reliability-based and robust design optimisations are contrasted and compared in Othman et al. in [143], for the aeroelastic tailoring of composite aircraft wings. A framework developed for wing structural sizing and detailed composite ply configurations computation is used with a representative regional jet airliner finite element wing box model. The PDFs in Fig.6.1 show the changes in a generic design response due to RBDO and RDO. The reliable design minimises the probability of failure P_f, whilst the robust design minimises the output's variance or standard variation around a target mean value μ_{target}.

6.2 Reliability-based analysis on the wing's secondary structure

Recall the weight breakdown for the secondary, amounting to 28% of the total wing weight.

TABLE 6.1. Wing's secondary weight breakdown.

Leading Edge	fixed	10.77%	2.80%
	movables		7.97%
Trailing Edge	fixed	16.07%	7.31%
	movables		8.76%
Miscellaneous		1.29%	
Secondary Mass Total		28.13%	

The secondary structure weight model is used as a test case for the methodologies implemen-

ted in this chapter.

The leading edge weight and its input parameters: the chordwise location of the front spar, f_{spr}, and the length and depth of the movable structure, $k_{l_{\text{mle}}}$ and $k_{d_{\text{mle}}}$ respectively; are used. The weight model formulae for the secondary structure is defined in sec.4.1.3.

For the results presented in this chapter, unless mentioned otherwise (a uniform distribution is used), normal PDFs were fitted to the distributions in order to obtain μ and σ.

The Artificial Neural Networks deployed in the analysis presented in this chapter used 10000 data points: 70% of which were used for training and to adjust the ANN according to their error; 15% for validation, i.e. to measure ANN's generalisation and stop training before overfitting or when the generalisation stops improving; And the remaining 15% for independent testing, i.e. to be used as a completely independent test of network performance during and after training. The network used to fit or map the data points is a two-layer feed forward network, with a sigmoid transfer function in the hidden layer and a linear transfer function in the output layer. There are 10 hidden neurons in the network and the training algorithm used is the Levenberg-Marquardt, also known as the damped least-squares method. This algorithm is used for non-linear least squares fitting, working to approximate the model to a linear regression and refine the parameters iteratively.

6.2.1 Wing weight with reliability level β

Consider the total wing weight obtained from an uncertainty study of the secondary weight variables, correspondent to the sum of the spanwise distribution in Fig.5.44. The probability density function of the set, and its 95% quantile, indicating the 95% reliability level, is shown in Fig.6.2. The probability of failure P_f is indicated in red.

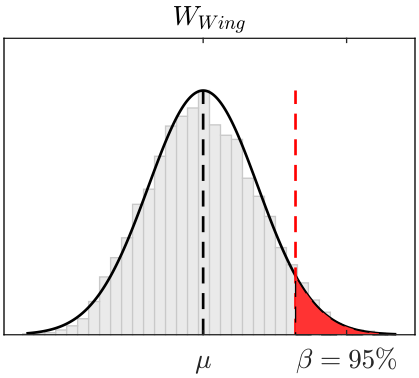

FIGURE 6.2. Wing weight PDF and reliability level $\beta = 1 - P_f$. The P_f is indicated in red.

The WeiCoS' wing structural sizing was run using the secondary weight input variables as the uncertain variables. The variation on the secondary weight impacts the aerodynamic loads used to compute the primary weight. Moreover, the location of the front and aft spar are two of

the uncertain variables to the secondary weight model. These two variables have a direct effect on the dimensions of the wing-box, namely the box chord c_{box}, and therefore on the primary weight as well. The simulated values obtained are explored with the use of parallel-coordinate plots. The latter are a great visual indicator of the input variability and correlations between variables, for specific areas of the PDF or input/output margins, e.g. the weight's P_f.

The values for W_{Wing}, W_{PW} and W_{SW} are shown in Fig.6.3. The total wing weight is obtained by the sum of its primary and secondary structures, and pylon and landing gear attachments (fixed weights), being that W_{PW} amounts to about 65% of the total, W_{SW} to 28% and the attachments to 7%. The P_f happens for greater values of W_{Wing}, and for a specific combination of W_{PW} and W_{SW}: for lower values of W_{SW}, W_{PW} takes greater values.

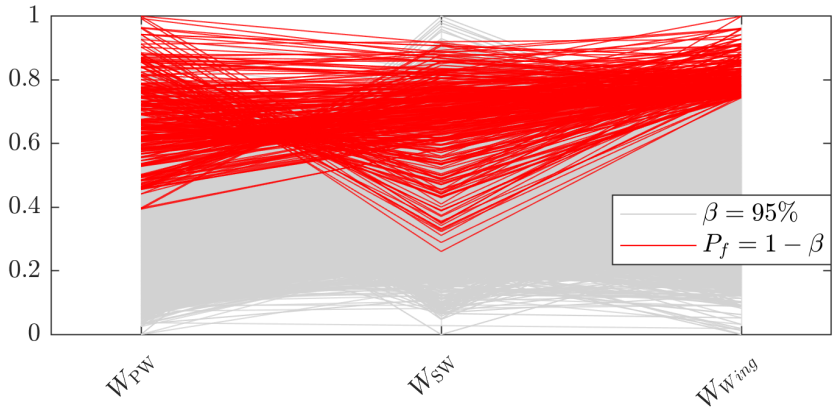

FIGURE 6.3. Parallel-coordinate plot showing the variability of the primary and secondary weight, for the P_f of a wing weight with reliability level $\beta = 95\%$.

Similarly, the secondary weight is obtained by the sum of the leading and trailing edge and miscellaneous items weights, respectively W_{le}, W_{te} and W_{misc}. These values are shown in Fig.6.4. Only greater values of W_{le} are included in the P_f set, which indicates a larger sensitivity of W_{Wing} towards W_{le}.

Lastly, the data values obtained for the W_{le}'s uncertain input variables: f_{spr}, $k_{l_{\text{mle}}}$ and $k_{d_{\text{mle}}}$, are shown in Fig.6.5. Two patterns can be distinguished for the P_f set of values: lower values of f_{spr}, combined with greater values of $k_{l_{\text{mle}}}$; or lower values of f_{spr}, combined with values around the nominal for $k_{l_{\text{mle}}}$ and $k_{d_{\text{mle}}}$.

The individual distributions of all the input design variables and component level weights are also obtained. Consider that there are other uncertain variables in this study that also impact the weight of the wing. As expected, higher primary and secondary weights are driving W_{Wing} to increase, leading to its P_f values; shown in Fig.B.5.

A heavier leading edge structure and a lighter trailing edge structure result in a greater wing weight, as shown in Fig.6.7. The front spar being pushed to the front of the wing and therefore resulting in a lighter FLE, is overruled by the geometric and weight increase of MLE (74% of the

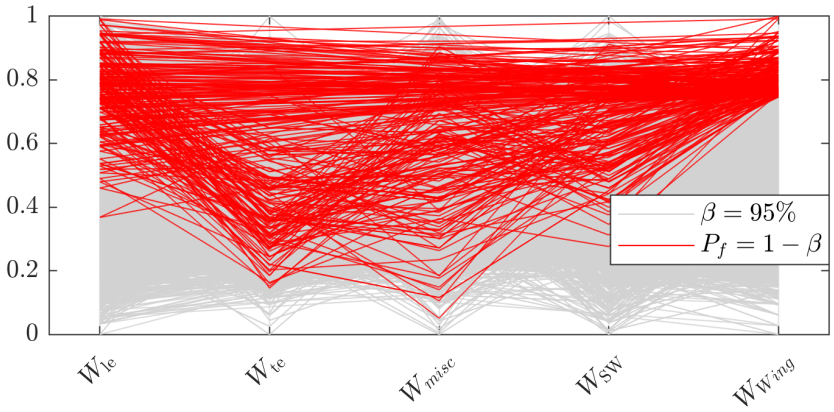

FIGURE 6.4. Parallel-coordinate plot showing the variability of the secondary weight components: leading and trailing edges and miscellaneous items; for the P_f of a wing weight with reliability level $\beta = 95\%$.

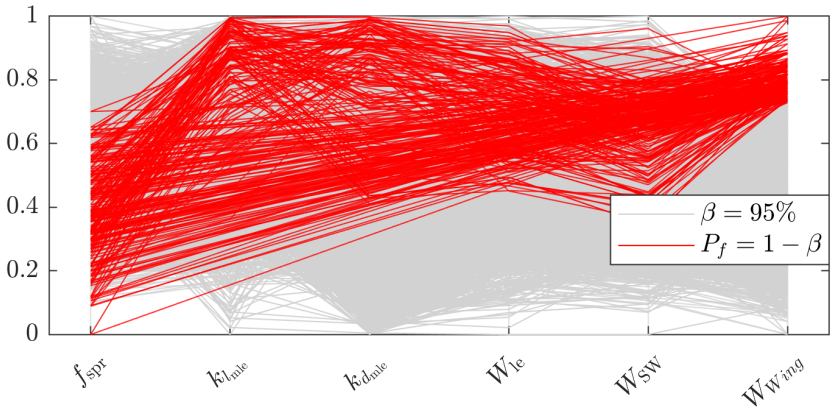

FIGURE 6.5. Parallel-coordinate plot showing the variability of the leading edge weight and respective input parameters, for the P_f of a wing weight with reliability level $\beta = 95\%$.

total W_{le}). The miscellaneous items weight has the same μ and σ than the original distribution, which indicates low sensitivity of the final W_{Wing} to W_{misc}.

At greater risk for failure are lower values for the front spar and larger values for the length and depth of the movable leading edge structure, as shown in Fig.6.8. If the spar is located further to the front of the wing, the wing-box chord will increase, which translates to an increase on the covers (primary) weight. This effect is greater than the increase on the fixed leading edge weight, when placing the front spar further to the back of the wing. Larger length and depth of the leading edge results in a heavier movable structure, and therefore in a heavier wing.

Understanding what might drive the design to a failure area, including the correlations and dependencies between drivers or input variables, correlated to the sensitivity of the final

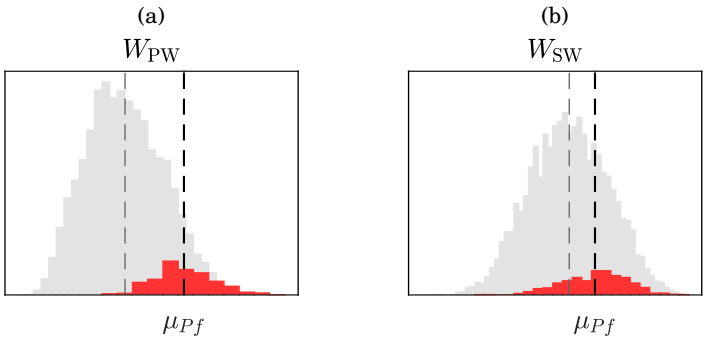

FIGURE 6.6. P_f distribution of the primary and secondary weights. (a) Primary weight; (b) Secondary weight.

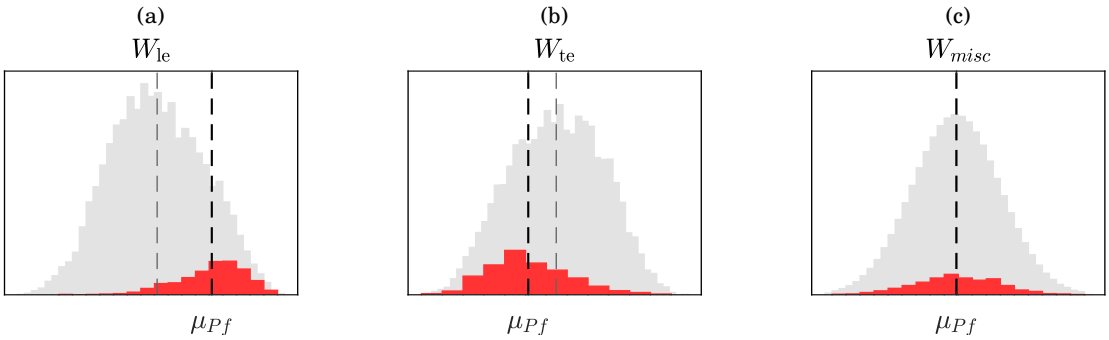

FIGURE 6.7. P_f distributions of the discretised secondary weights. (a) Leading edge; (b) Trailing edge; (c) Miscellaneous items.

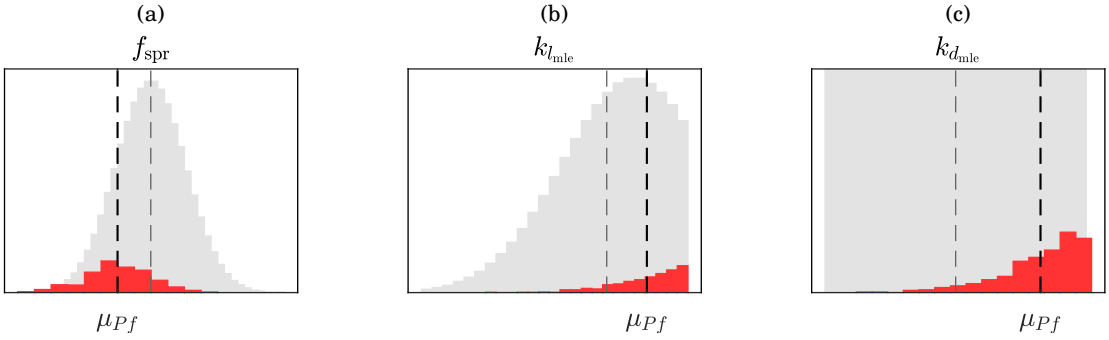

FIGURE 6.8. P_f distributions of the leading edge weight input parameters. (a) Front spar; (b) Length of movable leading edge structure; (c) Depth of movable leading edge structure.

Variable of Interest to each one, is crucial. In this case, the location of the front and aft spars is a design decision that has a great impact on the structural distribution of the weight of

the wing. This is a parameter in the secondary weight equations used in the framework, that also impacts the sizing of the wing-box and therefore impacts primary weight. It is a test case parameter to exercise the model and the methodology. With the addition of increased complexity modules into this framework, this parameter would expectedly be frozen at an early stage in the design and smaller changes would then be in scope. Additional parallel-coordinate plots and the individual distributions for P_f for the trailing edge, the miscellaneous items weights and their input variables, can be consulted in Appendix B. The correlations between the front and aft spar locations and the primary and secondary weights, for the P_f, is also presented.

6.2.2 Target wing weight with reliability level β

Often times, the aircraft's status weight is higher than the target weight. The expectation is that, throughout the design process, technological advancements and design optimisations will occur and, eventually, the weights will converge. Uncertainty backpropagation is able to predict what combination of design features are suitable to deliver the required target weight. In this section, the case of uncertain secondary weight structure variables, for wing sizing, is used to build a map between a target weight and the respective input variable distributions.

Consider the previous case of the total wing weight, mean value μ and standard deviation σ, shown in grey in Fig.6.9. Now consider its associated target weight with mean $\mu' < \mu$ (-2.29%) and $\sigma' < \sigma$ (-19.49%), and a reliability level of 95%, indicated in blue.

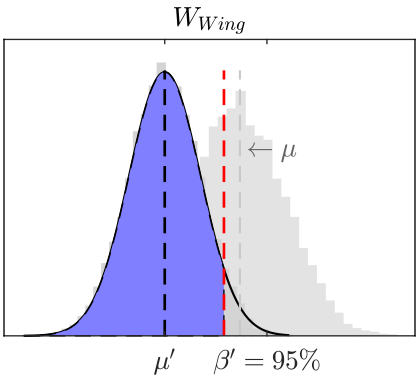

FIGURE 6.9. Wing target weight PDF and reliability level β.

The individual input distributions that result in this target weight are obtained using ANNs to propagate uncertainty backwards through the sizing. The primary and secondary weights' distributions are shown in Fig.6.10 and the new distributions for target wing weight are highlighted in blue. Both weights must be lighter, and their standard deviations reduced: for W_{PW}: $\mu' < \mu$ (-2.23) and $\sigma' < \sigma$ (-59.55%); for W_{SW}: $\mu' < \mu$ (-3.78) and $\sigma' < \sigma$ (-53.50%).

The original and new target distributions for leading and trailing edge and miscellaneous items weights are shown in Fig.6.11. W_{le} is computed to be lighter in order to achieve the desired

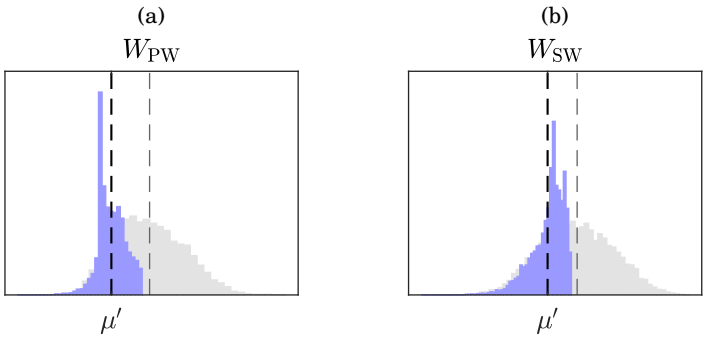

FIGURE 6.10. Distributions of the primary and secondary weights, for the wing target weight. (a) Primary weight; (b) Secondary weight.

target: $\mu' < \mu$ (-10.26) and $\sigma' < \sigma$ (-49.75%). However, W_{te} is predicted slightly heavier than the original weight: $\mu' > \mu$ (+1.53) and $\sigma' > \sigma$ (-39.12%). The location of the a_{spr} is pushed further to the front of the wing, from its nominal location, in order to bring c_{box} and consequently W_{PW} down. Consequently, W_{fte} resulted heavier. Despite of the rest of the input variables ($k_{S_{\mathrm{flap}}}$, $k_{S_{\mathrm{ail}}}$ and $k_{S_{\mathrm{spoi}}}$) contributing to a lighter W_{mte}, W_{te} is, overall, increased. Lastly, for W_{misc}, $\mu' > \mu$ (+0.10) and $\sigma' < \sigma$ (-73.21%). The miscellaneous items contribute to about 1% of the weight of the wing and t_{paint} is the main contributor to its uncertainty, see Fig.5.49. The estimated distribution for t_{paint} lands outside of its original (3σ space, $\mu' > \mu$ (+71.59%) and $\sigma' > \sigma$ (+33.47%)) and therefore it is deduced that the error induced by the ANN makes this distribution for W_{misc} inconclusive. As the overall contribution of the W_{misc} is small and, typically, engineering effort is limited due to incurring costs, keeping track of the amount of paint being used but not concentrating efforts on the rest would be a relevant course of action. The probability distributions for the input parameters to W_{te} and W_{misc} can be consulted in Appendix B.

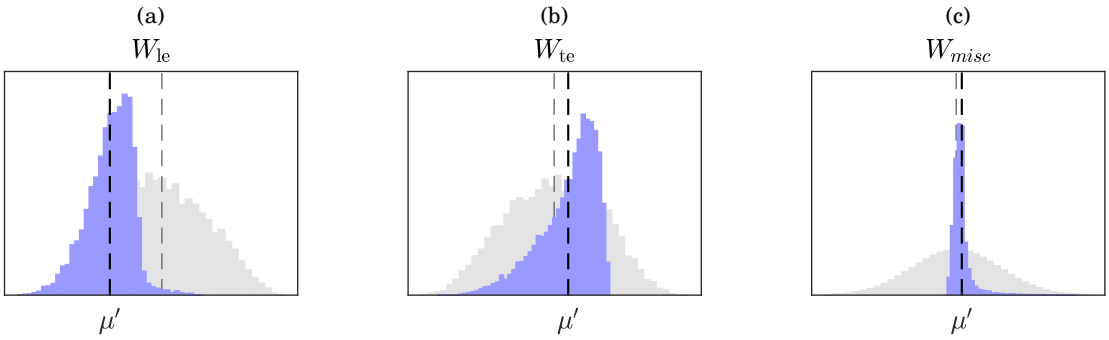

FIGURE 6.11. Distributions of the discretised secondary weights, for the wing target weight. (a) Leading edge; (b) Trailing edge; (c) Miscellaneous items.

Lastly, the input parameters to the variation of W_{le} are analysed individually. For f_{spr}: $\mu' > \mu$

(+5.41) and $\sigma' > \sigma$ (+45.62%). The location of the front spar impacts both secondary and primary weights and therefore its standard deviation increase. For $k_{l_{\text{mle}}}$: $\mu' < \mu$ (-5.60) and $\sigma' < \sigma$ (-9.83%). For $k_{d_{\text{mle}}}$: $\mu' < \mu$ (-8.65) and $\sigma' < \sigma$ (-39.31%). The change in distribution from uniform to quasi-normal is responsible for the decrease in standard deviation of $k_{d_{\text{mle}}}$. Moreover, both MLE inputs new distributions contribute to a lighter W_{mle}.

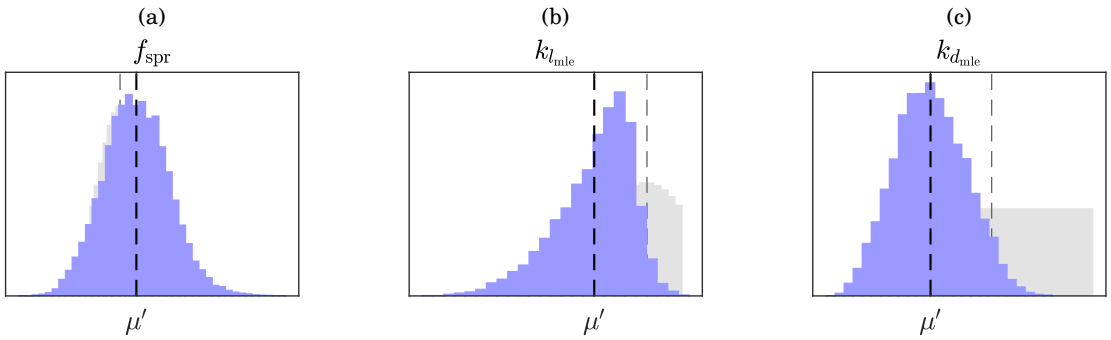

FIGURE 6.12. Distributions of the leading edge weight input parameters, for the wing target weight. (a) Front spar; (b) Length of movable leading edge structure; (c) Depth of movable leading edge structure.

Further down the level of complexity of a specific variable, i.e. going from W_{Wing} to W_{SW}, W_{le} and finally f_{spr}, uncertainty (equivalently σ) increases. There is more margin for variability at a lower level design feature, for the goal of achieving a desired target weight, than there is at higher levels of complexity. The neural networks obtained had an average maximum relative error of 15% in its predictions, i.e. the maximum difference between predicted and real values is on average 15% for the three ANNs computed. In an attempt to decrease the 15% estimated error, an increase in data points was investigated. It was concluded that the error plateaued at 15%, meaning that increasing the data set would not improve accuracy in the results. This suggests that the error might be in large affected by the algorithm used, i.e. the inability for Levenberg-Marquardt to deal with non-linearities in the data.

Performing backpropagation for target weights or target design features allows for rapidly predicting the margins for variability within lower level complexity variables, as well as target's viability. It is an essential tool to produce predictive scenarios for design solutions. Additionally, as changes are progressively embodied into the aircraft, they can be added to the predictive ANN, for more accurate estimations.

6.2.3 Convergence Corridor

Recall the representative evolution of the status, outlook and target weights, throughout the design phases, in the weight convergence corridor, shown in Fig.1.7. Now consider three representative project milestones in the corridor, numbers 1, 2 and 3, indicated in orange, yellow and

green, respectively, in Fig.6.13. In this section, WeiCoS is used to track the design variables and component weights' evolutions throughout the design process, specifically at milestones 1,2 and 3, against a target weight.

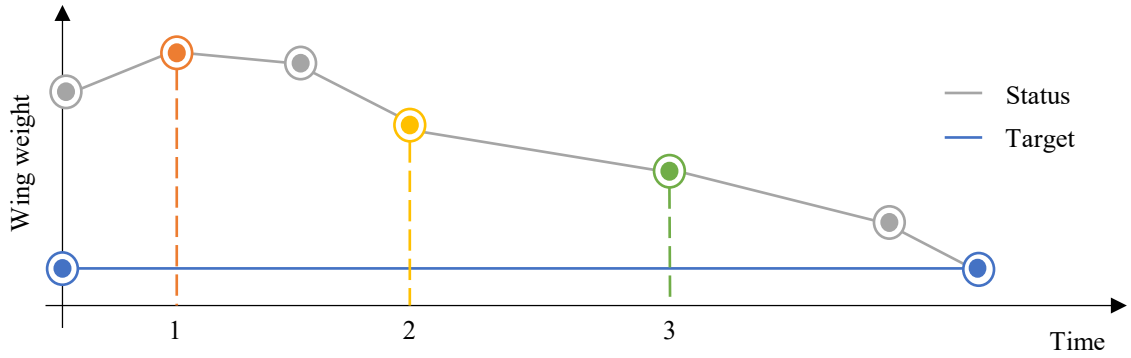

FIGURE 6.13. Weight convergence corridor for status and target weights, and project milestones 1, 2 and 3.

As the design process evolves, the amount of information on the final wing design increases and the likelihood of that information changing decreases. Design variables become fixed and are embodied into the aircraft. In WeiCoS, this translates to a decreasing level of uncertainty in the input variables being propagated in the sizing, through to the component weights, and finally the total wing weight. Aligning the weight tracking with a management process, so that the status weight reaches its desired target, within its reliability level and at the desired milestone, is the goal. Employing the weight in Fig.6.9 as target weight and $\beta = 95\%$, the backpropagation results for the individual input variables distributions are taken as guidelines for the design features. The results follow, for which the original distribution is represented in grey, the distribution at milestone 1 in orange, at 2 in yellow and green at 3.

The location of the front spar is shown in Fig.6.14. Its mean value is fixed early on in the design process and only its uncertainty continues to decrease until a CL of 95% is reached at milestone 3: $\mu_1 \approx \mu_2 \approx \mu_3 \approx \mu$; and $\sigma_1 < \sigma$ (-50.30%), $\sigma_2 < \sigma$ (-79.76%) and $\sigma_3 < \sigma$ (-95.04%).

The length of the movable leading edge structure is shown in Fig.6.15. Its mean value decreases from its original μ, and the uncertainty at milestone 3 is still 30%: $\mu_1 < \mu$ (-2.80%), $\mu_2 < \mu$ (-6.17%) and $\mu_3 < \mu$ (-9.59%); and $\sigma_1 < \sigma$ (-21.38%), $\sigma_2 < \sigma$ (-49.79%) and $\sigma_3 < \sigma$ (-69.97%).

The depth of the movable leading edge structure takes the form of an uniform distribution, contrary to the normal distributions of the two other inputs, and is shown in Fig.6.16. Its mean value decreases from its original μ, and so does the interval of values: $\mu_1 < \mu$ (-2.85%), $\mu_2 < \mu$ (-10.58%) and $\mu_3 < \mu$ (-11.27%); and $|a_1 - b_1| < |a - b|$ (-20.01%), $|a_2 - b_2| < |a - b|$ (-86.00%) and $|a_3 - b_3| < |a - b|$ (-91.00%).

Given the inputs at the 3 milestones, the weights obtained with the sizing are shown below, including leading edge weight in Fig.6.17, secondary weight in Fig.6.18 and final wing weight in

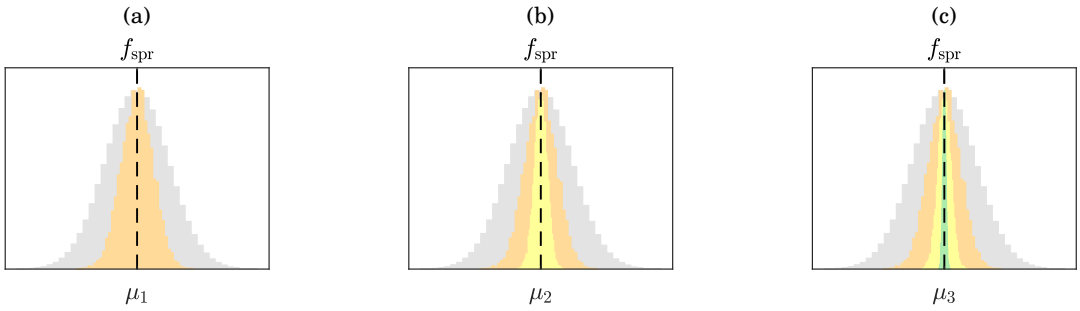

FIGURE 6.14. Front spar location evolution through the weight convergence corridor, at milestones (a) 1; (b) 2; (c) 3.

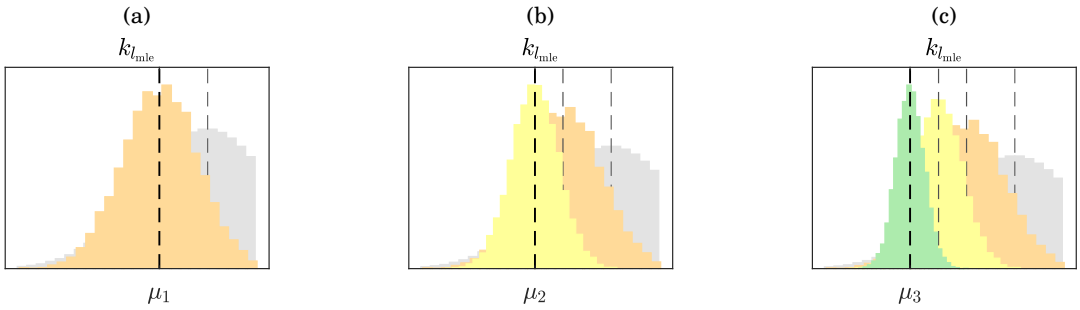

FIGURE 6.15. Length of MLE evolution through the weight convergence corridor, at milestones (a) 1; (b) 2; (c) 3.

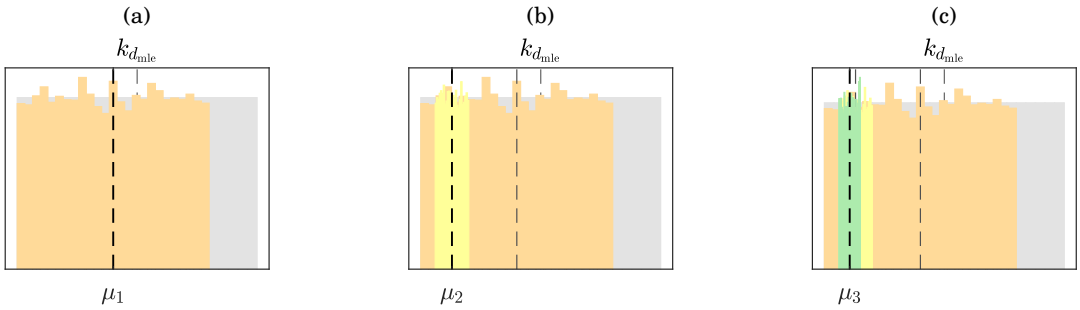

FIGURE 6.16. Depth of MLE evolution through the weight convergence corridor, at milestones (a) 1; (b) 2; (c) 3.

Fig.6.19. All of them decrease throughout the weight corridor, both in mean value and in standard deviation (or uncertainty):

	$\mu_1 < \mu$	$\sigma_1 < \sigma$	$\mu_2 < \mu$	$\sigma_2 < \sigma$	$\mu_3 < \mu$	$\sigma_3 < \sigma$
W_{le}	-4.86	-24.73	-13.90	-73.35	-17.02	-84.39
W_{SW}	-1.40	-29.94	-5.83	-72.48	-7.69	-85.50
W_{Wing}	-0.67	-47.94	-1.48	-81.69	-1.64	-90.31

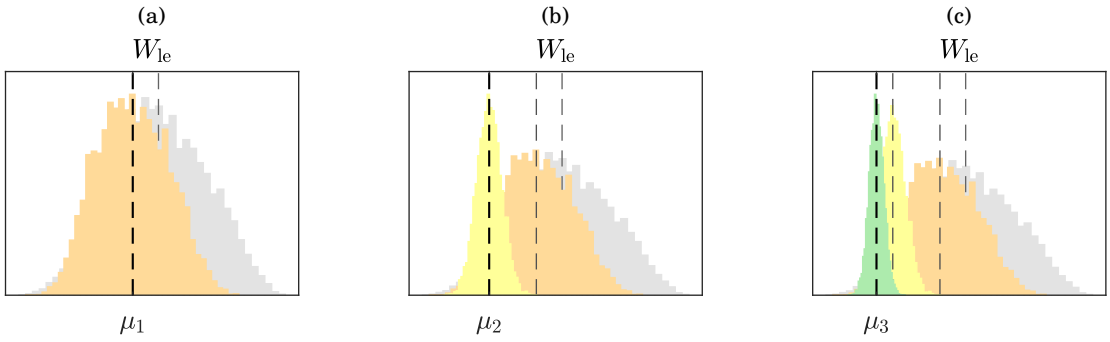

FIGURE 6.17. Leading edge weight evolution through the weight convergence corridor, at milestones (a) 1; (b) 2; (c) 3.

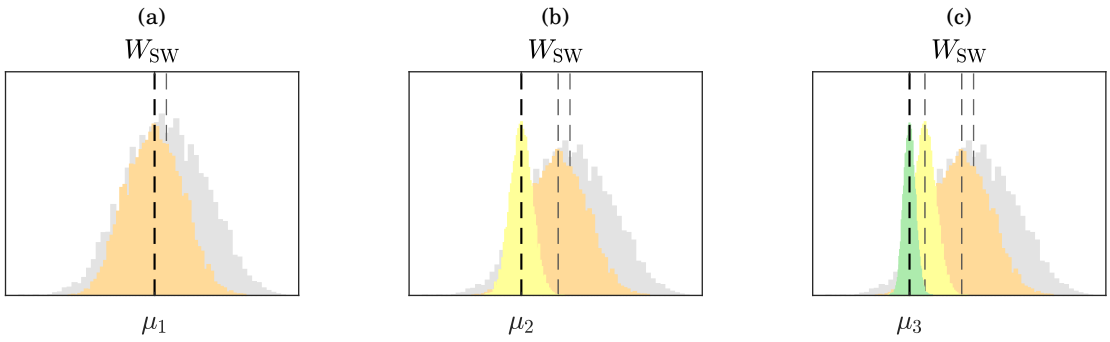

FIGURE 6.18. Secondary weight evolution through the weight convergence corridor, at milestones (a) 1; (b) 2; (c) 3.

The W_{Wing} is also compared to the target weight defined at the start μ'. The last mean value, obtained at milestone 3, despite not reaching the target mean value: $\mu_3 > \mu'$ (+0.66%), it is however within its reliability level: $\mu_3 < \mu_{q_{95}}$ (-1.15%). Regarding the primary mass and external lumped masses, continued optimisation and weight efficient design are necessary to reach the weight target. Alternatively, the target weight should be redefined at the start to set an achievable goal. Which, in a different way, also constitutes failure. Assuming sufficient real world drivers can be incorporated in a similar analysis, this would allow for an initial warning of likelihood of weight convergence rate, as well as facilitate the target weight estimation process.

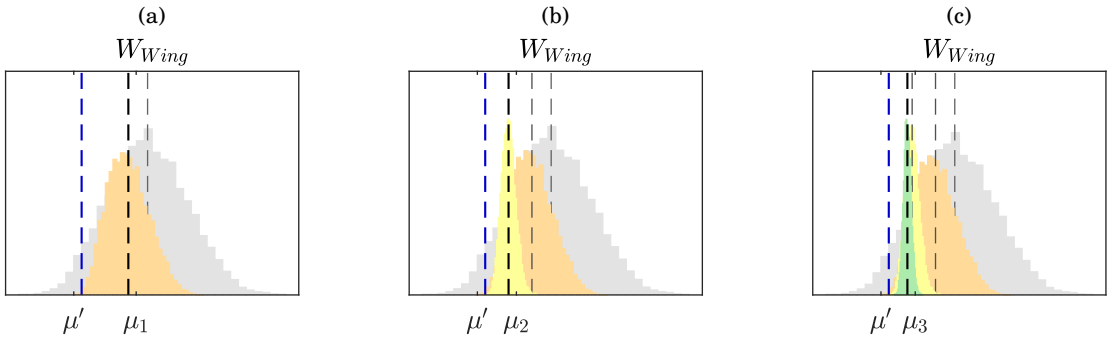

FIGURE 6.19. Wing weight evolution through the weight convergence corridor, at milestones (a) 1; (b) 2; (c) 3.

Similarly to what was done in sec.6.2.2 where Neural Networks were computed to predict the backwards propagation of uncertainty, in this section ANNs are computed to map the forward propagation of uncertainty in the wing sizing. In this case, the ANNs obtained had an average maximum relative error of 5% in its predictions, i.e. the maximum difference between predicted and real values is on average 5% for the ANNs computed.

6.3 Summary

In this chapter, reliability-based analysis, uncertainty back propagation and the weight convergence corridor are put into practice. Uncertainty in the secondary structure weights is used as the test case.

A reliability level is attributed to the final wing weight, much like the milestone project assessments, where the final aircraft weight is compared to the target, and its reliability computed. For $\beta = 95\%$, the P_f is calculated and, using data analysis alone, including parallel-coordinate plots, the input distributions that lead to the P_f set of values for wing weight are obtained. Generally, the inputs margin variability tightens with the increase in parameter complexity. For example, the margin variability for the leading edge weight is smaller than the one for its input variables. The correlation between secondary and primary structure weights is also demonstrated. The proportions of primary to secondary weight and their resultant total wing weight is shown in Fig.6.3. In appendix, a study was done on the varying front and aft spar locations and respective primary and secondary weights, see Fig.B.1. These correlations and what-if scenarios can and should be completely considered before making any design decisions.

Next, a new target weight is defined for the wing. Using Artificial Neural Networks, the same input distributions obtained before for P_f are now shown for the new target weight distribution. These results can prompt design decisions by, instead of testing different what-if scenarios and obtaining a final weight, a final weight is proposed, much like the target weight is proposed at the

start of product placement in market, and the inputs and input combination that will facilitate this value are obtained. The ANNs are computed using the data obtained for the secondary weight uncertainty and have no restrictions on design or inputs. Therefore, these have an estimated average error of 15% in their predictions. As the design process evolves and information matures, constraints in the form of data variability can be added to the ANNs in order to reduce that error. As a side effect, this analysis can also help identify the more robust or the riskier areas of design. These areas can then be managed accordingly or require additional studies in order to reduce uncertainty so that convergence to the desired target is reached.

The weight convergence corridor is presented as a summary and demonstration of how all the applications of UQ can be combined and integrated into meaningful information for the aircraft design process. The same target weight with reliability level $\beta = 95\%$ is set at the start of the process. Using the results obtained from the ANNs, the input variables were approximated to the values for which the target weight is reached. The weights are evaluated at three different milestones in the corridor, each with a different set of requirements and information available, translating into decreasing uncertainty. The wing weight at the start of the design process is defined by a normal distribution with parameters μ and σ, for full input variability, and the target weight is defined by μ' and σ'. At the first milestone, $\mu_1 = 99.73\%\mu$ and $\sigma_1 = 52.06\%\sigma$. At the second milestone, $\mu_2 = 98.52\%\mu$ and $\sigma_2 = 18.31\%\sigma$. At the third and final milestone, $\mu_3 = 98.36\%\mu$ and $\sigma_3 = 9.69\%\sigma$. Also, at the third milestone, the target weight, despite not reaching the target weight ($\mu_3 = 100.66\%\mu'$), it is within its reliability level.

CHAPTER 7

CONCLUSIONS

Aircraft weight estimation, including the the correct assumptions about weight drivers, its sensitivities and design margins is a complex task. In this work, different avenues of exploration were carried out, in order to provide an exhaustive study on how data analysis, uncertainty quantification and sensitivity analysis methodologies can be successfully applied to an aircraft design process, and what results one can expect from these. How can the process of delivering a target weight and managing the task of designing a new aircraft, be made more predictable, controlled and robust. Taking into account that the process can take up to several years, how can future technologies and advancements be incorporated at the start of the design definition and how accurate can the uncertainty predictions be throughout. Three main objectives were defined for this work, see Sec.1.4. The first one was to analyse historical weight management data. The second to model the weight estimation process for uncertainty quantification. And the third was to establish a physical basis for a proposed weight convergence corridor. How the research conducted has addressed and answered each one of these objectives is described below.

7.1 Analyse historical weight management data

The first step to understanding how to integrate uncertainty into every step of the aircraft design process is to review the industrial weight uncertainty assessment, including its tools and database. The Weight's Uncertainty Assessment (WUA) tool was reviewed and some areas for improvement were identified. Uncertainty assessment in WUA is done possibilistically and based on historical data and expert judgement. There is a need to incorporate a physics-based weight estimation model to accurately propagate uncertainties throughout, which would allow

for variables to be defined probabilistically. Using Expert Elicitation techniques to measure and combine experts' opinions in a systematic and robust manner is proposed, as to reduce the subjectivity of human error. Moreover there is a need for a dependence modelling of the different disciplines in the process of assessing uncertainty in weight, i.e. in aerodynamics, loads or structural sizing, and of the aircraft components. A dependence structure between aircraft components was tested in WUA, using three different scenarios: low $\delta = 0.1$, medium $\delta = 0.5$ and high $\delta = 0.9$ correlation between all. Respectively, these incurred variations on the total weight distribution of +39%, +24% and +4%, when compared to an independent case with $\delta = 0$.

The second step was to explore historical data, particularly the weight database. The evolution of component weights and their maturity levels throughout the different phases of design was analysed and it was concluded that there were significant variations in both not being captured in the data. The data was also clustered using custom techniques, one of which aimed at capturing correlations between the data. The information on the weights database was used to test and cross-validate the methodologies behind WUA. The fluctuations in the database weight were expected to be captured by the uncertainty bands computed by WUA, which was not always the case. This indicated potential improvements necessary to the tool WUA, as well as suggesting validation techniques between the two platforms. WUA's granularity, i.e. the level of complexity at which components are combined for overall uncertainty, was analysed. It was found that assessing one component individually versus assessing the same component by breaking down it down to sub-parts, could amount to about 10% difference in standard deviation of the weight result. Ultimately, historical aircraft data was unstandardised and insufficient to be able to draw any conclusive patterns or trends from, for the purpose of UQ.

7.2 Model the weight estimation process for uncertainty quantification.

A framework, named WeiCoS (Weight Convergence Simulation), was developed to perform uncertainty quantification and sensitivity studies on the structural sizing of a wing model and its weight estimation process. It combines a traditional wing-box, linear static, aeroelastic sizing routing for the primary structure with empirically obtained equations for the secondary structure. The baseline aircraft model used represents a typical configuration for a long range wide body aircraft. The copula formalism is used to model dependencies between input parameters, when applicable, and uncertainty is propagated by the means of Latin Hypercube sampling and Monte Carlo Simulation.

Forward uncertainty quantification and sensitivity analysis is applied to both the primary and secondary structures. The load case parameters were defined probabilistically to identify the critical loading scenario. It was concluded that the load factor is the main contributor to the sensitivities in the sizing routine and that, because the sizing is linear static, the critical load

case corresponds to the combination for the maximum M, h, n and f. A ΔL (load) ΔW (weight) analysis was computed, by varying the loads envelopes around its critical value. For an input uncertainty of 5%, the uncertainty on the overall weight of the wing was calculated at 2.56%. These values were also shown to be linearly scalable to different uncertainty levels. The impact of uncertainty on the material properties of the wing-box, specifically the stress allowable σ_{allow}, is examined. The overall weight are directly scalable for different uncertainty levels and for $u(\sigma_{\text{allow}}) = 5\%$, $\overline{u}(W_{\text{Wing}}) = 2.87\%$. The sensitivity of the final wing weight to the stress constraints is analysed. The impact of uncertainty on an external mass, lumped to the wing structural nodes, is inspected. For an uncertainty of 15% in the weight of the engine and pylon structures, the uncertainty in the total wing weight is 0.34%. The engine is located at around 0.3 of the wing span but its uncertainty affects the wing spanwise. Local effects can be captured and further explored by using empirically obtained weight functions or knowledge-based factors.

UQ is performed on the wing's secondary structure and, the impact of having an uncertain secondary weight on the primary structured is also captured. A varying secondary weight alters the mass distribution of the wing and therefore the aerodynamic loads. With the secondary weight amounting to about 30% of the wing weight, a variation on the secondary weight of 15% results in a 3.22% uncertainty on the total wing weight. Wing weight's sensitivity to all secondary weight inputs is also calculated.

WeiCoS allows for a full scope UQ and SA on the wing's sizing. This physics-based platform demonstrates the range of results using a probabilistic propagation of uncertainty.

7.3 Establish a physical basis for a proposed weight convergence corridor

Having explored the industrial process, historical data and simulated results for uncertainty in a physics-based model, it was time to combine this information into a single platform.

Reliability-based analysis is performed on the wing structural sizing using the secondary structure weight inputs as the test case uncertainty source. This analysis aims at exploring the input space and its different combinations that result in the new target weight and identify risk areas or areas in the input space that have a bigger impact on the final result.

A reliability level $\beta = 95\%$ was defined for the final wing weight. The design space that falls into the probability of failure to obtain said final weight with $\beta = 95\%$ was obtained. Following the same analysis, a new target wing weight, with the same reliability level $\beta = 95\%$, was defined. This time, inverse uncertainty quantification by the means of Artificial Neural Networks (ANNs) was used to predict the design space that would allow for the new target weight to be obtained. The ANNs are obtained using 10000 data points, with 10 uncertain input variables and have an estimated average error of 15% in their predictions.

A physical basis for the weight convergence corridor is proposed, based on the above mentioned

analysis. The weight convergence corridor is the concept of tracking the design evolution, through the design process, against a specific target. At certain project milestones, the weights are assessed in terms of nominal value and associated uncertainty, against the requirements of said milestones. Using the results obtained from the backwards propagation as guidelines for design input margins, ANNs were again used to compute the weight evolution at different milestones, with the objective of getting it to converge to the proposed target. As design features were frozen at different milestones, the inputs PDFs got narrower. The ANNs took the narrowing input PDFs and computed the respective component and wing weight. By using the results obtained by the backward propagation of uncertainty, the new target weight was reached within its reliability level. Using the weight convergence corridor allied with backward uncertainty propagation, allows the user to track weight fluctuations and all its effects, study several what-if scenarios and rapidly predict necessary inputs to reach a specific target.

* * *

A full spectrum of analysis were performed on aircraft data, including a thorough review of its methodologies and industrial process, using data analysis and machine learning techniques to learn from past aircraft data, transforming that knowledge into a framework that combines physics-based with empirical methods to obtain the weights estimates and finally employing forward and backward uncertainty propagation and reliability and sensitivity analysis, to deliver meaningful technical and managerial information for weight estimation management. The work presented here demonstrates the broad applicability of uncertainty analysis into the aircraft weight estimation process, as well as all the different results and data visualisation techniques one can expect and retrieve from it. The framework alludes to the possibility of further development, incorporating additional models and uncertainty sources to be used to give simulation environment to explore weight convergence scenarios, and give insight to engineering teams facing decision making which will impact weight.

Uncertainty is present in every aspect of our lives: whether known or unknown, epistemic or aleatory; uncertainties are central to modern understanding and representation of nature. In engineering, it is imperative that they become an integral part of numerical models and simulations, parametric definitions and accounts of randomness; only then can engineered systems make efficient use of limited resources and become more reliable.

7.4 Future Work

In order to develop this work further, it is suggested that the probabilistic UQ is applied to more complex physics based tools, in order to test their efficiency and expense with growing complexity in problems. The integration of the probabilistic propagation of uncertainty with possibilistic methods where applicable is also proposed. For the inverse propagation of uncertainty, ANNs

demonstrated an error of around 15% and, for that reason, other surrogate models or techniques are suggested. The application of the proposed weight convergence corridor methodologies in industrial problems is also recommended.

When discussing the subject of weight engineering, it is essential that one looks not only at absolute weight values but also at the way weight is distributed inside the aircraft. Incorporating uncertainty into the aircraft's loadability (its capability for being loaded) and centre of gravity studies is out of the scope of this PhD, nonetheless worth a mention because of its importance and possibility for complementary work. The c.g.'s limits are established during the aircraft design and are meant to encompass variations in OEW, operator items, payload and fuel, as shown in Figure 7.1. The aircraft's structure, systems and cabin are then designed to safely operate within these limits, as well as being able to support the primary loads.

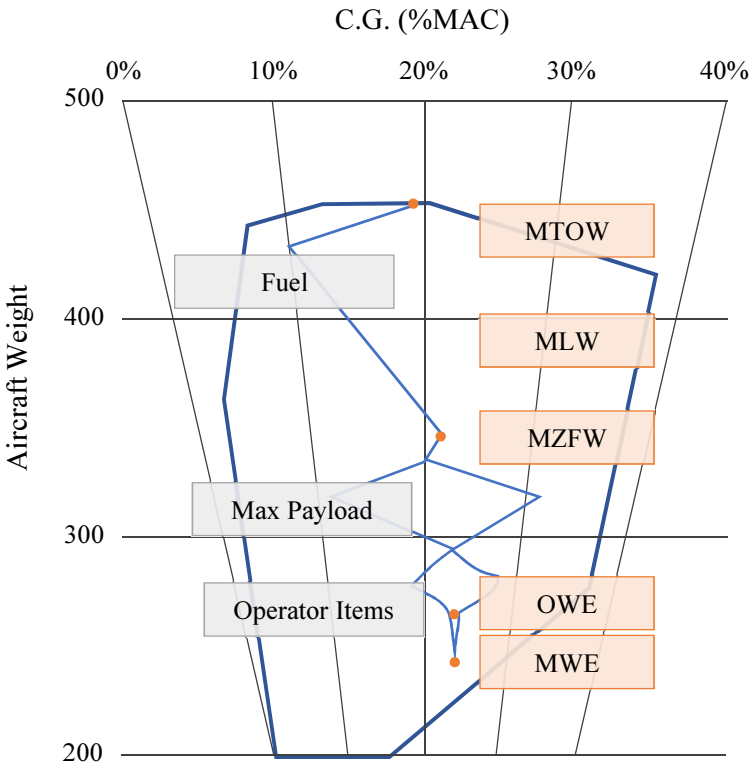

FIGURE 7.1. Centre of Gravity distribution for the different definitions of weight.

Lastly, the work presented in this thesis illustrates the capabilities of UQ and SA, as well as how these results can aid decision making and product management. Although applied to aircraft design, these are powerful methodologies that can and should be part of any engineering problem and product management process.

APPENDIX A

SIZING OPTIMISATION

The calculations involved in the sizing optimisation routine are here described in greater detail. These include the aeroelastic forces and moments description, the moments of area, stress analysis and stress constraints, applied to the wing-box section geometry see Fig.4.4. The assumption is made that the top and bottom skins are equivalent in thickness, as well as the front and rear spar.

A.1 Aeroelastic forces and moments

The aeroelastic forces and moments used in the sizing optimisation are listed in Table A.1.

The sizing is limited to the wing-box skins, spars and stringers and the sizing varies the mass and stiffness of these parts, while keeping the rest of the aircraft's mass constant. Thus, the mass of the empennage and fuselage is kept constant and not included in the sizing, however, it is included in the overall aircraft trim analysis. The second step, after defining the input parameters, is to calculate the inertial properties of the fuselage, pylon and engines, payload and landing gear, and transfer these properties to a beam formulation of the wing in the form of lumped masses. These masses are expressed by a 6×6 matrix and have an associated structural node. The initial estimation of MTOW is then used to calculate the secondary structure weight. The secondary structure weight, as well as the fuel weight, are expressed as lumped masses and distributed spanwise over the structural nodes of the wing. Their weights are distributed throughout the nodes according to the fraction of internal volume of each wing-box (and respective node) over the total internal volume of the wing-boxes combined. Pylon and landing gear attachments to the wing and ribs weight are also expressed as lumped masses and placed on specific locations along the wing span. The MTOW is kept constant for sizing, excepting the wing weight. An initial condition for t_{skn_0}, t_{spr_0} and A_{stg_0} is defined and these, along with the lumped masses

previously specified, allow to reduce the wing-box formulation to a beam formulation, where mass and stiffness matrices describe each beam element. The load cases are then used in a linear trim analysis and enveloped for sizing. A detailed description of the trim analysis, including the beam formulation and the static aeroelastic model used in this framework can be consulted in Calderon et al. [129].

Table A.1: Aeroelastic forces and moments.

F_y	Horizontal shear
F_z	Vertical shear
M_x	Torsional moment
M_y	Out-of-plane bending moment
M_z	In-plane bending moment

A.2 Moments of Area

The second moments of area, I_{yy}, I_{zz} and I_{zy} are described based on the geometry of the wing box sections, and y and z are the directions illustrated in Figure A.1.

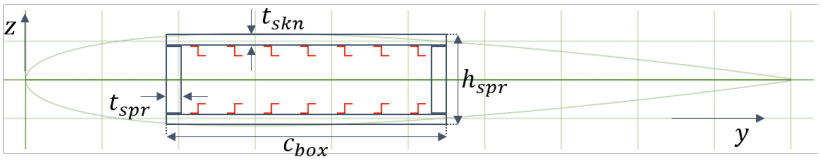

FIGURE A.1. Airfoil skins, spars and stringers geometry.

The area around the mean line of the wing-box cross-section is

$$\Omega = \left(c_{box} - t_{spr}\right) \cdot \left(h_{spr} - t_{skn} - d_s d - \frac{d}{2}\right) \tag{A.1}$$

where $d_s = 0.12$ is the thickness to length ratio of the stringer segments.

The second moment of area of an individual stringer about the centroid of the box section is expressed by

$$I_{yy}^{\text{stg}} = d^4 \left(\frac{2}{3} {d_s}^3 + {d_s}^2 + \frac{7}{12} d_s\right) + A_{\text{stg}} \left(\frac{h_{\text{spr}}}{2} - t_{\text{skn}} - \left(\frac{d}{2} + d_s d\right)^2\right) \tag{A.2}$$

The stringers are distributed evenly along the skin of the box and so the second moment of area of all the stringers about the centroid of the box is expressed by:

$$I_{zz}^{\text{stg}} = 2\left(\text{NS} \cdot I_{zz}^{\text{stg}} + A_{stg} \cdot {c_{\text{box}}}^2 \cdot \text{NS}\left(-0.25 + \frac{\text{NS} + 0.25}{3(\text{NS}+1)}\right)\right) \tag{A.3}$$

where NS refers to the number of stringers in a particular section, dependent on the geometry of the stringer itself, the SP and c_{box}.

The second moments of area of the wing-box section, excluding the stringers, are

$$I_{yy}^{\text{skn+spr}} = \frac{1}{12}\left(c_{\text{box}} \cdot {h_{\text{spr}}}^3 - \left(c_{\text{box}} - 2t_{\text{spr}}\right) \cdot \left(h_{\text{spr}} - 2t_{\text{skn}}\right)^3\right) \tag{A.4}$$

$$I_{zz}^{\text{skn+spr}} = \frac{1}{12}\left(h_{\text{spr}} \cdot {c_{\text{box}}}^3 - \left(h_{\text{spr}} - 2t_{\text{skn}}\right) \cdot \left(c_{\text{box}} - 2t_{\text{spr}}\right)^3\right) \tag{A.5}$$

Finally, the overall second moments of area of the wing-box section, including skins, spars and stringers, are

$$I_{yy} = 2 \cdot I_{yy}^{\text{stg}} \cdot \text{NS} + I_{yy}^{\text{skn+spr}} \tag{A.6}$$

$$I_{zz} = I_{zz}^{\text{stg}} + I_{zz}^{\text{skn+spr}} \tag{A.7}$$

A.3 Stress Analysis

The bending stresses on the skins (top and bottom) and spars are

$$\sigma_{\text{skn}} = \left(\frac{h_{\text{spr}}}{2} - \frac{t_{\text{skn}}}{2}\right)\frac{M_{\text{y}}}{I_{\text{yy}}} + \frac{F_{\text{z}}}{2c_{\text{box}}t_{\text{skn}}} \tag{A.8}$$

$$\sigma_{\text{spr}} = \left(\frac{c_{\text{box}}}{2} - \frac{t_{\text{spr}}}{2}\right)\frac{M_{\text{z}}}{I_{\text{zz}}} + \frac{F_{\text{y}}}{2h_{\text{spr}}t_{\text{spr}}} \tag{A.9}$$

The bending stress on the stringers is

$$\sigma_{\text{stg}} = \left(\frac{h_{\text{spr}}}{2} - t_{\text{skn}} - \left(d_s + \frac{1}{2}\right)d\right)\frac{M_{\text{y}}}{I_{\text{yy}}} \tag{A.10}$$

The shear stresses for the same geometries are

$$\tau_{\text{skn}} = \frac{M_{\text{x}}}{2\Omega t_{\text{skn}}} + \frac{F_{\text{y}}}{2c_{\text{box}}t_{\text{skn}}} + 0.5\frac{F_{\text{z}}}{2h_{\text{spr}}t_{\text{skn}}} \tag{A.11}$$

$$\tau_{\text{spr}} = \frac{M_{\text{x}}}{2\Omega t_{spr}} + \frac{F_{\text{z}}}{2h_{\text{spr}}t_{\text{spr}}} + 0.25\frac{F_{\text{y}}}{2c_{\text{box}}t_{\text{spr}}} \tag{A.12}$$

The first stress constraints implemented become

$$\frac{\left[\sigma_{\text{skn}};\sigma_{\text{spr}};\sigma_{\text{stg}}\right]}{\sigma_{\text{allow}}} \leq 1 \tag{A.13}$$

$$\frac{\left[\tau_{\text{skn}};\tau_{\text{spr}}\right]}{\tau_{\text{allow}}} \leq 1 \tag{A.14}$$

Using the Von Mises Yield Criterion, the bending and shear stresses above are combined for the skins and spars material strength

$$\sigma_{\text{skn}}^{v} = \sqrt{\sigma_{\text{skn}}^2 + 3\tau_{\text{skn}}^2} \tag{A.15}$$

$$\sigma_{spr}^{v} = \sqrt{\sigma_{\text{spr}}^2 + 3\tau_{\text{spr}}^2} \tag{A.16}$$

Resulting in the second set of constraints for the optimisation

$$\frac{\sigma^{v}_{\text{skn}}}{\sigma_{\text{allow}}} \leq 1 \tag{A.17}$$

$$\frac{\sigma^{v}_{\text{spr}}}{\sigma_{\text{allow}}} \leq 1 \tag{A.18}$$

A.4 Stress Constraints

A.4.1 Skin Buckling

The skins' critical buckling stress is given by

$$\sigma_{\text{skn}_{\text{b,cri}}} = \frac{k_c \pi^2 E}{12\left(1-v^2\right)} \left(\frac{t_{\text{skn}}}{b}\right)^2 \tag{A.19}$$

$$\tau_{\text{skn}_{\text{b,cri}}} = \frac{k_s \pi^2 E}{12\left(1-v^2\right)} \left(\frac{t_{\text{skn}}}{b}\right)^2 \tag{A.20}$$

where for simply supported edges $k_c = 4$ and $k_s = 5.6$, and $b = \min(\text{RP};\text{SP})$.

From the principal stress formulation, the skin buckling constraint is formulated

$$\sigma_P = 1 - \frac{2}{\frac{\sigma_{\text{skn}}}{\sigma_{\text{skn}_{\text{b,cri}}}} + \sqrt{\frac{\sigma_{\text{skn}}}{\sigma_{\text{skn}_{\text{b,cri}}}}^2 + 4\frac{\tau_{\text{skn}}}{\tau_{\text{skn}_{\text{b,cri}}}}^2}} \leq 1 \tag{A.21}$$

A.4.2 Stringer Buckling

From Niu et al. [144], the non-dimensional crippling stress for the individual segments of the stringers is given by

$$\frac{\sigma^{*}_{\text{cc}}}{\sigma_{\text{allow}}} = B\left(\sqrt{\frac{\sigma_{\text{allow}}}{E}}\left(\frac{d}{t_{\text{stg}}}\right)\right)^{A} \tag{A.22}$$

where σ_{allow} is the allowable stress and the coefficients A and B are given by

$$\text{for one free edge} \begin{cases} A = -0.7885 \\ B = 0.6194 \end{cases} \tag{A.23}$$

$$\text{for no free edge} \begin{cases} A = -0.8046 \\ B = 1.2117 \end{cases} \tag{A.24}$$

A cut-off stress is implemented so that the non dimensional crippling stress becomes

$$\frac{\sigma_{cc}}{\sigma_{\text{allow}}} = \min\left(\frac{\sigma^{*}_{cc}}{\sigma_{\text{allow}}}, 1.45\right) \tag{A.25}$$

A weighted average of the crippling stress of the 3 segments of the stringer, n being the segment subscript, is used to determined the crippling stress for the entire stringer by

$$\sigma_{\text{cc}} = \frac{\sum d_n t_{\text{stg}_n} \sigma_{cc_n}}{\sum d_n t_{\text{stg}_n}} \tag{A.26}$$

The stringer local buckling constraint yields

$$\frac{\sigma_{\text{stg}}}{\sigma_{\text{cc}}} \leq 1 \tag{A.27}$$

A.4.3 Column buckling of the skin-stringer panel

The effective width and area of the skin-stringer panel are defined by

$$w_{\text{eff}} = 1.7 t_{\text{skn}} \sqrt{\frac{E}{\sigma_{\text{stg}}}} \tag{A.28}$$

$$A_{\text{eff}} = w_{\text{eff}} \cdot t_{\text{skn}} \tag{A.29}$$

The radius of gyration is

$$\rho = \sqrt{\frac{I}{A_{stg} + A_{eff}}} \tag{A.30}$$

The slenderness ratio K and the critical slenderness ratio K_{cri} are

$$K = \frac{L}{\rho\sqrt{c}} \tag{A.31}$$

$$K_{cri} = \pi \sqrt{\frac{2E}{\sigma_{cc}}} \tag{A.32}$$

where the critical case is given by the crippling stress.

Employing the classical Euler equation or the Johnson-Euler formula, the allowable column stress is then calculated by

$$\sigma_c = \sigma_{cc}\left(1 - \frac{\sigma_{cc} K^2}{4\pi^2 E}\right) \qquad \text{for } K \leq K_{cri} \tag{A.33}$$

$$\sigma_c = \frac{\pi^2 E}{K^2} \qquad \text{for } K > K_{cri} \tag{A.34}$$

The skin-stringer failure constraint becomes:

$$\frac{\sigma_{\text{stg}}}{\sigma_{\text{col}}} \leq 1 \tag{A.35}$$

A.4.4 Farrar's efficiency factor

From Niu pg.618 [144], the Farrar's efficiency factor F accounts for a pure flexural instability of the skin-stringer panel. For Z-stringers, the optimal value for the structural efficiency is 0.95, yielding the last constraint:

$$N = \frac{1}{2} \cdot \frac{F_z}{\text{NS} \cdot d} \tag{A.36}$$

$$F = 0.95 \cdot \sqrt{\frac{N \cdot E}{\text{RP}}} \cdot \sigma_{\text{allow}} \leq 1 \tag{A.37}$$

APPENDIX B

RELIABILITY-BASED UNCERTAINTY BACKPROPAGATION AND THE WEIGHT CONVERGENCE CORRIDOR (EXTENDED)

B.1 Wing weight with reliability level β (extended)

These pictures support the section in 6.2.1, where data analysis is performed through parallel-coordinate plots, to visualise the cases for failure: $\beta = 1 - P_f$. Additionally, the distribution of values for the same probability was obtained.

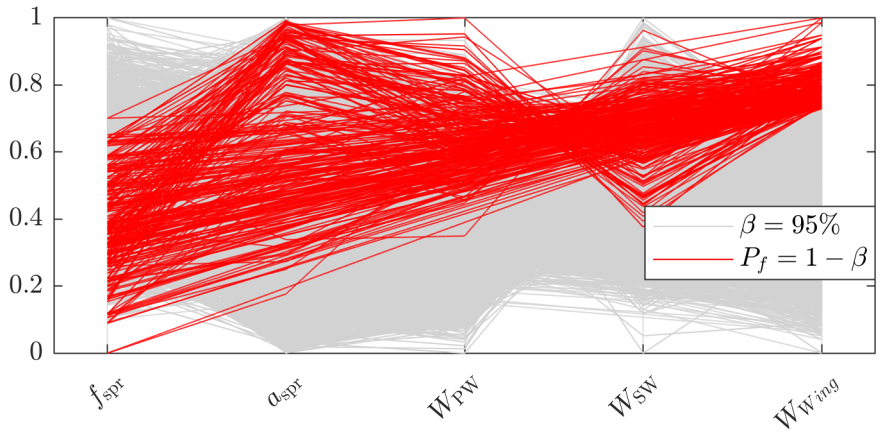

FIGURE B.1. Parallel-coordinate plot showing the variability of the location of the front and aft spars and the primary and secondary weights, for the P_f of a wing weight with reliability level $\beta = 95\%$.

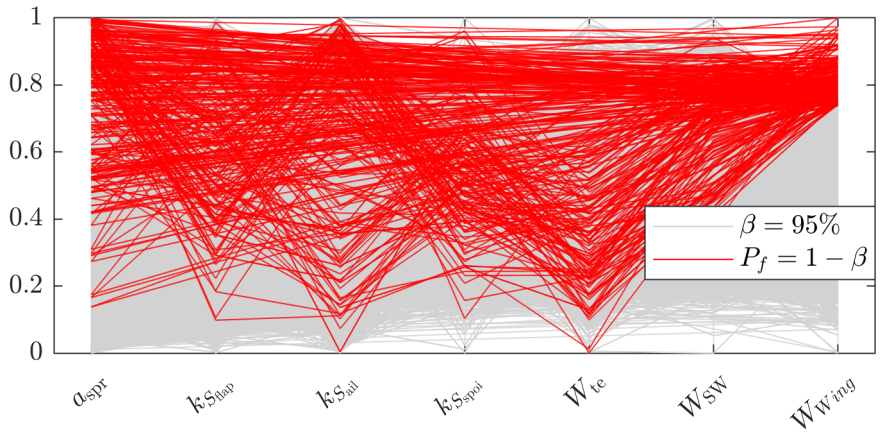

FIGURE B.2. Parallel-coordinate plot showing the variability of the trailing edge weight and respective input parameters, for the P_f of a wing weight with reliability level $\beta = 95\%$.

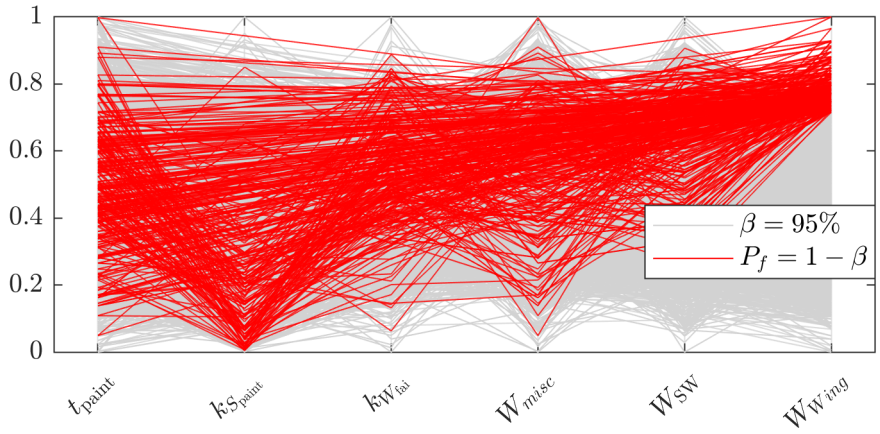

FIGURE B.3. Parallel-coordinate plot showing the variability of the miscellaneous items weight and respective input parameters, for the P_f of a wing weight with reliability level $\beta = 95\%$.

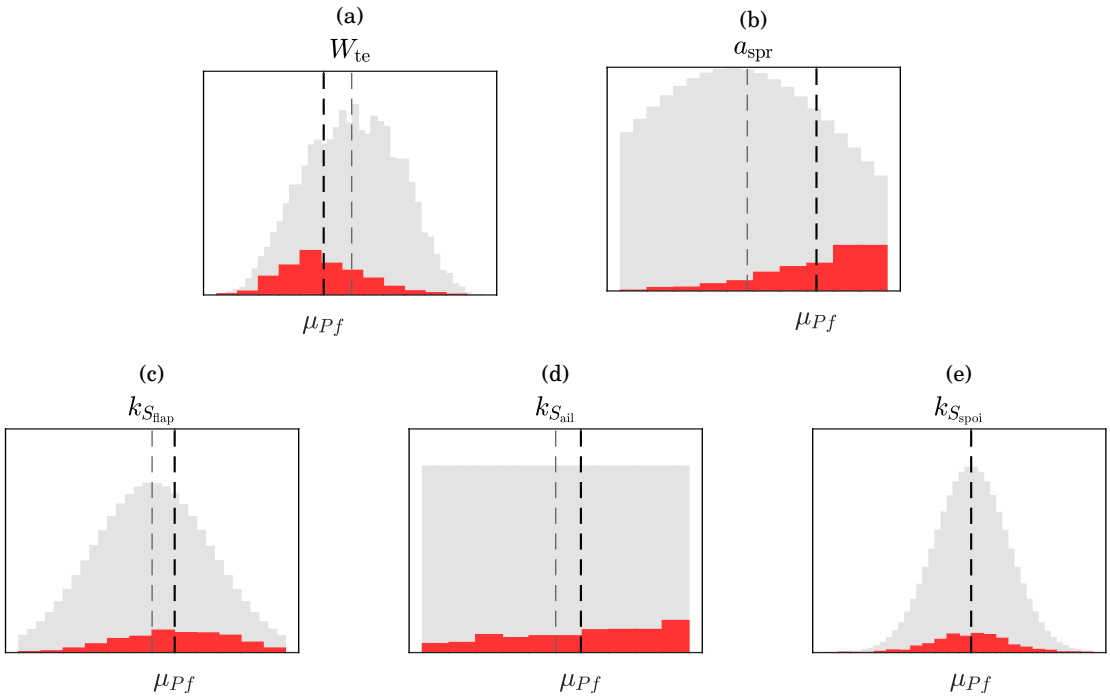

FIGURE B.4. P_f distribution of the trailing edge weight and its input parameters. (a) Trailing edge weight; (b) Aft spar; (c) Flaps surface area scaling factor; (d) Ailerons surface area scaling factor; (e) Spoilers surface area scaling factor.

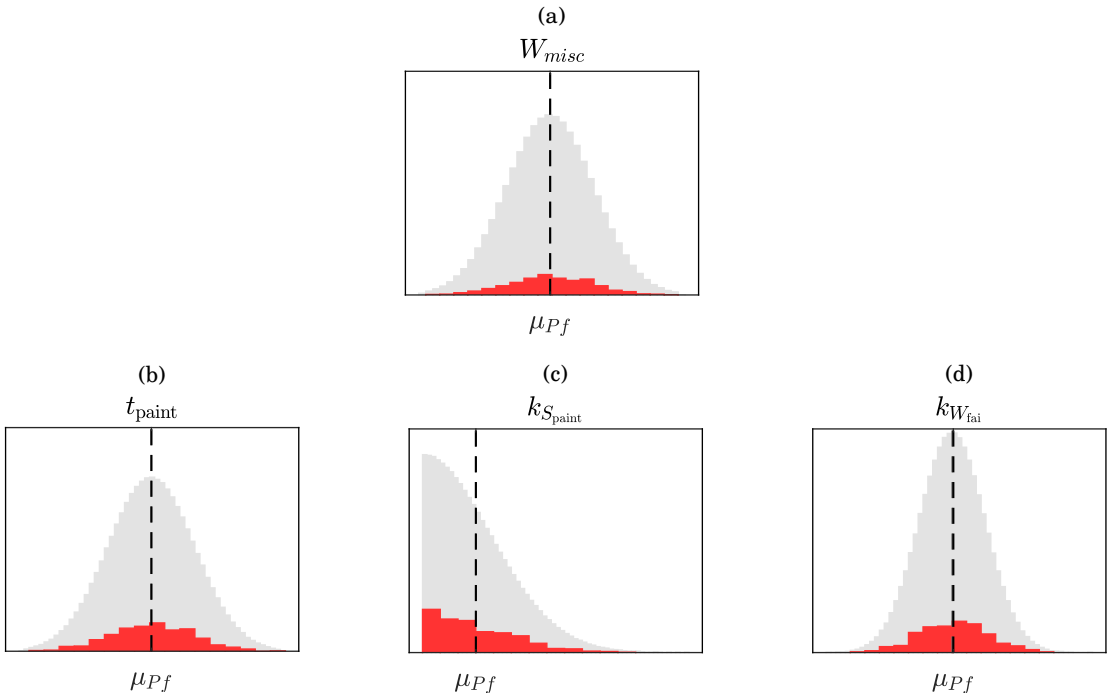

FIGURE B.5. P_f distribution of the miscellaneous items' weight and its input parameters. (a) Paint thickness; (b) Paint surface area scaling factor; (c) Fairings weight scaling factor.

B.2 Target wing weight with reliability level β (extended)

These pictures support the section in 6.2.2, where uncertainty backpropagation is applied to retrieve input distributions for an output target wing weight with reliability level β.

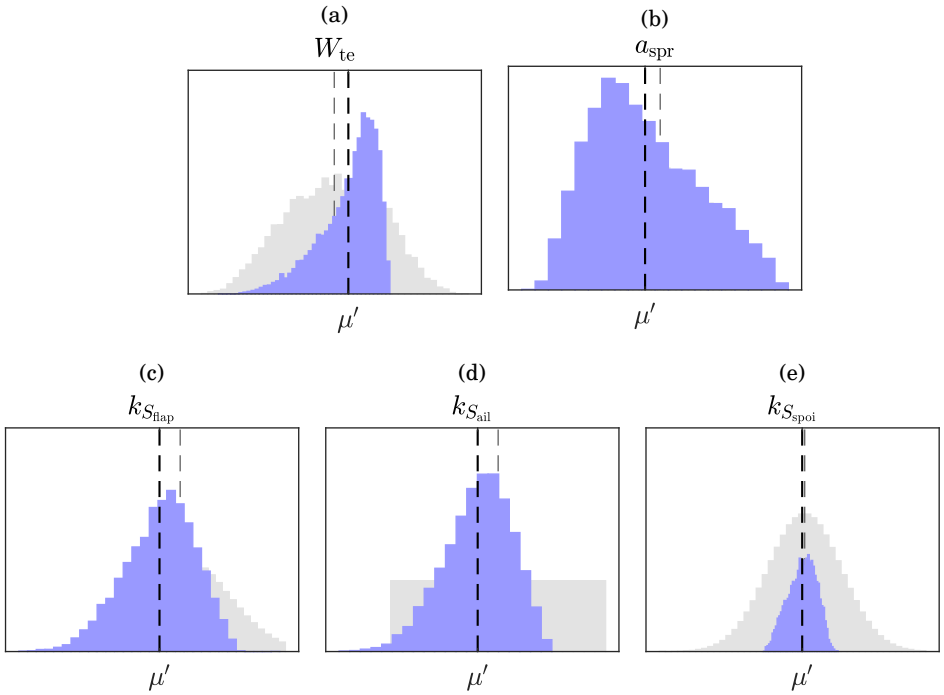

FIGURE B.6. Distributions of the trailing edge weight and its input parameters, for the wing target weight. (a) Trailing edge weight; (b) Aft spar; (c) Flaps surface area scaling factor; (d) Ailerons surface area scaling factor; (e) Spoilers surface area scaling factor.

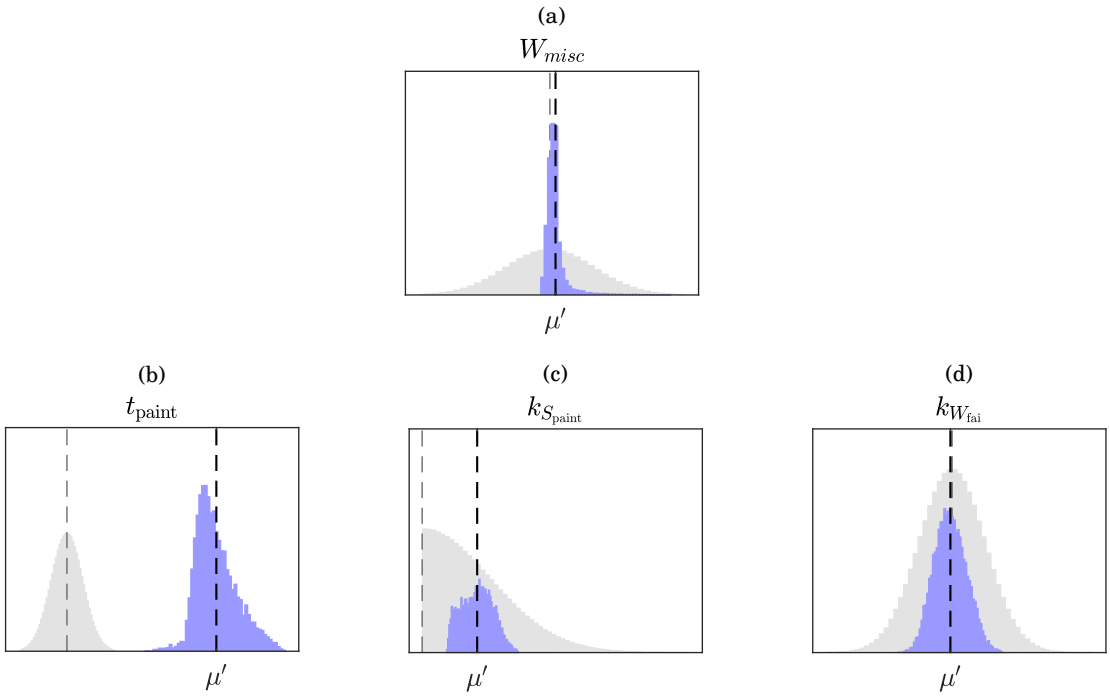

FIGURE B.7. Distributions of the miscellaneous items' weight and its input parameters, for the wing target weight. (a) Paint thickness; (b) Paint surface area scaling factor; (c) Fairings weight scaling factor.

B.3 Convergence corridor (extended)

These pictures support the section in 6.2.3, where the evolution of the design variables and correspondent weights, through the design process, is computed.

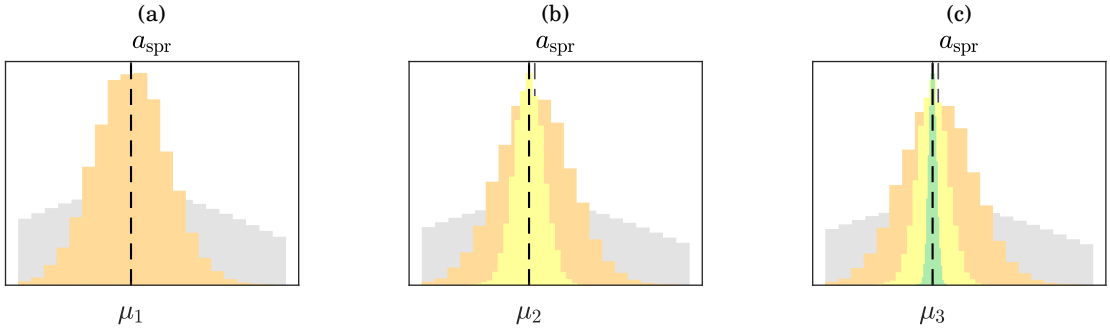

FIGURE B.8. Aft spar location evolution through the weight convergence corridor, at milestones (a) 1; (b) 2; (c) 3.

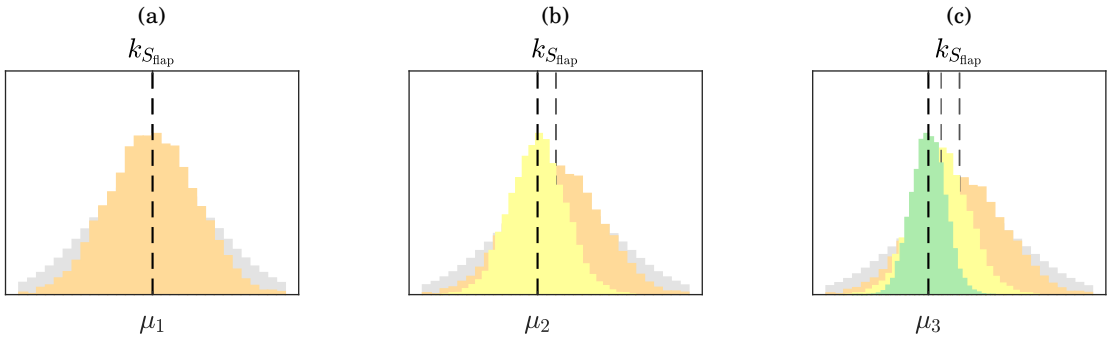

FIGURE B.9. Flaps surface area scaling factor evolution through the weight convergence corridor, at milestones (a) 1; (b) 2; (c) 3.

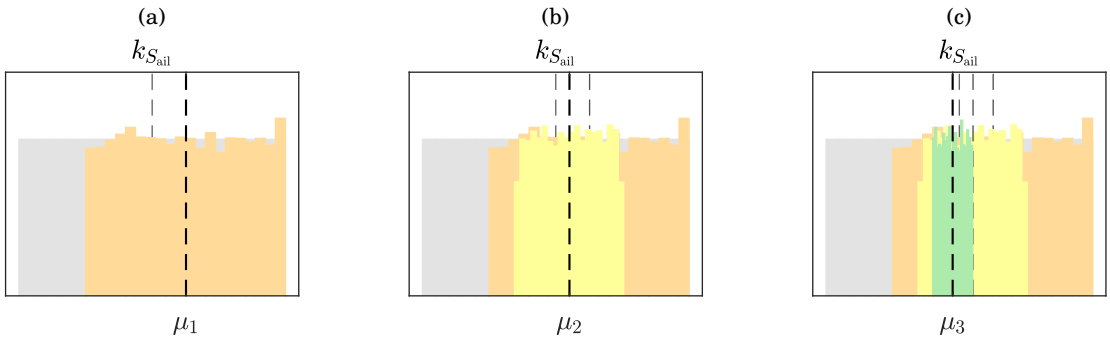

FIGURE B.10. Ailerons surface area scaling factor evolution through the weight convergence corridor, at milestones (a) 1; (b) 2; (c) 3.

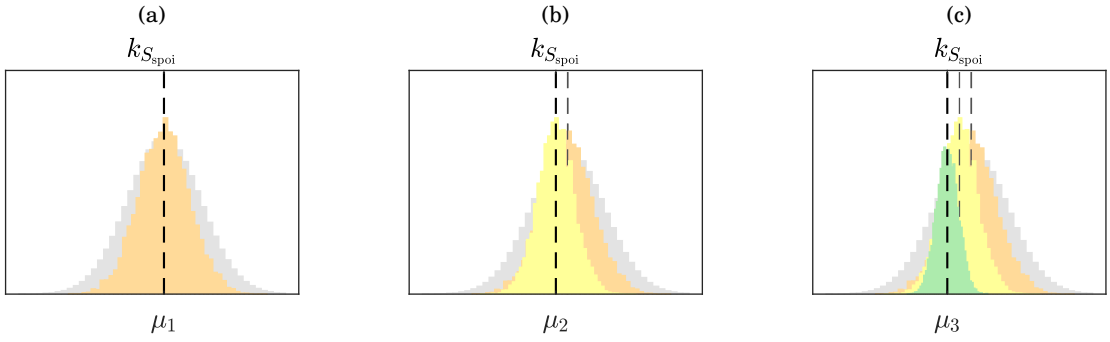

FIGURE B.11. Spoilers surface area scaling factor evolution through the weight convergence corridor, at milestones (a) 1; (b) 2; (c) 3.

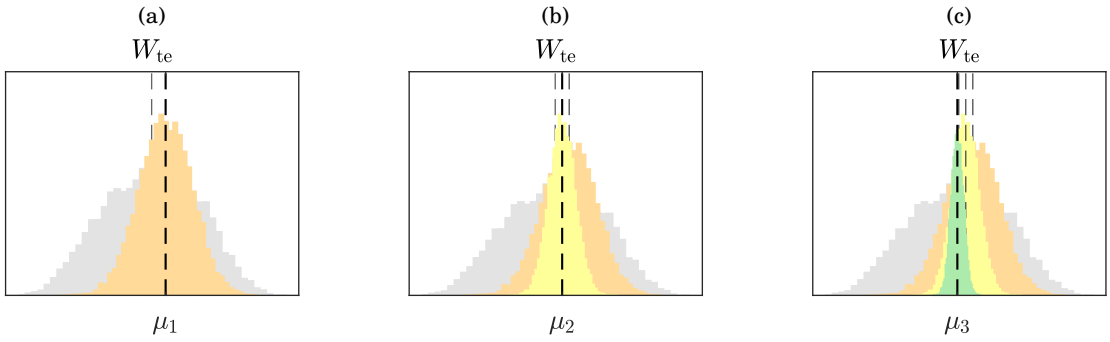

FIGURE B.12. Trailing edge weight evolution through the weight convergence corridor, at milestones (a) 1; (b) 2; (c) 3.

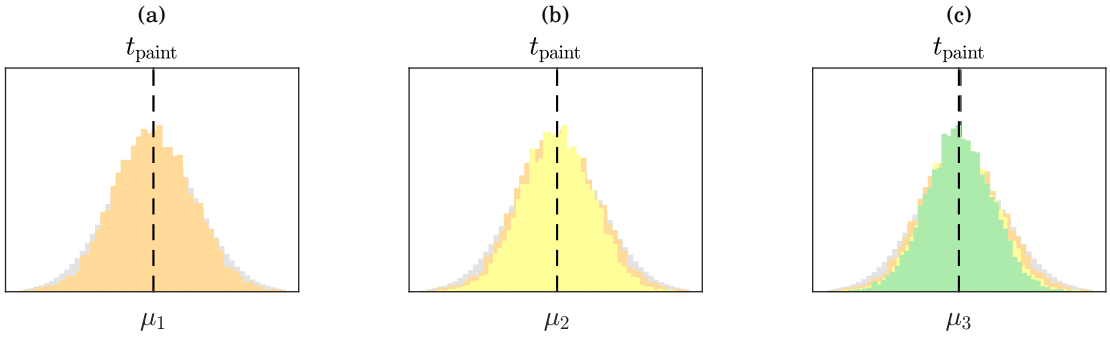

FIGURE B.13. Paint thickness evolution through the weight convergence corridor, at milestones (a) 1; (b) 2; (c) 3.

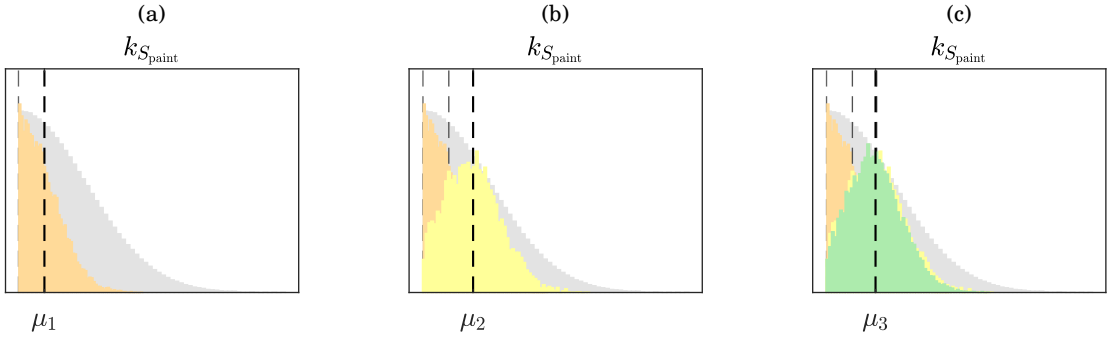

FIGURE B.14. Paint surface area scaling factor evolution through the weight convergence corridor, at milestones (a) 1; (b) 2; (c) 3.

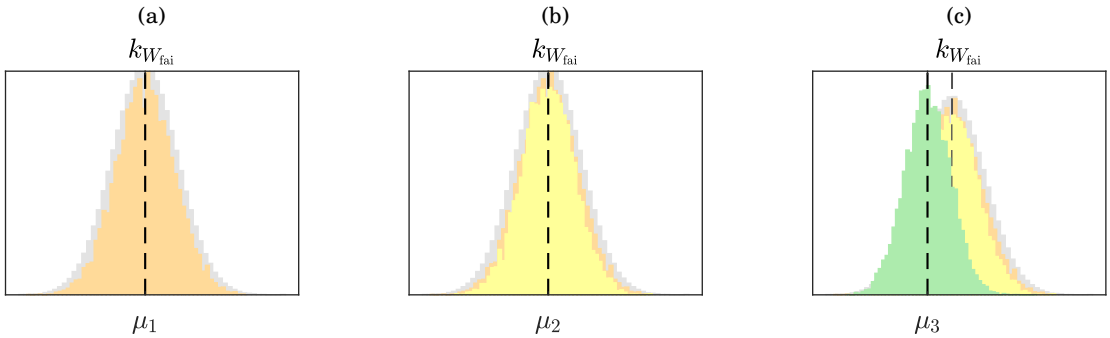

FIGURE B.15. Fairings weight scaling factor evolution through the weight convergence corridor, at milestones (a) 1; (b) 2; (c) 3.

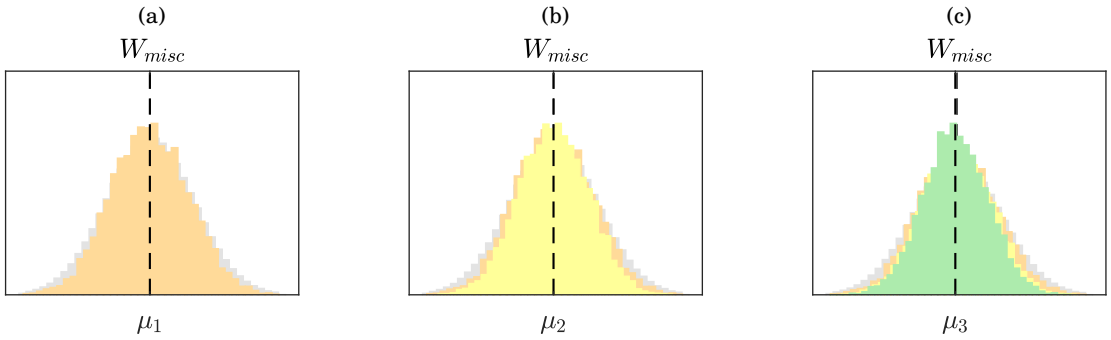

FIGURE B.16. Miscellaneous items' weight's evolution through the weight convergence corridor, at milestones (a) 1; (b) 2; (c) 3.

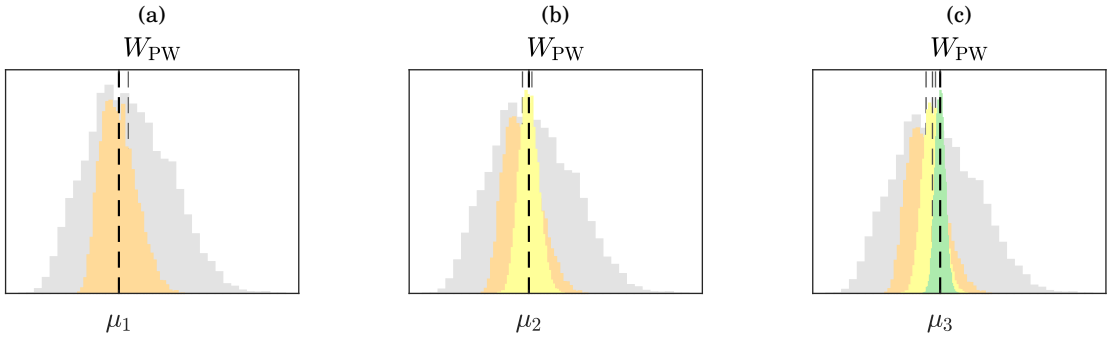

FIGURE B.17. Primary weight's evolution through the weight convergence corridor, at milestones (a) 1; (b) 2; (c) 3.

Viagem

É o vento que me leva.
O vento lusitano.
É este sopro humano
Universal
Que enfuna a inquietação de Portugal.
É esta fúria de loucura mansa
Que tudo alcança
Sem alcançar.
Que vai de céu em céu,
De mar em mar,
Até nunca chegar.
E esta tentação de me encontrar
Mais rico de amargura
Nas pausas da ventura
De me procurar...

MIGUEL TORGA, IN *Diário XII*

References

[1] S. Gortz, C. Ilic, M. Abu-Zurayk, R. Liepelt, J. Jepsen, T. Führer, R. Becker, J. Scherer, T. Kier, and M. Siggel, "Collaborative Multi-Level MDO Process Development and Application to Long-Range Transport Aircraft," in *ICAS*, 2016.

[2] J. Cheeseman, "The Mysterious Art of Weight Estimation of Large Civil Aircraft," in *73rd SAWE*, 2014.

[3] D. P. Raymer, R. Hibma, L. Hecq, H. Scott, R. Child, G. Owl, R. Maier, E. Mcgachan, D. Robinson, S. White, H. Hoge, M. Robinson, G. Palmer, H. Yang, R. Swaim, C. T. Sun, D. Schmidt, B. Reese, W. Heiser, and G. Raymer, *Aircraft Design: A Conceptual Approach*.
second ed., 1992.

[4] M. N. Beltramo, I. Trapp, Donald L. (Science Applications, B. W. Kimoto, and D. P. D. A. C. Marsh, "Parametric study of Transport Aircraft Systems Cost and Weight," tech. rep., NASA, 1977.

[5] J. Schiefelbein and C. Grierson, *Introduction to Aircraft Weight Engineering*.
Society of Allied Weight Engineers, 1996.

[6] R. H. Lange, "Review of Unconventional Aircraft Design Concepts," vol. 25, no. 5, 1988.

[7] A. Spohr, J. Schirra, J. Hoefling, and A. Schedl, "Wing Weight Estimation MEthodology for highly non-planar Lifting Systems During Conceptual Design," 2013.

[8] R. K. Schmidt, *A Semi-Analytical Weight Estimation Method for Oval Fuselages in Novel Aircraft Configurations*.
PhD thesis, Delft University of Technology, 2013.

[9] T. W. Laughlin, "A Parametric and physics-based approach to structural weight estimation of the hybrid wing body of the aircraft," 2012.

[10] O. Dababneh and T. Kipouros, "A review of aircraft wing mass estimation methods," 2018.

[11] E. Akay, M. E. Mear, and A. Chaput, "Conceptual Level FEM Based Wing Weight Estimation," 2010.

[12] G. Schuhmacher, F. Daoud, {\"O}. Petersson, and M. Wagner, "Multidisciplinary Airframe Design Optimisation," in *ICAS*, p. 13, 2012.

[13] F. Dorbath, "A Flexible wing modeling and physical mass estimation system for early aircraft design stages," *DLR Deutsches Zentrum fur Luft- und Raumfahrt e.V. - Forschungsberichte*, 2014.

[14] P. W. Scott and D. Nguyen, "The initial weight estimate," in *55th International Conference of the Society of Weight Engineers, Inc*, 1996.

[15] G. K. W. Kenway and J. R. R. A. Martins, "Multipoint High-Fidelity Aerostructural Optimization of a Transport Aircraft Configuration," *Journal of Aircraft*, 2014.

[16] M. Squair, "Epistemic, ontological and aleatory risk," 2009.

[17] S. Ferson and L. R. Ginzburg, "Different methods are needed to propagate ignorance and variability," *Reliability Engineering and System Safety*, 1996.

[18] S. C. Hora, "Aleatory and epistemic uncertainty in probability elicitation with an example from hazardous waste management," tech. rep., 1996.

[19] X. Du, "Unified Uncertainty Analysis by the First Order Reliability Method," *Journal of Mechanical Design*, p. 10, 2008.

[20] L. P. Swiler, T. L. Paez, R. L. Mayes, and M. S. Eldred, "Epistemic Uncertainty in the Calculation of Margins," 2009.

[21] G. Fernandez, C. Park, N. H. Kim, and R. Haftka, "Review of multi-fidelity models," no. March, 2017.

[22] E. de Rocquigny, N. Devictor, and S. Tarantola, *Uncertainty in Industrial Practice*. 2008.

[23] J.-B. Blanchard, G. Damblin, J.-M. Martinez, G. Arnaud, and F. Gaudier, "The Uranie platform: an open-source software for optimisation, meta-modelling and uncertainty analysis," *EPJ Nuclear Sciences & Technologies*, vol. 5, p. 4, 2019.

[24] J. K. Daggy, H. Xu, S. L. Hui, R. E. Gamache, and S. J. Grannis, "A practical approach for incorporating dependence among fields in probabilistic record linkage," *BMC Medical Informatics and Decision Making*, 2013.

[25] R. B. Nelsen, *An Introduction to Copulas*. Secaucus, NJ, USA: Springer-Verlag New York, Inc., 2006.

[26] S. Mahadevan, "Bayesian Network with Copula-based Sampling for Multidisciplinary Design Optimization under Uncertainty," tech. rep., National Institute of Aerospace, 2015.

[27] S. H. To), "Latin Hypercube Sampling: Simple Definition."

[28] S. Hosder, R. Walters, and M. Balch, "Efficient Sampling for Non-Intrusive Polynomial Chaos Applications with Multiple Uncertain Input Variables," in *48th AIAA/ASME/ASCE/AHS/ASC Structures, Structural Dynamics, and Materials Conference*, 2007.

[29] A. Olsson, G. Sandberg, and O. Dahlblom, "On Latin hypercube sampling for structural reliability analysis," *Structural Safety*, vol. 25, pp. 47–68, 2002.

[30] L. Chrisman, "Latin Hypercube vs. Monte Carlo Sampling," 2014.

[31] M. Faes and D. Moens, "Recent Trends in the Modeling and Quantification of Non-probabilistic Uncertainty," no. February, 2019.

[32] Y. Ben-haim, "A non-probabilistic concept of reliability," vol. 14, no. February 1995, pp. 227–245, 1994.

[33] M. Colyvan, "Is Probability the Only Coherent Approach to Uncertainty ?," vol. 28, no. 3, 2008.

[34] A. A. Alola, M. Tunay, and V. Alola, "Analysis of Possibility Theory for Reasoning under Uncertainty," no. January 2015, 2013.

[35] D. Dubois and H. Prade, "Possibility Theory and Its Applications : Where Do We Stand ?," no. May 2016, 2017.

[36] D. Moens and D. Vandepitte, "A survey of non-probabilistic uncertainty treatment in finite element analysis," vol. 194, pp. 1527–1555, 2005.

[37] G. Alefeld and G. Mayer, "Interval analysis : theory and applications," vol. 121, pp. 421–464, 2000.

[38] N. Dăneţ, "Interval Analysis - A Powerfull Trend in Numerical Analysis," no. June 2007, 2014.

[39] A. Omerovic and K. Stølen, "Interval-Based Uncertainty Handling in Model-Based Prediction of System Quality," no. August 2010, 2017.

[40] Y. Luo, J. Zhan, J. Xing, and Z. Kang, "Non-probabilistic uncertainty quantification and response analysis of structures with a bounded field model," *Computer Methods in Applied Mechanics and Engineering*, vol. 347, pp. 663–678, 2019.

[41] T. Eifler, M. Wiebel, M. Haydn, T. Hauer, H. Birkhofer, and A. Bohn, "NON-PROBABILISTIC UNCERTAINTY ANALYSIS IN EARLY DESIGN STAGES," pp. 827–836, 2012.

[42] L. A. Zadeh, "The Concept of a Linguistic Variable and its Application to Approximate Reasoning," vol. 249, 1975.

[43] A. Abusam, K. J. Keesman, and G. Van Straten, "Forward and backward uncertainty propagation: An oxidation ditch modelling example," *Water Research*, vol. 37, pp. 429–435, jan 2003.

[44] K. W. Chau, "Reliability and performance-based design by artificial neural network," *Advances in Engineering Software*, vol. 38, no. 3, pp. 145–149, 2007.

[45] R. M. Cooke, T. A. Zang, D. N. Mavris, and J. C. Tai, "Sculpting: A Fast, Interactive Method for Probabilistic Design Space Exploration and Margin Allocation," in *16th AIAA/ISSMO Multidisciplinary Analysis and Optimization Conference*, 2015.

[46] B. Looss and A. Saltelli, "Introduction to sensitivity analysis," in *Handbook of Uncertainty Quantification*, pp. 1103–1122, Springer International Publishing, jun 2017.

[47] F. Pianosi, K. Beven, J. Freer, J. W. Hall, J. Rougier, D. B. Stephenson, and T. Wagener, "Sensitivity analysis of environmental models: A systematic review with practical workflow," 2016.

[48] R. Cooke, D. Kurowicka, D. Ababei, A. Hanea, O. Morales, and D. Lewandowski, "UNINET BBN Platform,"

[49] M. J. Small, "Updating Uncertainty in an Integrated Risk Assessment: Conceptual Framework and Methods," Tech. Rep. 6, 1995.

[50] M. D. McKay, J. D. Morrison, and S. C. Upton, "Evaluating prediction uncertainty in simulation models," *Computer Physics Communications*, 1999.

[51] P. D. Arendt, D. W. Apley, and W. Chen, "Quantification of Model Uncertainty: Calibration, Model Discrepancy, and Identifiability," *Journal of Mechanical Design*, vol. 134, p. 12, 2012.

[52] M. J. Bayarri, R. Paulo, J. O. Berger, J. Sacks, J. A. Cafeo, J. Cavendish, C. H. Lin, and J. Tu, "A framework for validation of computer models," *Technometrics*, no. 1537-2723, p. 18, 2007.

[53] C. Li and S. Mahadevan, "Role of calibration, validation, and relevance in multi-level uncertainty integration," *Reliability Engineering and System Safety*, 2016.

[54] R. K. Wong, C. B. Storlie, and T. C. Lee, "A frequentist approach to computer model calibration," *Journal of the Royal Statistical Society. Series B: Statistical Methodology*, vol. 79, no. 2, 2017.

[55] E. Patelli, Y. Govers, M. Broggi, H. M. Gomes, M. Link, and J. E. Mottershead, "Sensitivity or Bayesian model updating: a comparison of techniques using the DLR AIRMOD test data," *Archive of Applied Mechanics*, 2017.

[56] J. Norton, "An introduction to sensitivity assessment of simulation models," *Environmental Modelling and Software*, 2015.

[57] D. M. Hamby, "A Comparison of Sensitivity Analysis Techniques," *Health Physics*, vol. 68, no. 2, pp. 195–204, 1995.

[58] R. Pastres A'l, K. Chart, C. Solidoro, and C. Dejak, "Global sensitivity analysis of a shallow-water 3D model," tech. rep., 1999.

[59] G. Chastaing, "The design and sensitivity analysis of experiments," 2016.

[60] S. Marelli, C. Lamas, B. Sudret, and K. Konakli, "UQLab User Manual – Sensitivity Analysis,"

[61] M. L. Stein, "Design and Analysis of Computer Experiments," *Statistical Science*, vol. 4, pp. 432–433, dec 1989.

[62] G. Blatman and B. Sudret, "Sparse polynomial chaos expansions and adaptive stochastic finite elements using a regression approach," *Comptes Rendus - Mecanique*, vol. 336, pp. 518–523, jun 2008.

[63] S. Razavi, B. A. Tolson, and D. H. Burn, "Review of surrogate modeling in water resources," 2012.

[64] T. Crestaux, O. Le Maître, and J. M. Martinez, "Polynomial chaos expansion for sensitivity analysis," *Reliability Engineering and System Safety*, vol. 94, pp. 1161–1172, jul 2009.

[65] N. Wiener, "The Homogeneous Chaos," *American Journal of Mathematics*, vol. 60, p. 897, jul 2006.

[66] D. Xiu and G. E. Karniadakis, "Modeling uncertainty in flow simulations via generalized polynomial chaos," *Journal of Computational Physics*, vol. 187, pp. 137–167, may 2003.

[67] M. Eldred and J. Burkardt, "Comparison of Non-Intrusive Polynomial Chaos and Stochastic Collocation Methods for Uncertainty Quantification," American Institute of Aeronautics and Astronautics (AIAA), nov 2013.

[68] P. Ni, Y. Xia, J. Li, and H. Hao, "Using polynomial chaos expansion for uncertainty and sensitivity analysis of bridge structures," *Mechanical Systems and Signal Processing*, vol. 119, pp. 293–311, mar 2019.

[69] A. O 'hagan, "Bayesian Analysis of Computer Code Outputs: A Tutorial," 2004.

[70] M. C. Kennedy and A. O'Hagan, "Bayesian calibration of computer models," *Journal of the Royal Statistical Society: Series B (Statistical Methodology)*, 2001.

[71] J. Oakley and A. O'Hagan, "Bayesian inference for the uncertainty distribution of computer model outputs," *Biometrika*, vol. 89, no. 4, pp. 769–784, 2002.

[72] J. E. Oakley and A. O 'hagan, "Probabilistic sensitivity analysis of complex models: a Bayesian approach," *J. R. Statist. Soc. B*, vol. 66, no. 3, pp. 751–769, 2004.

[73] F. Pedregosa, G. Varoquaux, A. Gramfort, V. Michel, B. Thirion, O. Grisel, M. Blondel, P. Prettenhofer, , R. Weiss, V. Dubourg, J. Vanderplas, A. Passos, and E. Cournapeau, D. and Brucher, M. and Perrot, M. and Duchesnay, "Scikit-learn: Machine Learning in {P}ython," *Journal of Machine Learning Research*, vol. 12, pp. 2825—-2830, 2011.

[74] I. A. Basheer and M. Hajmeer, "Artificial neural networks: fundamentals, computing, design, and application," tech. rep., 2000.

[75] Y. Hu, F. Xie, B. Wu, and Y. Wang, "An Uncertainty Quantification Method Based on Generalized Interval," in *2013 12th Mexican International Conference on Artificial Intelligence*, 2013.

[76] C. Österheld, W. Heinze, and P. Horst, "Influence of Aeroelastic Effects on Preliminary Aircraft Design," in *ICAS 2000 CONGRESS*, 2000.

[77] G. Bindolino, G. Ghiringhelli, S. Ricci, and M. Terraneo, "Multilevel Structural Optimization for Preliminary Wing-Box Weight Estimation," *Journal of Aircraft*, 2010.

[78] A. Sanchez-Carmona, C. Cuerno-Rejado, and L. Garcia-Hernandez, "Unconventional Tail Configurations for Transport Aircraft," *Progress in Flight Physics*, vol. 9, pp. 137–140, 2017.

[79] L. Green, H.-Z. Lin, and M. Khalessi, "Probabilistic Methods for Uncertainty Propagation Applied to Aircraft Design," in *20th AIAA Applied Aerodynamics Conference*, 2002.

[80] E. Kesseler, W. J. Vankan, A. Collaborative, and M. Design, "Multidisciplinary design analysis and multi-objective optimisation applied to aircraft wing," vol. 1, no. 2, 2006.

[81] W. J. Vankan, E. Kesseler, M. Laban, and A. Collaborative, "Multi-objective Optimisation of Aircraft Range and Fuel Consumption," pp. 10–13, 2008.

[82] J. J. Alonso, P. Legresley, and V. Pereyra, "Aircraft design optimization," vol. 79, pp. 1948–1958, 2009.

[83] A. Kale, E. Acar, R. T. Haftka, and W. J. Stroud, "Why are Airplanes so Safe Structurally? Effect of Various Safety Measures on Structural Safety of Aircraft," in *45th AIAA/ASME/ASCE/AHS/ASC Structures, Structural Dynamics & Materials Conference*, 2004.

[84] E. Acar and R. T. Haftka, "Reliability Based Aircraft Structural Design Optimization with Uncertainty about Probability Distributions," in *6th World Congresses of Structural and Multidisciplinary Optimization*, p. 10, 2005.

[85] M. J. Daskilewicz, B. J. German, T. T. Takahashi, S. Donovan, and A. Shajanian, "Effects of disciplinary uncertainty on multi-objective optimization in aircraft conceptual design," *Structural and Multidisciplinary Optimization*, 2011.

[86] D. Neufeld, J. Chung, and K. Behdinian, "Aircraft Conceptual Design Optimization Considering Fidelity Uncertainties," *Journal of Aircraft*, 2011.

[87] J. Miguel, P. Liquito, D. Maria, A. Dos, S. Gonçalves De Aguiar, and G. Sintra, *Design of Wing Structural Elements with Uncertainty in Materials, Loads and Sizing*.
PhD thesis, Instituto Superior Técnico, 2012.

[88] D. Böhnke, F. Dorbath, B. Nagel, and V. Gollnick, "Multi-Fidelity Wing Mass Estimations based on a Central Model Approach," in *71th Annual Conference of Society of Allied Weight Engineers*, p. 18, 2012.

[89] L. Jaeger, C. Gogu, S. Segonds, and C. Bes, "Aircraft Multidisciplinary Design Optimization Under Both Model and Design Variables Uncertainty," *Journal of Aircraft*, 2013.

[90] A. Elham, *Weight Indexing for Multidisciplinary Design Optimization of Lifting Surfaces*.
PhD thesis, 2013.

[91] A. Elham, G. La Rocca, and M. J. L. Van Tooren, "Development and implementation of an advanced, design-sensitive method for wing weight estimation," *Aerospace Science and Technology*, 2013.

[92] J. A. Corman, D. Rancourt, C. H. Lee, D. N. Mavris, T. Wilson, and b. A. Jason Corman, "Preliminary Wing Weight Estimation Under Probabilistic Loads for a Transport Aircraft," *55th AIAA SciTech Forum*, 2014.

[93] H. U. Park, J. Chung, and D. Neufeld, "Uncertainty based aircraft derivative design for requirement changes," *Aeronautical Journal*, 2016.

[94] V. S. JOHNSON, "Minimizing life cycle cost for subsonic commercial aircraft," *Journal of Aircraft*, 1990.

[95] L. DeLaurentis and D. Mavris, "Uncertainty modeling and management in multidisciplinary analysis and synthesis," in *38th Aerospace Sciences Meeting and Exhibit*, 2000.

[96] K. Gantois and A. J. Morris, "The multi-disciplinary design of a large-scale civil aircraft wing taking account of manufacturing costs," *Struct Multidisc Optim*, vol. 28, pp. 31–46, 2004.

[97] M. Hüseyin Kudak and S. Ercan, "Uncertainty Assessment of Aircraft Maintenance Times," *Journal of Aeronautics and Space Technologies January*, vol. 4, no. 1, pp. 89–97, 2009.

[98] A. R. Mileham, M. E. Saravi, C. A. McMahon, L. B. Newnes, and Y. M. Goh, "Uncertainty in Through-Life Costing-Review and Perspectives," *IEEE Transactions on Engineering Management*, vol. 57, no. 4, pp. 689–701, 2010.

[99] N. W. Simone, M. E. Stettler, and S. R. Barrett, "Rapid estimation of global civil aviation emissions with uncertainty quantification," *Transportation Research Part D: Transport and Environment*, 2013.

[100] R. Torres and C. Bes, "Uncertainty Tolerance of Multiobjective Environmentally Friendly Departure Procedures for Civil Aircraft," *Journal of Aircraft*, 2011.

[101] N. Lindsley, P. Beran, and C. Pettit, "Effects of Uncertainty on Nonlinear Plate Response in Supersonic Flow," in *9th AIAA/ISSMO Symposium on Multidisciplinary Analysis and Optimization*, 2002.

[102] M. Karpel, B. Moulin, and M. Idan, "Robust Aeroservoelastic Design with Structural Variations and Modeling Uncertainties," *Journal of Aircraft*, 2003.

[103] C. L. Pettit, "Uncertainty Quantification in Aeroelasticity: Recent Results and Research Challenges," *Journal of Aircraft*, 2004.

[104] T. Kier, G. Looye, and J. Hofstee, "Development of Aircraft Flight Loads Analysis Models With Uncertainties for Pre-Design Studies," *International Forum on Aeroelasticity and Structural Dynamics 2005*, pp. 1–13, 2005.

[105] X. Wu, W. Zhang, and S. Song, "Uncertainty Quantification and Sensitivity Analysis of Transonic Aerodynamics with Geometric Uncertainty," *International Journal of Aerospace Engineering*, 2017.

[106] H. N. Najm, "Uncertainty Quantification and Polynomial Chaos Techniques in Computational Fluid Dynamics," *Annual Review of Fluid Mechanics*, 2009.

[107] S. Hosder and R. Walters, "Non-Intrusive Polynomial Chaos Methods for Uncertainty Quantification in Fluid Dynamics," in *48th AIAA Aerospace Sciences Meeting Including the New Horizons Forum and Aerospace Exposition*, 2010.

[108] L. Zhao and X. Zhang, "Uncertainty Quantification of a Flapping Airfoil with Stochastic Velocity Deviations Using the Response Surface Method," tech. rep., 2011.

[109] Y. Zhang, *Efficient uncertainty quantification in aerospace analysis and design*. PhD thesis, 2013.

[110] G. Georgiou, H. H. Khodaparast, and J. E. Cooper, "Uncertainty Quantification of Aeroelastic Stability," in *Mathematics of Uncertainty Modeling in the Analysis of Engineering and Science Problems*, ch. 16, pp. 329–356, IGI Global, 2014.

[111] I. Tartaruga, J. E. Cooper, M. H. Lowenberg, P. Sartor, S. Coggon, and Y. Lemmens, "Prediction and uncertainty propagation of correlated time-varying quantities using surrogate models," *CEAS Aeronautical Journal*, p. 14, 2016.

[112] I. Tartaruga, J. E. Cooper, G. Georgiou, and H. Khodaparast, "Flutter Uncertainty Quantification for the S4T Model," *55th AIAA Aerospace Sciences Meeting*, pp. 1–16, 2017.

[113] I. Tartaruga, J. E. Cooper, G. Georgiou, and H. H. Khodaparast, "Uncertainty Quantification of Flutter for a Supersonic Vehicle," *55th AIAA Aerospace Sciences Meeting*, pp. 1–16, 2017.

[114] C. L. Pettit and P. S. Beran, "Effects of Parametric Uncertainty on Airfoil Limit Cycle Oscillation," *Journal of Aircraft*, 2019.

[115] A. Manan and J. Cooper, "Design of Composite Wings Including Uncertainties: A Probabilistic Approach," *Journal of Aircraft*, 2009.

[116] A. Manan and J. E. Cooper, "Prediction of uncertain frequency response function bounds using polynomial chaos expansion," *Journal of Sound and Vibration*, 2010.

[117] G. Georgiou, A. Manan, and J. E. Cooper, "Modeling composite wing aeroelastic behavior with uncertain damage severity and material properties," *Mechanical Systems and Signal Processing*, 2012.

[118] C. Scarth, J. E. Cooper, P. M. Weaver, and G. H. Silva, "Uncertainty quantification of aeroelastic stability of composite plate wings using lamination parameters," *Composite Structures*, 2014.

[119] C. Scarth, P. N. Sartor, J. E. Cooper, P. M. Weaver, and G. H. C. Silva, "Robust and Reliability-Based Aeroelastic Design of Composite Plate Wings," *AIAA Journal*, 2017.

[120] C. Scarth and J. E. Cooper, "Reliability-based aeroelastic design of composite plate wings using a stability margin," *Structural and Multidisciplinary Optimization*, 2018.

[121] D. Allwright, M. Brown, and P. Munday, "Independent review and enhancement of weight estimation methods for aircraft weight outlook," tech. rep., Smith Institute, 2014.

[122] Bilal M. Ayyub, *Elicitation of Expert Opinions for Uncertainty and Risks*. Boca Raton: CRC Press, 2001.

[123] R. M. Cooke, *Experts in uncertainty: Opinion and subjective probability in science*. New York, NY: Oxford University Press, 1991.

[124] W. Aspinall, "A route to more tractable expert advice," *Nature*, vol. 463, p. 294, jan 2010.

[125] M. G. Tyshenko, S. ElSaadany, T. Oraby, S. Darshan, W. Aspinall, R. Cooke, A. Catford, and D. Krewski, "Expert elicitation for the judgment of prion disease risk uncertainties," *Journal of Toxicology and Environmental Health - Part A: Current Issues*, vol. 74, pp. 261–285, jan 2011.

[126] M. Aseeri, M. R. Ahmed, M. Aseeri $, S. Kaiser, N. Z. Zenia, and Z. I. Chowdhury, "A Novel Algorithm for Malicious Attack Detection in UWSN Mitigating voltage emergencies in Chip-Multiprocessors (CMP) View project CMOS Circuits for Single Chip Vehicle Radar View project A Novel Algorithm for Malicious Attack Detection in UWSN," tech. rep., 2015.

[127] K. SENTZ and S. FERSON, "Combination of Evidence in Dempster-Shafer Theory," tech. rep., 2002.

[128] D. Xu and Y. Tian, "A Comprehensive Survey of Clustering Algorithms," *Annals of Data Science*, vol. 2, no. 2, pp. 165–193, 2015.

[129] D. E. Calderon, J. E. Cooper, M. Lowenberg, and S. A. Neild, "On the Effect of including Geometric Nonlinearity in the Sizing of a Wing," in *AIAA SciTech Forum, Kissimmee, Florida*, 2018.

[130] T. Lefebvre, P. Schmollgruber, C. Blondeau, and G. Carrier, "Aircraft Conceptual Design in a Multi-Level, Multi-Fidelity, Multi-Disciplinary Optimization Process," in *28th International Congress of the Aeronautical Sciences*, 2012.

[131] T. Bach, T. Führer, and S. Dähne, "Automated Sizing of a composite wing for the usage within a multi-disciplinary design process," in *4th EASN Workshop. Flight Physics. Aircraft Design*, p. 12, 2014.

[132] Egbert Torenbeek, *Advanced Aircraft Design*. 2013.

[133] D. Hansen, "Painting versus Polishing of Airplane Exterior Surfaces," 1999.

[134] X. Lu and H.-X. Li, "Perturbation Theory Based Robust Design Under Model Uncertainty," *Journal of Mechanical Design*, 2009.

[135] H. G. Beyer and B. Sendhoff, "Robust optimization - A comprehensive survey," *Computer Methods in Applied Mechanics and Engineering*, 2007.

[136] K. H. Lee and G. J. Park, "Robust optimization considering tolerances of design variables," *Computers and Structures*, 2001.

[137] M. S. Eldred, "Design under Uncertainty Employing Stochastic Expansion Methods," *International Journal for Uncertainty Quantification*, 2011.

[138] X. Du and W. Chen, "Efficient Uncertainty Analysis Methods for Multidisciplinary Robust Design," *AIAA Journal*, 2002.

[139] L. Brevault, M. Balesdent, N. Bérend, and R. Le Riche, "Decoupled Multidisciplinary Design Optimization Formulation for Interdisciplinary Coupling Satisfaction Under Uncertainty," *AIAA Journal*, 2016.

[140] Y. K. Wen, "Reliability and performance-based design," *Structural Safety*, vol. 23, pp. 407–428, 2001.

[141] N. B. Price, M. Balesdent, S. Defoort, R. L. Riche, N. H. Kim, and R. T. Haftka, "Safety-margin-based design and redesign considering mixed epistemic model uncertainty and aleatory parameter uncertainty," apr 2019.

[142] X. Du, "Reliability-based design optimization with dependent interval variables," *International Journal for Numerical Methods in Engineering*, 2012.

[143] M. F. Othman, G. H. C. Silva, P. H. Cabral, and A. P. Prado, "A Robust and Reliability-Based Aeroelastic Tailoring Framework for Composite Aircraft Wings," 2018.

[144] M. C. Niu, *Airframe Stress Analysis and Sizing*.
Hong Kong : Conmilit Press; Los Angeles, Calif. : Technical Book Co. (distributor), 3 ed., 2011.